CRANFIELD UNIVERSITY

ESTIVALIZ LOZANO MINGUEZ

FATIGUE & FRACTURE MECHANICS OF OFFSHORE WIND TURBINE SUPPORT STRUCTURES

SCHOOL OF ENERGY, ENVIRONMENT AND AGRIFOOD
Energy Division

Thesis Submitted for the Degree of Doctor of Philosophy
Academic Year: 2015

Supervisor: Professor Feargal Brennan
Doctor Athanasios Kolios
July 2015

CRANFIELD UNIVERSITY

SCHOOL OF ENERGY, ENVIRONMENT AND AGRIFOOD
Energy Division

Thesis Submitted for the Degree of Doctor of Philosophy

Academic Year 2015

ESTIVALIZ LOZANO MINGUEZ

FATIGUE & FRACTURE MECHANICS OF OFFSHORE WIND TURBINE SUPPORT STRUCTURES

Supervisor: Professor Feargal Brennan
Doctor Athanasios Kolios
July 2015

ABSTRACT

Wind power, especially offshore, is considered to be one of the most promising sources of ‘clean’ energy towards meeting the EU targets for 2020 and 2050. However, its popularity has always fluctuated with the price of fossil fuels since nowadays wind electricity production cannot compete with nuclear or coal electricity production. Support structures are thought to be one of the main drivers for reducing costs in order to make the wind industry more economically efficient. Foundations and towers should be fit for purpose, extending their effective service life but avoiding costs of oversizing.

An exhaustive review of the background and state of the art of the Fatigue-Life assessment approaches has been carried out, combining analysis of the gathered experimental data and the development of Finite Element models based on contemporary 3D solid models with diverse Regression Analyses, in order to identify their weakness and evaluate their accuracy. This research shows that the guides and practices currently employed in the design and during the operation of the offshore wind turbine support structures are obsolete and not useful for optimisation, which generally leads to conservationism and an unnecessary increase in costs.

The basis for a comprehensive update of the Girth Weld and Tubular Joint S-N curves and the Stress Concentration Factors of Tubular Joints has been set out. Furthermore, a reliable methodology for deriving the Stress Intensity Factor at the deepest point of a semi-elliptical surface saddle crack in a tubular welded T-joint has been proposed.

Keywords:

Tubular Joint, Offshore Wind Support Structure, Stress Concentration Factor, Stress Intensity Factor, S-N curve, Semi-elliptical crack, Tubular Joint Weld Profile

ACKNOWLEDGEMENTS

The research period has been more challenging than I or anyone could imagine. I have learned much more than I expected and have needed more support than I would have wished; therefore, it is not possible to individually thank all the people who have helped me.

I grant the deepest gratitude to my main supervisor, Prof. F.P. Brennan, for his invaluable supervision, exceptional guidance, and continuous encouragement. I am also extremely grateful to my second supervisor, Dr. A. Kolios, for encouraging me to do a PhD and for his excellent advice. Their faith in me has given me the strength to complete this research.

I would like to express my appreciation to all current and past staff and my colleagues in the Department of Offshore Process & Energy Engineering, especially to Mr. E. Pérez-López and Mrs. S. Skears, for their help.

I would also like to express my sincere thanks to Prof. E. Giner-Maravilla for giving me the opportunity to do a Research Stay at the Department of Mechanical and Materials Engineering of the Universidad Politécnica de Valencia (UPV) and for his numerous and masterful suggestions. Special thanks are also due to my colleagues in the UPV who have made this stay a constructive and pleasant experience.

Last but not least, I would like to acknowledge my family and my fiancé, Carlos, because I would not have been able to carry on without their support, sacrifices, patience, and love.

Dedicated to my parents, Ernesto and María José

"The greatest glory in living lies not in never falling, but in rising every time we fall."

Ralph Waldo Emerson

American essayist, lecturer, and poet

(1803-1882)

TABLE OF CONTENTS

LIST OF FIGURES

LIST OF TABLES

LIST OF ABBREVIATIONS

x_1, x_{2b} and x_{2c}	Extrapolation points
a	Crack depth
c	Half crack length
a/c	Crack aspect ratio
a/T	Normalised crack depth
A, B, D	Weldment nodes
ALS	Accidental Limit State
API	American Petroleum Institute
AVS	Average stress
AWS	American Welding Society
BS	British Standard
C_i	Axis intercept
C_0 , C_1 , C_2	Regression coefficients
C_D	Drag coefficient
C_M	Coefficient of virtual mass
CJP	Complete Joint Penetration
CP	Cathodic Protection
CT	Compact Tension
d	Brace diameter
$\frac{da}{dN}$	Crack propagation rates
D	Chord diameter
D_C	Cumulative fatigue damage
D_D	Design fatigue damage
DECC	Department of Energy and Climate Change
DEn	Department of Energy
DFF	Design Fatigue Factor
DoB	Degree of Bending
ECSC	European Coal and Steel Community
ECCS	European Convention for Constructional Steelwork
EWEA	European Wind Energy Association

F	Fillet weld size
F_D	Drag force
F_I	Inertia force
FE	Finite Element
FIT	Feed-in tariffs
FLS	Fatigue Limit State
G	Energy release rate
HAWT	Horizontal Axis Wind Turbine
HMSO	Her Majesty's Stationery Office
HSE	Health & Safety Executive
HSS	Hot Spot Stress
IIW	International Institute of Welding
IPB	In-Plane Bending
K_{Ic}	Fracture toughness
l	Brace length
L	Chord length
LEFM	Linear Elastic Fracture Mechanics
LR	Lloyd's Register
LSM	Least Squares Method
m	Slope of the S-N curve
MLM	Maximum Likelihood Method
N	Number of cycles
n_{sd}	Number of standard deviations
OD	Outer diameter
OPB	Out-Plane Bending
O&M	Operation and maintenance
$\vec{q}$	Crack extension direction
r	Brace radius
R	Chord radius
$\mathbb{R}$	Root opening
R_d	Design resistance
R_σ	Stress ratio

R_w	Weldment curvature
S	Ratio of the SCF_{av} to the SCF_{HS}.
S_d	Design load effect
SCF	Stress Concentration Factor
SCF_{av}	Average stress concentration factor
SCF_{HS}	Hot spot stress concentration factor
SE	Standard Error
SIF (or K)	Stress intensity factor
SLS	Serviceability Limit State
S-N	Stress-life
SSE	Sum of Squared Deviations
SSR	Sum of squared Residuals
SWL	Sea water line
t	Brace thickness
T	Chord thickness
t_w	Theoretical weld
TPM	Two-phase model
$\vec{u}$	Velocity of the wave particles
UCL	University College London
UK	United Kingdom
UKOSRP	United Kingdom Offshore Steels Research Project
ULS	Ultimate Limit State
VAWT	Vertical Axis Wind Turbine
WT	Wall thickness
w	Plate width
x	Distance from the crack mouth
Y	Stress intensity modification factor
ΔK_{th}	Threshold stress intensity factor range
$\Delta\sigma$	Stress Range
σ_{HS}	Hot spot stress
σ_m	Mean stress
σ_{nom}	Nominal stress

σ_{sd}	Standard deviation of $\log_{10} N$
σ_y	Yield stress
φ	Brace to chord inclination angle
α	Chord stub slenderness ratio
β	Brace to chord diameter ratio
γ	Chord wall slenderness ratio
γ_f	Partial safety factor for loads
γ_m	Partial safety factor for materials
τ	Brace to chord thickness ratio
θ	Angle measured around intersection from saddle toe
Ψ	Dihedral angle
ω	End preparation angle
ϕ	Joint included angle
ζ	Weld angle
ζ_t	Weld toe angle
ρ	Weld toe radius
χ	Thickness exponent
3D	Three-dimensional space

1 INTRODUCTION AND BACKGROUND

1.1 Introduction

Energy forecasts predict significant growth in demand in the coming decades, approximately 57% over the next 25 years [1], caused by increasing economic growth rates all over the world but especially in developing countries, as can be appreciated from Figure 1-1 [2].

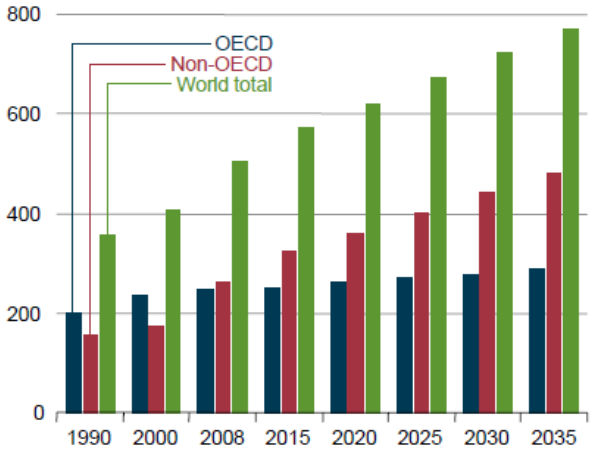

Figure 1-1 World energy consumption, 1990-2035 (quadrillion Btu) [2].

Fossil fuels – coal, oil, and gas – supplied 81% of world primary energy demand in 2010 [3]. It is estimated that the world's total liquids, coal and natural gas consumption increased by 1, 1.5 and 1.6% per year on average from 2008 to 2035 respectively; while renewables consumption increases by 2.8% per year on average, as shown in Figure 1-2 [2].

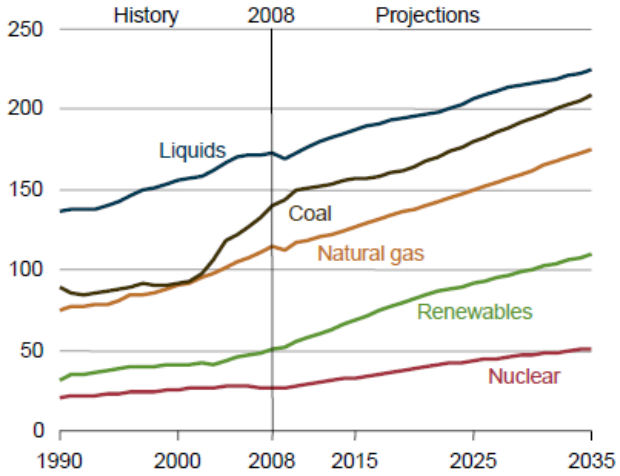

Figure 1-2 World energy consumption by fuel, 1990-2035 (quadrillion Btu) [2].

Renewable energy may be obtained from a wide range of sources, as can be observed in Figure 1-3.

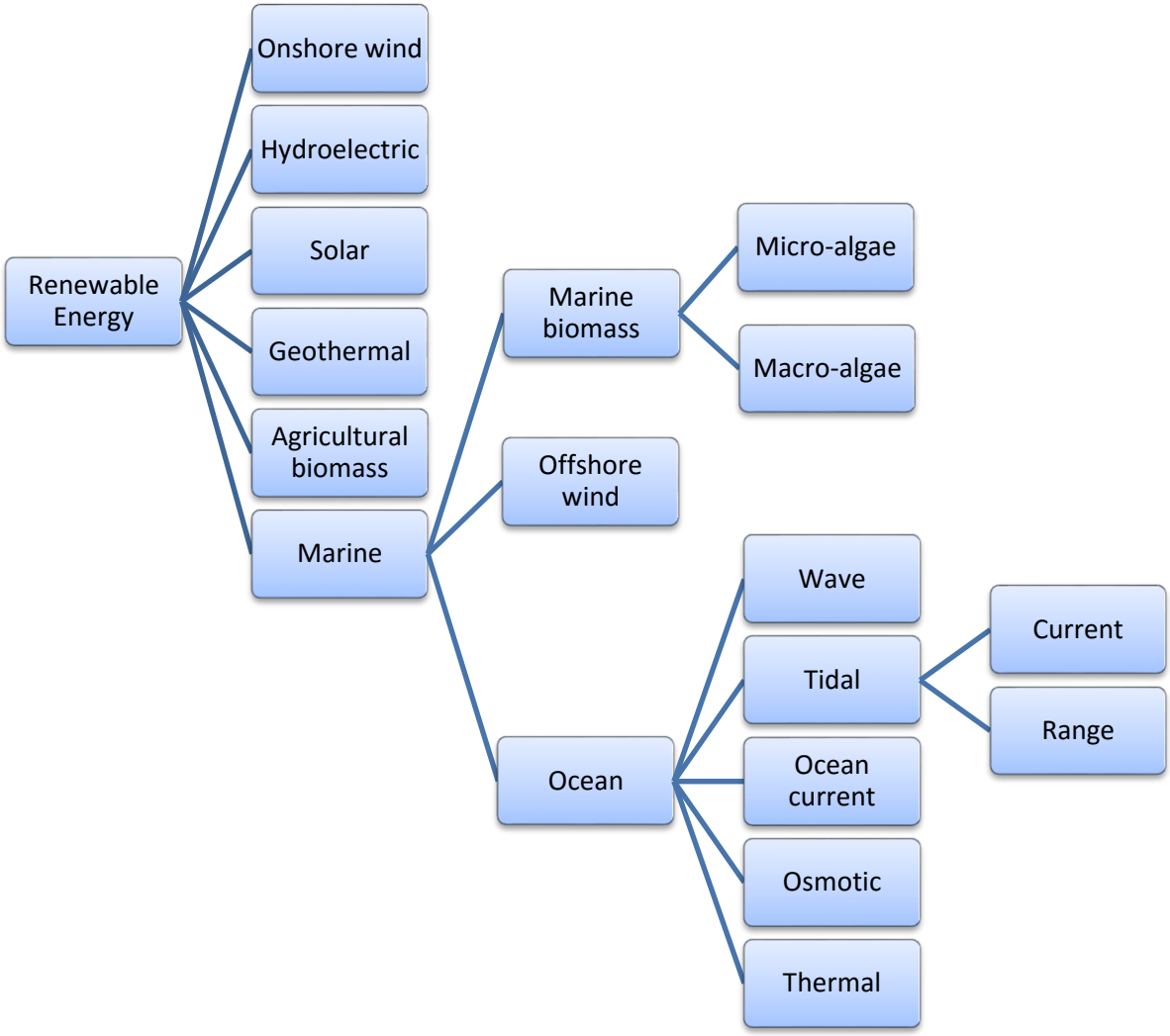

Figure 1-3 Renewable energy classification.

This commitment to renewable energy is not only caused by the depletion of fossil fuels, since oil and gas reserves are enough to last for decades and in the case of coal for centuries, and possible undiscovered resources will extend these projections [4]. A real driver for renewable energy is that fossil energy resources contain significant amounts of carbon that are released during combustion and carbon dioxide (CO_2) emissions are estimated to contribute 75% of the potential global warming effect [5]. The concentration of CO_2 in the atmosphere has risen from 280 ppm before the start of the industrial era to around 390 ppm today [6]. If no measures are implemented, current climate models predict CO_2

concentrations of more than 700 ppm [7], a rise of up to 6°C [8] and sea levels rising between 9 and 88 centimetres by 2100 [9]. Considering human health, the World Health Organization (WHO) has estimated that between 25 and 33% of the global burden of disease is caused by environmental factors [10]. Figure 1-4 shows the mean values of health effects, presented as deaths/TWh, for the respective forms of electricity generation throughout the EU [11].

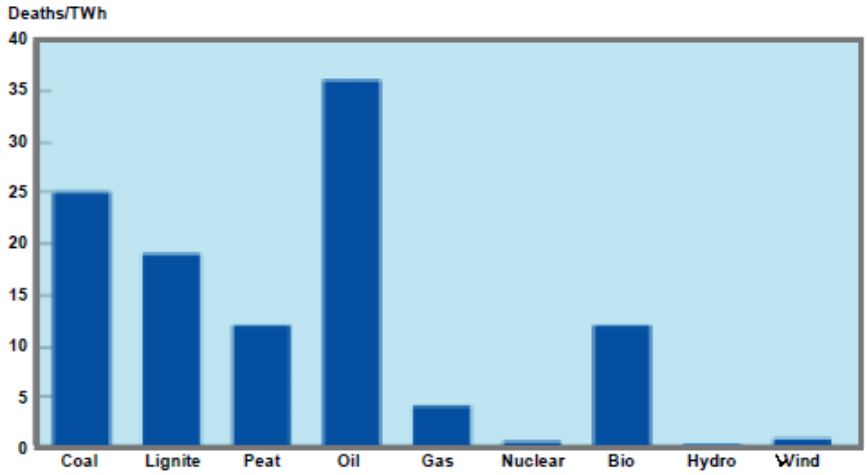

Figure 1-4 Mean values of health effects throughout the EU by fuel [11].

The Kyoto Protocol was drawn up in 1997 at the United Nations Framework Convention on Climate Change aiming to fight global warming, but it did not become international law until 2005 [12]. To meet the commitment of the Kyoto Protocol, the European leaders agreed a reduction in EU greenhouse gas emissions of at least 20% below 1990 levels through a 20% share of total energy from renewable sources by 2020 [13]. At the same time, the EU aims to increase energy security in order to provide affordable and reliable supplies to consumers, as well as create employment since renewable energy is local.

Marine renewable energy could provide up to 50% of Europe's electricity needs by 2050; which would contribute to energy supply and security, reduce CO_2 emissions, improve the overall state of the environment, create jobs and improve quality of life [14]. Wind power, especially offshore, is considered one of the most promising sources of ‘clean’ energy towards meeting the EU and UK targets for 2020 and 2050. Comprehensive Marine Spatial Planning frameworks must be established in order to minimise and manage potential conflicts; since this sector

will compete for space with other legitimate uses of the sea such as aquaculture, fisheries, maritime transport or recreation [14].

Nowadays wind electricity production cannot compete with nuclear or coal electricity production, as shown in Figure 1-5. Therefore, it is an essential requirement to make these renewable sources more economically efficient in order to achieve the EU's targets.

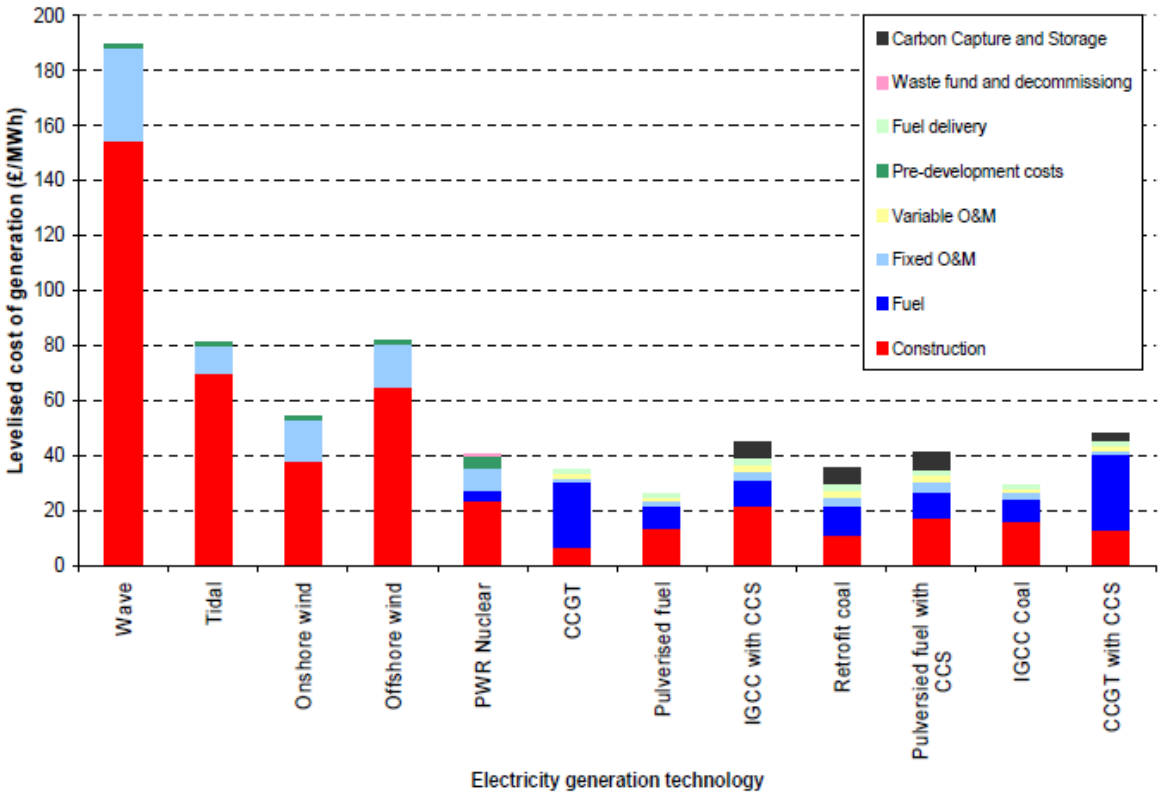

Figure 1-5 Cost of generating electricity (£pence per MWh) [15].

Some key design decisions, which may help to reduce energy costs, are on: structural material and size, redundancy, distance to shore, maintenance location – onshore or offshore –, frequency and duration of maintenance, types of vessels required for deployment and maintenance, health and safety.

This First Chapter of the thesis will briefly review the background to the fatigue and fracture research of tubular structures, to better identify and understand the key design concepts. Particular attention is given to the stress analysis based on the Finite Element (FE) Method, since it will be applied in the remaining chapters.

1.2 Stress Analysis

Marine and offshore structures are subjected to environmental and operational loads, withstanding cyclic stresses which will deteriorate their mechanical properties; hence, fatigue damage assessment is crucial for estimating service life. Steel tubular welded elements are widely used in marine and offshore structures because of their relatively high strength, non-directional bending strength and low drag coefficient.

The stresses in tubular welded connections may be classified in three groups:

- Nominal stresses, which represent the structural response of individual members to applied loads.
- Geometric stresses, which are developed because of the differences in the deformation of brace and chord under applied loads.
- Notch stresses, which occur in the weld toe region caused by the extra stiffening effect of the weld on the tube walls.

The hot spot stress, or geometrical stress approach, has been adopted in the development of most design guidance for offshore structures, since it greatly improves correlation with observed fatigue life [16]. The definition of hot spot stress (HSS) was drafted by the review panel of the United Kingdom Offshore Steels Research Project (UKOSRP) and adopted by the UK Department of Energy (DEn) Guidance Notes [17] and states that it is the value calculated by the extrapolation to the weld toe of the maximum principal stresses at a distance x_1 and x_2 (see Figure 1-6).

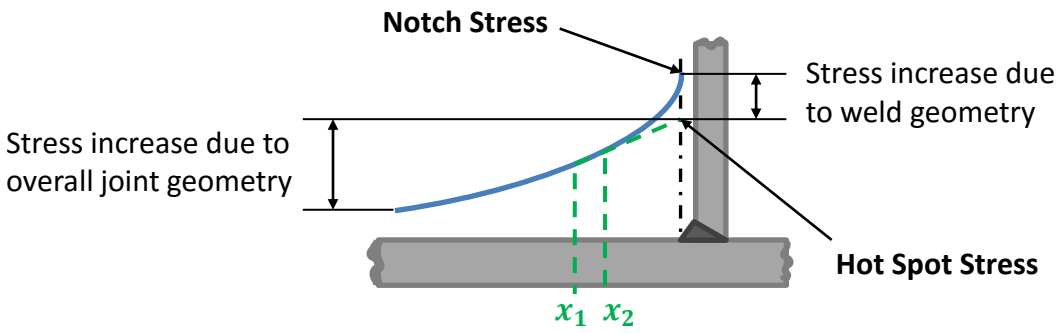

Figure 1-6 Different stresses.

The notch stress is the peak stress, which is situated at the weld toe region. The notch stress concept is attractive since it is a real stress, in contrast to the extrapolated conceptual HSS which incorporates the effects of joint geometry but neglects the influence of the weld. However, the HSS approach has been adopted in the development of most design guidance for offshore structures, since notch stresses cannot be measured directly at the weld using strain gauge measurements.

1.2.1 Definition of Stress Concentration Factor

The changes of section and the welds at the intersection result in modifications of the stress distribution, causing high stress concentrations where structures are susceptible to failure. This location of high stress is referred to as stress concentration and is quantitatively measured by the stress concentration factor (SCF); which is defined as the ratio of the maximum stress in the body (σ_{max} , τ_{max}) to the nominal stress (σ_{nom} , τ_{nom}):

$$SCF_t = \frac{\sigma_{max}}{\sigma_{nom}} \quad \text{for normal stress (tension or bending)} \qquad \textbf{Eq. 1-1}$$

$$SCF_t = \frac{\tau_{max}}{\tau_{nom}} \quad \text{for shear stress (torsion)} \qquad \textbf{Eq. 1-2}$$

Where the subscript t indicates that it is a theoretical factor. In general, the stress of interest is usually on the net cross section.

Assessing the magnitude of the stress concentration is a requirement to deal with the fatigue problem, because its presence has aggravated the fatigue of tubular joints in many existing offshore structures [18]. For tubular welded joints, much research has been carried out towards the estimation of the HSS range through the SCF; SCFs may be obtained analytically from the Elasticity Theory, computationally from the FE method, and experimentally using methods such as photoelasticity or strain measurements. Although the analytical solutions assume that the material is isotropic and homogeneous, it is possible to achieve a good agreement with the experimental work if it is conducted with precision [19].

As Ref. [19] points out: “two or more stress concentrations occurring at the same location in a structural member are said to be in a state of multiple stress

concentration"; for example, a radial hole through a groove which will lead to a higher stress than would occur with the groove alone. In general, the multiple SCF (SCF_{tm}) of the element cannot be deduced from the different SCF_t, but it can be considered that SCF_{tm} is equal to the product of the different SCF_t as this will be its maximum value:

$$\max(SCF_{t_i}) < SCF_{tm} \leq \prod_{i=1}^{n} SCF_{t_i} \qquad \textbf{Eq. 1-3}$$

Where n is the number of stress concentrations and i takes values from 1 to n.

If several types of loads act over a structural member, the stress for each type of load has to be evaluated separately and then the individual stresses are superimposed [19], as follows:

$$\sum_{i=1}^{n} \sigma_{max_i} = \sum_{i=1}^{n} \sigma_{nom_i} SCF_{t_i} \qquad \textbf{Eq. 1-4}$$

Where n is the number of loads, i takes values from 1 to n, σ_{nom_i} represents the different reference nominal stresses, and σ_{max_i} represents the different maximum stresses.

This is known as the Principle of Superposition, which presupposes a linear relationship between the applied loading and resulting response (the elastic limit of the material must be greater than the maximum stress).

1.2.2 Degree of Bending

The fatigue life of welded tubular joints in offshore structures is significantly influenced by the through thickness stress distribution, which may be characterised by the degree of bending (DoB). This is defined as the ratio of bending stress (σ_B) over total external stress (the sum of the bending and membrane stress (σ_M) components) on the outer surface of the chord, and is expressed as:

$$DoB = \frac{\sigma_B}{\sigma_B + \sigma_M} \qquad \textbf{Eq. 1-5}$$

The stress components can be expressed as:

$$\sigma_M = \frac{1}{T}\int_0^T \sigma(x)\, dx \qquad \textbf{Eq. 1-6}$$

$$\sigma_B = \frac{6}{T^2}\int_0^T \sigma(x)\left(\frac{T}{2} - x\right)\, dx \qquad \textbf{Eq. 1-7}$$

Where T is the chord wall thickness, $\sigma(x)$ is the local notch stress distribution, and x is the distance from the surface.

1.3 Fatigue-Life Assessment

There are two basic approaches used in the fatigue-life assessment of tubular joints: the first based on S-N curves obtained from carrying out constant amplitude fatigue test on tubular joints in combination with Miner's Linear Damage Summation rule; the second based on linear elastic fracture mechanics (LEFM) crack growth models. Both approaches are often used sequentially, the S-N approach would be used at the 'design' stage and then the fracture mechanics approach would be used to determine inspection intervals or time to repair [20].

1.3.1 S-N approach to Fatigue Life Predictions

The S-N approach relates the stress range ($\Delta\sigma$) at a point under consideration to the number of cycles (N) to failure [21], allowing the designer to estimate the safe life of individual connections subjected to varied levels of cyclic stress [22].

$$log_{10}N = C_{SN} - m\ log_{10}\Delta\sigma \qquad \textbf{Eq. 1-8}$$

Where C_{SN} is the intercept of the S-N curve with the $Log_{10}N$ axis and m is the negative inverse slope of the S-N curve.

It is necessary to define the two parameters that describe the S-N curves:

- Number of cycles (N)

Four states of failure were suggested by the UK Design Guidance Review Panel as follows [22]:

N_1 First discernible surface cracking as noted by any available method. This stage is considered to have passed if the initial surface length is found to be greater than 20 mm.

N_2 Intermediate surface cracking as detected by visual examination without the use of crack enhancement fluids or optical aids. However, if Non-Destructive Testing (NDT) techniques indicate a crack length of 30 mm, this stage is considered to have been reached.

N_3 First through-wall cracking as detected either visually or, more accurately, by loss of internal pressure or by NDT.

N_4 End of test occasioned by complete severance of a brace member, extensive cracking leading to loss of load symmetry or exhaustion of actuator stroke.

Ref. [23] observed that once the crack has gone through the thickness of wall, the stiffness of the joint decreases quickly. Moreover, it is unlikely to achieve the N_4 stage because the load redistribution in the structure configuration will make the joint redundant and possibly non-load carrying when N_3 has been attained [21]. For these reasons, N_3 has been defined as the end of fatigue life of a tubular joint. Although in general, the choice between one of these failure criteria depends on NDT capabilities.

- Stress range ($\Delta\sigma$)

The stress range is the difference between maximum and minimum stress values in the constant stress amplitude fatigue test. Different approaches to the S-N analysis can be found in the literature, depending on the stress analysis results selected as reference (see Section 1.2). The majority of material and structure fatigue properties are expressed in terms of a constant amplitude stress range because it is not possible to provide material or component fatigue behavioural information for each combination of load sequence [24]. Being necessary to determine equivalent cyclic spectrums from irregular loading sequences. Various methods for cycle counting variable amplitude load sequences have been developed, such as Peak counting methods [25] and Range Pair counting method

[24], but the most sophisticated and generally accepted is the Rainflow or Padoga roof counting method [26].

The decrease in fatigue strength for thicker joints, which is known as the "thickness effect", is a generally accepted trend; however, the scale of the decrease and the reasons for the shorter lives for thicker joints are still the subject of some controversy. The main reasons given for thicker sections having lower fatigue resistance for the same stress range are: the "geometric effect", where the decrease is primarily caused by the increased local weld toe stresses caused by the change in weld geometry of the thicker joints; the “volumetric effect”, where simply having more material implies a greater likelihood of having more defects; and the “stress gradient effect”, which applies to thin sections under bending and the associated steep stress decay gradient which has been demonstrated to make thinner sections relatively strong against fatigue.

For convenience, the effects of thickness on fatigue strength are given by the parameter χ, which is obtained from the relationship:

$$\chi = \frac{\log\left(\frac{\Delta\sigma}{\Delta\sigma_o}\right)}{\log\left(\frac{t_o}{t}\right)} \qquad \textbf{Eq. 1-9}$$

Where $\Delta\sigma_o$ refers to the stress range for a reference thickness t_o.

For variable amplitude loading, the Miner’s Linear Damage Summation Rule [27] assumes that each load cycle causes damage (d_i) proportional to the number of cycles (n_i) at the stress range ($\Delta\sigma_i$) and inversely proportional to the corresponding mean fatigue life (N_i) under the stress range ($\Delta\sigma_i$). These damages accumulate until failure occurs.

$$D = \sum d_i = \sum \frac{n_i}{N_i} \qquad \textbf{Eq. 1-10}$$

1.3.2 Linear Elastic Fracture Mechanics approach

LEFM harness the elastic stress analysis of a cracked body, particularly the stress field surrounding the crack tip, to estimate the conditions under which the pre-existing crack will propagate. It is assumed that: the material is a

homogeneous isotropic continuum, stress is proportional to strain, strains are small, and distortions are neglected [28].

The Energy Balance Theory developed by Griffith [29] [30] is the foundation of the modern theory of LEFM. The criterion states that a crack in an ideally brittle material will propagate when the energy available for crack growth is equal to or greater than the resistance of the material. Using the stress analysis developed by Inglis [31] and considering an infinite plate of unit thickness with a crack of $2a$, Griffith formulated the fracture stress as:

$$\sigma_f = \sqrt{\frac{2E\gamma_s}{\pi a}} \qquad \textbf{Eq. 1-11}$$

Where E is the Young's modulus of the material and γ_s is the surface energy of the material.

Experimental data for ductile materials such as steel show that the surface energy estimated by Griffith's theory is usually higher, which is caused by the fact that the dissipated energy is composed not only of the surface energy but also of the plastic energy dissipated by dislocation movement within the material near the crack tip. Therefore, Irwin [32] and Orowan [33] modified Griffith's fracture stress accordingly:

$$\sigma_f = \sqrt{\frac{2E(\gamma_s + \gamma_p)}{\pi a}} \qquad \textbf{Eq. 1-12}$$

Where γ_p is the plastic deformation energy associated with crack extension.

Later, Irwin [34] observed that the extension of the plastic zone of the crack is usually small compared with the crack length and other characteristic dimensions; hence, for this reason the plasticity behaviour may not be considered and the non-linear material deformation may be approximated as a flaw. Therefore, he introduced the strain energy release rate (G), as a measure of the elastic energy released (U) for an infinitesimally small crack extension:

$$G = -\frac{dU}{da} = \frac{\pi\, {\sigma_f}^2\, a}{E} \qquad \textbf{Eq. 1-13}$$

Subsequently, Irwin [35] realised that the singularity in stress at the crack tip may be characterised by the stress intensity factor (K or SIF), which is directly related to the displacements and stress near to the crack tip. K depends on the geometry of the cracked component, the size and shape of the crack, and the applied stress field [36]. There are three types of stress field corresponding to the three basic modes of crack surface displacement (See Figure 1-7) [28]:

- Mode I or the opening mode, where the crack surfaces move directly apart.
- Mode II or the edge-sliding mode, where the crack surfaces move normal to the crack front.
- Mode III or the shear mode, where the crack surfaces move parallel to the crack front.

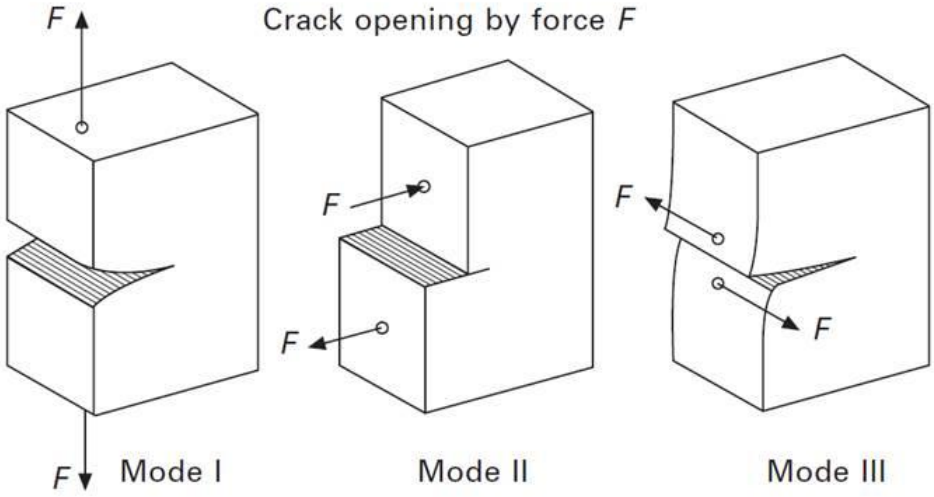

Figure 1-7 Basic modes of crack surface displacement [37].

Mode I is predominant in isotropic materials under essentially elastic conditions for both static and fatigue loadings, independently of their initial orientation [28].

The SIF for Mode I is defined as:

$$K_I = \sigma\sqrt{\pi a}\,.Y(a) \qquad \textbf{Eq. 1-14}$$

Where σ is the nominal surface stress, a is the crack depth, and Y is a modification factor which accounts for the effects of geometry and loading conditions.

The critical value of $\mathrm{K_I}$ at which the crack begins to grow when the load is increased is known as the fracture toughness of the material. For part thicknesses equal to or greater than $2.5(\frac{\mathrm{K_I}}{\sigma_\mathrm{Y}})^2$, where σ_Y is the yield stress, the plastic zone is small compared with the thickness and conditions of plane strain development; hence, the critical value of $\mathrm{K_I}$ is considered to be a material property and is denoted as $\mathrm{K_{IC}}$. The plastic zone becomes comparable with the thickness when this is smaller than $2.5(\frac{\mathrm{K_I}}{\sigma_\mathrm{Y}})^2$, and the stress state near the crack tip changes to plane stress; hence, toughness depends on thickness and developed plasticity and is designated as $\mathrm{K_C}$. Plastic zone sizes at the fracture are much smaller in thick parts, compared to thin parts.

The relationship between the strain energy release rate and the SIF is:

For plane stress: $$G_I = \frac{{K_I}^2}{E}$$ **Eq. 1-15**

For plane strain: $$G_I = \frac{{K_I}^2(1-\upsilon^2)}{E}$$ **Eq. 1-16**

Under mixed mode loading, the relationship is:

For plane stress: $$G = \frac{{K_I}^2}{E} + \frac{{K_{II}}^2}{E} + \frac{{K_{III}}^2\,2(1-\upsilon)}{E}$$ **Eq. 1-17**

For plane strain: $$G = \frac{{K_I}^2(1-\upsilon^2)}{E} + \frac{{K_{II}}^2(1-\upsilon^2)}{E} + \frac{{K_{III}}^2\,2(1-\upsilon)}{E}$$ **Eq. 1-18**

For cyclic stresses the SIF range is used:

$$\Delta K_I = K_{I\,max} - K_{I\,min}$$ **Eq. 1-19**

Where $\mathrm{K_{I\,max}}$ and $\mathrm{K_{I\,min}}$ are the maximum and minimum Mode I SIFs in the cycle.

Eq. 1-14 then takes the form:

$$\Delta K_I = \Delta\sigma\sqrt{\pi a}\,.Y(a)$$ **Eq. 1-20**

Where $\Delta\sigma$ is the nominal surface stress range.

If three identical fatigue cracked specimens, for example the compact tension (CT) specimen, are subjected to different constant amplitude fatigue tests and the data recorded are presented in a crack length (a) versus number of cycles

(N) curve, it will be observed that the fatigue life depends on the magnitude of the applied stress in addition to the material's fracture resistance (see Figure 1-8). At higher stresses the crack lengths at the fracture are shorter, and the crack propagation rates (da/dN, slope of the curves) are higher.

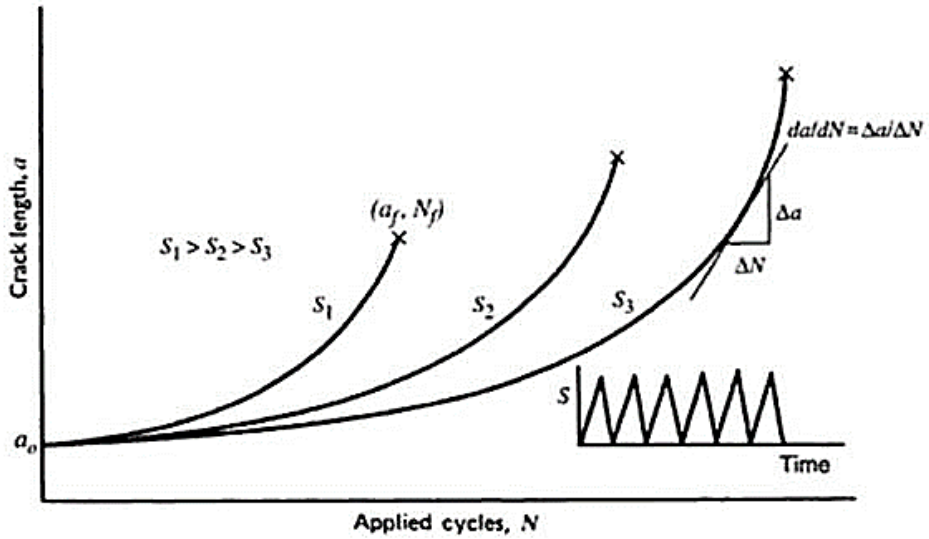

Figure 1-8 Crack length vs. Number of cycles [38].

The corresponding applied SIF ranges of each specimen may be calculated through the SIF solution for the part in question, in this particular case for the CT specimen, knowing the crack lengths and the applied stress ranges. When da/dN data are plotted against ΔK_I on a log-log scale, three different regions may be appreciated in the curve (See Figure 1-9).

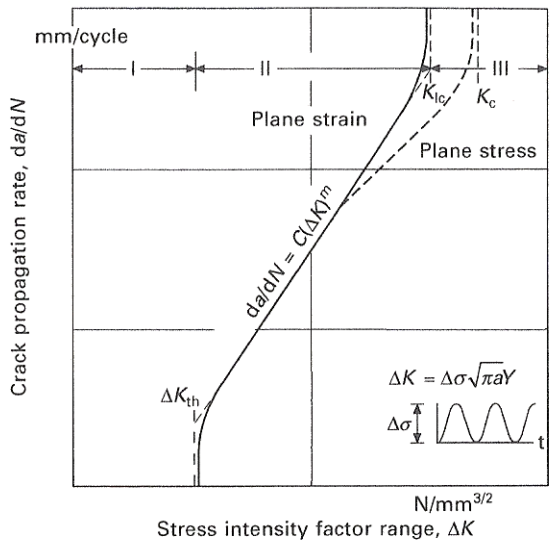

Figure 1-9 Crack propagation rate vs. SIF [37].

In region I, $\log\frac{da}{dN}$ decreases asymptotically to zero when $\log\Delta K_I$ approaches a threshold value ($\Delta K_{I\,th}$), which means that there is a fatigue limit. In region III, $\log\frac{da}{dN}$ increases asymptotically when $\log\Delta K_I$ approaches K_{IC} for plane strain (K_C for plane stress). In region II, $\log\frac{da}{dN}$ varies linearly with respect to $\log\Delta K_I$ which may be expressed as:

$$\log\frac{da}{dN} = m\ \log\Delta K_I + \log C \qquad \textbf{Eq. 1-21}$$

Where $\log C$ is the intercept of the curve and m is the slope of the curve, these constants depend on the material and the environment and must be obtained empirically.

This equation is known as the Paris-Erdogan law [39] and is usually formulated as:

$$\frac{da}{dN} = C\ \Delta K_I{}^m \qquad \textbf{Eq. 1-22}$$

Therefore, using the LEFM approach may yield the following information [40]:

- the expected life,
- the remaining life of a cracked part,
- the tolerable size of a crack,
- the required fracture toughness,
- the in-service inspections frequency,
- the required accuracy of the inspections, and
- the effects of proposed improvements.

A variety of methods have been developed to derive SIFs, which may be classified into three categories: theoretical, numerical, and experimental. For relatively simple geometrical configurations of cracks and boundary conditions use can be made of theoretical methods, but for complex geometries and complicated loading systems one must resort to numerical and experimental procedures. Generally numerical methods are more accurate [41]; however, experimental methods are considered the most reliable technique of obtaining

SIF solutions on welded tubular joints [42]. For some typical geometries, SIF solutions may be available in handbooks or compendia such as Ref. [43] and [44]. Some of the most common methods are provided in Table 1-1. The selection of one of these approaches will depend on the geometry of the structure, the required accuracy, the time available, the cost, and the number of iterations [41].

Table 1-1 Methods of determining SIFs.

Theoretical	Numerical	Experimental
Westergaard semi-inverse method [45] [46]	Alternating method [47]	Caustics [48]
Method of complex potentials [51]	Boundary collocation [49]	Holography [50]
	Body force method [52]	Moiré [53]
	Compounding [54]	Photoelasticity [55]
	Continuous dislocations [56]	Compliance method [57]
	Edge function method [58]	Strain gauge methods [59]
	Finite element method [60]	
	Green's function [61]	
	Integral transforms [62]	
	Method of lines (MOL) [63]	
	Superposition [64]	
	Weight functions [65] [66]	

When numerical methods are applied, the approaches for SIF calculations may be classified within two groups:

- Local (or direct) methods, are based on the crack tip deformation and/or stress fields. Their main disadvantage is that the parameters used are affected by the singularity (where stresses tend to infinity), requiring a proper characterisation of the singularity by using singular elements. Some of the most common methods are:
    - The extrapolation of displacement or stresses [60],
    - Displacement Correlation Technique (DCT) [67],
    - Least Squares Fitting Method [68],
    - Force Method [69], and
    - Quarter Point Displacement Technique (QPDT) [70].

- Energy (or indirect) methods, are based on the energy release rate (G) calculation in the body and then the SIF is calculated from it. It is possible to achieve accurate results without a special refinement mesh or singular elements. Some of the most common methods are:
    - Contour Integral Method [71],
    - Equivalent Domain Integral Method (EDI) [72],
    - J-Integral Method [73],
    - Stiffness Derivative Method [74], and
    - Virtual Crack Closure Technique (VCCT) [75].

The VCCT is widely used by engineers and researchers because of its simplicity, flexibility and accuracy [76]. For instance, ABAQUS [77] uses a modified VCCT for the LEFM approach.

The VCCT is based on Irwin's crack closure integral concept [78], and states that the strain energy release rate is equivalent to the virtual work required to close the crack to its original length.

The formulation for using this approach with FEA for two-dimensional problems was first defined by Rybicki and Kanninen [79] as:

$$G_I = \lim_{\Delta c \to 0} \frac{1}{2\Delta c} \int_0^{\Delta c} \sigma_y(\Delta c - r, 0)\bar{v}(r, \pi)dr \qquad \textbf{Eq. 1-23}$$

$$G_{II} = \lim_{\Delta c \to 0} \frac{1}{2\Delta c} \int_0^{\Delta c} \tau_{xy}(\Delta c - r, 0)\bar{u}(r, \pi)dr \qquad \textbf{Eq. 1-24}$$

Where r represents the distance normal to the crack front, Δc is the crack extension at the crack tip, $\bar{v}$ and $\bar{u}$ are the relative opening and sliding displacements of nodes c and d (See Figure 1-10), and σ_y and τ_{xy} are the stresses required to hold c and d together.

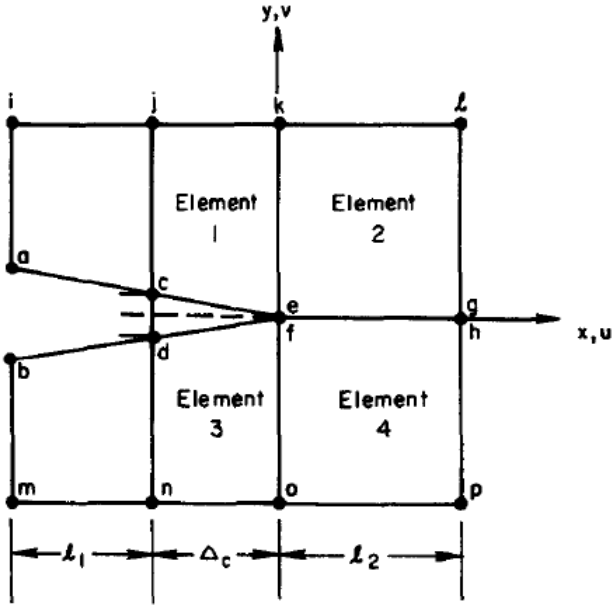

Figure 1-10 Finite-element nodes near crack tip [79].

The extended version for three-dimensional problems was proposed by Shivakumar et al. [75] as:

$$G_i = \lim_{\Delta c \to 0} \frac{1}{2w_i \Delta} \int_{s_{i-1}}^{s_{i+1}} \int_0^{\Delta} \sigma_y(r,s) \bar{V}(\Delta - r, s) dr\, ds \qquad \textbf{Eq. 1-25}$$

Where s represents the distance along the crack front, $\sigma_y(r,s)$ is the stress distribution ahead of the crack front, $\bar{V}(\Delta c - r, s)$ is the total displacement distribution behind the crack front, Δ is the element length on each side and normal to crack front, and w_i is the element length along the crack front. Distorted hexahedral elements are not allowed to be placed at the crack front [80].

1.3.3 Comparison between S-N Curve and Fracture Mechanics Approaches

There is not always enough information about the material constants, therefore, sometimes the Paris' parameters are determined by calibration of the fracture mechanics model to the S-N curve model. In this case, the predicted fatigue lifetimes from the two approaches would be the same but this is not always fulfilled. There may be large discrepancies between the fatigue life predictions from the two approaches [81] [82], since these models were developed under different assumptions.

The S-N curve approach does not distinguish between steel grades assuming similar fatigue behaviour for all structural steels, while fracture mechanics fatigue life predictions are quite sensitive to the variation of the material constants.

The fracture mechanics approach cannot be used for fatigue design since the stress intensity factor applies if the crack length is greater than zero; opposite to the S-N curve approach which may not be used for evaluation of remaining fatigue life, since it does not directly take into account the influence of small crack behaviour or crack propagation. Moreover, Paris' law does not describe the regions near ΔK_{th} and K_{Ic}, therefore, fatigue life predictions using the fracture mechanics approach can only be calculated for the stable crack growth period.

S-N curves are usually derived carrying out constant amplitude fatigue test at a stress ratio ($R_\sigma = \sigma_{min}/\sigma_{max}$) of zero or fully reversed ($R_\sigma = -1$); while fatigue crack growth data is always derived at a stress ratio of zero or close to zero, since the crack is closed during compression loading. Fatigue crack propagation depends on mean stress ($\sigma_m = \frac{\sigma_{min}+\sigma_{max}}{2}$) since a compressive mean stress retards the fatigue process while a tensile mean stress accelerates it.

1.3.4 Uncertainty consideration in fatigue damage estimation

The fatigue life predictions of offshore welded joints are impaired by uncertainties in the loads, strengths and numerical models. According to Ref. [83], these uncertainties may be classified into four groups:

- Physical or inherent uncertainty, is related to natural variability. For example: marine growth, wind speed, current velocity, wave height and period, corrosion, scour, heat affected zone, or yield stress due to production variability.
- Measurement uncertainty, is produced by imperfect measurements. For example: crack length, strain, or stress measurements.
- Statistical uncertainty, is caused by limited sample sizes of observed quantities. For example: drag and inertia coefficients, S-N curve coefficients, or soil properties.

- Model uncertainty, is due to limited knowledge or idealizations of the mathematical models used or to the choice of probability distribution types for the stochastic variables. For example: joint thickness effect, wave theory selection, element type and mesh density of FE models, or the use of a linear damage accumulation concept instead of a nonlinear approach.

The common trend in current design standards is to design according to limit states, in order to account for these uncertainties and the importance of structural components with respect to the consequences of failure. As Ref. [84] states: "*a limit state is a condition beyond which a structure or structural component will no longer satisfy the design requirements*". The safety level of a structure or structural component is satisfactory when the design resistance (R_d) is larger than the design combined load effect (S_d):

$$S_d \leq R_d \qquad \text{Eq. 1-26}$$

For the design of the support structure and foundation with the load effects in the tower applied as a boundary condition, the design load effect (S_{di}) is obtained from a structural analysis for the design load (F_{di}), where the design load is obtained by multiplication of the characteristic load (F_{ki}) by a specified load factor (γ_{fi}):

$$F_{di} = \gamma_{fi} F_{ki} \qquad \text{Eq. 1-27}$$

The design combined load effect (S_d) resulting from the occurrence of n independent loads (F_i), $i = 1, \dots, n$, can be taken as:

$$S_d = \sum_{i=1}^{n} S_{di}(F_{ki}) \qquad \text{Eq. 1-28}$$

where $S_{di}(F_{ki})$ denotes the design load effect corresponding to the characteristic load (F_{ki}).

The design resistance (R_d) is obtained by dividing the characteristic resistance (R_k) by a specified material factor (γ_m):

$$R_d = \frac{R_k}{\gamma_m} \qquad \text{Eq. 1-29}$$

The characteristic resistance of a material is defined as that value of resistance expected to be exceeded by 95% of the cases, and the characteristic load is defined as that value of load exceeded 5% of the life span of the structure. The values of the partial safety factors are usually based on experience or calibrated to measures of the reliability obtained by probabilistic techniques [85], and vary according with the limit states (see Ref. [84]). Although this research focuses on the analysis of fatigue failure (Fatigue Limit State, FLS), these other limit states may be identified for design purposes:

- Ultimate Limit State (ULS), ensures that the structure resists the maximum load.
- Serviceability Limit State (SLS), ensures that the structure resists normal use.
- Accidental Limit State (ALS), ensures that the structure withstands accidental loads and maintain integrity.

The design criterion for the FLS is:

$$D_D = DFF \cdot D_C = DFF \cdot \sum_{i=1}^{k} \frac{n_i}{N_i} \leq 1.0 \qquad \text{Eq. 1-30}$$

Where n_i is the number of stress cycles in the i^{th} stress block, N_i is the number of cycles to failure at stress range of i^{th} stress block, and the design fatigue factor (DFF) is a partial safety factor to be applied to the characteristic cumulative fatigue damage (D_C) in order to obtain the design fatigue damage (D_D). I.e. the fatigue limit state is reached when the accumulated damage exceeds 1.

The values of DFF depend on the importance of the structural components regarding structural integrity and availability for inspection and repair [85]. The partial safety factors for loads and material are 1.0 and 1.15 respectively (for further details refer to Ref. [84]).

1.4 Finite Element Method

The Finite Element Method has been consolidated over the last four decades as the most versatile numerical technique for the analysis of solid mechanics

problems. It may be defined as an approximation procedure of continuum problems, and is characterised by the following process:

- Domain discretization, the continuum is divided into a finite number of units or parties (known as elements) interconnected at specified points (known as nodes).
- Element Analysis, the local stiffness matrix of each element is determined and any loading is transformed into equivalent nodal forces.
- System Analysis, assemble a global stiffness matrix based on the combination of the local stiffness matrices. The static equilibrium conditions and all conditions of compatibility (continuity of the displacements) must be satisfied.
- Equation system resolution, the nodal displacement vector is determined.
- Results post-processing, element stresses and strains can be calculated from the nodal displacements.

For further details on this method and its formulation refer to Ref. [86] or [87].

1.4.1 Types of element

The behaviour of an element is mainly characterised by the following aspects:

- Cell shape:
    - Two-dimensional, where all nodes lie in the same plane. The most common 2D elements are triangles and rectangles.
    - Three-dimensional, where all nodes are not constrained to lie in the same plane. The most common 3D elements are tetrahedra, hexahedra, pyramids, and triangular prisms.
- Degrees of freedom are the fundamental variables calculated during the analysis. Examples of degrees of freedom are: translations, rotations, temperatures.
- Number of nodes or Geometric order, determines how the nodal degrees of freedom will be interpolated over the element domain.
    - Linear (first order) interpolation, where elements have nodes only at their corners.

    - Quadratic (second order) interpolation, where elements contain midside nodes.
- Formulation, refers to the mathematical theory used to describe the behaviour of an element. Basically there are two types:
    - Lagrangian (or material) description, where elements deform with the material.
    - Eulerian (or spatial) description, where elements are fixed in space and the material flows through them.
- Numerical Integration (or quadrature), refers to the number of points over the volume of each element used by the numerical techniques to integrate. ABAQUS [77] uses Gaussian quadrature for most elements, therefore, for this study:
    - Full integration, is characterised by a Gaussian quadrature with at least $2l$ points in each coordinate direction (where l is the polynomial degree of the derivatives of the shape function) [88].
    - Reduced integration, normally uses one point less in each coordinate direction.

1.4.2 Grid type

Grids may be categorised into three groups according to their connectivity:

- Structured, is characterised by regular connectivity.
- Unstructured, is characterised by irregular connectivity.
- Hybrid, contains both structured and unstructured portions.

1.4.3 Mesh quality

The main indicators of mesh quality are:

- Shape factor (or skewness), defined as the ratio between the element area (or volumen) and the optimal element area (or volumen). Therefore, 1 is the optimal element shape.
- Aspect ratio, defined as the ratio between the longest and shortest edge of an element. Solvers have different tolerances, for example, the maximum value for ABAQUS is 10 [89].

- Face corner angle, which must be within a tolerance range. Solvers have different tolerance limits, for example, for a quadrilateral element in ABAQUS the range is 10º to 160º [89].
- Smoothness, the change in mesh size from fine to coarse should be progressive.

1.5 Summary and Scope

To meet the commitment of the Kyoto Protocol, the European leaders agreed to reduce the EU greenhouse gas emissions using renewable energy sources. Wind power, especially offshore, is considered one of the most promising sources. Nowadays wind electricity production cannot compete with nuclear or coal electricity production, being necessary to make this renewable source more economically efficient in order to achieve the EU's targets.

Structural designs, frequency and duration of maintenance, and safety are some of the key aspects to reduce energy costs. Hence, fatigue damage assessment is crucial. The S-N approach – applied at the 'design' stage – and then the LEFM approach – applied to determine inspection intervals or time to repair – are the two basic approaches used in the fatigue-life assessment of tubular welded joints. Much research has been carried out towards the estimation of the HSS range through the SCF, and the prediction of the SIF. Both factors may be obtained experimentally using methods such as photoelasticity or strain measurements, and computationally from the FE method.

This research intends to show that the guides and practices currently employed both in the design and during the operation of the offshore wind turbine support structures are obsolete, and aims to set out the basis for a comprehensive update in order to achieve a more competitive wind industry. To this end the approaches used in the fatigue-life assessment will be reviewed exhaustively, combining Finite Element Analysis simulations based on contemporary 3D solid models with Regression Analysis.

Accordingly, the subsequent chapters of the thesis will be organised as follows:

- The Second Chapter will summarise the background and the state-of-the-art of the Offshore Wind Technology from an engineering, economic and environmental perspective, to have a better understanding of the main challenges.
- The Third Chapter will analyse the evolution of design standards of the Stress-Life approach pointing out its weaknesses by means of the experimental data gathered, and will report the findings.
- The Fourth Chapter will outline the existing SCF parametric equations for tubular welded joints, and will evaluate them by comparison against 3D solid FE models.
- The Fifth Chapter will summarise the main developments in the modelling of fatigue cracks grown in tubular joints, and will set out a reliable methodology for estimating the SIFs. Tubular welded T-joint subjected to axial loading will be modelled because it is the most used combination in the available data, which will be used for modelling validation.
- Finally, the Sixth Chapter will gather together the conclusions of the research and will propose the areas which need further investigation towards the optimisation of Offshore Wind Support Structures.

2 OFFSHORE WIND TECHNOLOGIES

2.1 Introduction

Wind energy is the kinetic energy derived from the movement of air masses, i.e. generated by wind. Air currents are mainly due to differences in temperature and air pressure around the Earth. Since ancient times, wind energy has been used for human activities such as grinding grain using windmills, to propelling sailboats, or for water drainage or pumping. In the late nineteenth century, wind power began to be employed to generate electricity. The result of over a century of development has led to the existence of a wide range of wind turbines manufactured worldwide. The smallest capacity turbines are used for battery charging or to power equipment such as traffic warning signs or parking meters. Medium capacity turbines are used for domestic power supply; in some countries the surplus power produced may be sold to the utility company via the electrical grid. The largest capacity turbines are often grouped together, in what is known as a wind farm, to provide power to the local electrical grid. Onshore and offshore wind farms are an important source of renewable energy in many countries, to mitigate the risks of climate change and to reduce their reliance on foreign fossil fuels.

Interest in offshore wind energy is continuously increasing – GBI Research forecasts that the total global offshore wind installed capacity will reach 80 GW by 2020 [90]. This interest is mainly motivated by the higher wind speed in the marine environment, unrestricted space, and lower social impact [91]. It is estimated that an additional 50% of electricity can be generated for the same turbine in an offshore wind environment [92]. Despite the great offshore potential, offshore wind farms will represent only around 12% of the global cumulative wind power capacity installed by 2020 [93], because of its high construction cost, especially foundation and electrical connection with the shore, and limitations in operation and maintenance.

2.2 Offshore Wind Energy Background and State-of-the-Art

The first time that wind power was employed to generate electricity was in July 1887, when Prof James Blyth of Anderson's College (currently the University of Strathclyde in Glasgow) built a 33 foot (10 metres) cloth-sailed wind turbine in the garden to charge accumulators to light his holiday cottage in Marykirk (Scotland) [94]. Blyth's vertical axis wind turbine did not become widely accepted and was considered uneconomical. Despite this, in May 1895, he developed an improved turbine which supplied emergency power to the local Lunatic Asylum, Infirmary and Dispensary of Montrose for the next 27 years [94]. Several months after Blyth's first turbine, in the winter of 1887-1888, Charles Francis Brush constructed the first automatically operated wind turbine with a multiple-bladed picket-fence rotor of 17 metres in diameter to power his mansion in Cleveland (Ohio) [95]. Current produced by the dynamo was utilised to charge 12 batteries [96]. Unlike Blyth's, Brush's turbine had a control mechanism for braking and could be manually shut down [97]. In the summer of 1891, Poul La Cour built the first electrical output wind machine with a four-bladed rotor for lighting the Askov Folk High School in Denmark [95]. La Cour later solved the problem of producing a steady supply of power by inventing a regulator, the Kratostate, and improved his wind turbine until, in 1895, he transformed it into a prototype electrical power plant capable of lighting the village of Askov [98]. La Cour was a pioneer in the field of aerodynamics, and was the first to discover that fast rotating wind turbines with more rotor blades were actually less efficient in electricity production [99]. The first small wind turbine company did not arrive until 1930 – the Jacobs Wind Electric Company in Minneapolis [100]. The brothers Marcellus and Joseph Jacobs built their first wind turbine in 1922 for their family's Montana Ranch; and after experimenting for a few years with the device, they settled on a final design in 1927 which became really popular among their neighbours and brought them a request for manufacturing a few in Montana [101]. The firm produced two models, one rated 45 amps and the other 60 amps, which were very reliable and efficient [100]. The first lift based vertical axis wind turbine design was patented by Georges Jean Marie Darrieus in 1931 in the U.S. [102].

Despite the efforts of these and many other researchers, the popularity of using wind turbines has always fluctuated with the price of fossil fuels. After the Second World War, interest in wind energy disappeared because fuel prices fell; conversely, it resurged when the price of oil sky-rocketed in the 70s [103]. Oil availability and future prices started to raise concerns, which have forced several countries to turn towards wind energy, aiming to reduce their reliance on fossil fuels. Feed-in tariffs (FITs) are the most widely used energy-supply policy instruments focused on supporting the development of renewable energy generation [104]. The world's first FIT was implemented in the U.S. in 1978, the Public Utility Regulatory Policies Act in the National Energy Act [105]. Thereby the world's first wind farm was installed in December 1980, almost a century after Blyth's turbine, on the shoulder of Crotched Mountain in southern New Hampshire (U.S.) [106]. It consisted of 20 wind turbines rated at 30 kilowatts each [107]. Like many firsts, the wind farm was a failure since turbines frequently broke down and the developers overestimated the wind resource [99].

Through the 80s and the 90s, northern Europe wind farm installations increased continuously thanks to the excellent wind resources and the higher cost of electricity, which led to the creation of a small but firm market [108]. But Europe still needed to keep on preparing to exploit its largest indigenous resource, offshore wind power [109]. The first offshore wind turbine of 220 kW was installed in Sweden in 1990 as a test plant, located at a distance from shore of 250 m in a water depth of 6 m [110] [111]. Finally in 1991 the first offshore commercial wind farm was constructed at Vindeby (the southern part of Denmark), consisting of 11 wind turbines of 450 kW, each supported by a gravity base foundation at a distance from shore of 1.8 km and depth range of 2-4 m [112]. By the end of the 90s, about 75% of the new grid-connected wind turbines were installed in Europe which shifted the most market activity [113], consisting of a cumulative capacity of 9.6 GW [109], of which only 32.28 MW were offshore [113]. The first test floating wind turbine of 80 kW capacity was installed at the Italian coast in 2008, and was decommissioned after one year of testing and data collection [114]. In the meantime, the world's first large scale grid connected floating wind turbine was constructed in Norway in 2009, consisting of one wind turbine of 2.3 MW

capacity, located at a distance from shore of 10 km in a water depth of 210 m [115]. Figure 2-1 shows the evolution of the cumulative EU wind energy capacity from 1990 to 2013. The United Kingdom is the current leader in the offshore energy sector, since it overtook Denmark in 2008 [116], with 733 MW connected to the grid, which represents 47% of Europe's offshore capacity [117]. The European Wind Energy Association (EWEA) estimates that 40 GW offshore wind capacity could be operational in Europe by 2020 [114].

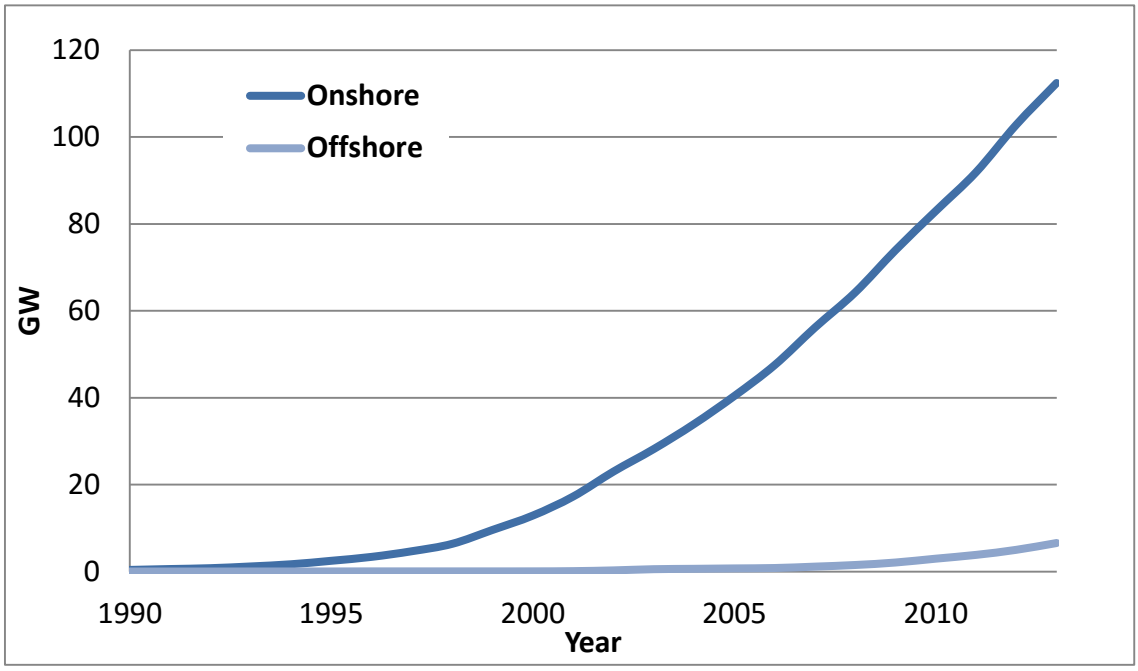

Figure 2-1 Cumulative EU Wind Energy Capacity (1990-2013) [109] [117] [118].

The first Asian commercial offshore wind farm, consisting of 34 wind turbines of 3 MW each installed at a distance from shore of approximately 8 km and at a depth range of 7-10 m [119], was commissioned in Shanghai (China) in June 2010 to provide electricity to the 2010 Shanghai Expo. At present there are approximately 500 MW of offshore installations in Asia: about 438.3 MW in China, about 49.7 MW in Japan, and 10.5 in South Korea [120]. Asia's installed offshore wind power capacity is expected to reach 35 GW by 2020 [121].

The first American offshore wind farm could be commissioned by 2016 [122] [123]. Cape Wind farm will be located in Federal waters of the coast of Cape Cod (Massachusetts), and will consist of 130 Siemens 3.6 MW turbines [124].

The global trend of offshore wind farms is to move further away from the coast into deeper waters and install higher capacity machines, as can be observed in Figures 2-2 and 2-3. Increasing depths requires the use of more expensive foundations and marine vessels for installation, raising the price of construction.

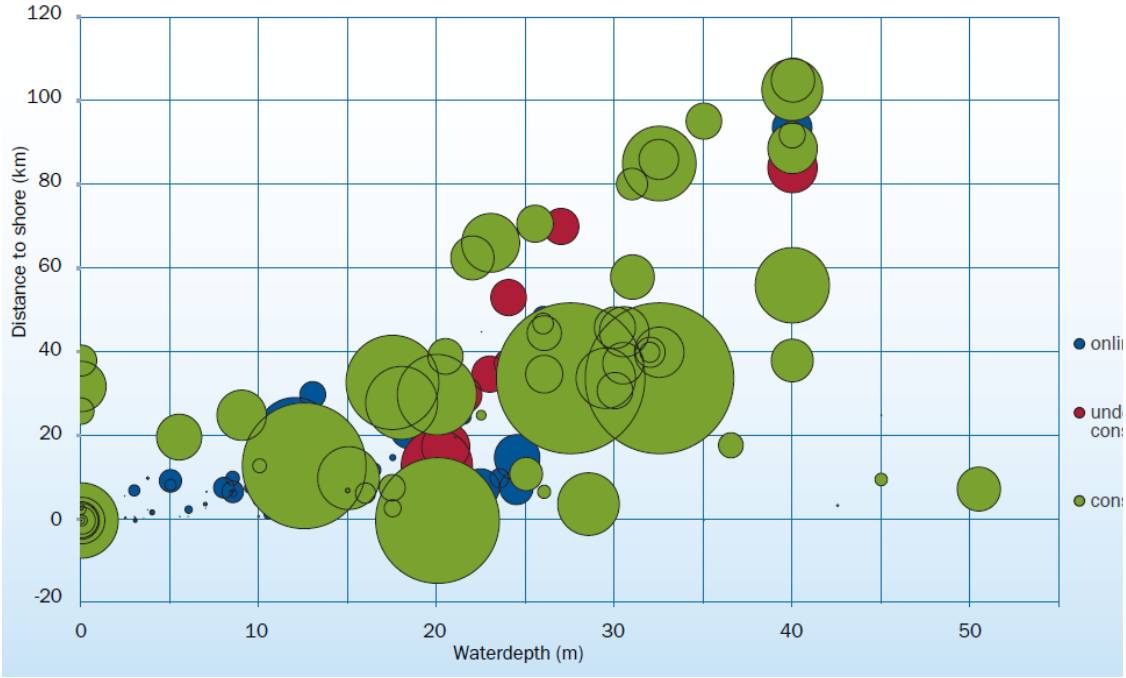

Figure 2-2 Average water depth and distance to shore [117].

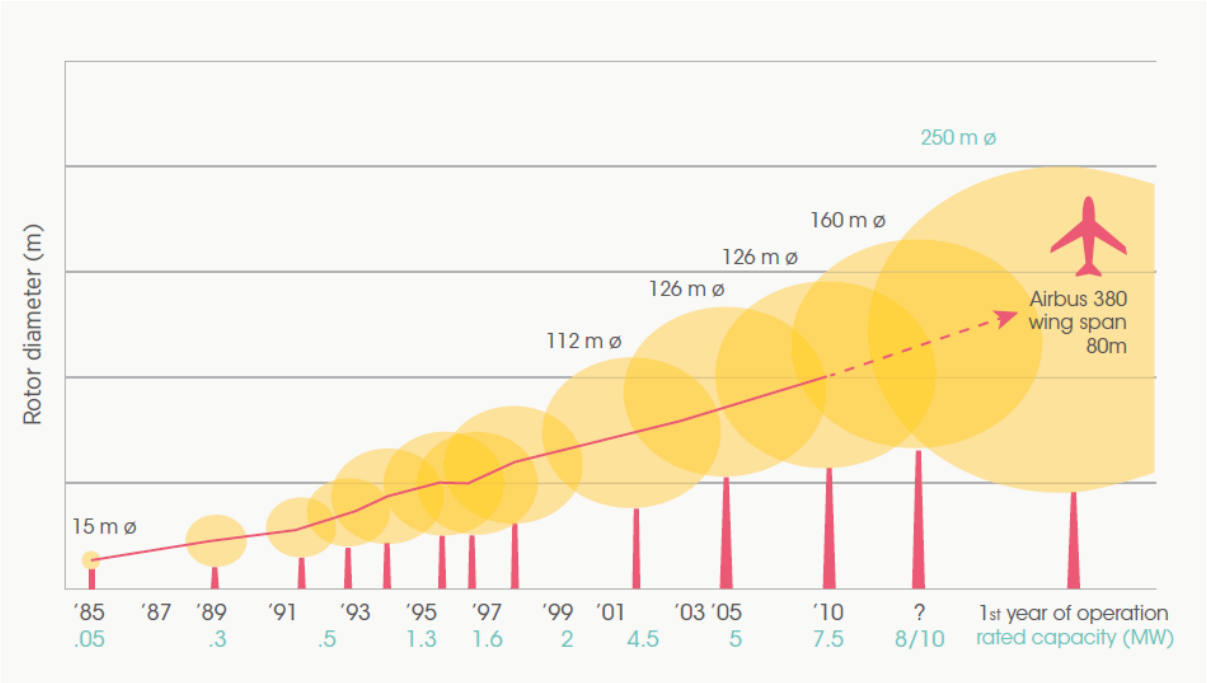

Figure 2-3 Growth in the size of wind turbines since 1985 [125].

2.3 The Largest Offshore Wind Farms

Table 2-1 shows the main characteristics of the world's 10 largest offshore wind farms:

Table 2-1 Top 10 Offshore Wind Farms.

Wind farm	Location	Commissioning Date	Total Capacity (MW)	Turbines & model	Foundation
London Array [126] [127]	UK	2012	630	175 × Siemens 3.6-120	Monopile
Greater Gabbard [128]	UK	2012	504	140 × Siemens 3.6-107	Monopile
Anholt [129]	Denmark	2013	400	111 × Siemens 3.6-120	Monopile
BARD Offshore 1 [130]	Germany	2013	400	80 × BARD 5.0	Tripile
Walney [131] [132]	UK	2011 (phase 1) and 2012 (phase 2)	367.2	102 × Siemens SWT-3.6-107	Monopile
Thorntonbank [133] [134] [135]	Belgium	2009 (phase 1)	30	6 x REpower 5MW	Gravity-Base
		2012 (phase 2)	184.5	30 × REpower 6.15MW	Jacket
		2013 (phase 3)	110.7	18 × REpower 6.15MW	Jacket
Sheringham Shoal [136]	UK	2012	315	88 × Siemens 3.6-107	Monopile
Thanet [137] [138]	UK	2010	300	100 × Vestas V90-3MW	Monopile
Lincs [139]	UK	2013	270	75 × 3.6MW	Monopile
Horns Rev 2 [140]	Denmark	2009	209.3	91 × Siemens 2.3-93	Monopile
Rødsand II [141]	Denmark	2010	207	90 × Siemens 2.3-93	Gravity-Base

2.4 Wind Turbine Configurations

There are basically two types of wind turbine, distinguished according to the axis of the rotor's rotation: horizontal axis wind turbines (HAWTs) and vertical axis wind turbines (VAWTs). The axis of the HAWTs is parallel to the wind stream and the ground, while the VAWTs have their main rotor shaft arranged vertically.

2.4.1 Horizontal axis wind turbines

The horizontal-axis, or propeller-type, configuration is the most popular [113]. As can be observed in Figure 2-4, there are two categories of HAWT: the upwind wind turbines, in which the rotor faces the wind first; and the downwind wind turbines, in which the tower faces the wind first. The most widely used configuration is the upwind wind turbine, since it avoids the wind shade behind the tower [142]. However, downwind turbines do not require a yaw mechanism to turn the rotor against the wind [142]. The number of blades is variable, but three-bladed wind turbines dominate the market since the rotor moment of inertia is easier to understand [113]. Two-bladed wind turbines are lighter and incur lower costs but they require a higher rotational speed [143].

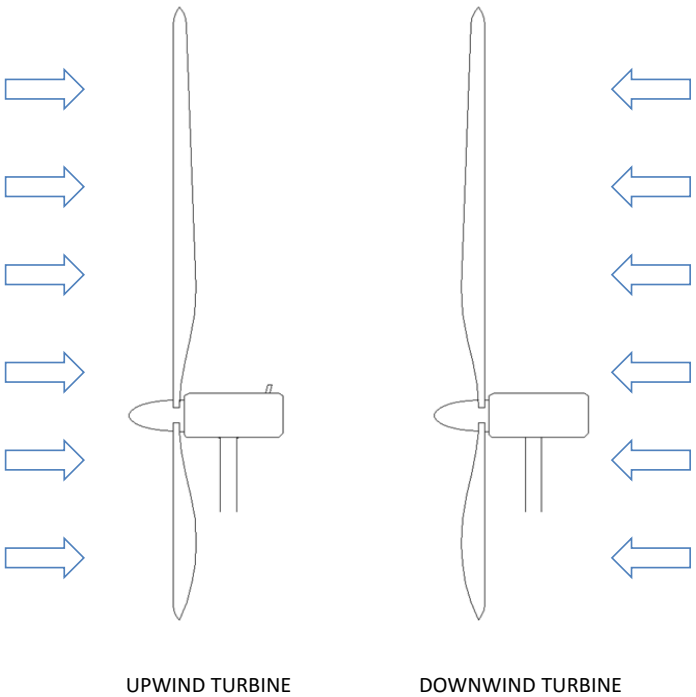

Figure 2-4 Horizontal axis wind turbine configurations.

2.4.2 Vertical axis wind turbines

VAWTs are characterised by having a set of blades that spin around a vertical axle. In contrast to the HAWTs, the gearbox and generating machinery can be located at the base level. There are two categories of VAWT: Darrieus and Savonius turbines. The rotor of the Darrieus wind turbine has curved, long, thin blades connected to the top and bottom of the axis [102]; and is not self-starting [144]. It is built with two or three blades, since for a given solidity it is structurally better to have fewer blades of larger chord rather than more blades of smaller chord [145]. The two main subtypes of the Darrieus turbine are: the Giromill or H-rotor design, in which the curved blades are replaced with straight vertical blades with a constant aerofoil cross section attached to the central tower with horizontal supports [146]; and the Gorlov helical design, in which the vertical blades are helical (initially designed as a water turbine) [147]. The Savonius design is a drag-type device, which uses a half-cylinder fixed to a shaft to catch the wind. The two half-cylinders' machine is S-shaped if viewed from above. The Savonius turbine is self-starting [148]; however, it extracts only about half of the wind's power compared with other, similarly-sized, lift-type turbines [149].

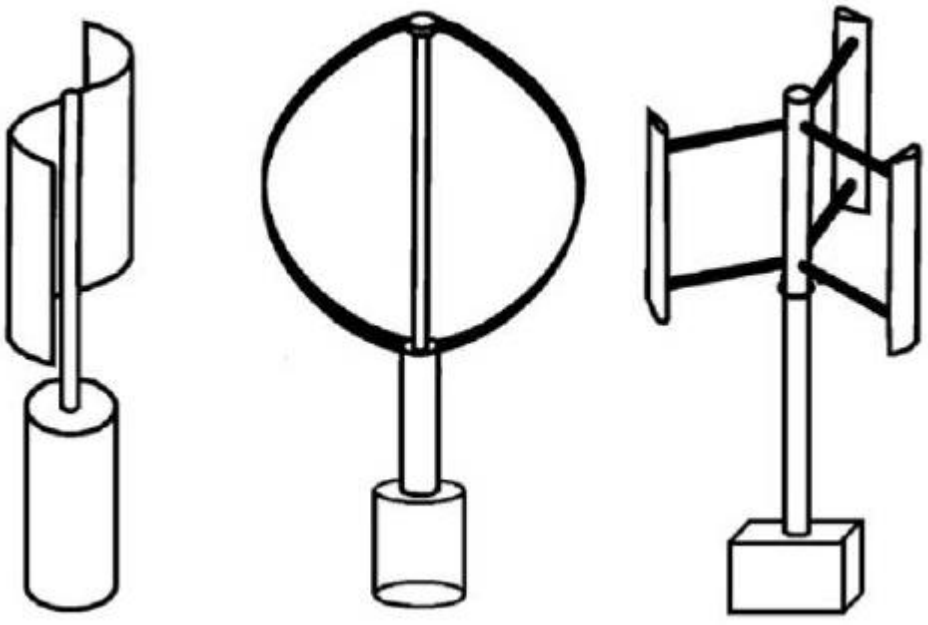

Figure 2-5 Vertical axis wind turbine configurations [102].

Table 2-2 summarises the main advantages and disadvantages of the two wind turbine configurations:

Table 2-2 HAWT vs. VAWT.

	Horizontal axis wind turbines	Vertical axis wind turbines
Advantages	- Well developed, mature and proven technology. - High efficiency. - The tower length is variable, allowing the blades to face much higher velocity winds in high altitudes. - The angle of attack can be remotely adjusted.	- Easy to maintain since the components are placed at the base. - There is no need for a yaw mechanism. - A tower is not needed to support the system. - More densely packed in a wind farm. - Big potential for upscaling to large powers.
Disadvantages	- Difficult to maintain - Needs a strong tower to support the system. - May need yaw mechanism. - Upscaling limits because of gravitational fatigue loads.	- Machine may not be self-starting. - Low efficiency - Replacing the main bearing for the rotor is difficult. - High cyclic loading. - Not widely used on a large scale.

2.5 Wind Turbine Components

1. The foundations are designed to transfer the loads to the ground.

2. The tower supports the nacelle, contains all the cables which transfer the electricity from the converter to the grid, and has lifts or step ladders to permit access by engineers to the top of the wind turbine.

3. The transition piece is joined to the foundation and transfers all the loads and forces from the wind turbine tower.

4. The blades convert the wind´s kinetic energy into rotational energy. The special shape of the blades facilitates the rotational movement.

5. The wind vane provides the wind direction which enables the best possible positioning of the wind turbines. The anemometer measures the horizontal wind

speed, and helps the wind turbine to operate safely according to the wind power to guarantee maximum efficiency.

6. The nacelle is situated at the top of the wind turbine and houses the drive train (gearbox, low-speed and high-speed shafts), generator, controller and brake.

7. The pitch system controls the pitch angle of the blades with respect to the wind, ensuring that the blades are operating at the optimum angle of attack.

8. The hub consists of the hub housing and pitch system, connects the blades to the low speed shaft, is rigid and has a nose form, and absorbs high levels of vibration. It is one of the heaviest components of a wind turbine.

The rotor consists of the blades and hub.

9. The bearing system is placed between the rotor and low speed shaft, and supports the rotor, thus counteracting the horizontal and vertical loads.

10. The low-speed shaft transmits the mechanical torque generated by the rotor to the gearbox.

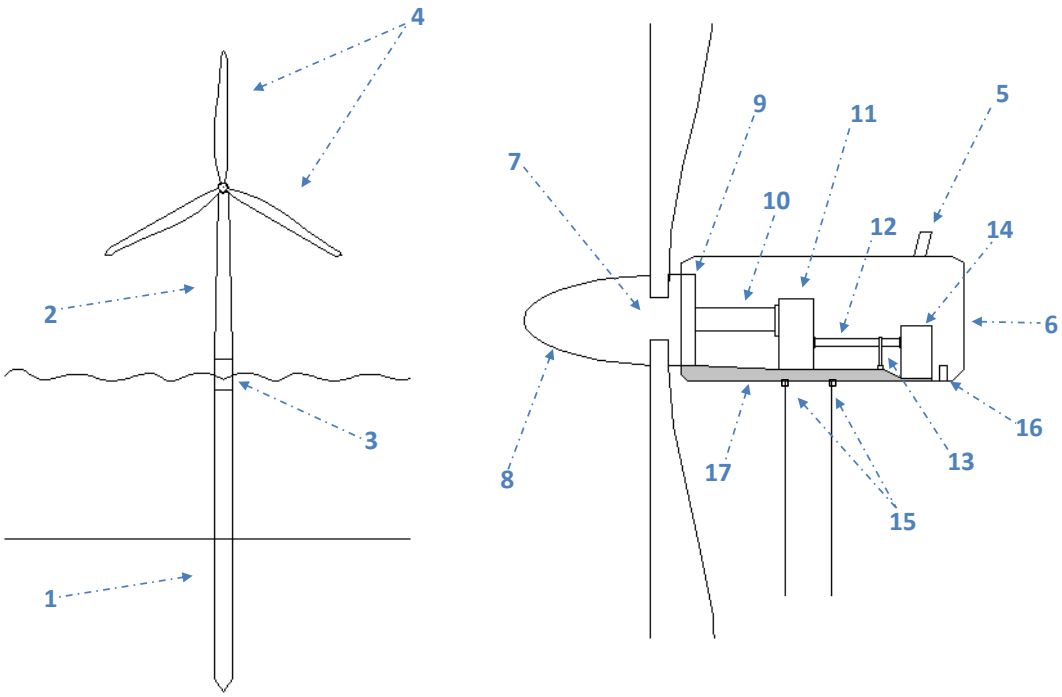

Figure 2-6 Horizontal axis wind turbine components.

11. The gearbox is the system placed between the low-speed shaft and high-speed shaft. Its role is to increase the slow rotational speed of the rotor blades to the generator rotation.

12. The high-speed shaft connects the gearbox to the generator.

13. The brake system stops the rotation of the blades in order to leave the wind turbine inoperative for maintenance or security purposes.

14. The generator transforms mechanical energy into electrical energy.

15. The yaw system keeps the rotor upwind when the wind direction changes, and has a brake to stop the turbine from rotating and to stabilise it when required.

16. The power converter consists of a power module and the associated electrical equipment, and connects the generator output to the local power system.

17. The nacelle bedplate has a girder structure, supports the whole assembly (except the yaw system), and transmits loads from the tower.

2.6 Offshore Substructures

There are different types of support structure configurations for offshore wind farms; the selection of the most preferable should be based on engineering, economics, and environmental attributes [91]. One of the most influencing factors is the depth of water [150]. The existing configurations to date are:

- The monopile is a simple design, consisting of a tubular structure which extends into the seabed. It is normally used in shallow waters, at water depths of up to 25-30 m [151] [152]. The typical pile diameter is around 5 m, and wall thickness (WT) is 50-90 mm [153].

- The gravity based foundation is normally a steel reinforced concrete structure with ballast (sand, iron ore, or rock) filled into the base; including a central concrete or steel shaft acting as a transition piece, and a form of scour protection. The seabed requires preparation to ensure flat and homogeneous soil properties [154]. This configuration is suitable for water depths greater than 20 m and up to 55 m [155]. The typical base outer diameter (OD) is around 30-35 m, top shaft

OD is around 6-7 m, concrete volume is around 1500-3000 m^3, and steel reinforcement is around 600-900 tonnes [156] [157].

- The suction bucket or caisson configuration consists of a steel tubular column connected in a centred manner through flange-reinforced stiffeners to a circular steel bucket. The tower is attached to the tubular centre column with a flange connection. The foundation is installed by sucking water. This configuration is suitable for water depths greater than 20 m and up to 40 m [158]. The typical base OD is around 120 m, top OD is around 5 m, and length is 10-15 m [159].

- The tripod configuration is a three-legged structure made of cylindrical steel tubes, and there is a transitional piece which transfers the forces from the tower into the three legs. Piles or suction caissons can be utilised to fix the structure to the seabed [160]. This structure is used for depths between 25 and 50 m [151].

- The jacket configuration is normally a four-legged structure, which is interconnected with welded bracings with diameters up to 2m [161]. There is a transitional piece for transferring the forces from the tower into the structure, which is anchored to the seabed at each leg by piles or suction caissons [162]. This configuration is suitable for installations at water depths between 25 and 50m [151], like the tripods. The lattice structure differs from the jacket structure in which it acts as a foundation and as a tower, sustaining the nacelle.

- Floating offshore structures are not fixed support structures, and are being developed for deep waters (greater than 50 m) [163]. These structures may be classified by the method used to achieve static stability with respect to the rotational degrees of freedom [164]:

- The spar is a deep cylindrical buoy stabilised mainly by having a large ballast mass at the bottom of the structure, which lowers the centre of gravity (CG) well below the centre of buoyancy (CB): the downward weight force acting on the CG and the upward buoyancy force acting on the CB will then compose a stabilising moment. Usually a catenary mooring system is utilised or station-keeping. Due to its configuration, it is suitable for deep waters (above 100 m),

but its small waterplane area (which is at waterline level) guarantees low wave loads.

- The Tension Leg Platform (TLP) structure is stabilised by the tension in the mooring system. The mooring system is kept under tension since the draft of the structure is such that the buoyancy force is much higher than the weight of the structure, resulting in a net upward force pulling under tension the mooring system. The cables are then fixed to a frame, which is in turn fixed to the seabed usually with piles. It is claimed that this structure can be used for relatively shallow waters floating wind turbines (50-100m), even if they have been used for deeper waters in the oil & gas industry. Among the three options, due to its high rigidity it is the structure with the smallest displacements.
- The Barge is a floating structure using buoyancy as the main mechanism for stabilisation, similarly to ships. As such, it does not need deep waters, and it is suitable for relatively shallow waters (above 40 m). Relying on the waterplane area for stabilisation, it is characterised by a large waterplane aera and therefore experiences higher wave loads and oscillations.

In 2013 the most popular substructure type was the monopile, with 79% of those installed shown in Figure 2-7 [117]. However, increasing depths will make monopile and gravity foundations impractical.

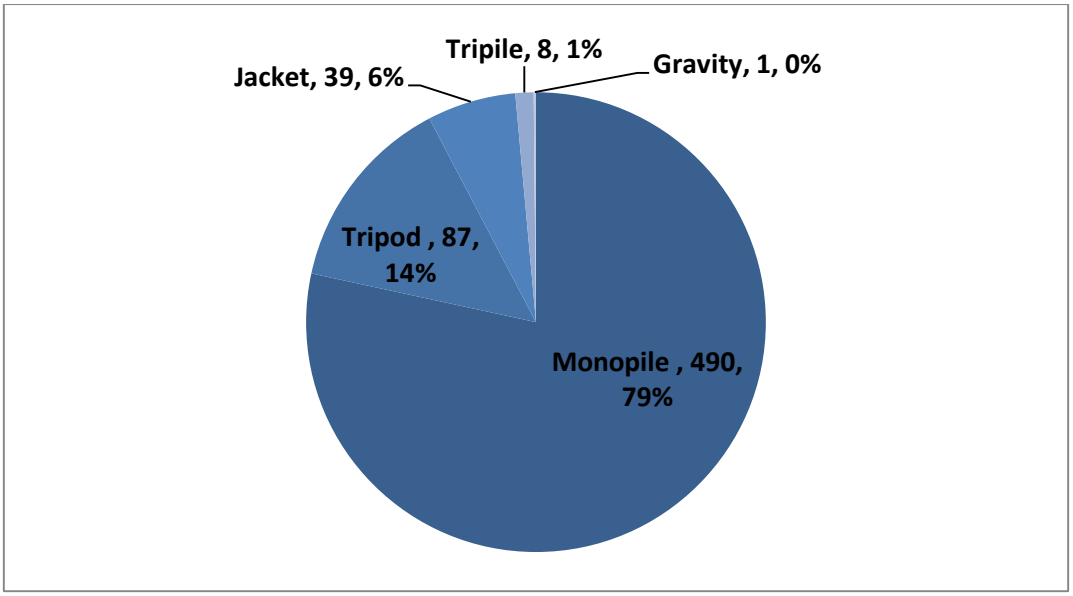

Figure 2-7 Foundation types' share of 2013 annual market [109].

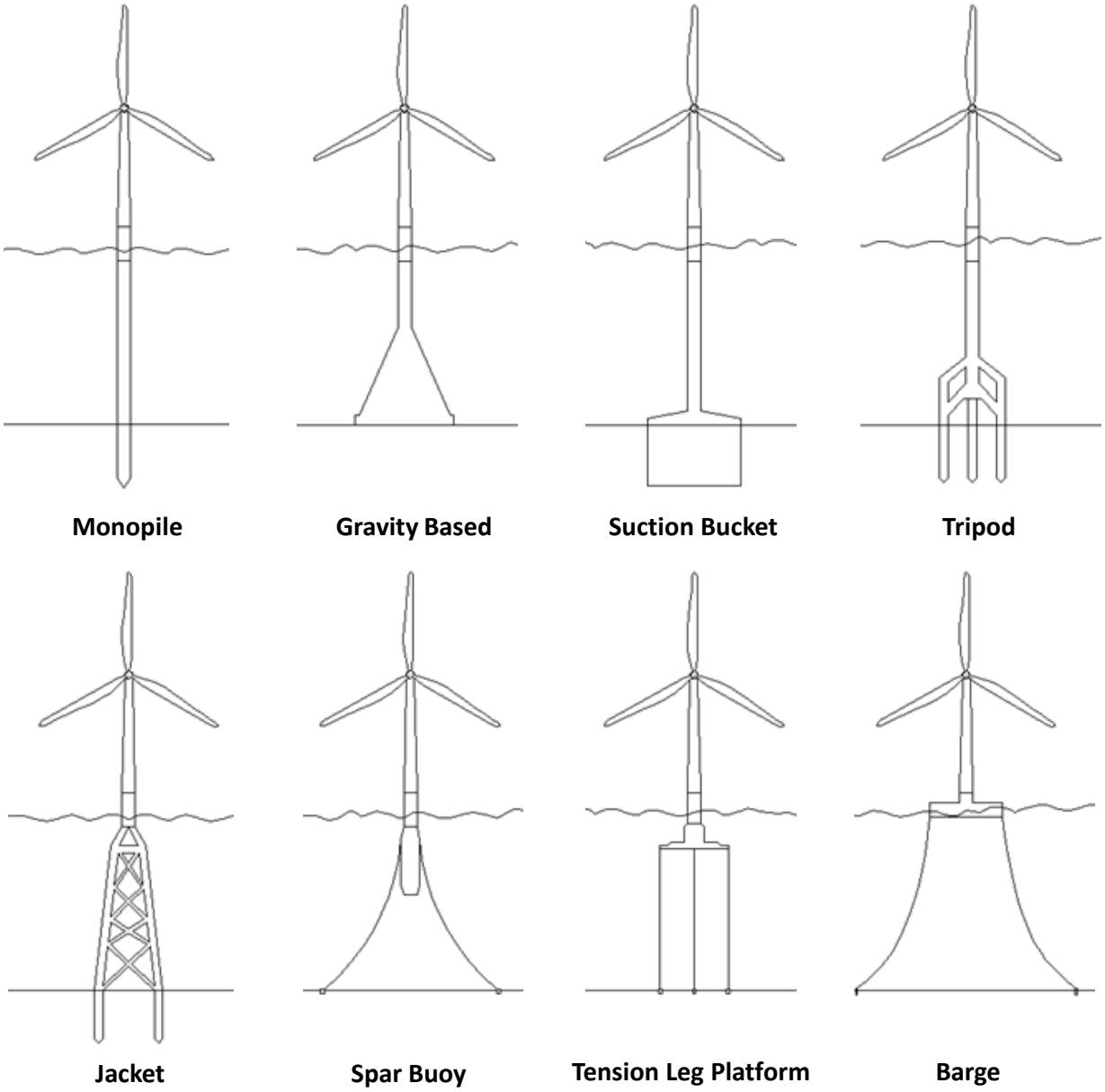

Figure 2-8 Support structure configurations for offshore wind farms.

2.7 Loads

The design load cases should consist of a set of design situations covering the most significant conditions that an offshore wind turbine support structure may experience, combining normal or extreme external conditions with wind turbine operational modes or other design situations (such as transportation, installation, maintenance, or fault). For further details refer to Ref. [165].

Loads described below should be considered for the design calculations.

2.7.1 Gravitational and inertial loads

Gravitational and inertial loads are static and dynamic loads resulting from seismic activity, the weight of the entire structure and any equipment imposed on the structure during operation, and the forces exerted on the structure from operations.

2.7.2 Aerodynamic loads

Aerodynamic loads are dynamic and static loads produced by the interaction of the airflow with the stationary and moving components of wind turbines. The magnitude of the loads varies depending on the density of the air, the average wind speed and turbulence across the rotor plane, and the aerodynamic shapes of the wind turbine components and their interactive effects. These loads may be calculated by aeroelastic load models.

2.7.3 Environmental loads

Environmental loads are loads produced by environmental phenomena, i.e. the set formed by wave force, current force and wind force.

2.7.3.1 Wave forces

Wave loads are dynamic loads caused by waves and its interaction with the support structure of an offshore wind turbine. The following three methods are the most widely used for modelling wave forces on offshore structures [166]:

- Morison's equation, which is applied when the structure is small in scale compared to the water wave length and when the induced drag force is significant.
- Froude-Krylov theory, which is applied when the drag force is small and the inertia dominates, but the structure is still relatively small in scale.
- Diffraction theory, which is applied when the size of the structure is comparable to the wave and can alter the surrounding wave field.

Offshore fixed structures are considered to be drag dominated, therefore the Morison's equation is employed by most researchers. The Morison's equation assumes that the total wave forces acting on a structure can be calculated by linear superimposition of the drag and inertia forces [167], mathematically formulated as:

$$\vec{f} = \overrightarrow{F_D} + \overrightarrow{F_I} = \frac{1}{2} C_D \rho D |\vec{u}| \vec{u} + \frac{1}{4} C_M \pi \rho D^2 \frac{\partial \vec{u}}{\partial t} \qquad \textbf{Eq. 2-1}$$

Where F_D is the drag force, F_I is the inertia force, C_D is the drag coefficient, C_M is the coefficient of virtual mass, ρ is the mass density of water (1025 kg/m^3), D is the diameter, $\vec{u}$ is the velocity of the wave particles and $\frac{\partial \vec{u}}{\partial t}$ is the local water particle acceleration. Assuming that the cylinder extends from the seabed (d) to the sea water line (SWL), the wave force on the cylinder is given by:

$$\vec{\mathrm{F}} = \int_{-\mathrm{d}}^{0} \vec{\mathrm{f}} \, \mathrm{dz} \qquad \textbf{Eq. 2-2}$$

For smooth cylinders, Ref. [168] recommends the use of 0.65 for C_D and 1.6 for C_M.

Wind-generated gravity waves will be modelled in order to obtain $\vec{u}$ and $\frac{\partial \vec{u}}{\partial t}$, since they are responsible for a significant proportion of the environmental forces acting on offshore structures [169]. There are three basic forms of wave: solitary, cnoidal and sinusoidal; each can be examined with low- and high-order wave theory. In general, the solitary wave theory is recommended for extremely shallow water, the cnoidal wave theory for shallow water and the sinusoidal wave theories for deep-water [167]. Le Mehaute's graph, which is shown in Figure 2-9, indicates

the range of validity of each wave theory and may be used to obtain the most suitable theory for given wave characteristics – wave height (H), wave period (T) and water depth (d) –.

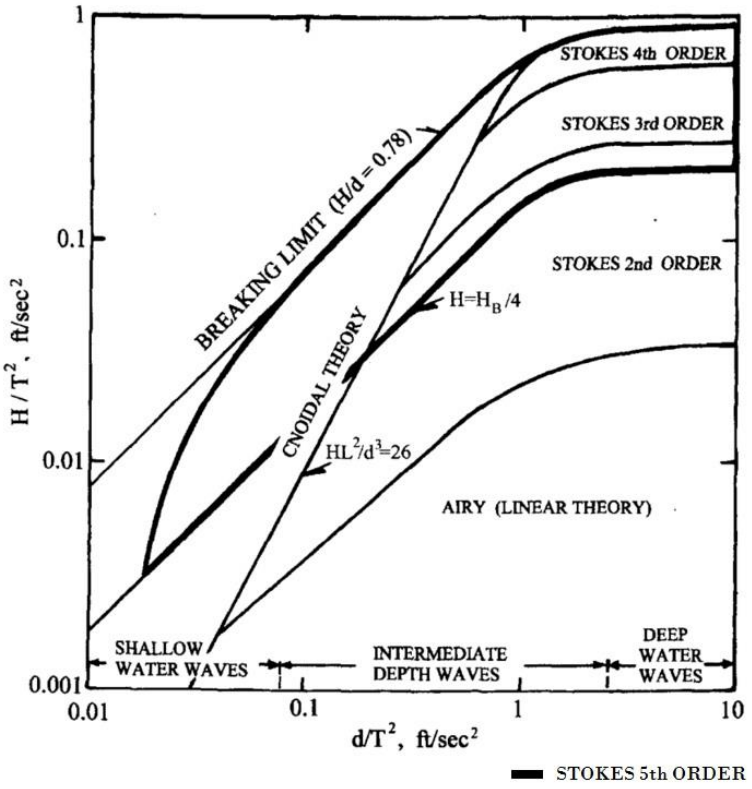

Figure 2-9 Le Mehaute's graph [166].

Stokes Wave theory is the most commonly used in the analysis of offshore structures because of its accuracy in predicting the kinematic properties of the wave [166].

According to Ref. [168], the wave amplitude may be calculated as follows:

$$a = \frac{H'}{2} = \frac{1.86\ H}{2} \qquad \textbf{Eq. 2-3}$$

2.7.3.2 Current forces

Current loads are dynamic loads which are caused by the water flow from external sources, other than surface waves. The current force on a rigidly held, horizontal, circular cylinder of diameter D is calculated as [166]:

$$F(z) = \frac{1}{2} C_D \rho D l u(z)^2 \qquad \textbf{Eq. 2-4}$$

Where C_D is the drag coefficient, ρ is the mass density of water (1025 kg/m^3), l is the length, z is the depth location (a negative number measured downward from the sea surface), and $u(z)$ is the current velocity at z.

Tidal currents and wind-stress currents, which are the components generated by the local wind, are the two most important components considered in the structural design of offshore support structures [170]. In the absence of vortex shedding, the total current velocity of a stationary, submerged, tubular member can be calculated as [166]:

$$u(z) = u_t(z) + u_w(z) = \left(1 + \frac{z}{d}\right)^{\frac{1}{7}} u_t(0) + \left(1 + \frac{z}{d}\right) u_w(0) \quad \textbf{Eq. 2-5}$$

Where $u_t(z)$ is the tidal current, $u_w(z)$ is the current generated by local wind, d is the total water depth, $u_t(0)$ is the tidal velocity at the surface, and $u_w(0)$ is the current generated by local wind at the surface, which can be calculated as follows [171]:

$$u_w(0) = 0.02\, W_{10} \quad \textbf{Eq. 2-6}$$

Where W_{10} is the wind velocity measured 10 m above SWL.

2.7.3.3 Wind forces

The obstruction to the free flow of wind by a structure produces a differential pressure, which results in wind forces [167]. The static drag force due to wind on large-scale structures accounts for approximately 25% of the total overturning moment and about 15% of the total force on the structure [166]. The general wind force on a rigidly held, horizontal, circular cylinder is calculated as [166]:

$$F(z) = \frac{1}{2} C_D \rho S U_G(z)^2 \quad \textbf{Eq. 2-7}$$

Where C_D is the drag coefficient, ρ is the density of the air (1.2 kg/m^3), S is the frontal area (facing the wind), z is the depth location, and $U_G(z)$ is the gust wind speed at z. The gust wind speed is defined as the average wind speed over a time interval of 3 seconds measured at an elevation of 10 m above SWL, and can be estimated as:

$$U_G(z) = U_G(10).\left(\frac{z}{10}\right)^{0.1} \quad \textbf{Eq. 2-8}$$

Where $U_G(10)$ is the gust wind speed at 10 m above SWL.

2.7.3.4 Other loads

Other loads such as ice loads, earthquake loads, etc., may occur and shall be included where appropriate.

2.8 Offshore Maintenance

Maintenance of offshore structures is a very demanding process. It involves highly qualified personnel and special means of transportation, including helicopters and high capacity specialized vessels, and equipment such as ship cranes and jack ups, raising the cost of intervention. Therefore, it has to be operated by external suppliers due to its high capital cost. Availability of those delicate requirements is restricted predominantly by the environmental conditions. This downtime for assembly and positioning imposes a factor of uncertainty in the level of adequate forecasting of the whole maintenance process.

Different types of failure raise different requirements of maintenance. As Table 2-3 shows, maintenance classes are categorised according to their level of equipment and personnel required. Categories 3 and 4 require limited external equipment and can be accommodated by the internal crane, which is installed in the tower. However, for categories 1 and 2, which contribute the most to the total maintenance cost, the use of external lifting equipment is essential.

Table 2-3 Definition of maintenance classes [172].

Maintenance Classes	
Nr.	**Description**
4A	Repair, Cleaning Reset Inside
4B	Repair, Cleaning Reset Outside
3	Replacement small parts (<1 MT)
2	Replacement large parts (>50 MT)
1	Replacement rotor and nacelle, shaft, main bearing and yaw gear (<300 MT)

Failure rates of sub-assemblies should be considered for conducting and evaluating a comprehensive maintenance schedule for a wind turbine, because this is the factor that indicates the requirements of external equipment. Offshore wind is a very young technology, therefore, the statistical information is limited, making it necessary to use general findings from onshore wind. There are several studies available that provide failure rates of operational onshore wind turbines, for instance Figure 2-10 shows the average failure rates referring to any type of failure (class 1-4) for wind turbine components. The most important components of a wind turbine from the aspects of component cost and downtime are the blades, the generator and the gearbox [172] [173] [174].

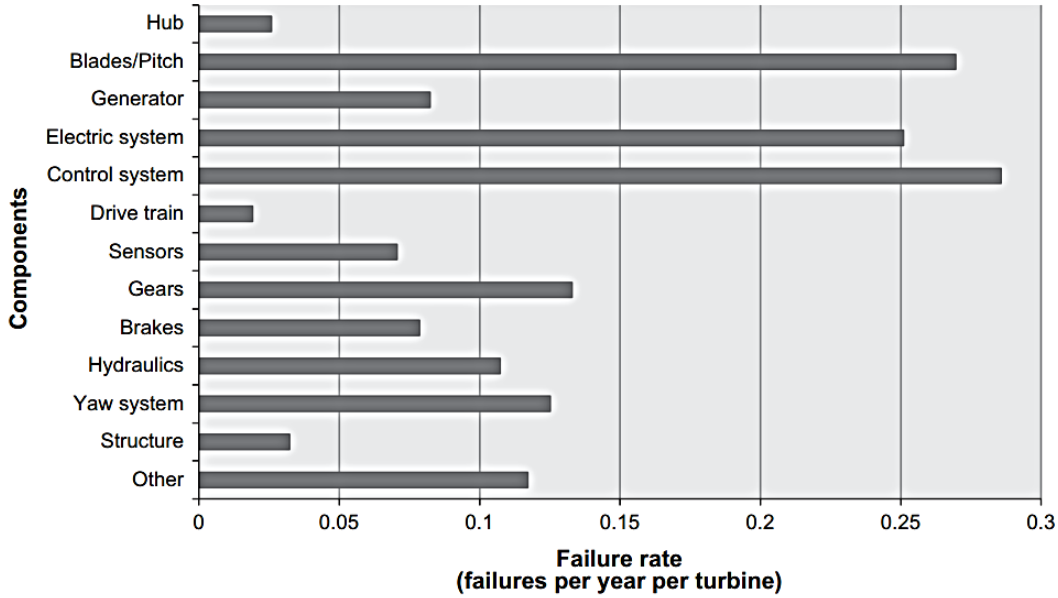

Figure 2-10 Average rate of failure vs. WT components [175].

2.9 Offshore Wind Energy Economics

Offshore wind energy cost may be derived as the sum of all the capital expenditure (CAPEX) costs and the operational expenditure (OPEX) costs over the service life of the project, divided by the total energy output of the project: in technical terms this is called the Levelised Cost of Energy (LCoE). Thus cost of energy is calculated as unit of currency per unit of energy. Costs have to be converted in terms of present value, as the conversion allows these to be

commensurable across time. The further in time a benefit or cost happens, the lower the present value [176].

Electricity production costs vary widely between countries, since there are different tax structures, availability of resources, etc. Some studies indicate that offshore project costs have been increasing over time, which is mainly caused by the trend to move further away from the coast into deeper waters and install higher capacity machines [177]. The average reported capital cost for projects installed in 2009 was $4.1m* per MW [178], and in 2012 was $5.4m per MW [177]. A gradual decrease in capital costs is expected, arriving at $3.4m* per MW by 2020, thanks to the improvement in market conditions for turbines, maturing of existing processes, and deployment of new technology in greater quantities [179]. Equipment installation, foundation manufacture and turbine tower production are the areas of the supply chain where cost reductions are most likely to occur; a fall of approximately 6.6%, 6.1% and 5.4% respectively is estimated [180]. The estimated CAPEX cost breakdown for a typical offshore wind project is shown in Figure 2-11. The Department of Energy and Climate Change (DECC) of the United Kingdom Renewables Service estimates that the typical offshore wind OPEX may be around $29-34/MWh* [179]. In the same way as for the CAPEX cost, there are opportunities for OPEX cost reductions, especially from increases in wind farm scale; a decline of 5% by 2015 is expected [181]. The estimated OPEX cost breakdown for a typical offshore wind project is shown in Figure 2-12.

Besides the direct profit on the sale of the produced energy, there are other indirect benefits such as an increase in employment. The EU wind energy sector employed approximately 154,000 people in 2007 [182]. By 2030, the EWEA estimates that more than 215,000 people could be employed in the European offshore wind energy sector [182]; and the U.S. Department of Energy estimates that more than 43,000 permanent operations and maintenance jobs could be created in the U.S. [183].

* Currency exchange: 1 U.S. dollar = 0.59 British pounds [322].

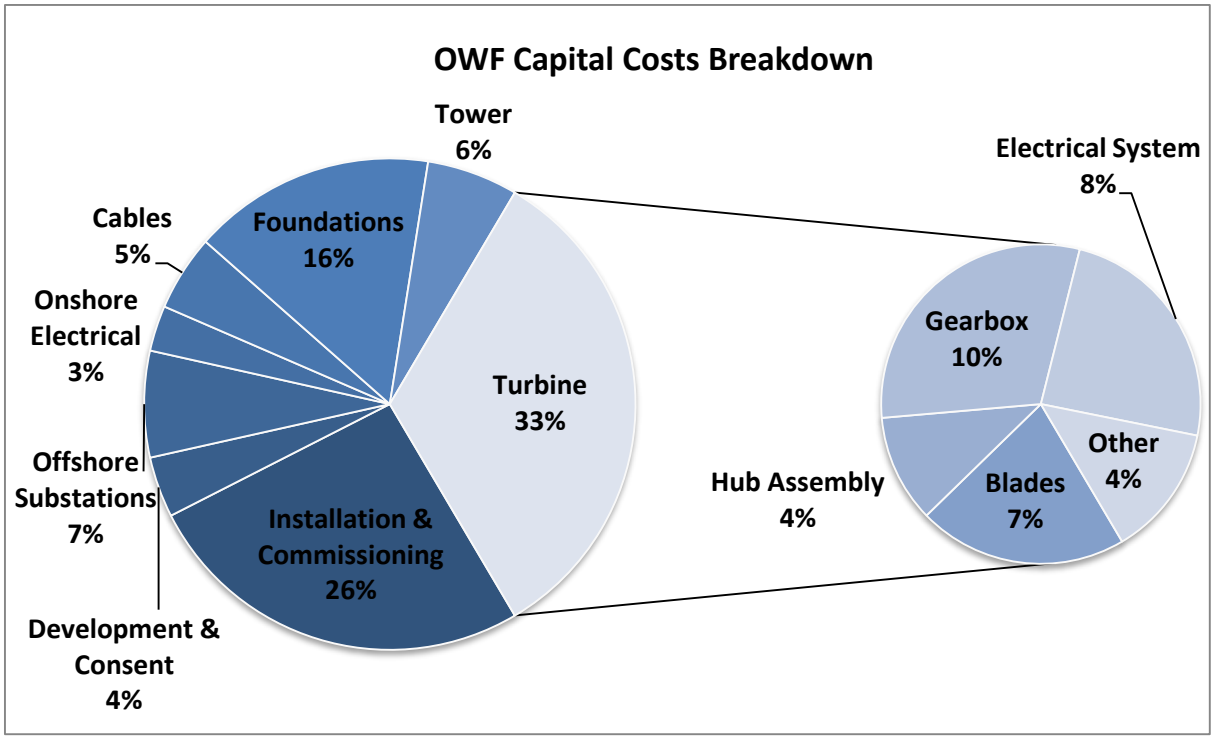

Figure 2-11 Offshore Wind Capital Costs Breakdown [179].

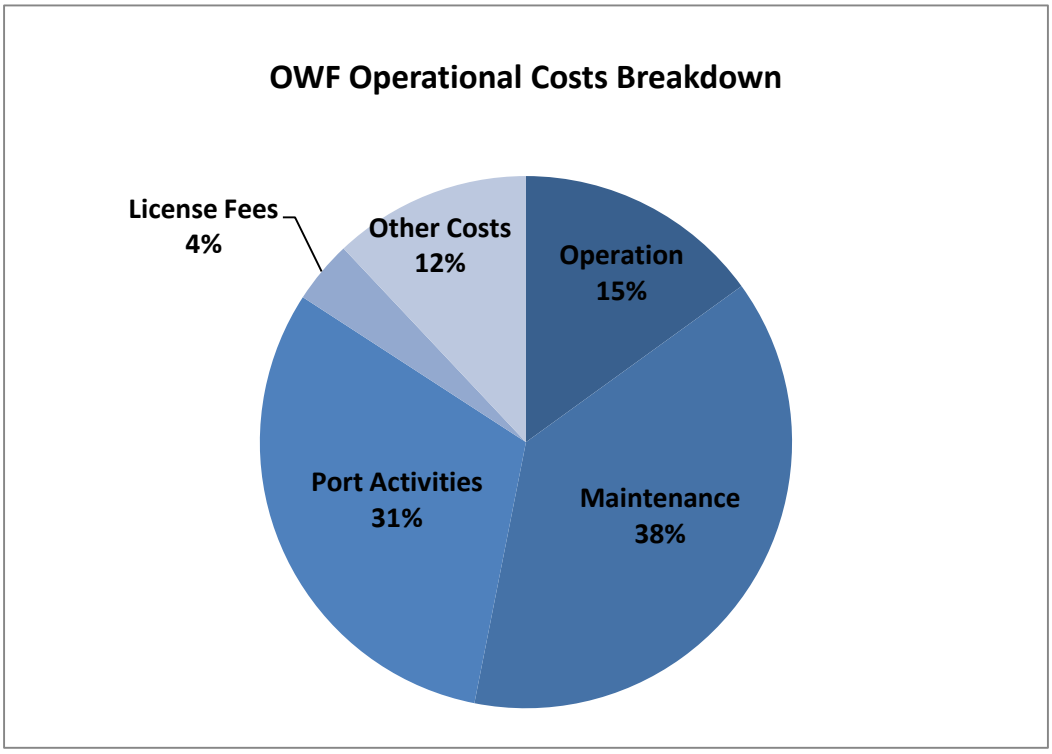

Figure 2-12 Offshore Wind Operational Costs Breakdown [179].

2.10 Environmental Impact

Offshore wind farms produce both beneficial and detrimental environmental impacts to the marine environment, which are local effects, and the atmosphere. In contrast to fossil fuels and nuclear power, wind power is considered to be 'carbon neutral' technology since it does not emit CO_2 during wind turbine operations [184]. Low carbon emissions (as well as negligible emissions of nitrous oxides, mercury and sulphur oxides) arise during extraction, construction, maintenance, and decommissioning. The main positive local impact is the artificial reef creation, as a consequence of the additional substrata of the support structures, moorings and scour protection for colonization by epifaunal communities [185] [186]. The main negative local consequences are:

- Electromagnetic interference

Certain marine species (such as rays, sharks, and skates) use electromagnetic fields to avoid predators, detect food or prey, locate other fish, and navigate. The alternating current (AC) transmission cables emit electromagnetic fields which affect animal behaviour; however, there are still large uncertainties regarding the significance of such behavioural changes [187] [188].

- Impact on birds

There are several studies which provide evidence of an increase in avian mortality caused by colliding with wind turbines. Birds with higher risk of collision are seabirds and migrating passerines. However, the rate of mortality is highly dependent on the wind farm site and is relatively low, from 0.01 to 23 mortalities per turbine per year [189]. Other studies, such as the study conducted at the Nysted offshore wind farm in Denmark [190], state that some birds understand the presence of wind turbines, even during night time, and change their route to avoid flying through wind farms. This will decrease their mortality from collision, but they will expend a significant amount of energy flying around the farm. Moreover, placing an offshore wind farm in a feeding ground could be a great limitation since some marine bird species have specific areas in which they may successfully feed [191].

- Underwater noise and vibration

Marine species, such as cetaceans (dolphins, porpoises or whales) and pinnipeds (seals or sea lions), have developed their acoustic sensory systems in order to communicate, navigate, detect food or prey, and avoid predators.

Wind turbines cause both aerodynamic and mechanical noise. Aerodynamic noise is produced by the flow of air around the blades. Mechanical noise is produced by the motion of the wind turbine components; such as bearings, gearbox, and generator. Noise and vibration are transmitted to the water through the tower and foundations. During the operational phase, the turbine noise level is around 150 decibels (dB) re 1 μPa (reference pressure) at 1m [187] which may affect animal behaviour; but there is no identified degree to which this actually reduces their fitness [192] [193].

During construction, there are several sources of underwater disturbance: geophysical surveys, machinery and vessels, pile-driving, drilling, cable trenching, rock laying, foundation installation, turbine structure installation, etc. These activities may disrupt normal behaviour, interfere with reception of auditory cues, and even induce hearing impairment at close range [194] [191] [192] [195]. Pile-driving seems to produce the highest perturbation of all [193], since measurements indicate a source level of around 250 dB re 1 μPa at 1 m [196]. Sea mammals monitoring (during and after construction) has shown that the number of specimens observed decreased during the construction period; however, they seem to return a considerable time afterwards, although in lower numbers than before [194] [197] [198].

- Water turbidity

Installation (or decommissioning) of wind turbine support structures and undersea cables will affect the seabed and sediments, increasing local water turbidity which may result in the removal or physical disruption of benthic and planktonic communities [199] [200]. Changes in water flow patterns will affect sedimentation patterns which may cause bathymetric modification. Further research is required to determine the extent of the impact [199].

2.11 Offshore Technology Challenges

Offshore wind technology must solve both technical and economic issues to ensure development and reliance on this industry. The main challenges are given below:

- Lowering the cost of offshore wind energy is likely to be the greatest, since it involves optimising every stage of development, manufacture, installation, and operation to reduce the capital and operational expenditure.

- Obtaining project approvals for offshore wind farms is an uncertain and lengthy regulatory process; estimates vary based on the data collection, environmental studies, site characterisation, and developer's diligence.

- The offshore wind resource has not been well characterised, which has increased uncertainty over the power production potential.

- New materials and larger capacity turbines should be developed for the designs to be more viable.

- Validating modelling tools, which combine the turbine and substructure operating conditions for deep offshore designs, is required.

- Handling and installing mooring lines and anchors.

- It is good to learn from the experience of the oil and gas industry, but complacency could lead to a lack of concentration and failure to follow procedures.

- Building a strong supply chain; for being able to compete with other industrial sector for materials such as copper, high modulus carbon fibre, etc.

- Lack of suitably qualified people. Moreover, there is the risk of the migration of skilled workers from the offshore wind sector to the offshore oil and gas sector, caused by the offer of better pay and conditions [201].

- Shortfall in infrastructure, such as offshore transmission and suitable harbours with long deep water quays, and capable vessels. A deficit in available maintenance vessels is expected if all the planned wind farms go ahead [202].

- Increase reliability performance in order to maximise electricity production and minimise operation and maintenance costs.

- Improve ergonomy of wind turbines and predictive maintenance, which will reduce costs.

- Decrease financing costs. Banks and financial institutions view these uncertainties as risks which affect the ability of wind farm owners to raise the capital required to build offshore wind farms.

- Grid connections and high-voltage cables require to be better understood to achieve reliable integration.

2.12 Summary

In 1887, wind power began to be employed to generate electricity. Despite the efforts of many researchers, the popularity of using wind turbines has always fluctuated with the price of fossil fuels, and the world's first wind farm was not installed until 1980 (almost a century after the first turbine). Finally in 1991 the first offshore commercial wind farm was constructed in Denmark. The United Kingdom is the current leader in the offshore energy sector.

There are basically two types of wind turbine, distinguished according to the axis of the rotor's rotation. The axis of the HAWTs is parallel to the wind stream and the ground, while the VAWTs have their main rotor shaft arranged vertically. Three-bladed horizontal axis wind turbines dominate the market. The existing support structure configurations to date can be classified into two groups: fixed support structures (monopile, gravity based, suction bucket, tripod, and jacket), and floating offshore structures (spar buoy, TLP, and barge). The selection of the most preferable should be based on engineering, economics, and environmental attributes. One of the most influencing factors is the depth of water. The most popular substructure type is the monopile.

The design load cases should consist of a set of design situations covering the most significant conditions that an offshore wind turbine support structure may

experience, combining normal or extreme external conditions with wind turbine operational modes or other design situations.

Offshore wind energy costs may be derived as the sum of all the capital expenditure costs and the operational expenditure costs over the service life of the project, divided by the total energy output of the project. Thus cost of energy is calculated as unit of currency per unit of energy. The electricity production costs vary widely between countries, since there are different tax structures, availability of resources, etc. Some studies indicate that offshore project costs have been increasing over time, which is mainly caused by the trend to move further away from the coast into deeper waters and install higher capacity machines.

Offshore wind farms produce both beneficial and detrimental environmental impacts to the marine environment, which are local effects, and the atmosphere. In contrast to fossil fuels and nuclear power, wind power is considered a ‘carbon neutral’ technology since it does not emit CO_2 during wind turbine operation.

Although interest in offshore wind energy is continuously increasing (mainly motivated by the higher wind speed in the marine environment, unrestricted space, and lower social impact), this offshore technology must solve both technical and economic issues to ensure development and reliance on this industry.

3 S-N APPROACH TO FATIGUE LIFE PREDICTIONS

As outlined in the First Chapter, the S-N approach is used in fatigue-life assessment at the design stage. This chapter will analyse the evolution of the S-N design curves for girth welds and tubular joints over the years by gathering experimental data and comparing different guides, in order to identify weaknesses and evaluate their accuracy.

3.1 Girth welds

3.1.1 Background to the Current Fatigue Guidance

In 1976 Gurney [203] published the S-N curves for the various joint classes based on statistical analyses of experimental data obtained under tensile loading in his research into the fatigue of welded structures at Abington, UK. He suggested that these new curves should be simpler to use than those in British Standard (BS) 153 [204] as the stress analysis was greatly simplified. From a statistical analysis it was assumed that the mean S-N curve could be represented by straight lines of slopes -4.0 for Class B, -3.5 for Class C, and -3.0 for all the others. The confidence limits of the S-N curves are hyperbolae; however, it was assumed that the confidence limits could be represented by straight lines tangential to the hyperbolae and parallel to the mean S-N curve. The resulting design S-N curves are defined by Eq. 3-1, whose parameters are given in Table 3-1.

$$\log_{10} N = \log_{10} a_i - n_{sd}\sigma_{sd} + m \log_{10} \Delta\sigma \qquad \textbf{Eq. 3-1}$$

Where $\Delta\sigma$ is the applied stress range, N is the number of cycles to failure under constant amplitude loading conditions, σ_{sd} is the standard deviation of $\log_{10} N$, n_{sd} is the number of standard deviations below the mean, m is the slope, and C_i is the axis intercept.

Table 3-1 Details of S-N Curves.

Class	C_i	m	σ_{sd}
B	2.343E15	-4	0.1822
C	1.082E14	-3.5	0.2041
D	3.988E12	-3	0.2095
E	3.289E12	-3	0.2509
F	1.726E12	-3	0.2183
F2	1.231E12	-3	0.2279
G	0.566E12	-3	0.1793
W	0.368E12	-3	0.1846

BS 5400-10 [205] for the fatigue assessment of bridge parts which are subject to repeated fluctuations of stress, incorporated these new S-N curves in 1980. Thirteen years later, they were also applied into BS 7608 [206] for the fatigue design and assessment of steel structures, including a horizontal cut-off at 10 million cycles for operation in air and in seawater with adequate protection against corrosion. For free corrosion joints exposed to seawater, the curves should be reduced by a factor of 2 on life for all joint classes. In this document a correction on the stress range for joints with a thickness greater than 16 mm for welded joints or 25 mm for bolt diameters was included for the first time. At this stage in the case of butt welds with the weld reinforcement machined flush, the thickness correction is not required. The thickness correction is of the following form:

$$\Delta\sigma = \Delta\sigma_B \left(\frac{T_B}{T}\right)^{\frac{1}{4}} \qquad \textbf{Eq. 3-2}$$

Where $\Delta\sigma$ is the fatigue strength of the joint under consideration, $\Delta\sigma_B$ is the fatigue strength of the joint using the basic S-N curve, T is the actual thickness of the member or bolt diameter, and T_B is the reference thickness.

The design recommendations for cyclic loaded welded steel structures, prepared by a Joint Working Group of Commission XIII "Fatigue testing" and Commission XV "Fundamentals of design and fabrication for welding" of the International Institute of Welding (IIW) in 1982 [207] proposed two sets of S-N curves: one with a slope of 3, and the other of 3.5. The S-N curves were obtained from the experimental results of connections involving plates with a thickness of

approximately 15 mm [208]. These recommendations were applicable to welded joints, which do not operate in a severely corrosive environment, in any steel. Each S-N curve is identified by its fatigue strength at 2 million cycles. The fatigue strength at 5 million cycles is known as the constant amplitude fatigue limit. The curves have the following form:

$$N\Delta\sigma^m = C_i \quad \textbf{Eq. 3-3}$$

Where $\Delta\sigma$ is the applied stress range, N is the number of cycles to failure under constant amplitude loading conditions, m is the slope, and C_i is the axis intercept whose values are given in Tables 3-2 and 3-3 for the design S-N curve. The stress ranges recommended for the design correspond to the mean S-N curve minus two standard deviations.

Table 3-2 Details of design S-N curves for m=3.

Class	C_i	Fatigue limit (N/mm^2)
125	3.91E12	92
112	2.81E12	82
100	2.00E12	74
90	1.46E12	66
80	1.02E12	59
71	7.16E11	52
63	5.00E11	46
56	3.51E11	41
50	2.50E11	37
45	1.82E11	33

Table 3-3 Details of design S-N curves for m=3.5.

Class	C_i	Fatigue limit (N/mm^2)
125	4.37E13	96
112	2.97E13	8686
100	2.00E13	77
90	1.38E13	69
80	9.16E12	62
71	6.03E12	55
63	3.97E12	48
56	2.63E12	43
50	1.77E12	38
45	1.22E12	35

These recommendations were presented at the European Convention for Constructional Steelwork (ECCS) fatigue design recommendations produced in 1985 [209]. These fatigue curves were characterised by a change in slope from 3 to 5 at 5 million cycles, and by a cut-off at 100 million cycles. Ref. [206] states the change of slope in the curves from m to 2m-1 is a mathematical device to avoid difficulties in cumulative damage calculations using Miner's rule. The same constant amplitude fatigue limits as the IIW recommendations were considered. It was considered that for plate thicknesses greater than 25 mm these curves might be unsafe; therefore, in order to calculate the reduced fatigue strength, the following formula was applied:

$$\Delta\sigma = \Delta\sigma_B \sqrt[4]{\frac{25}{T}} \qquad \textbf{Eq. 3-4}$$

Where $\Delta\sigma$ is the fatigue strength of the joint under consideration, $\Delta\sigma_B$ is the fatigue strength of the joint using the basic S-N curve, and T is the actual thickness of the member or bolt diameter. These S-N curves with double slope constants and a cut-off limit were incorporated in DD ENV 1993-1-1 [210] in 1992, and in 1996 in the first edition of the IIW recommendations for the fatigue design of welded joints and components [211]; their parameters are given in Table 3-4. Finally, BS EN 1993-1-9:2005 (EC 3 Part 9) [212] replaced BS 5400-10:1980 and DD ENV 1993-1-1:1992. Neither IIW nor EC 3 give recommendations for the fatigue design of offshore structures in a corrosive environment [213].

Table 3-4 EC 3/IIW constants, constant amplitude fatigue limit and cut-off limits.

Class	C_i for S-N curve at 5E6 cycles, m=3	Constant amplitude fatigue limit	C_i for S-N curve at 5E6 cycles, m=5	Cut-off limit
160	8.192E12	118	1.139E17	64.8
140	5.488E12	103	5.840E16	56.7
125	3.906E12	92.1	3.313E16	50.6
112	2.810E12	82.5	1.913E16	45.3
100	2.000E12	73.7	1.086E16	40.5
90	1.458E12	66.3	6.411E15	36.4
80	1.012E12	58.9	3.558E15	32.4
71	7.158E11	52.3	1.959E15	28.7
63	5.001E11	46.4	1.078E15	25.5
56	3.512E11	41.3	5.980E14	22.7
50	2.500E11	36.8	3.393E14	20.2
45	1.823E11	33.2	2.004E14	18.2
40	1.280E11	29.5	1.112E14	16.2
36	9.331E10	26.5	6.565E13	14.6

Ref. [214] concludes that DNV-RP-C203 [215] gave the most comprehensive coverage of life assessment methods for air and seawater. There are strong similarities with EC 3. The first Det Norske Veritas (DNV) recommended practice for fatigue strength analysis of offshore steel structures was published in 2001; since then it has incorporated some modifications, for example a change in the slope of B1 and B2 S-N curves from 3.0 to 4.0 in order to be more in line with fatigue test data for the base material [216].

Ref. [213] notes that the shape of the S-N curves in EC 3/IIW may be non-conservative, especially for variable amplitude loading, and recommends using the S-N curves with slope 3 for N < 1E7 cycles and 5 for N > 1E7 cycles. This implies that the constant amplitude fatigue limit is shifted from 5E6 cycles to 1E7 cycles; however, the axis intercepts remain the same. The fatigue strength is reduced for plate thicknesses larger than 25 mm for bolts and welded connections other than tubular joints, and 32 mm for tubular joints. The resulting DNV design S-N curves are defined by Eq. 3-5, whose parameters are given in Table 3-5.

$$\log_{10} N = \log_{10} C_i - m \log_{10}(\Delta\sigma \left(\frac{T}{T_{ref}}\right)^{\chi}) \quad \textbf{Eq. 3-5}$$

Where $\Delta\sigma$ is the applied stress range, N is the number of cycles to failure under constant amplitude loading conditions, $\log_{10} C_i$ is the intercept of log N-axis by S-N curve, m is the slope, χ is the thickness exponent, T is the actual thickness of the member or bolt diameter, and T_{ref} is the reference thickness (25 mm for bolts and welded connections other than tubular joints, and 32 mm for tubular joints).

Table 3-5 DNV design S-N curves in air.

S-N curve	N ≤ 1E7cycles m_1	N ≤ 1E7cycles $\log_{10} C_{i1}$	N > 1E7 cycles m_2= 5 $\log_{10} C_{i2}$	Fatigue limit at 1E7 cycles	χ
B1	4.0	15.117	17.146	106.97	0
B2	4.0	14.885	16.856	93.59	0
C	3.0	12.592	16.320	73.10	0.05
C1	3.0	12.449	16.081	65.50	0.10
C2	3.0	12.301	15.835	58.48	0.15
D	3.0	12.164	15.606	52.63	0.20
E	3.0	12.010	15.350	46.78	0.20
F	3.0	11.855	15.091	41.52	0.25
F1	3.0	11.699	14.832	36.84	0.25
F3	3.0	11.546	14.576	32.75	0.25
G	3.0	11.398	14.330	29.24	0.25
W1	3.0	11.261	14.101	26.32	0.25
W2	3.0	11.107	13.845	23.39	0.25
W3	3.0	10.970	13.617	21.05	0.25

Ref. [217] shows that the fatigue life of joints with cathodic protection (CP) in a seawater environment is no shorter than that for joints in air for N > 1E7 cycles [213]. Moreover, Ref. [218] states that the fatigue life obtained in seawater with CP for N < 1E6 cycles is reduced by a factor of approximately 2.5 with respect to that obtained in air [213]. The resulting DNV S-N curves in seawater with CP can be observed in Table 3-6.

Table 3-6 DNV design S-N curves in seawater with CP.

S-N curve	N ≤ 1E6 cycles m_1	$\log_{10} C_{i1}$	N > 1E6 cycles m_2= 5	$\log_{10} C_{i2}$	Fatigue limit at 1E7	χ
B1	4.0	14.917	17.146		106.97	0
B2	4.0	14.685	16.856		93.59	0
C	3.0	12.192	16.320		73.10	0.05
C1	3.0	12.049	16.081		65.50	0.10
C2	3.0	11.901	15.835		58.48	0.15
D	3.0	11.764	15.606		52.63	0.20
E	3.0	11.610	15.350		46.78	0.20
F	3.0	11.455	15.091		41.52	0.25
F1	3.0	11.299	14.832		36.84	0.25
F3	3.0	11.146	14.576		32.75	0.25
G	3.0	10.998	14.330		29.24	0.25
W1	3.0	10.861	14.101		26.32	0.25
W2	3.0	10.707	13.845		23.39	0.25
W3	3.0	10.570	13.617		21.05	0.25

For unprotected joints exposed to seawater, it is assumed that curves have a constant slope of 3 without any cut-off level. Furthermore, Ref. [218] states that the fatigue life obtained in seawater without CP for N < 1E6 cycles is reduced by a factor of approximately 3.0 compared to that obtained in air [213]. The resulting DNV S-N curves in seawater for free corrosion are shown in Table 3-7:

Table 3-7 DNV design S-N curves in seawater for free corrosion.

S-N curve	$\log_{10} C_{i1}$ for $m1 = 3$	χ
B1	12.436	0
B2	12.262	0
C	12.115	0.15
C1	11.972	0.15
C2	11.824	0.15
D	11.687	0.20
E	11.533	0.20
F	11.378	0.25
F1	11.222	0.25
F3	11.068	0.25
G	10.921	0.25
W1	10.784	0.25
W2	10.630	0.25
W3	10.493	0.25

Finally, BS 7608:1993 has been replaced by BS 7608:2014 [219], where the standard basic design S-N curves for operation in air remain the same, for free corrosion have been modified, and new design S-N curves for operation in seawater have been incorporated. These design curves were derived by applying fatigue life reduction factors (the same factors as the DNV curves) to the design curves for operation in air, and the resulting parameters are shown in Tables 3-8 and 3-9. It was considered that CP offers some resistance to corrosion fatigue but only in the high-cycle regime (transition at constant amplitude endurance of approximately one million cycles, depending on the class), so design curves should be reduced by a factor of 2.5 on life before the transition, and there is a horizontal cut-off at 10 million cycles. For unprotected joints exposed to seawater, a penalty of 3 on life is applied. The thickness correction is of the following form:

$$\Delta\sigma = \Delta\sigma_B k_{TB} \qquad \textbf{Eq. 3-6}$$

Where,

for T > 25 mm:

$$k_{TB} = \left(\frac{T_B}{T_{eff}}\right)^{\Omega} [1 + 0.18\, DoB^{1.4}] \qquad \textbf{Eq. 3-7}$$

for 4 mm ≤ T ≤ 25 mm:

$$k_{TB} = [1 + DoB^{1.4}\{\left(\frac{T_B}{T_{eff}}\right)^{\Omega} - 1\}][1 + 0.18\, DoB^{1.4}] \qquad \textbf{Eq. 3-8}$$

and

$\Delta\sigma$ is the fatigue strength of the joint under consideration, $\Delta\sigma_B$ is the fatigue strength of the joint using the basic S-N curve, T is the actual thickness of the member or bolt diameter, T_B is the reference thickness (tubular nodal joints: 16 mm, non-nodal joints: 25 mm, and bolts: 25 mm), T_{eff} is the greater of T_B or T, Ω is 0.25 or 0.2 [219], and DoB is the degree of bending.

Table 3-8 BS 7608 design S-N curves in seawater with CP.

	$\Delta\sigma \geq \Delta\sigma_T$			$\Delta\sigma_T > \Delta\sigma \geq \Delta\sigma_{N\leq 10^7}$		$\Delta\sigma < \Delta\sigma_{N\leq 10^7}$
	$\Delta\sigma_T$ (N/mm^2)	C_i	m	C_i	m	Cut-off limit
B	252	4.05E14	4	1.02E17	5	100.4
C	144	1.69E13	3.5	2.25E18	5	186.4
D	85	6.08E11	3	4.29E15	5	53.3
E	75	4.14E11	3	2.28E15	5	46.9
F	63	2.53E11	3	9.88E14	5	39.7
F2	56	1.72E11	3	5.18E14	5	34.9
G	46	9.91E1	3	2.05E14	5	29.0
G2	39	5.92E10	3	9.77E13	5	25.0
W1	33	3.73E10	3	4.02E13	5	20.9
X	52	1.40E11	3	3.9E14	5	33.0

Table 3-9 BS 708 design S-N curves for unprotected joints in seawater.

	C_i	m
B	1.41E13	3.5
C	1.41E13	3.5
D	5.07E11	3
E	3.47E11	3
F	2.10E11	3
F2	1.42E11	3
G	8.33E10	3
G2	4.93E10	3
W1	3.11E10	3
X	1.17E11	3

The evolution from less to more conservative curves may be appreciated in Figures 3-1 and 3-2, where the different recommended curves for double-sided ground flush welds reported as free from significant welding flaws (Curve C/112), and for down-hand double-sided welds (Curve D/90), are shown as examples. Moreover, an overall summary of the C and D S-N curves background is shown in Figure 3-3.

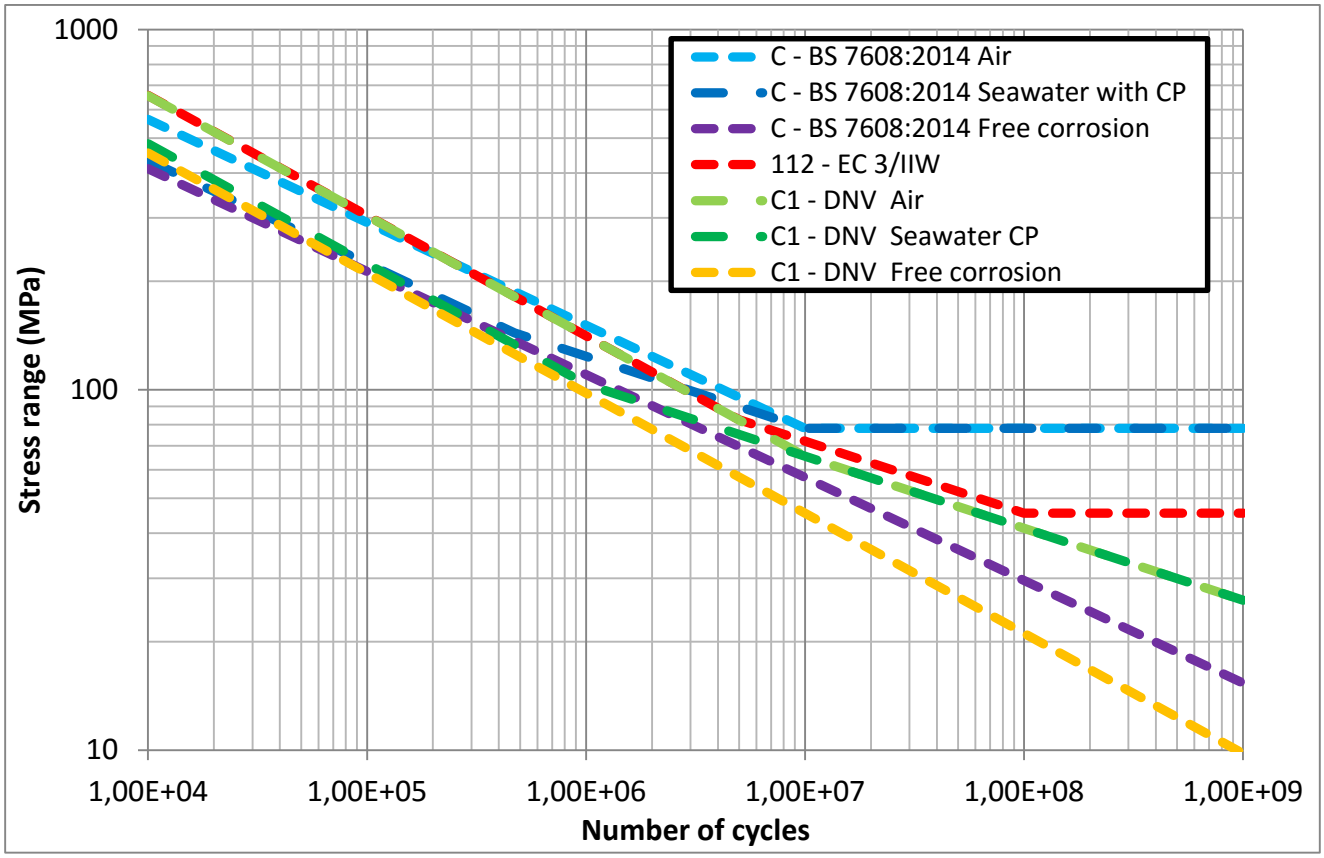

Figure 3-1 S-N curves for double-sided welds, subsequently ground flush.

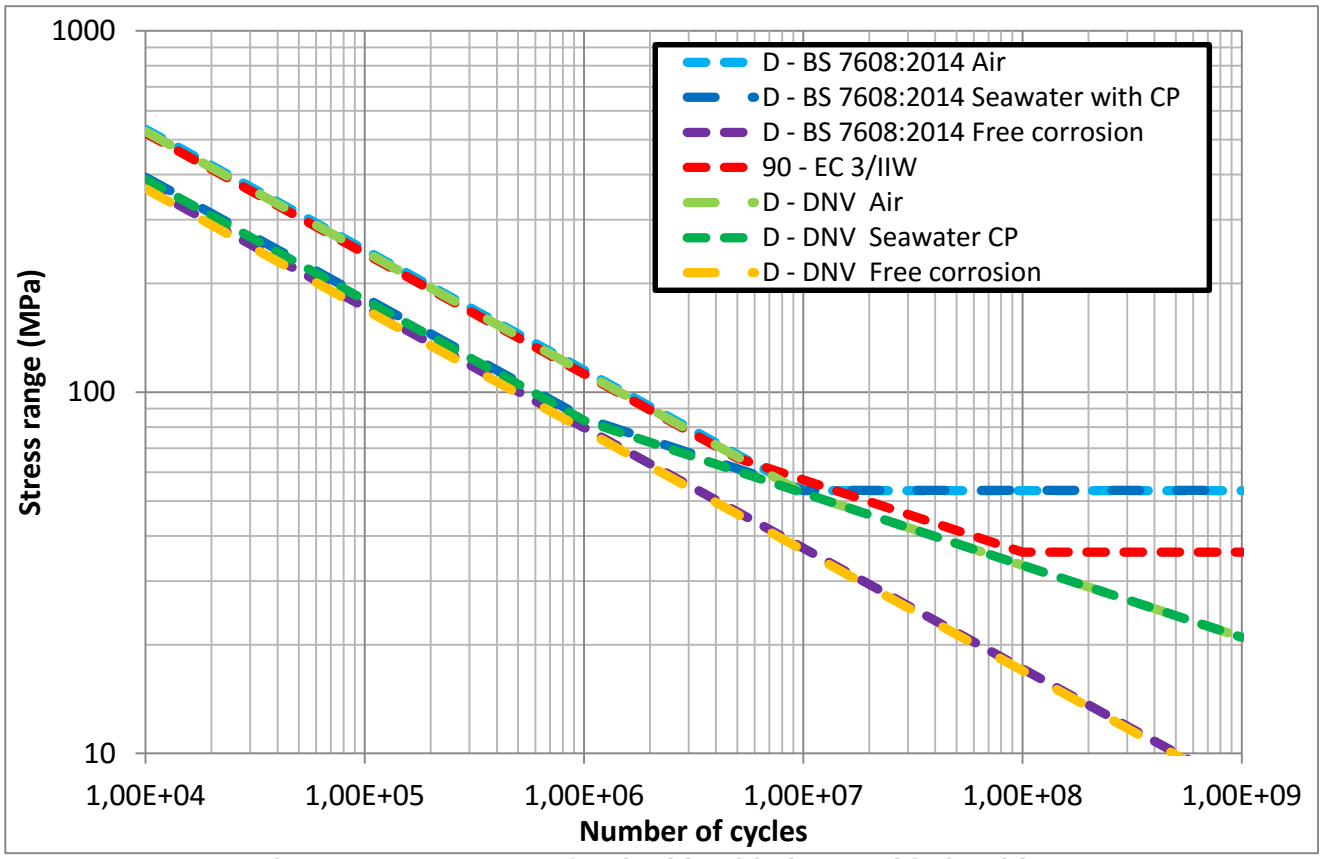

Figure 3-2 S-N curves for double-sided, as-welded welds.

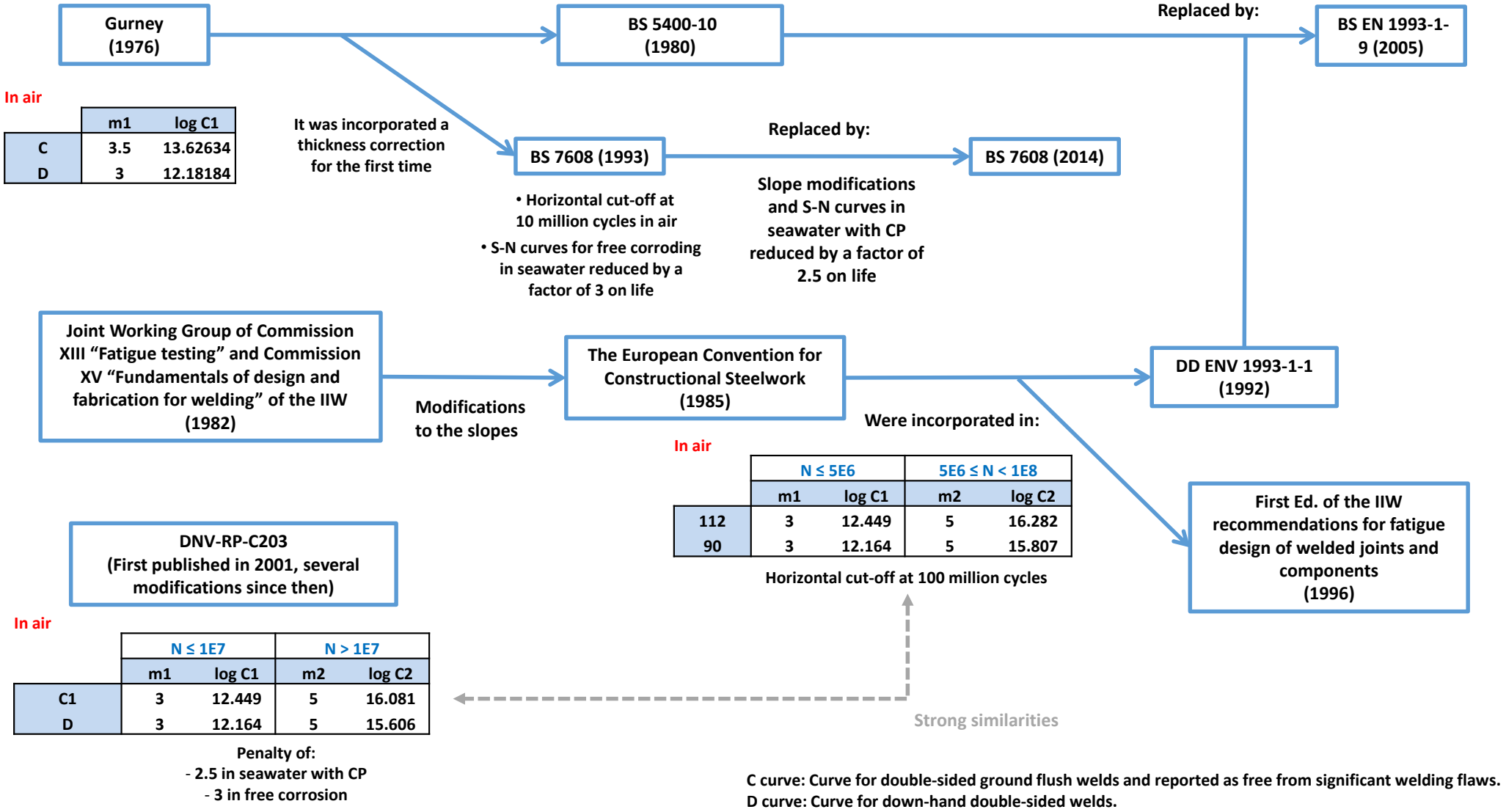

Figure 3-3 C and D curves background summary.

3.1.2 Comparison between DNV and BS 7608 Girth Welded Curves

This section of the thesis aims to show how these modifications to the S-N curves, which at first glance seem small, have a major impact on design. The less conservative curves (BS 7608 curves) will be compared with the more conservative ones (DNV curves). Firstly the Class D curves for down-hand double-sided welds in air will be compared (see Figure 3-4). The thickness correction factor of BS 7608 takes into consideration the effect of the DoB, but for this case it is assumed to be zero as the bending stress component would be due to misalignment [219]. Thus both BS 7608 and DNV thickness correction factors are the same, therefore an actual thickness of 25 mm has been considered.

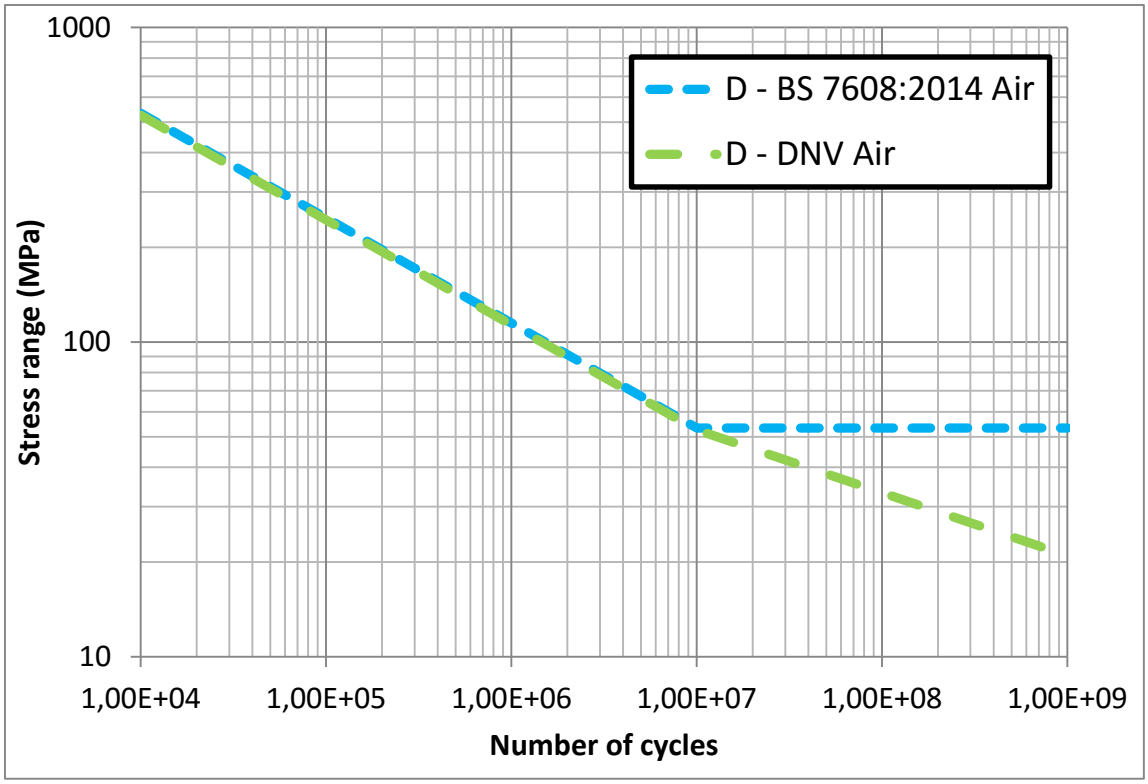

Figure 3-4 DNV and BS 7608 Class D curves.

For illustrative purposes, the BS D curve is selected to estimate the fatigue life at 100 MPa stress range; this shows a small difference of 4% (60683.27 cycles) compared to the more conservative DNV curve. However, below 53.4 MPa there would be a greater difference, since the BS D curve indicates that the joint will

last for ever. For example, at 50 MPa stress range, the DNV D curve indicates a joint fatigue life of 12,916,652.6 cycles. Considering 5 million cycles per year, which corresponds to an average period of 6.3 sec –i.e. 100 million cycles in 20 years' service life – [215], it would last 2.58 years.

Comparing Class C curves for double-sided ground flush welds, the percentage reduction of life is even greater since BS 7608 does not require the application of a thickness correction for this kind of weld. For example, if the DNV C1 curve for joints in a freely corroding marine environment is considered in order to estimate the fatigue life of a member of 87 mm thick for a stress range of 40 MPa, there will be a life reduction of 76% compared to the BS C curve which, using the same time basis as above, is approximately 5.3 years (see Figure 3-5).

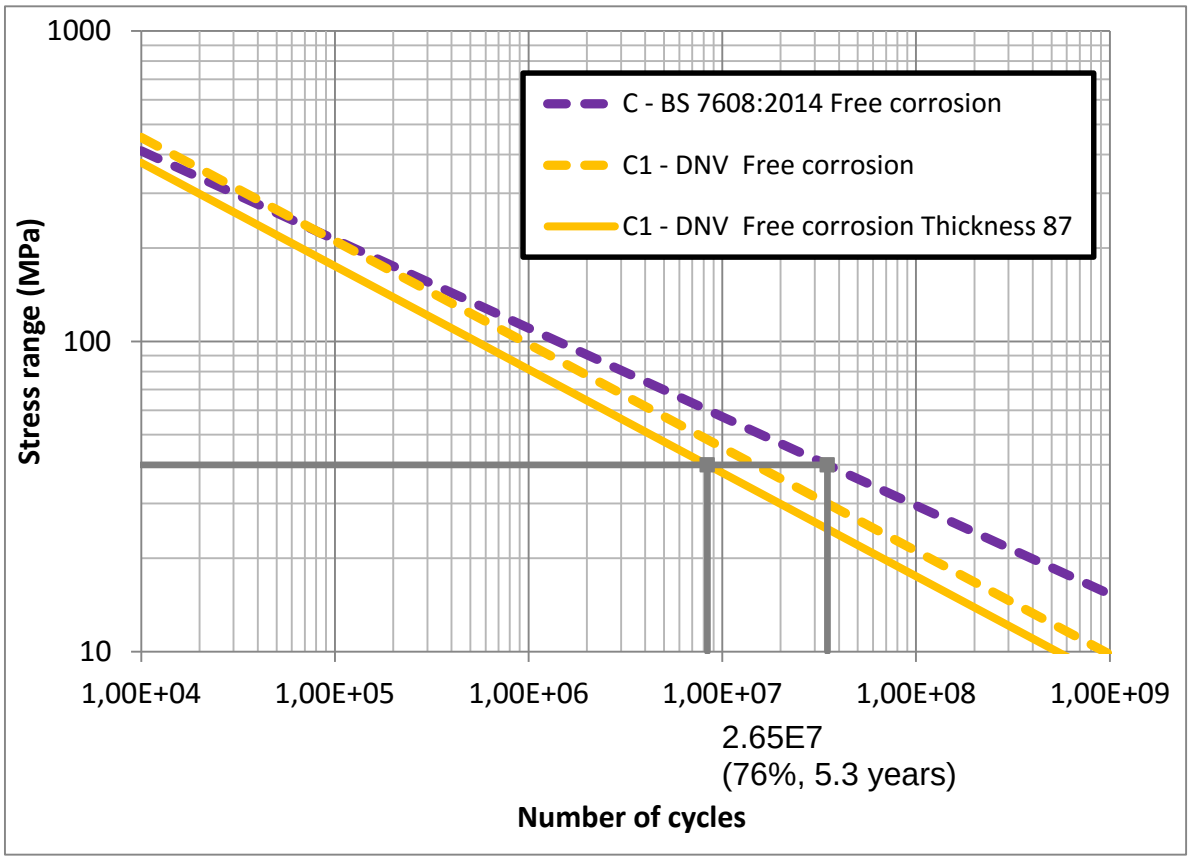

Figure 3-5 DNV and BS 7608 Class C curves with and without thickness correction for 87 mm for free corrosion in seawater.

Note that the thickness correction was applied to modify the S-N curve for illustrative purposes, where normally thickness correction applied in design is to raise the effective stress range.

The decrease in fatigue strength for thicker joints is a generally accepted phenomenon, however, the scale of the decrease and the reasons for the shorter lives for thicker joints are still the subject of some controversy. Ref. [220] argued that the decrease is primarily caused by the increased local weld toe stresses which are caused by the change in weld geometry of the thicker joints. The stress concentration (SCF_t) of a weld depends on the plate thickness (T_P) and the local weld toe radius (R_w); the ratio will be higher if the thickness is increased, therefore, also the stress concentration (see Figure 3-6).

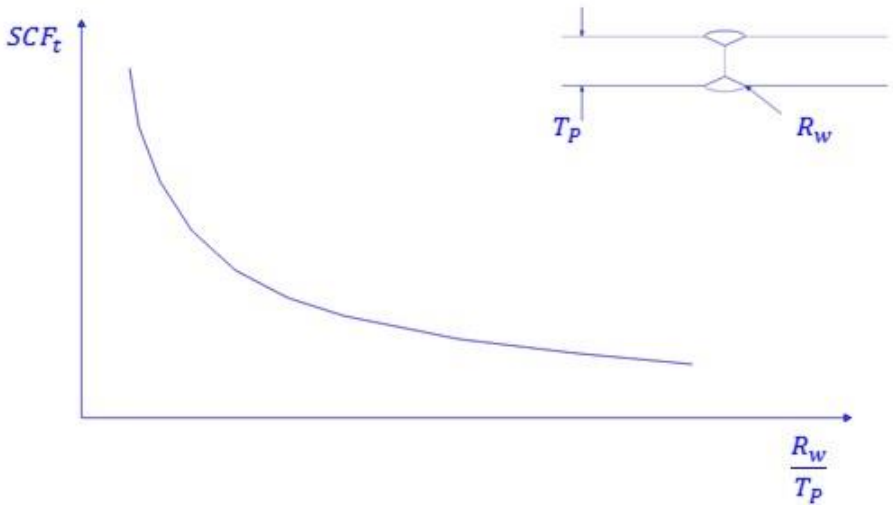

Figure 3-6 Stress concentration dependence on the plate thickness and local weld toe radius.

Other reasons for thicker sections having lower fatigue resistance for the same stress range are known as the “volumetric effect”, where simply having more material implies a greater likelihood of having more defects, and the “stress gradient effect”, which applies to thin sections under bending and the associated steep stress decay gradient which has been demonstrated to make thinner sections relatively strong against fatigue. However, given that neither of the above two effects is relevant here and that the weld toe radius tends to infinity for flush ground welds, the argument to apply thickness correction for flush ground

and low SCF joints is particularly weak. Table 3-10 shows the differences in fatigue life in applying the thickness correction for the DNV C1 curve in air for an 87 mm thickness member. For high stress ranges the difference is negligible, but for low stress ranges, such as 25 MPa, there is a reduction in fatigue life of approximately 115 years (based on 5 million cycles per year).

Table 3-10 Life reduction.

Stress Range (MPa)	$N \quad T = 25mm$	$N \quad T = 87mm$	**% Reduction of Life**	**Life reduction (Years)**
200	351487.60	241788.83	31.21	0.02
150	833155.80	573129.09	31.21	0.05
100	2811900.83	1934310.67	31.21	0.18
50	38561150.09	20670946.19	46.39	3.58
25	1233956802.94	661470277.94	46.39	114.50

3.1.3 Published Literature Concerning Girth Welds

Published data from fatigue tests on full-scale girth welds are very scarce, and are not really representative for offshore support structures. As can be observed in Figure 3-15, most of the published results are characterised by specimens with an OD of 609 mm with a WT of 20 mm; while the typical pile diameter for monopiles is of 4-5 m, and the WT is 50-90 mm [153]. Although these data are not really representative for this study, they can be used to evaluate and compare the BS 7608 and DNV S-N curves in order to draw certain conclusions.

Comparing data from fatigue tests of double-sided as-welded girth weld joints presented in **Figure 3-7**, both BS 7608 D and DNV D curves would provide approximately 81% probability of survival for the low-cycle regime, since they are pretty close to the design curve of 18 specimens with a confidence level of 97.73%. It is not possible to judge BS and DNV D curves with respect to the high-cycle regime because of the lack of data. On the other hand, they could be too conservative, since most of the fatigue test data were obtained in 1998 and both the welding processes and the flaw detection processes have greatly advanced since then.

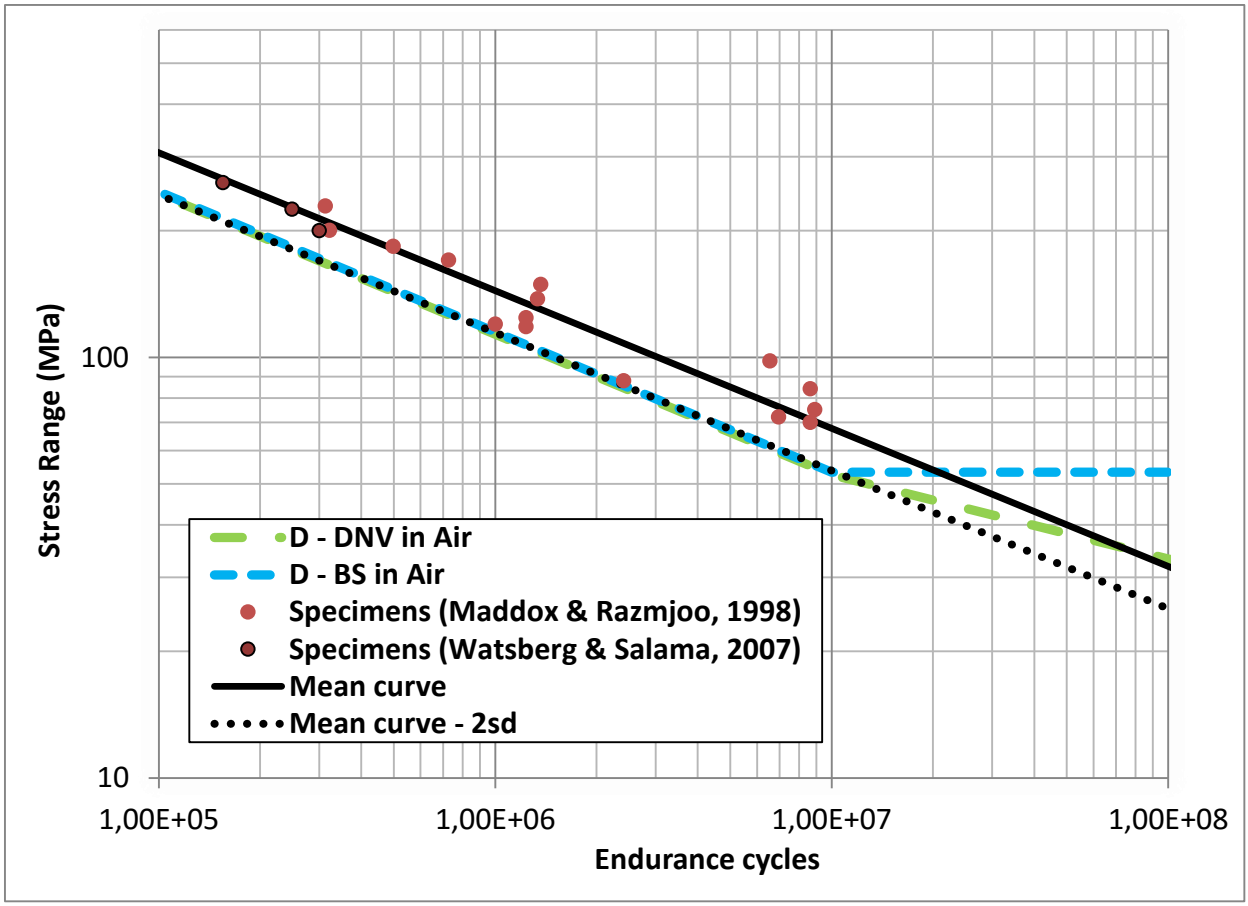

Figure 3-7 Double-sided as-welded girth weld data.

Table 3-11 Published fatigue data for grith welds.

Reference	Steel grade	Yield strength	Dimensions	Welding geometry	Weld root bead and cap	Welding process	Welding positions	Stress Ratio	Loading
Light & Frank (1993) [221]	API-5L X52		324mm x 14.3mm WT	Single-sided		TIG / SAW / MMA	5G / 1G / 2G	> 0	Axial
Maddox & Razmjoo (1998) [221]	API-5L X60 UOE	443	609mm x 20mm WT	Single-sided / Double-sided		TIG / MIG / MMA	5G		Axial
Maddox & Branco (1998) [221]	EN10210P4 / S355J2H	397	100mm x 6mm WT	Single-sided		TIG / Plasma	1G	-1	Bending
Maddox et al. (2002) [222]	API 5L-X65 / API 5L-X80		609mm OD x 21.4mm WT / 273mm OD x 12.6mm WT	Single-sided	Flush ground	SAW / GTAW	1G		
Maddox & Zhang (2008) [223]	API-5L X65 UOE		508mm OD x 22mm WT	Single-sided onto temp. backing		GMAW	5G	0.16 - 0.71	Axial
Morgan & Tubby (2006) [224]			30" x 33.7 mm						
Newman, R.P. (1956) [221]	BS 806 B		168mm OD x 9.5mm WT	Single-sided		MMA / Oxy-acetylene	3GQ	-1 / 0.1	Bending / Axial
Haagensen, P. (2008) [224]			6" ID x 9.9 mm						
Pereira, M. (2004) [225]	BSI 7191 GR 355EN	350	324mm x 12.7mm WT	Single-sided		SMAW			Bending
Salama, M.M. (1999) [226]	UOE X65	450	609mm x 20.6mm WT		As-welded / Flush ground			0.1	Axial
Scholte & Buisman (1988) [221]	API-5L X52		457mm x 15.9mm WT	Single-sided		MMA	3GQ	-1	Bending
Watanabe et al. (1981) [221]	JIS G3456 38		89.1x5.5/7.6/11.1	Single-sided		TIG / MMA		-1	Bending
Wästberg & Salama (2007) [227]	UOE X60		609mm x 20.6mm WT	Single-sided / Double-sided		PGMAW / FCAW / GTAW	5G	0.1	Axial
Wirsching et al. (2005) [228]	API-5L X60 UOE		610mm OD x 20mm WT		Flush ground				

Considering the data for double-sided flush ground welds with and without defects presented by Ref. [227], both BS and DNV curves could be too conservative (see Figure 3-8). The mean curves and standard deviations of the different curves of the BS guide are known, therefore, it is possible to calculate a new curve which has been reduced by just one standard deviation. This new curve would remain safe for this data; however, this is based on only three specimens and this simply does not provide sufficient reliability (approximately 68.2% probability of survival with approximately 68.3% confidence level).

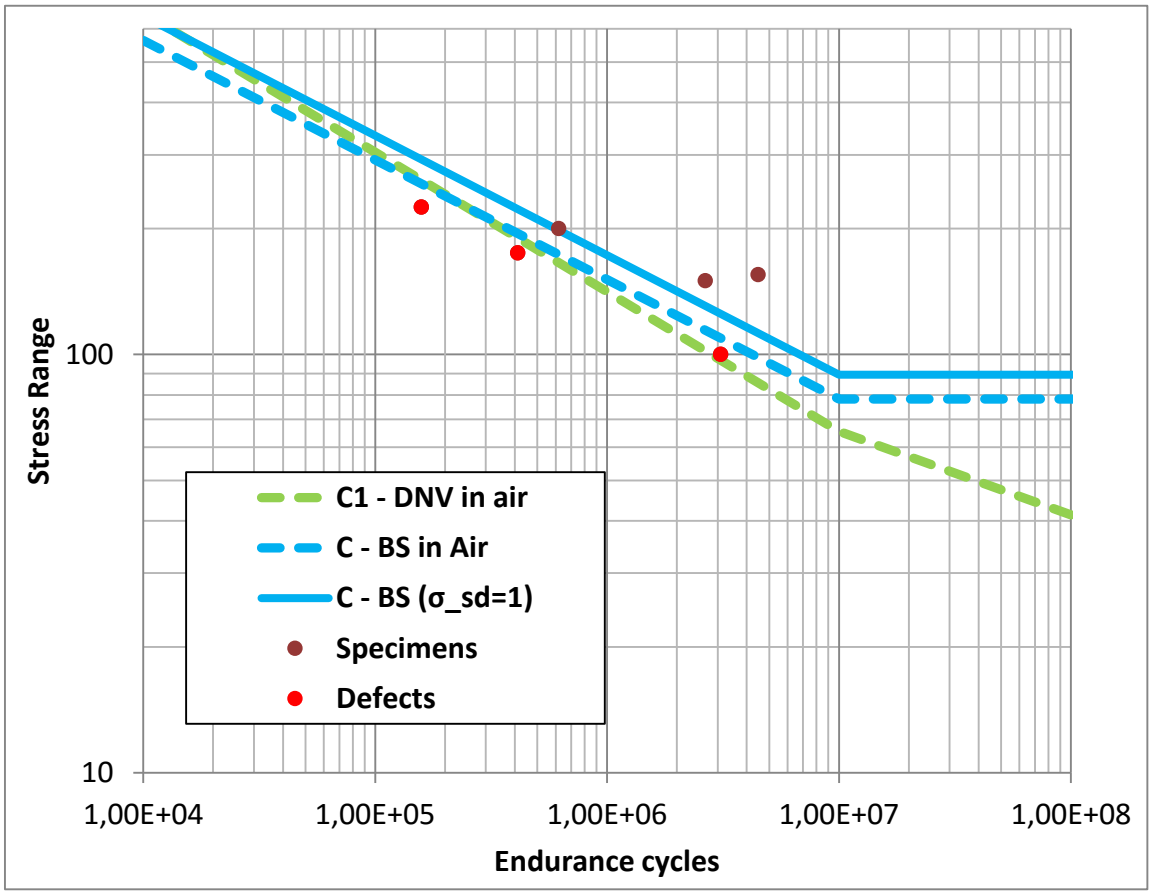

Figure 3-8 Double-sided flush ground girth weld data.

Fatigue test data obtained by Razmjoo et al. (1998) [222] in strip specimens extracted from flush ground girth welded pipes of 12 m length, 1118 mm OD x 38 mm WT in pipeline steel (API 5L X70), show that both BS and DNV C curves for stress ranges lower than 600 MPa could be too over-conservative (See Figure 3-9). However, this is based on only 11 specimens and does not provide sufficient

reliability (approximately 71% probability of survival with 97.73% confidence level).

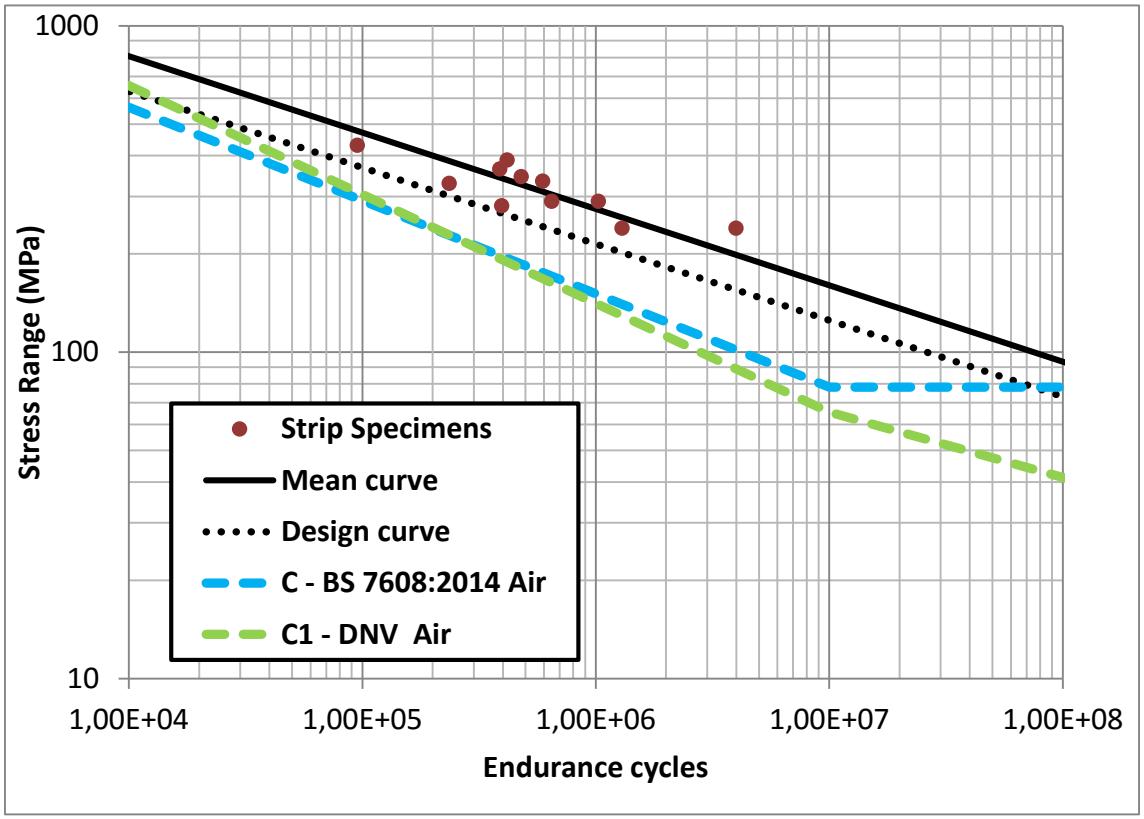

Figure 3-9 Flush ground strip specimens cut from girth welds.

It cannot be ignored that both flush ground and as-welded fatigue test data have generally been obtained for N < 1E7 cycles, while the range from 1E6 to 1E8 cycles contributes most to the damage [213], so fatigue test data with lower stress ranges would be more representative.

Ref. [223] suggests that strip specimens cannot be relied upon to establish the S-N curve in the high-cycle regime or the fatigue limit of a girth welded pipe, since significant differences were found in their high-cycle fatigue lives (see Figure 3-10). He suggests that these differences may be mainly due to the fact that girth welded pipes are subject to high residual stresses, which are relieved when strip specimens are extracted from the pipe, and the increased likelihood of finding a significantly large defect in a larger volume.

However, the residual stresses released by longitudinally cutting a pipe section are in the circumferential direction and not those normally associated with the development of circumferential cracks from girth welds.

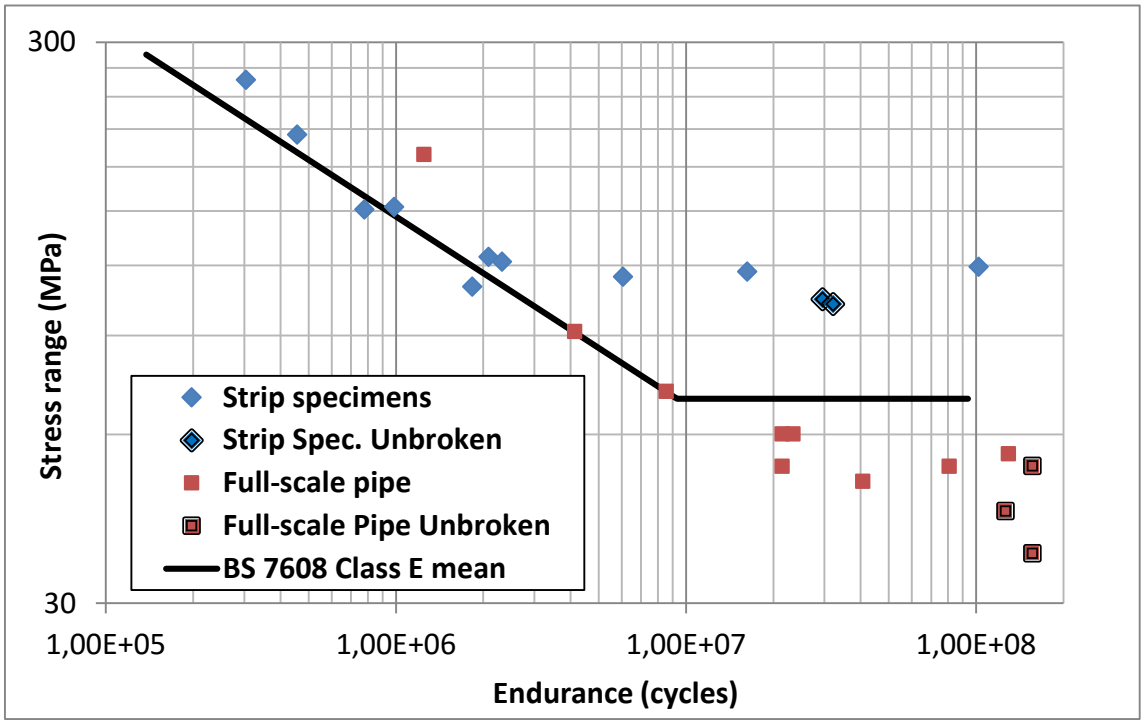

Figure 3-10 Fatigue test results obtained from pipes and strip specimens.

However, Ref. [226] reported that if strip specimens are tested under a condition that simulates the presence of high residual stresses, such as maintaining the maximum cyclic stress equal to the yield strength, the results could be considered to be similar to those of the pipes (see Figure 3-11).

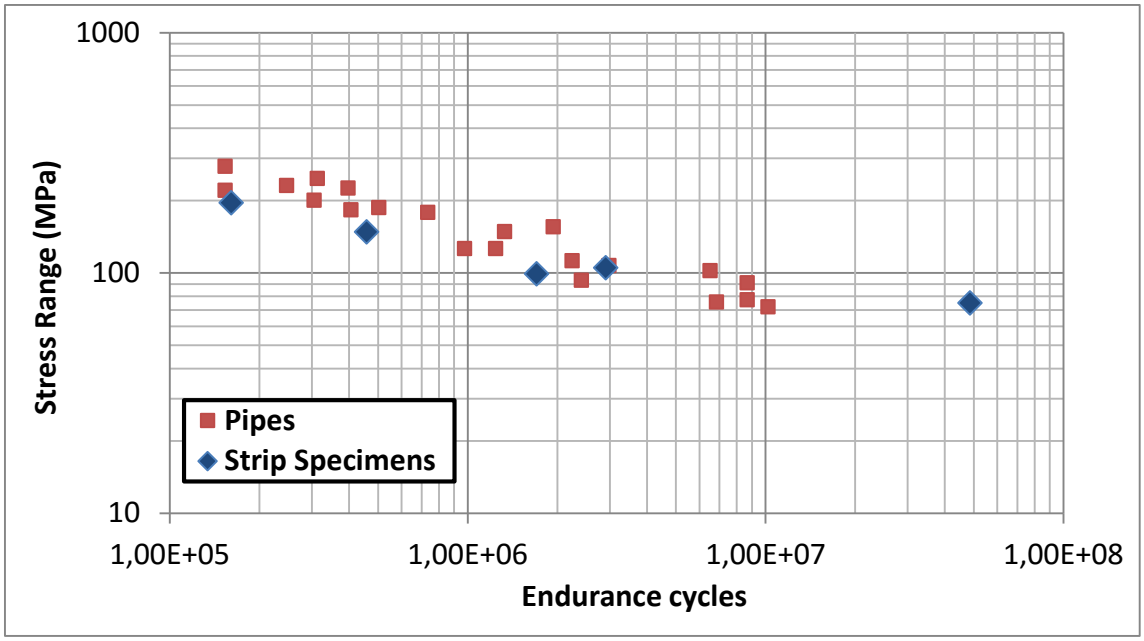

Figure 3-11 Fatigue test results on girth welded pipes and strips machined from the pipes.

3.2 Tubular joints S-N curve

A tubular joint is formed by one or more tubular members (braces) connected by welding to the main tubular element of equal or larger size (chord), as can be observed in Figure 3-12, where the non-dimensional terms which depend on the parametric equations can be appreciated.

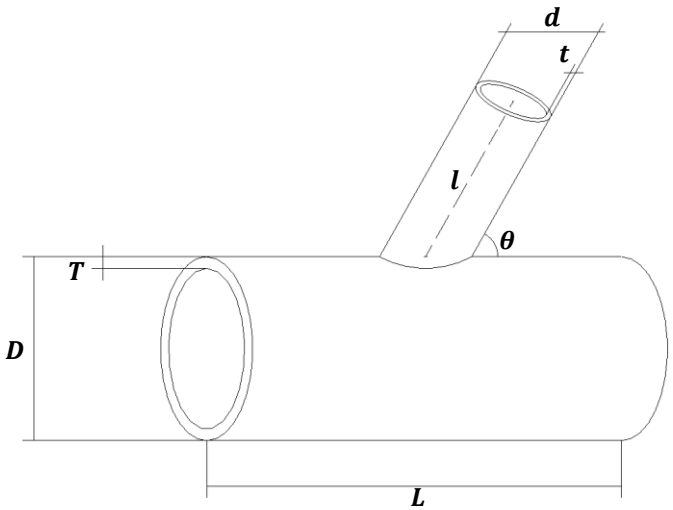

$$Geometric\ ratios\text{: } \alpha = \frac{2L}{D}, \beta = \frac{d}{D}, \gamma = \frac{D}{2T}, \tau = \frac{t}{T}$$

Figure 3-12 Geometric notation for tubular joints.

3.2.1 The T' curve

The first recommendations for the design of tubular joints against fatigue, based on the use of S-N curves, were given by the American Petroleum Institute (API) and the American Welding Society (AWS) in 1972 [229]. The first S-N curves based on joint hot spot stress were referred to as **X curves** in the two American documents, API RP 2A [230] and AWS D1.1-72 [231]. The data used to obtain the S-N curve were composed mainly of fillet-welded plate data and some small-scale tests on tubular joints tested in air under constant amplitude [229] [232].

The 2nd edition of the UK Department of Energy Guidance Notes [233] recommended the **Q curve**, which is based on the data generated by Marshall [234] [235], Smedley [236] and Gurney [237]. Since this curve was published, two major revisions have taken place. The first revision was in 1984, the results from the UKOSRP and the ECSC sponsored research programmes highlighted that the Q curve could be unconservative under certain conditions [232]. The S-N curve recommended in this revision became known as the **T curve**. Ref. [229] explains that a total of 64 T-, X- and K-joint test results were used to obtain this curve. More specifically, the curve was formulated from the mean 32 mm chord WT data curve less two standard deviations based on the 16 mm chord WT data, representing a confidence level of 97%. Obtaining the curve was based on the hot spot stress, and the same definition as in the UKOSRP and ECSC test programmes was used. It is recommended for joints in air or seawater where adequate protection against corrosion has been provided.

The T curve is formulated as [229]:

$$log_{10}N = 12.164 - 3 . log_{10}\Delta\sigma \qquad \textbf{Eq. 3-9}$$

The thickness correction recommended is [229]:

$$\Delta\sigma = \Delta\sigma_o . \left(\frac{32}{t}\right)^{\frac{1}{4}} \qquad \textbf{Eq. 3-10}$$

Where t is the chord wall thickness; for thicknesses smaller than 22 mm a value of 22 mm is imposed for calculating fatigue lives.

The second revision was in 1996 incorporating a significant amount of new data which became available on the fatigue behaviour of welded tubular joints [217]. The new curve for tubular joints has been designated the **T' curve.** Ref. [217] explains that a total of 59 T-, Y-, X- and K-joints of 16 mm were used to obtain this curve, because this was the largest subset of data with the widest range of joint geometries and loading modes. This second revision retained the hot spot stress definition used previously. A preliminary assessment of the data showed that the slope (m) of the mean $\log_{10}$N vs. $\log_{10}$S line had a value which was very close to 3, and a fixed value of m equal to 3 was retained for consistency with earlier guidance. The new T' design S-N curve for tubular joints in air with a chord WT of 16 mm are expressed below [238]:

$$log_{10}N = 12.476 - 3\ log_{10}\Delta\sigma \qquad \text{for } N < 10^7 \qquad \textbf{Eq. 3-11}$$

$$log_{10}N = 16.127 - 5\,.\,log_{10}\Delta\sigma \qquad \text{for } N > 10^7 \qquad \textbf{Eq. 3-12}$$

The thickness correction recommended is of the form [239]:

$$\Delta\sigma = \Delta\sigma_o\,.\left(\frac{16}{t}\right)^{0.3} \qquad \textbf{Eq. 3-13}$$

3.2.2 Linear Regression Analyses

Regression analysis is a statistical tool for the study of the behaviour of the dependent (or explained) variable in relation to the behaviour of one or more independent (or explanatory) variables.

The assumptions of the Linear Regression Model are:

- Linearity, the regression model is linear in the parameters;
- Independence, the explanatory variable(s) is(are) uncorrelated with the error term;
- Homoscedasticity, the variance of the residuals is constant;
- Normality, residuals are normally distributed with a zero mean value;
- No autocorrelation, there is no correlation between residuals; and
- No collinearity, there is no exact linear relationship between the two explanatory variables.

3.2.2.1 Two-Variable Linear Regression Analyses

3.2.2.1.1 Sample 1: 59 tubular joints of 16 mm

The statistical regression package IBM SPSS [240] was used for the statistical assessment. A sample size of 59 tubular joints of 16 mm was selected in order to match the same specimens which were used for the T' curve. In first place the departure from normality was analysed, since lack of normality on the data may result in flawed results. As may be observed in Table 3-12, the distribution for N_3 (the dependent variable) is not normally distributed since the standard scores are not within the span of -1.96 to 1.96, skewed to the right and leptokurtic with an acute peak around the mean.

Table 3-12 Analysis of Descriptive Statistics.

	Number of joints	**Std. Deviation**	**Variance**	**Skewness**	**Standard Error (SE)**	**Kurtosis**	**SE**
N_3	59	2965971.32	8.797E12	2.750	0.311	8.716	0.613
Valid	59						

A logarithmic transformation has been applied to both variables in order to improve normality, although the independent variable was already quite normally distributed. The dependent variable ($logN_3$) follows a fairly normal distribution, since the standard scores are within the span, have a slightly flat distribution and are faintly skewed to the right, as shown in Table 3-13.

Table 3-13 Analysis of Descriptive Statistics for Log Transformation.

	Number of joints	Std. Deviation	Variance	Skewness	SE	Kurtosis	SE
$logN_3$	59	0.506	0.256	0.610	0.311	-0.434	0.613
Valid	59						

Although there are several methods for estimating the regression coefficients, the method that is used most frequently is the Least Squares Method (LSM) [241], where the values of the slope and intercept correspond to the coefficients that minimise the sum of squared deviations (SSE). Therefore, the Regression Curve (RC) 1 will have the form:

$$logN_3 = 12.386 - 2.761\ log\Delta\sigma$$ **Eq. 3-14**

The t-test (p-values < 0.05) indicates that the independent variable makes a statistically significant, unique contribution to the prediction, and that the intercept has to be included in the analysis.

Linearity was analysed by Pearson's coefficient [242], obtaining a value of -0.893 which indicates that there is an almost perfect negative linear relation between the two variables. Residuals (or error terms, which are simply the differences between the actual and estimated values) in the scatter plot are randomly dispersed and the variances along the line of best fit remain similar (see Figure 3-13), therefore, there is independence.

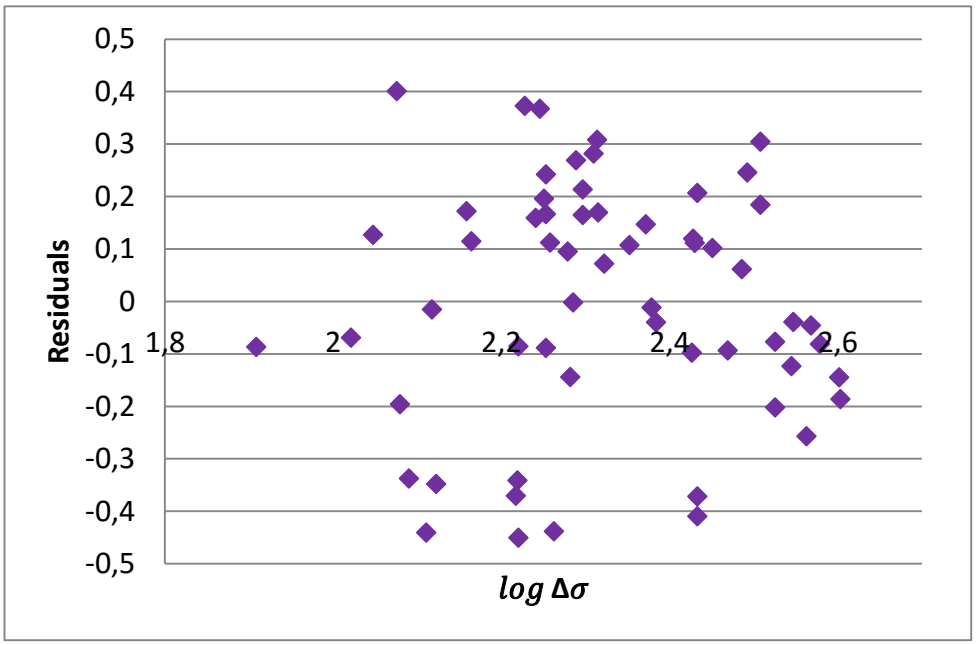

Figure 3-13 Residual Plot of RC 1.

The Durbin-Watson statistic [243] was applied for detecting autocorrelation, which ranges in value from 0 to 4. A value close to 0 indicates positive autocorrelation and a value close to 4 indicates negative autocorrelation; therefore, the closer the value is to 2, the more the evidence is in favour of no autocorrelation [241]. Herein this statistic value is 1.43, which is closer to 2 than to 0, thus there is no autocorrelation.

Bartlett's test [244] was used to examine homoscedasticity, dividing the residuals into two groups: the first one consisting of T- and Y-shaped joints, and the second one of the remainder. As 0.009 is smaller than 3.841 (see Table 3-14), there is homogeneity of variance and all the data could be used as one sample.

Table 3-14 Bartlett's test results.

	Number of joints	Variance	Bartlett's test		Chi-square
Group 1	45	0.053		df	1
Group 2	14	0.051		alfa	0.05
Total	59		0.009		3.841

The Shapiro-Wilk test [245] (p-value=0.047 < 0.05) indicates that residuals are not normally distributed, although skewness (0.363, SE=0.311) and kurtosis (-0.706, SE=0.613) are within the span. Therefore, all the assumptions of linear regression are not satisfied.

As the design curve was taken to be that corresponding to a 2.3% probability of failure, the expression will be in the form:

$$logN_3 = 11.931 - 2.761\ log\Delta\sigma \qquad \textbf{Eq. 3-15}$$

Ref. [217] clarifies that the slope of the T´ design curve was rounded to 3 in order to retain consistency with earlier guidance, which affects the value of the intercept, changing it from 11.931 (see Eq.3-15) to 12.476 (see Eq.3-11); it also explains that a fatigue endurance limit is usually assumed in the high-cycle region (beyond 10 million cycles). All test results had relatively short lives ($<10^7$), therefore, beyond this life the constant-amplitude stress-life relationship is indeterminate. The slope curve above the endurance limit may need some modification. The T' design curve below an HSS range of 190.7 MPa increases the probability of failure (see Figure 3-14). It would seem that there is little difference because if for example we consider an HSS range of 70 MPa there is a difference of approximately 1.9 million cycles, but if the stress range is 50 MPa there is a difference of approximately 25.5 million cycles; i.e. it will be assumed that the structure will last for five years more (considering 5 million cycles per year [215]).

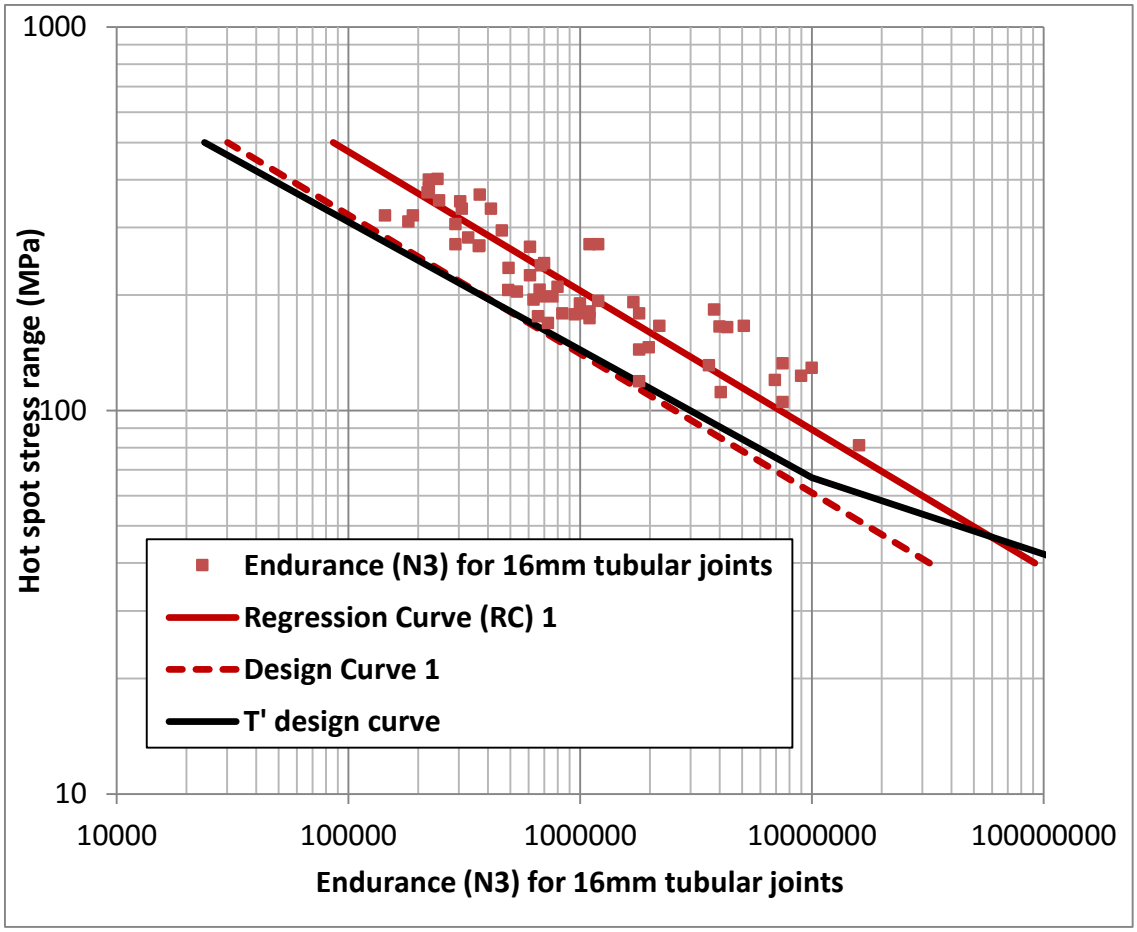

Figure 3-14 Best fit design curve and Guidance Curve (T').

3.2.2.1.2 Sample 2: 44 T-shaped joints

Only 44 of the results from the UKOSRP and the ECSC sponsored research programmed were coming from T-shaped joints, which were subjected to the three principal modes of loading: 21 joints to axial, 9 joints to IPB, and 14 to OPB [238]. A complete regression analysis was performed on this sample in order to consider the impairment produced by the joint configuration. Only the LSM was used to calculate the regression coefficients, hence the principle of Maximum Likelihood Method (MLM) [246], which is quite commonly used, is equivalent to the LSM criterion for ordinary linear regression.

3.2.2.1.2.1 The Logarithmic transformation curve

As with the previous sample, although the values are lower, the distribution for N_3 is not normally distributed; it is skewed to the right (1.829, SE=0.357) and leptokurtic (2.402, SE=0.702), while the logarithmic transformation follows a fairly

normal distribution with slightly flat distribution (-0.806, SE=0.702) and is faintly skewed to the right (0.517, SE=0.357). The regression coefficients were calculated, obtaining the RC 2 of the form:

$$logN_3 = 12.588 - 2.841\ log\Delta\sigma \qquad \textbf{Eq. 3-16}$$

The t-test (p-values < 0.05) indicates that the independent variable makes a statistically significant, unique contribution to the prediction, and that the intercept has to be included in the analysis. The value of the Pearson's coefficient is -0.900 which reflects that there is an almost perfect negative linear relation between the two variables. There is also a negative linear relation between $logN_3$ and $\Delta\sigma$ but it is lower, the Pearson's coefficient value is -0.852, reflecting that the logarithmic transformation has improved the correlation.

Residuals are randomly dispersed (see Figure 3-15), the Durbin-Watson statistic (1.58) indicates that there is no autocorrelation, and there is homogeneity of variance (see Table 3-15); however, the Shapiro-Wilk test (p-value=0.043 < 0.05) indicates that distribution is not normally distributed.

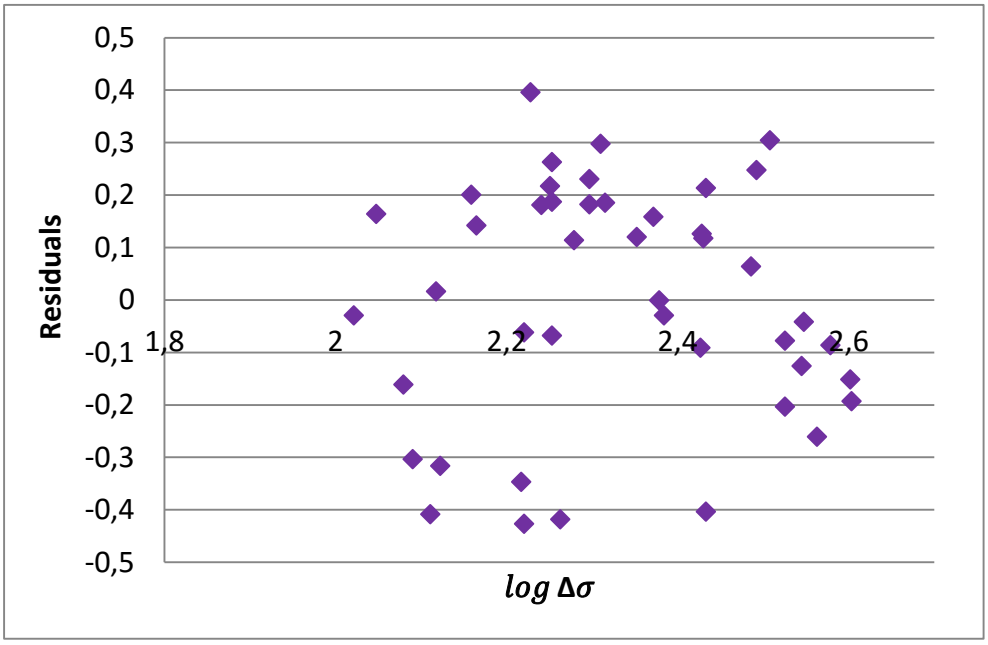

Figure 3-15 Residual plot of the RC 2.

Table 3-15 Bartlett's test results for the RC 2.

	Number of joints	Variance
Axial	14	0.033
IPB	9	0.096
OPB	21	0.040
Total	44	

Bartlett's test		Chi-square
	df	2
	alfa	0.05
3.441		5.991

The design curve, corresponding to a 2.3% probability of failure, will be in the form:

$$logN_3 = 12.139 - 2.841\ log\Delta\sigma \qquad \textbf{Eq. 3-17}$$

3.2.2.1.2.2 The Box-Cox transformation curve

In this section the non-normally distributed data were transformed to a set of data that has an approximately normal distribution, by the Box-Cox power transformation [247]. It is defined as:

$$T(N_3) = \frac{{N_3}^{\lambda} - 1}{\lambda} \qquad \textbf{Eq. 3-18}$$

This transformation involves the MLM [246] to estimate the transformation parameter (λ) which maximises the probability of obtaining the observed data.

For the N_3 transformation, with a -0.2425 transformation parameter, the Shapiro-Wilk test (p-value=0.158) indicates that it is approximately normal with a slightly flat distribution (-0.964, SE=0.702) and weakly skewed to the right (0.105, SE=0.357). Although the independent variable was already normally distributed, the Box-Cox transformation (with a transformation parameter of -0.0164) was applied to improve skewness.

The regression coefficients were calculated, obtaining RC 3 of the form:

$$\frac{{N_3}^{-0.2425} - 1}{-0.2425} = 4.525 - 0.108\ \frac{\Delta\sigma^{-0.0164} - 1}{-0.0164} \qquad \textbf{Eq. 3-19}$$

The t-test (p-values < 0.05) indicates that the independent variable makes a statistically significant, unique contribution to the prediction, and that the intercept

has to be included in the analysis. Linearity was analysed by Pearson's coefficient, and there is an almost perfect negative linear relation between the two transformed variables (-0.913). The regression model was a good fit since the residuals were randomly dispersed (see Figure 3-16), the Shapiro-Wilk test indicates that the residuals follow a normal distribution (p-value=0.762), there is no autocorrelation (Durbin-Watson statistic is 1.79), and the Bartlett's test indicates that there must be homoscedasticity (see Table 3-16).

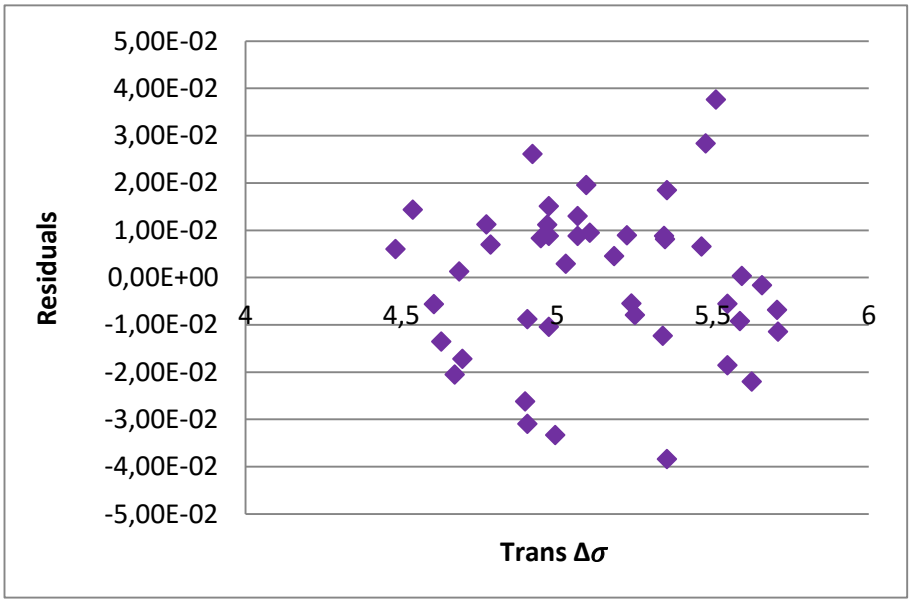

Figure 3-16 Residuals plot of the RC 3

Table 3-16 Bartlett's test results for the RC 3

	Number of joints	Variance
Axial	14	1.79E-4
IPB	9	5.10E-4
OPB	21	2.23E-4
Total	44	

Bartlett's test		Chi-square
	df	2
	alfa	0.05
3.207		5.991

The design curve will be in the form:

$$\frac{{N_3}^{-0.2425}-1}{-0.2425} = 4.492 - 0.108\,\frac{\Delta\sigma^{-0.0164}-1}{-0.0164} \qquad \textbf{Eq. 3-20}$$

The regression analysis undertaken in Section 3.2.2.1.2.1 reflects that Design Curve 2 obtained for Sample 2 (44 T-shaped joints) gives higher values of endurance than Design Curve 1 obtained for Sample 1 of Section 3.2.2.1.1 (see Figure 3-17). The lifespan of the sample of 59 tubular connections is impaired by failing to distinguish between intersections, which suggests that it would be beneficial to have different curves for each type of joint configuration.

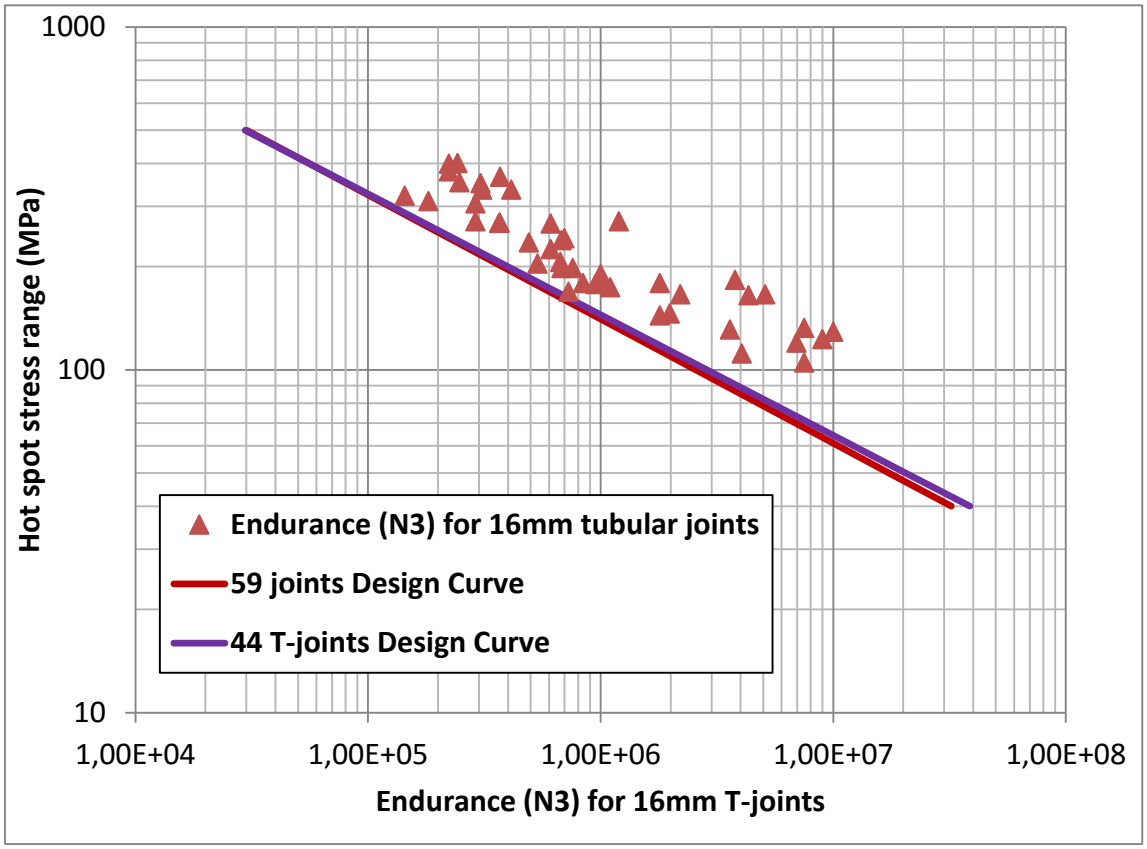

Figure 3-17 Design curves of the different samples.

The assumption that the residuals are normally distributed is violated for both RC1 and RC2 (see Section 3.2.2.1.1 and Section 3.2.2.1.2.1.), hence regression may not be appropriate. However, the Shapiro-Wilk test indicates that if these residuals are divided into three subsets (considering load cases) the distributions are fairly normal (see Table 3-17), which reflects that the applied load clearly affects fatigue life. BS ISO 12107 [248] states that for reliability purposes at least 28 specimens are recommended; it would be interesting to have enough specimens for each main loading case to study their influences over the fatigue life. Axial loading mode is thought to decrease the fatigue life of joints [217].

Table 3-17 Test of Normality

Shapiro-Wilk test		Statistic	df	p-value
RC1	Axial	0.956	21	0.438
	IPB	0.904	9	0.277
	OPB	0.951	29	0.193
RC2	Axial	0.925	14	0.256
	IPB	0.897	9	0.238
	OPB	0.952	21	0.379

By comparing the residual plots obtained in the regression analysis for the different transformations of Section 3.2.2.1.2 (see Figures 3-15 and 3-16), it seems the Box-Cox transformation results in better predictions. However, if a new graph which includes the residuals of each curve on the vertical axis and the independent variable without any transformations is analysed, it may be observed that the Box-Cox RC (RC3) could incur the greatest under-prediction, leading to increasing the probability of failure for the lowest stress ranges (see Figure 3-18). The residual sum of squares (RSS) is lower for the log-transformation (1.09E14) than for the Box-Cox transformation (1.18E14).

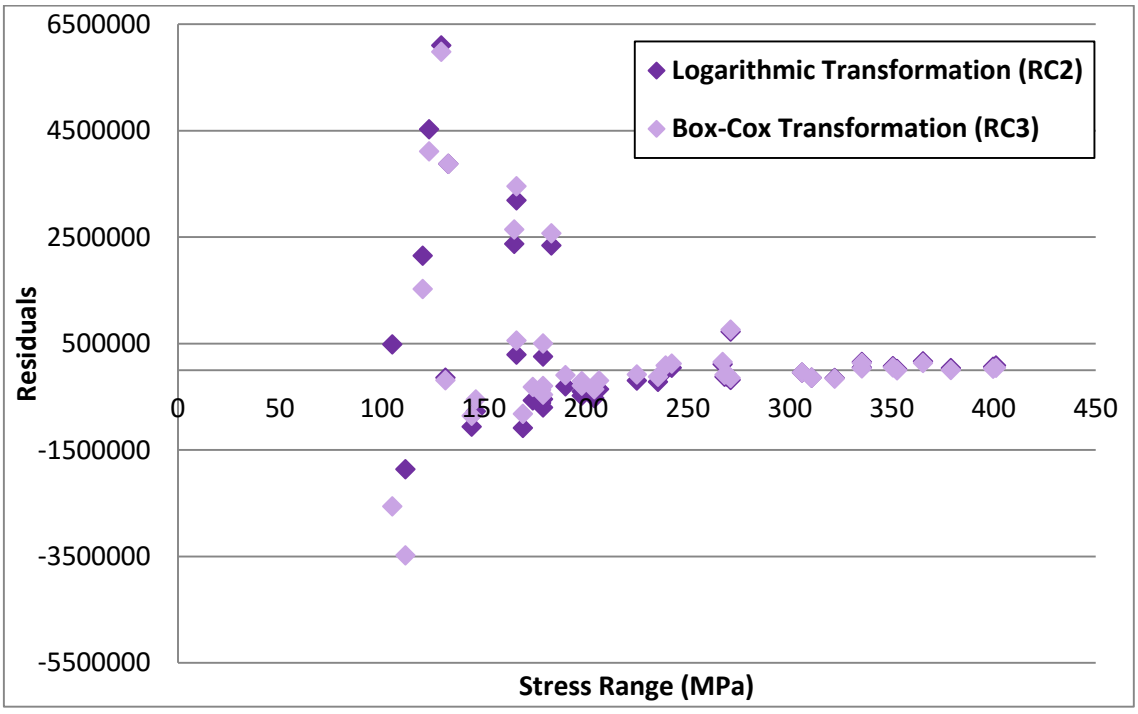

Figure 3-18 Residual Plot Comparison

The difference between the observed values and the predicted values increases significantly below 190 MPa, for both transformations; hence, the sample was divided into two groups and a new regression analysis was performed. The regression coefficients were calculated, obtaining a regression line of the form:

$$logN_3 = 10.063 - 1.782\ log\Delta\sigma \qquad \Delta\sigma \geq 190\ MPa \qquad \textbf{Eq. 3-21}$$

$$logN_3 = 13.848 - 3.443\ log\Delta\sigma \qquad \Delta\sigma < 190\ MPa \qquad \textbf{Eq. 3-22}$$

This new RC seems to improve the correlation since it decreases the RSS to 9.87E13. Future analyses should take into account the change of the slope in more than two sections, aiming to avoid these great differences in the residuals.

3.2.2.2 Multiple Linear Regression Analysis of the complete sample

All the specimens from the UKOSRP and ECSC, a total of 92 joints, were used for this regression analysis, and both the stress range and thickness were taken into consideration as independent variables. To improve normality, a logarithmic transformation was applied to N_3 and $\Delta\sigma$, and inverse logarithmic transformation to the thickness (T).

The LSM was applied to calculate the regression coefficients, so the RC 4 shown in Figure 3-19 will have the form:

$$logN_3 = 11.134 - 2.922\ log\Delta\sigma + \frac{1.968}{log\ T} \qquad \textbf{Eq. 3-23}$$

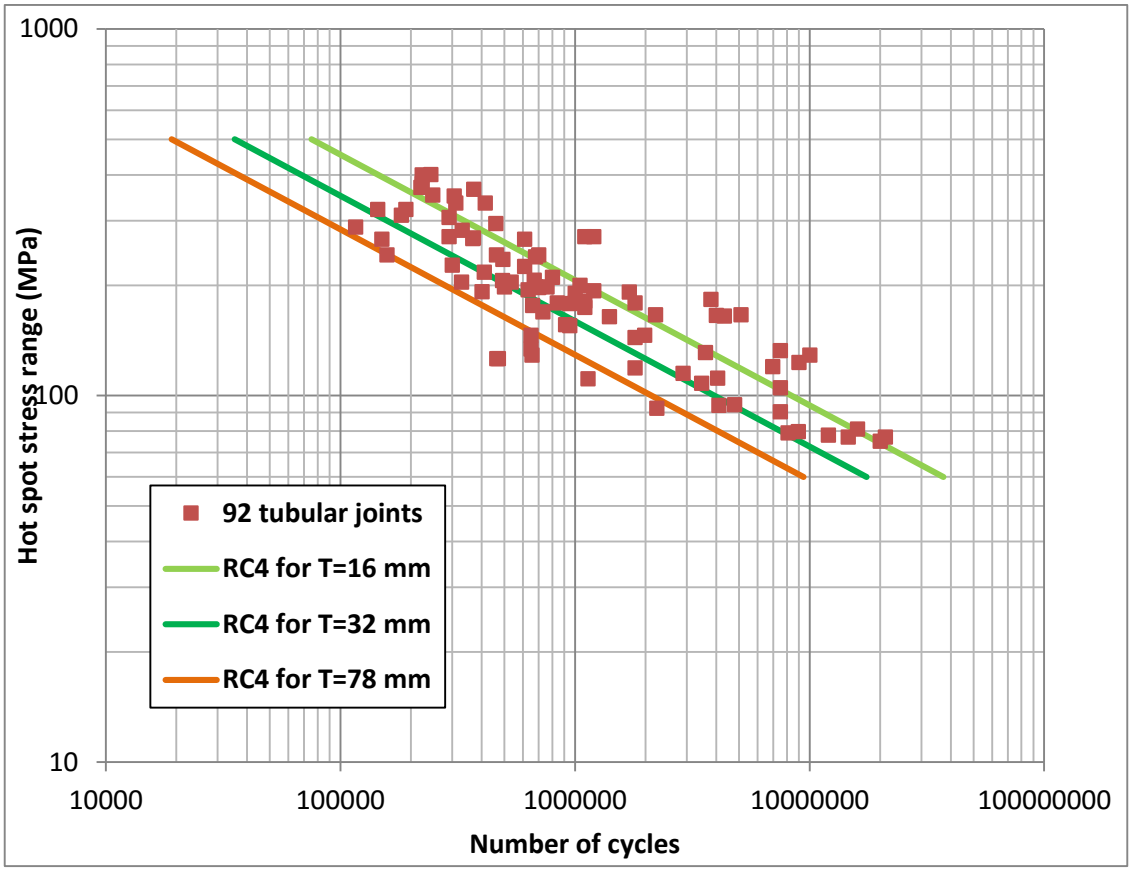

Figure 3-19 Regression Curve 4 for different thicknesses.

The t-test (p-values < 0.05) indicates that both independent variables make a statistically significant, unique contribution to the prediction, and that the intercept has to be included in the analysis. The analysis of variance (ANOVA) verifies that the explanatory variables jointly provide significant information about the response variable (p-value < 0.05). The multiple coefficient of determination (R^2) indicates that 82.7% of the variance in fatigue life can be predicted by a combination of stress range and thickness.

Residuals in the scatter plot are randomly dispersed (see Figure 3-20). The Shapiro-Wilk test (p-value=0.204) shows that the residuals' distribution is fairly normally distributed with skewness (0.046, SE=0.251) and kurtosis (-0.548, SE=0.498) within the span. The Durbin-Watson statistic (1.52) indicates that there is no autocorrelation. Sample 3 (92 specimens) was divided into three subsets, considering thickness ranges, the Bartlett's test indicates that there is homoscedasticity (see Table 3-18). The variance inflation factor [249]

(VIF=1.215, 1 being the smallest possible value) shows that there is no multicollinearity problem; therefore, the residual assessment indicates that the regression is good and all the assumptions were satisfied.

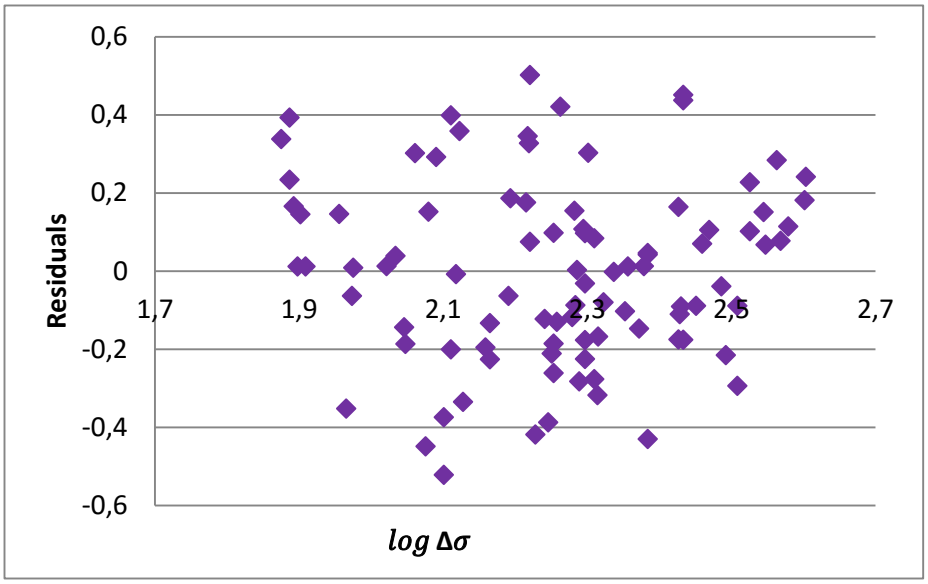

Figure 3-20 Residual Plot of the RC 4.

Table 3-18 Bartlett's test results for the RC4.

	Number of joints	Variance
$T \leq 16\ mm$	34	0.056
$16 < T < 40\ mm$	45	0.048
$T \geq 40\ mm$	13	0.059
Total	92	

Bartlett's test		Chi-square
	df	2
	alfa	0.05
0.289		5.991

Increasing the number of specimens and considering a new explanatory variable have led to obtaining a curve that satisfies all the assumptions of the regression model, i.e. reliability has been increased. The RSS, without any transformation, is lower for the RC 4 (4.80E14) than for the T' curve (1.24E15). Moreover, the values of the highest over-predictions for the RC4 are lower than 4 million cycles (see Figure 3-21), hence it may not be necessary to use a design curve corresponding to a 2.3% probability of failure.

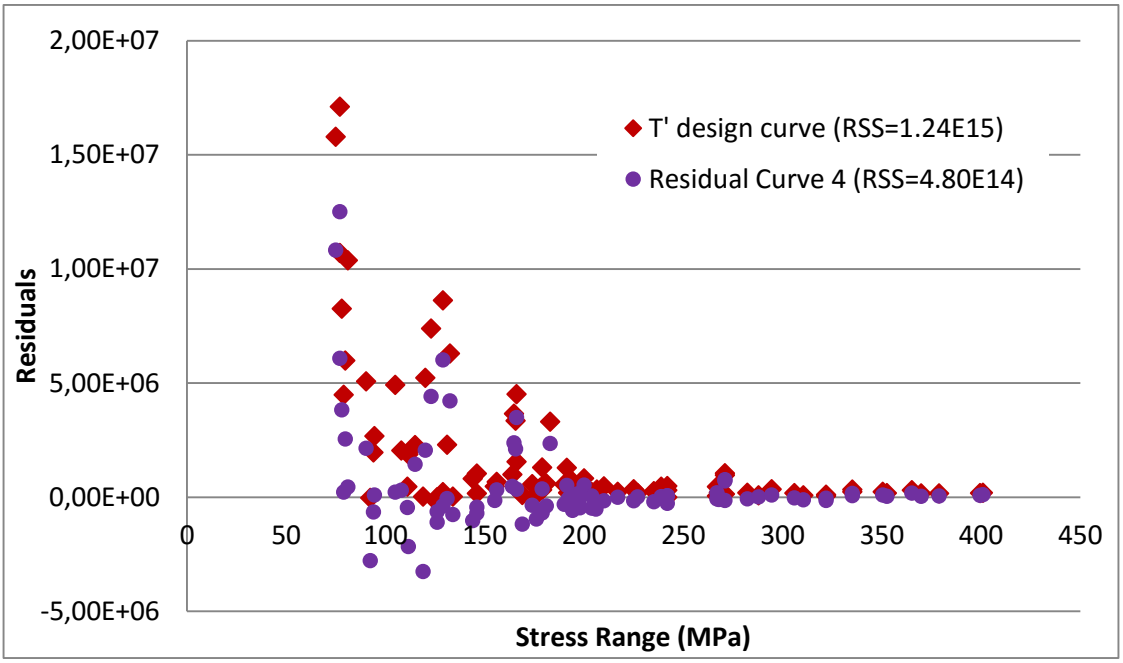

Figure 3-21 Residual plot comparison.

The magnitude of the under- or over-predictions of the T' curve, with reference to the RC4, will vary depending on stress range and thickness (see Table 3-19). For example, for a stress range of 90 MPa and a thickness of 32 mm, there will be an under-prediction of approximately 7 months, and it will be of around 1.47 years for a thickness of 16 mm. These differences are greatly increased if the stress range is lower. For example, for a stress range of 35 MPa and a thickness of 78 mm there will be an under-prediction of about 2.15 years; however, for a thickness of 16 mm there will be an over-prediction of approximately 14.9 years.

Table 3-19 Over- and Under-predictions of the T' curve.

T (mm)	HSS range (MPa)	N_3 (T' curve)	N_3 (RC4)	Differences Cycles	Years
16	90	4104615.414	11431204.92	7326589.51	1.47
32	90	2440618.927	5385354.361	2944735.434	0.59
78	90	1251098.509	2909514.415	1658415.906	0.33
16	35	255070232.6	180560104.4	-74510128.26	-14.90
32	35	107243822.1	85063661.48	-22180160.65	-4.44
78	35	35212065.68	45956854.96	10744789.29	2.15

3.3 Concluding Remarks

Both Girth Weld and Tubular Joint S-N curves have been developed using best judgement by leading specialists, but for Offshore Wind Support Structures, the curves are based on unrepresentative tests on a range of samples with varying degrees of quality control and reporting. On the other hand, most of the fatigue test data were obtained in the late 90s; and steel grades, welding processes and flaw detection processes have greatly advanced since then. Therefore, they are not fit for the cost-effective design optimisation.

It is not always possible to test full-scale geometries and the evidence is that the choice of fatigue test specimen is critical to the resulting S-N curve. Specimens need to be as representative as possible of the true situation. The most influential aspects are: parent material, welding specification, loading and boundary conditions, plate thickness, misalignment, residual stresses, and environmental conditions.

From the point of view of the author, it is inappropriate to apply the Thickness Correction factor to the Flush Ground Girth Welds and its formulation for the rest of the weldment configurations is debatable.

DNV C1 and D Curves are the most conservative of all currently used design curves for Girth Welds. Both BS and DNV curves seem to be on the safe side in the low-cycle regime for the available data, but even they might be considered too conservative and it could be possible to consider an S-N curve for 84.1% probability of survival (one standard deviation of $logN$ below the mean). However, it is not possible to judge BS and DNV curves with respect to the high-cycle regime because of the lack of data. Both flush ground and as-welded fatigue test data have generally been obtained for the low-cycle regime, so fatigue tests with lower stress ranges would be required for assessing the fatigue limits.

Furthermore, Girth Weld S-N curves are based on small diameter tubulars and are likely to be more affected by misalignment than the larger diameter girth welds encountered in offshore wind applications.

The RC 4 of Section 3.2.2.2 is the best fit for the available data; its predictions are more accurate than the T' curve predictions. This curve used the biggest sample size and took into account both stress range and thickness as explanatory variables. Applying this RC would favour the use of less severe safety factors.

All the design curves were taken to correspond to a 2.3% probability of failure for consistency with the T' curve, but it would be convenient to carry out an assessment of the consequences of increasing the probability of failure before deriving new design curves because they are different in an offshore oil or gas platform from in an offshore wind farm. A slight increase in the probability of failure can be a major decrease in investment costs; for instance, if Design Curve 1 of Section 3.2.2.1.1 is taken to correspond to a 6.68% probability of failure (i.e. the mean curve minus 1.5 times the standard deviation) there will be an endurance of 5.21 million cycles (more than a year).

It is not evident that the logarithmic transformation is the best transformation for the regression analysis in all the stress ranges; therefore, more data from over all the stress ranges will be necessary. Moreover, future analysis should take into account the change of the slope in more than two sections, aiming to avoid these great differences in the residuals. Much research should be performed to know how the constant amplitude fatigue endurance limit affects the S-N curve over the high-cycle region.

It would be beneficial to have different T’ curves for each type of joint configuration, and to consider the effect on the loading cases.

The results of this study should not be used to assess fatigue; a more comprehensive study should be undertaken. This research sets out the basis for a comprehensive update for C, D, and T fatigue classes both in air and seawater environments, and thus to reduce safety factors and costs, without incurring an unnecessary increase of the probability to failure.

The requirements of offshore oil and gas platforms are not the same as those of offshore wind farms; therefore, further consideration should be taken before deriving new design curves.

4 STRESS CONCENTRATION FACTOR PREDICTIONS FOR TUBULAR T-JOINTS BASED ON A COMPLETE WELD PROFILE

For tubular welded joints, much research has been carried out into the estimation of the magnitude of the HSS concentration factors. Some empirical equations have been based on the strain gauge measurements of numerous tests on tubular joints under the three principal modes of loading (axial, in-plane bending (IPB) and out-plane bending (OPB)). The high costs of testing scaled steel models have led most of the studies to use shell FE models for deriving the SCF parametric equations for all three load cases.

The existing hot spot SCF parametric equations, which are outlined in Section 4.1, are mostly several decades old. Therefore, this chapter aims to show that offshore and marine renewable application practices need to be based on contemporary FE models if the objective is to achieve optimum design while avoiding unnecessary costs of over-conservatism. For this purpose, a comparison between the fatigue life predictions obtained by the SCFs of 3D solid FE models considering the weldment and the existing SCF parametric equations for tubular T-joints, was made. The validation of the 3D solid FE models with the weldment was carried out by analysing the results obtained by 3D solid and 3D shell FE models without the weldment, as they were used in obtaining the existing parametric equations.

4.1 Review of SCF parametric equations

Equations proposed by Kuang et al. in 1975 [18], which have the most restricted validity range of the geometrical parameters, considered three types of non-reinforced joint: T-, K- and TK-joints. For each joint configuration approximately 35-40 thin-shell FE models were produced. The joints in axial or IPB loading were modelled with the chord simply supported at the ends, whereas the joints subjected to out-of-plane bending loads were modelled with fixed end conditions. The stresses were measured at the mid-section of the brace-chord intersection, without considering the effect of a weld fillet. Although these equations are widely

used, there is the possibility of the underestimation of SCFs since no account is given of chord length effects [250].

In 1978 Gibstein [251] published a set of parametric equations for the prediction of SCFs of tubular T-joints. The FE program NV332 was used for modelling 17 thin-shell T-joints with both chord ends rigidly fixed for all three load cases – axial, IPB and OPB – without considering the effect of a weld fillet. The length of the chord was considered 5.3 times the chord diameter. Gibstein did not investigate the influence of α; he uses Kuang's relationship but its validity range was reduced. In the course of the investigation, the formulae were compared with a substantial number of experimental data showing a very successful agreement with the SCF at the chord; however, for the SCF at the brace these were less satisfactory.

The Wordsworth & Smedley equations [252] for predicting SCFs of tubular T-, Y- and X-joints were published in 1978. These empirical equations were based on the strain gauge measurements of numerous tests on the tubular joints under the three principal modes of loading. There was no special consideration of the fillet welds. The HSSs were derived following the DEn recommendations, using maximum principal stresses from outside the notch zone. In 1981 Wordsworth [253] expanded the formerly published formulae in order to take into account K- and KT-joints. The acrylic model tests were carried out with unstiffened, non-overlapped K- and KT- joints in a range of sizes from 25 mm to 300 mm diameter and from 3 mm to 6 mm WT, and under three basic loading conditions.

In 1985 the Efthymiou & Durkin parametric equations [254] were published for estimating SCFs in tubular T-, Y- and K-joints with emphasis on overlapped joints. The PMBSHELL FE program, which is able to model explicitly the tube thickness and standard weld dimensions, was used for the stress analysis of over 150 joints under various load cases. A three-dimensional 16-node shell element was used in the brace and the chord, and an 8-node shell element was used in the weld regions. All SCFs presented in that publication were obtained by extrapolating maximum principal stresses to the weld toes in accordance with DEn

recommendations. Ref. [255] affirms that these equations gave the best mean fit to the SCF database, therefore, had more joint underpredictions.

The UEG equations [229] were published in 1985; a reliable database for SCFs was gathered and a statistical analysis of the performance of the existing parametric equations was carried out. This study concluded that the most reliable formulae were the Wordsworth & Smedley equations, and some modifications were made to resolve previous anomalies.

The Hellier et al. equations [256] were published in 1990, and were the first set of equations which gave the characteristics of the stress distribution along the intersection. The stress analyses simulations of nearly 900 tubular Y- and T-joints under different axial, IPB and OPB load cases were performed with the PAFEC FE package, using semi-loof thin shell elements. A half-joint mesh was used with the displacement components u_x and u_y fixed at all points on the x-y plane for OPB, and a half-joint mesh with the displacements u_z and rotations φ_x and φ_y were restrained at all nodes which lie on the x-y plane. In order to reduce computational time, the mesh was optimised with fine elements near the intersection and coarser elements in regions where the stresses were more evenly distributed. The SCFs were calculated by dividing the greatest principal stress at a given point around the intersection by the appropriate nominal stress. The statistical package MINITAB was used for regression analysis.

The Lloyd's Register (LR) equations [255] were proposed in 1991, and predict the SCFs for tubular T-, Y-, X-, K- and KT-joints. The database used for deriving these was formed by 175 T/Y, 57 X, 69 K and 9 KT single-plane, unstiffened, ungrouted, non-overlapped acrylic and steel tubular joints, with a chord diameter greater or equal to 150 mm. The DEn recommendations regarding extrapolation techniques were applied. An assessment of different ways of calculating the SCF by utilising the strain gauge results was undertaken. The equations were derived using a multi-variable LSM, and used the Efthymiou and Durkin short chord correction factors.

The set of parametric equations derived by Chang and Dover [257] [258] in 1998 predicted stress distributions along the intersection of tubular T-, Y-, X- and DT-

joints. Comprehensive thin shell FE analyses were carried out for 660 different tubular joints by the FEA package ABAQUS/Standard. Both chord ends were rigidly fixed for all loading cases. Only one half joint geometry was modelled; therefore, no out-of-plane displacements and rotations were permitted at nodes on the symmetry plane under axial and IPB, and the in-plane displacements were restrained over the bisecting plane for OPB. The stresses were measured at the mid-section, without considering the effect of a weld fillet. The HSSs at the weld toe were estimated directly from the value obtained at the brace/chord intersection. To derive the equations, the maximum principal stresses on external surfaces were chosen. The statistical package MINITAB was used for regression analysis.

Most of these studies measured the stresses at the mid-section of the brace-chord intersection without considering the effect of a weld fillet; excepting the Efthymiou & Durkin's models, where welds were modelled using three-dimensional sixteen node shell elements in the brace and the chord, and eight node shell elements in the weld regions. All SCFs presented in that publication were obtained by extrapolating maximum principal stresses to the weld toes in accordance with DEn recommendations.

4.2 Finite Element Analyses (FEAs)

Following this comprehensive literature review, the SOLIDWORKS [259] 3D CAD software and the FEA package ABAQUS/CAE were used for modelling tubular T-joints in order to analytically obtain HSSs for calculating SCFs.

4.2.1 Shell FE tubular T-joint models

4.2.1.1 Modelling and meshing

Shell elements are commonly used for tubular joint stress analysis; for this reason initial models were formed by thin four-node quadrilateral elements. Models were subjected to axial, IPB and OPB load cases. The stresses were measured at the mid-section, without considering the effect of a weld fillet. The SCFs were estimated by dividing the maximum principal stress obtained at the brace/chord intersection by the appropriate nominal stress. Maximum principal stresses were

selected for this research to maintain consistency with DEn recommendations and the existing SCF parametric studies. For axial loading, the nominal stress was defined as the total applied load divided by the hollow cross-sectional area of the brace. For IPB, the nominal stress was calculated from the Euler–Bernoulli Beam Theory, using a moment arm measured from the brace end along its outer surface to the crown position. For OPB, nominal stress was also derived from the Euler–Bernoulli Beam Theory but the moment arm measured to the saddle position. For all models, all degrees of freedom were fixed at the chord ends.

Only one joint geometry will be presented but several geometries have been modelled; the magnitude of the results is different but the trend is the same. The chosen geometric ratios for the models are shown in Figure 4-1, and were selected with the purpose of comparing the effectiveness of these models with the study shown in Ref. [257]. All these ratios are within the validity range of the different parametric equations pointed out in Section 4.1.

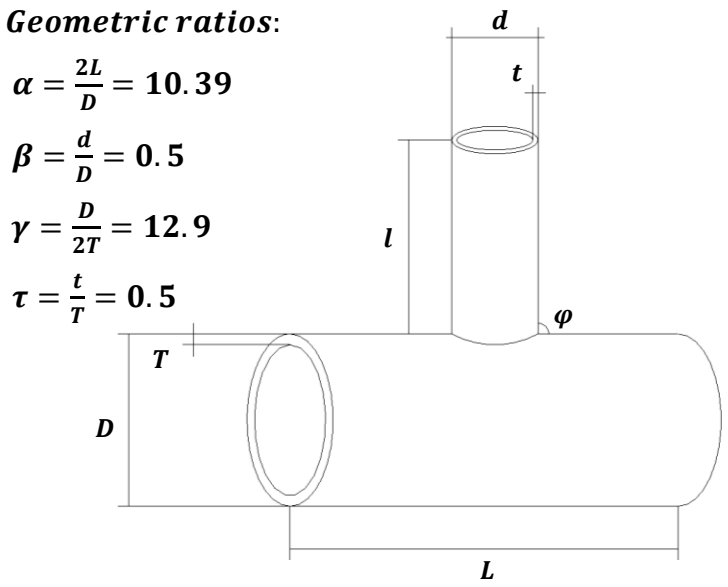

Figure 4-1 Geometric notation and selected values for the tubular T-joints.

In order to reduce computational time, the mesh of all the models is characterised by fine elements near the intersection and coarser elements in regions where the stresses are more evenly distributed, as can be observed in Figure 4-2. Elongated or distorted elements were avoided. T-joints with a brace length of about $0.4L$ were used in order to avoid the effect of short brace length [258].

Chord lengths greater than $6D$ were used to ensure that stresses at the brace/chord intersection were not affected by the boundary conditions [260]. The density, Young's modulus and Poisson's ratio were taken to be 7850 kg/m^3, 207 GPa and 0.3 respectively.

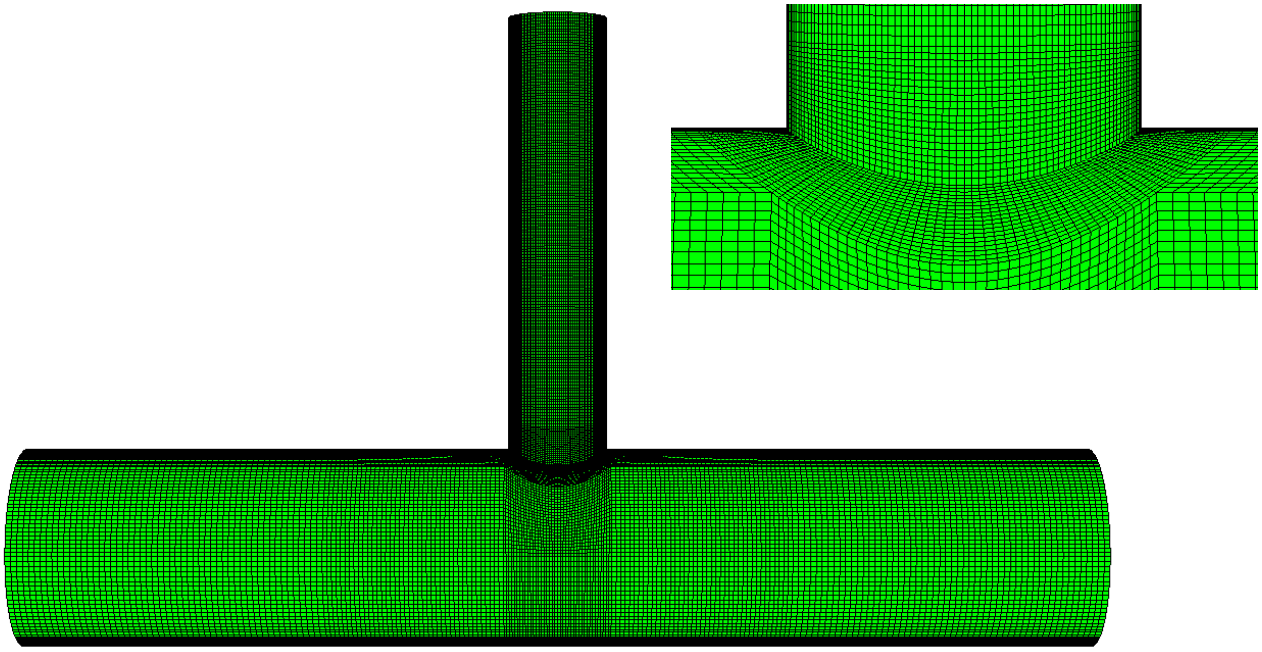

Figure 4-2 Typical mesh used to model the T-joint.

4.2.1.2 Mesh verification

A convergence test was carried out aiming to verify that the meshes used for this research were sufficiently fine to accurately predict the SCFs. Four meshes with 32, 64, 112, and 160 elements respectively around the joint intersection were analysed. Comparison of SCF values (see Table 4-1) shows a good convergence. The finest mesh, which has 160 elements around the intersection with a side length of 9.22 mm, was selected for the rest of the analysis as there is acceptable compromise between computational time and accuracy. It has to be noted that the T-joint was subjected to different axial loads in order to prove that the SCF does not depend on the magnitude of the load.

Table 4-1 Comparison between the SCFs along the intersection from coarse to fine meshes.

Axial Loading [N/mm2]	Number of elements	CHORD		BRACE	
		Crown	Saddle	Crown	Saddle
1	**16x2**	1.805	4.960	2.054	6.175
4	**32x2**	1.792	5.460	2.424	7.338
4	**56x2**	1.788	5.661	2.622	8.012
10	**80x2**	1.788	5.805	2.681	8.218

4.2.1.3 Results comparison

Once the mesh was selected, the T-joint model was subjected both to IPB and OPB loading. The higher stress concentration is located at the saddle for axial and OPB cases, and close to the crown for IPB cases, as may be appreciated from Figure 4-3.

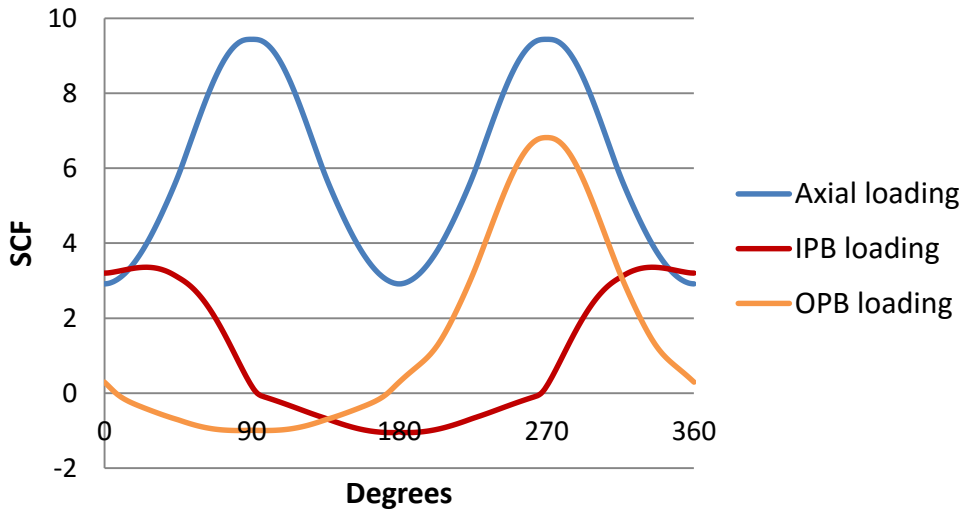

Figure 4-3 SCF distributions along the T-joint intersection for the different load cases.

The shell FE results were compared with the results presented in Ref. [257] and the solutions for the different parametric equations outlined in Section 4.1, which are presented in Table 4-2.

Table 4-2 SCFs comparison.

		CHORD		BRACE	
		CROWN	**SADDLE**	**CROWN**	**SADDLE**
Axial	**Kuang et al. Eq.** [18]		6.106		8.553
	Efthymiou et al. Eq. [254]	2.203	6.602	2.400	6.407
	Hellier et al. Eq. [256]	2.833	7.047	2.579	8.109
	Lloyds's Register of Shipping Eq. [250]	2.596	5.960	1.883	4.707
	Chang et al. [257]	2.199	7.497	2.813	9.171
	Shell FE results	**1.788**	**5.805**	**2.681**	**8.218**
IPB	**Kuang et al. Eq.** [18]	1.633		2.169	
	Efthymiou et al. Eq. [254]	2.175		2.494	
	Hellier et al. Eq. [256]	2.505	0.000	3.035	0.087
	Lloyds's Register of Shipping Eq. [250]	1.895		1.067	
	Chang et al. [257]	2.578	0.056	3.330	0.181
	Shell FE results	**2.020**	**0.064**	**2.865**	**0.247**
OPB	**Kuang et al. Eq.** [18]		4.457		5.586
	Efthymiou et al. Eq. [254]		5.060		5.391
	Hellier et al. Eq. [256]	0.000	5.348	0.000	4.522
	Lloyds's Register of Shipping Eq. [250]		4.380		3.390
	Chang et al. [257]	0.177	5.553	0.434	6.621
	Shell FE results	**0.092**	**4.591**	**0.391**	**6.097**

If these results are only compared with the results presented by Ref. [257], it seems that SCFs are underestimated at the chord saddle and brace saddle for axial loading, and at the chord saddle for OPB loading. However, for the rest of the load cases, the results are of the same magnitude; small differences are attributed to the finest mesh.

Taking into consideration all the different SCF values, it is difficult to characterise if the obtained results were under- or over-predicted because of some rather high variations. For instance, LR's SCF at the brace saddle for axial loading is 4.707 while for Kuang et al. it is 8.553. It is the author's view that the FEA results are reasonable and hence acceptable since they are within this range.

4.2.2 Solid FE tubular T-joint models

Solid models were characterised by eight-node hexahedral elements. Models were subjected to axial, IPB and OPB load cases, and both chord ends were rigidly fixed. The SCFs for the solid FE models without fillet weld were estimated directly from the values obtained at the brace/chord intersection in the same manner as for the Shell FE models, except that the maximum principal stresses were measured at the external surface. The mechanical properties and the restrictions of the brace and chord lengths used for the shell FE models of Section 4.2.1.1 were also applied to the solid FE models without the weldment.

When producing the meshing of the 3D solid models, 8-node linear isoparametric elements with reduced integration (C3D8R) were used and the number of elements around the joint intersection was 160 as the solid FE models were going to be validated with the shell FE models. A convergence test was carried out aiming to verify the number of elements through thickness. Comparison of SCF values shows a good convergence (see Table 4-3). Ten elements through the thickness proved to have an acceptable compromise between computational time and accuracy.

Table 4-3 Comparison between the SCFs along the thickness from coarse to fine meshes

Number of elements through thickness	Intersection	
	Crown	Saddle
5	2.338	7.829
7	2.616	8.613
9	2.828	9.195
10	2.917	9.434
11	2.958	9.545

Table 4-4 shows the results obtained for the same tubular T-joint geometry modelled with solid elements instead of shells.

Table 4-4 Solid FE SCFs.

Load case	Number of elements	Intersection	
		Crown	Saddle
Axial	**80x2**	2.917	9.434
IPB	**80x2**	3.199	0.184
OPB	**80x2**	0.294	6.815

As observed for the shell FE models, the higher stress concentration is located at the saddle for axial and OPB cases, and close to the crown for the IPB case. If the shell FEA results are compared with these results, it can be observed that there is an increase of the SCF of 14.8% for axial loading and 11.8% for OPB loading at the saddle. At the crown, there is an increase in the SCF of 11.7% for IPB loading. It is reasonable that the solid SCFs are slightly higher, since the shell results are measured at the mid-section, whereas the solid results are measured on the external surface.

4.2.3 Complete weld profile: Solid FE tubular T-joint models

4.2.3.1 Modelling and meshing

The mesh conditions, mechanical properties, geometric ratios and restrictions of the brace and chord lengths used for the shell and solid FE models, as explained in Sections 4.2.1 and 4.2.2, were also applied to the complete weld profile Solid FE tubular T-joint models.

For modelling the weldment, the recommendations for complete joint penetration (CJP) groove welds provided by the AWS Structural Welding Code [261] were applied (see Table 4-5). It is necessary to define the coordinates of nodes A, B and D (shown in Figure 4-4) in order to incorporate the weldment within the tubular joint.

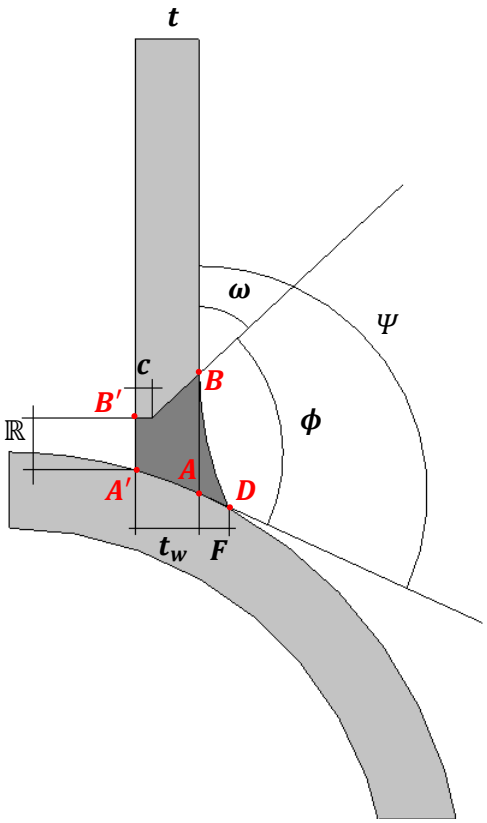

Figure 4-4 Prequalified joint details for CJP groove welds in tubular T-Connections.

Table 4-5 Prequalified joint dimensions and groove angles for CJP groove welds in tubular T-Connections with 50º<Ψ<150º.

	Saddle		Crown	
	min	**max**	**min**	**max**
ω	45°	90°	10°	90°
ℝ	2mm	ϕ ≤45° 8mm ϕ >45° 6mm	2mm	ϕ ≤45° 8mm ϕ >45° 8mm
c	0mm	2mm	0mm	2mm
ϕ	37.5°		37.5°	60°
F	0mm	t/2 mm	0mm	t/2 mm
t_w	≥ t mm		≥ t mm	
$F + t_w$	≥ t mm		≥ t mm	

The coordinates of node A may be defined by the brace, chord and intersection equations shown in Fig. 4-5 as:

$$Node\ A = \{r\ cos\ \theta\ , \sqrt{(r\ sin\ \theta)^2 - (r^2 - R^2)}, r\ sin\ \theta\} \quad \textbf{Eq. 4-1}$$

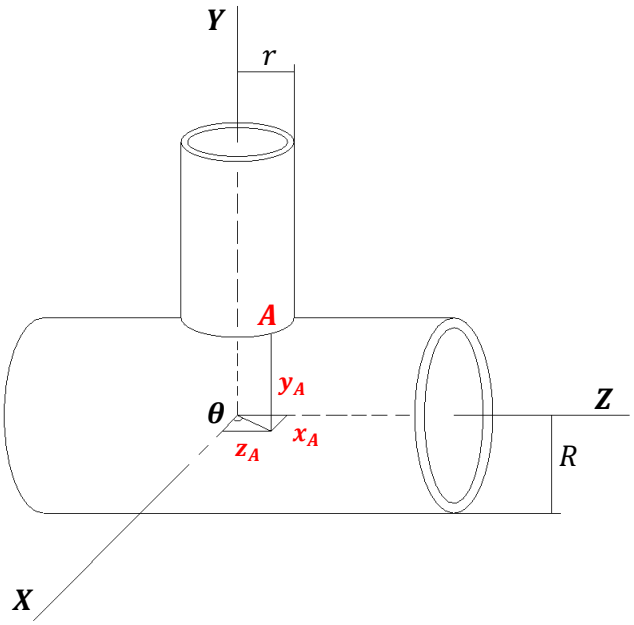

Chord equation:
$$x^2 + y^2 = R^2$$

Brace equation:
$$x^2 + z^2 = r^2$$

Intersection equation:
$$z^2 - y^2 = r^2 - R^2$$

Figure 4-5 Coordinate system.

In the same way, the coordinates of node A' are defined as:

$$Node\ A' = \{(r - t)\ cos\ \theta\ , \sqrt{\left((r - t)\ sin\ \theta\right)^2 - ((r - t)^2 - R^2)}, (r - t)\ sin\ \theta\} \quad \textbf{Eq. 4-2}$$

Assuming that for this geometry the root opening ($\mathbb{R}$) has a constant value equal to 4 mm, which is an intermediate value in the range of validity, the coordinates of node B' can be derived from the coordinates of node A'. To simplify some calculations, it has been considered that root face (c) equals 0 mm because the dihedral angle (Ψ) will be equivalent to the sum of the joint included angle (ϕ) and the end preparation angle (ω). Considering an end preparation angle of 50º, which is the intermediate value of the range of validity at the crown, the coordinates of node B are defined as:

$$Node\ B = \{r\ cos\ \theta\ , \sqrt{\left((r-t)\ sin\ \theta\right)^2 - ((r-t)^2 - R^2)} + \mathbb{R} + \frac{t}{tan\ \omega}, r\ sin\ \theta\}$$ **Eq. 4-3**

Assuming a fillet weld size (F) equal to half the brace thickness (t), which is its maximum value, the coordinates of node D are defined as:

$$Node\ D = \{(r+F)\ cos\ \theta\ , \sqrt{R^2 - \left((r+F)\cos\theta\right)^2}, (r+F)\ sin\ \theta\}$$ **Eq. 4-4**

The dihedral angle is defined as:

$$\Psi = \pi - \ arctan\frac{y_D}{\sqrt{R^2 - {y_D}^2}}$$ **Eq. 4-5**

To calculate the weldment curvature (R_w) is necessary to define some parameters, shown in Figure 4-6 as:

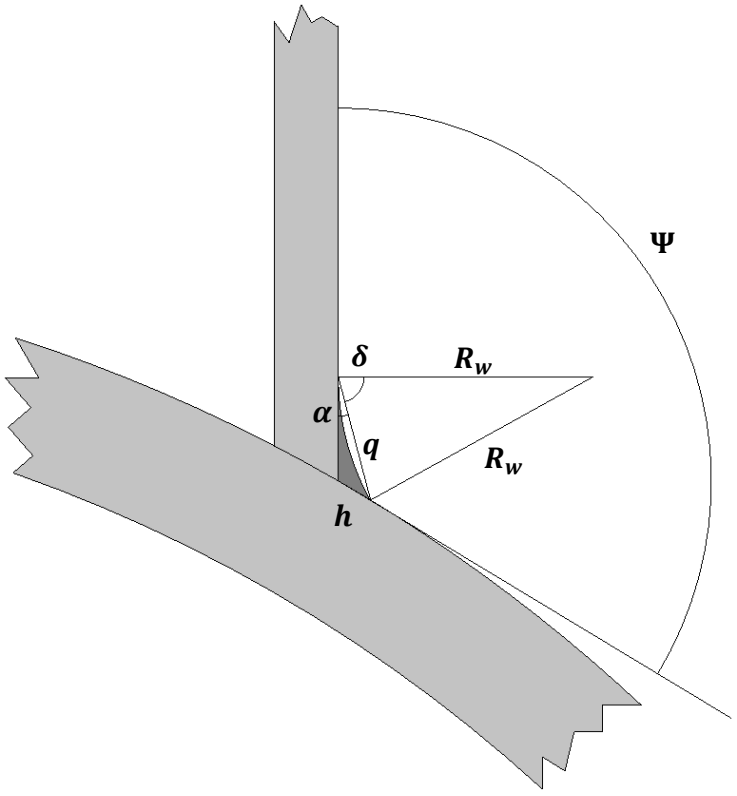

Figure 4-6 Parametric definitions for the calculation of R_w.

$$h = \sqrt{(y_A - y_D)^2 + (x_D - x_A)^2}$$ **Eq. 4-6**

$$q = \sqrt{(y_B - y_D)^2 + (x_D - x_B)^2}$$ **Eq. 4-7**

Using the sine rule, the weld angle (ζ) is defined as:

$$\zeta = arc\,sin\left(\frac{h}{q} sin\,\Psi\right) \quad \textbf{Eq. 4-8}$$

Finally, the weldment curvature is expressed as:

$$R_w = \frac{\frac{q}{2}}{cos\,\delta} = \frac{\frac{q}{2}}{cos\left(\frac{\pi}{2} - \zeta\right)} \quad \textbf{Eq. 4-9}$$

A concave round fillet has been selected because most joints are generally modelled to a concave weld profile, since it will always give lower stress than a straight fillet [250]. The final configuration is shown in Figure 4-7.

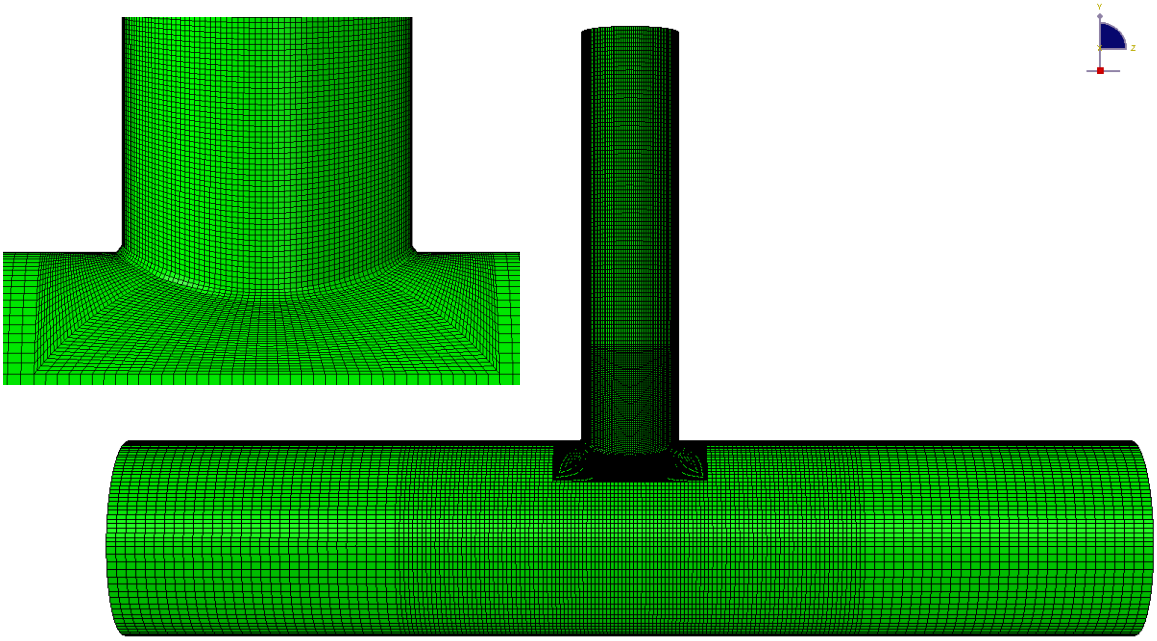

Figure 4-7 Complete profile solid FE model.

4.2.3.2 Complete weld profile Solid FE results

For the complete weld profile solid FE model, two different SCFs may be obtained, distinguished by the stress analysis results selected as reference.

There is no general agreement on the value of the distances from the weld toe for obtaining the HSS; the extrapolation regions defined by Ref. [262], and adopted by the UKOSRP and the ECSC Technical Working Party on Tubular joint Testing are shown in Figure 4-8. This definition of HSS was selected because

there must be consistency between the generation of the design S-N curve and the SCF.

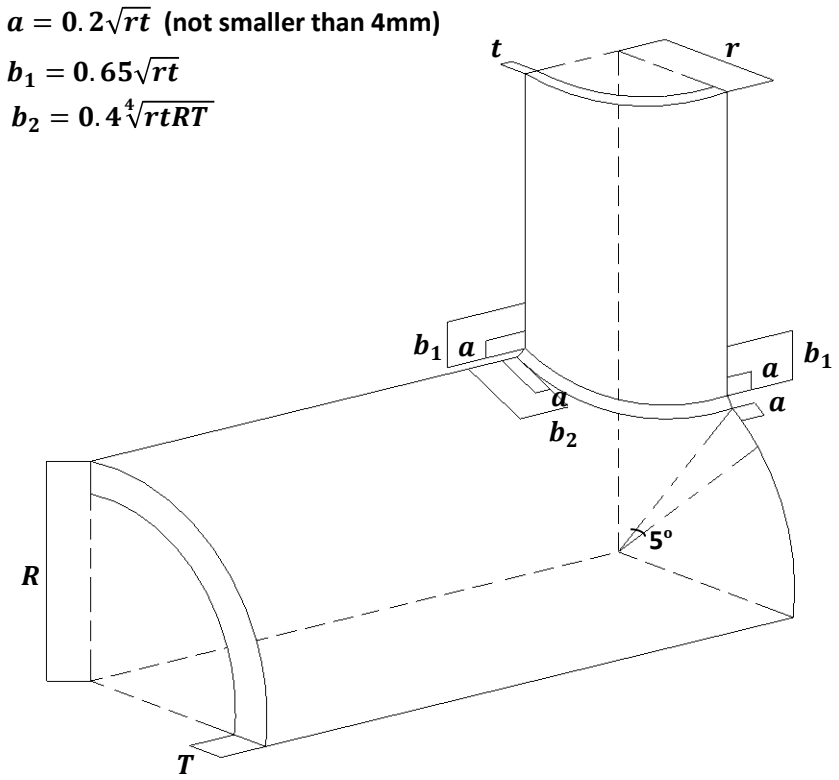

Figure 4-8 Location of strain gauges for linear extrapolation to weld toe.

The notch stress is the peak stress, which is situated at the weld toe region. The notch stress concept is attractive since it is a real stress, in contrast to the extrapolated conceptual HSS, which incorporates the effects of joint geometry but neglects the influence of the weld.

Table 4-6 shows both hot spot and notch SCF values obtained by measuring the maximum principal stresses at the external surface.

Table 4-6 Hot Spot and Notch SCFs for the T-joint.

		Number of	CHORD		BRACE	
Stress	**Load case**	**elements**	**Crown**	**Saddle**	**Crown**	**Saddle**
	Axial	**80x2**	2.070	5.019	1.365	5.049
HS	**IPB**	**80x2**	1.642	0.082	1.685	0.107
	OPB	**80x2**	0.053	3.813	0.285	3.502
	Axial	**80x2**	2.510	6.962	1.504	5.256
Notch	**IPB**	**80x2**	2.295	0.149	1.679	0.102
	OPB	**80x2**	0.174	5.168	0.239	3.671

As expected, both hot spot and notch SCF values are lower than the intersection values of the previous shell and solid FE models, since the change in the section is less sharp, i.e. the weldment reduces stress levels because the change in the direction of force flow is more progressive.

Generally notch SCFs are higher than hot spot SCFs, although the increase is not proportional; for instance, the increase at the chord saddle for OPB loading is 35.5% while at the brace saddle for axial loading it is 4.1%. Therefore, selecting the HSS as a reference could lead to designing a structure very conservatively, since an important reduction of the stress concentration could be achieved through the improvements on the weld profile and this is not taken into account. For example, employing safety factors over the brace crown SCF for IPB loading would produce a very high overestimation since the notch SCF is smaller than the hot spot SCF.

4.3 Fatigue life predictions

In order to know to what extent the slight variations on the SCF values affect the fatigue life predictions, an assessment using the HSS T' curve was carried out. The T' design S-N curve for tubular joints in air with a chord WT of 16 mm is expressed below [238]:

$$log_{10}N = 12.476 - 3\ log_{10}\Delta\sigma \quad \text{for } N < 10^7 \qquad \textbf{Eq. 4-10}$$

$$log_{10}N = 16.127 - 5\,.log_{10}\Delta\sigma \quad \text{for } N > 10^7 \qquad \textbf{Eq. 4-11}$$

The decrease in fatigue strength for thicker joints, which is known as the "thickness effect", is a generally accepted trend; however, the scale of the decrease and the reasons for the shorter lives of thicker joints are still the subject of some controversy. The main reasons given for thicker sections having lower fatigue resistance within the same stress range are: the "geometric effect", where the decrease is primarily caused by the increased local weld toe stresses caused by the change in weld geometry of the thicker joints; the “volumetric effect”, where simply having more material implies a greater likelihood of having more defects; and the “stress gradient effect”, which applies to thin sections under bending and the associated steep stress decay gradient which has been demonstrated to

make thinner sections relatively strong against fatigue. The thickness correction recommended for the T' curve is of the form [239]:

$$\Delta\sigma = \Delta\sigma_o \cdot \left(\frac{16}{T}\right)^{0.3} \quad \textbf{Eq. 4-12}$$

The hot spot SCF values obtained by the solid FEA models with the weldment, which are the most representative models, were used as references for being compared with the Efthymiou & Durkin SCFs, which were the only parametric equations derived by shell FE models taking into account the weldment, and the SCFs obtained with the solid FE models without weldment. A nominal stress of 20 MPa was considered for the comparison in order to be within the range of cycles for a service life of 20 years [215]. Table 4-7 shows the results for the most critical points: at the chord saddle for axial and OPB loading, and at the chord crown for IPB loading.

Table 4-7 Comparison between fatigue life predictions at the chord for all load cases.

	CHORD		σ_{nom} (MPa)	SCF	$\Delta\sigma_o$ (MPa)	THICKNESS CORRECT. $\Delta\sigma$(MPa)	N (cycles)
AXIAL	SADDLE	Efthymiou & Durkin	20	6.602	132.04	104.51	2.62E+06
		Solid FE model without weldment	20	9.434	188.68	149.34	8.98E+05
		Solid FE model with weldment (HSS)	20	5.019	100.38	79.45	5.97E+06
IPB	CROWN	Efthymiou & Durkin	20	2.175	43.5	34.43	2.77E+08
		Solid FE model without weldment	20	3.199	63.98	50.64	4.02E+07
		Solid FE model with weldment (HSS)	20	1.642	32.84	25.99	1.13E+09
OPB	SADDLE	Efthymiou & Durkin	20	5.060	101.2	80.10	5.82E+06
		Solid FE model without weldment	20	6.815	136.3	107.88	2.38E+06
		Solid FE model with weldment (HSS)	20	3.813	76.26	60.36	1.67E+07

Considering 5 million cycles per year, which corresponds to an average period of 6.3 sec, i.e. 100 million cycles in 20 years' service life [215], these variations would represent an overestimation of between 0.64 and 217.74 years (see Figure 4-9). These results clearly show that even slight overestimations of the SCFs will represent a great reduction in service lives, since the scale is logarithmic. This reduction in the service life affects the design, i.e. structures would be oversized.

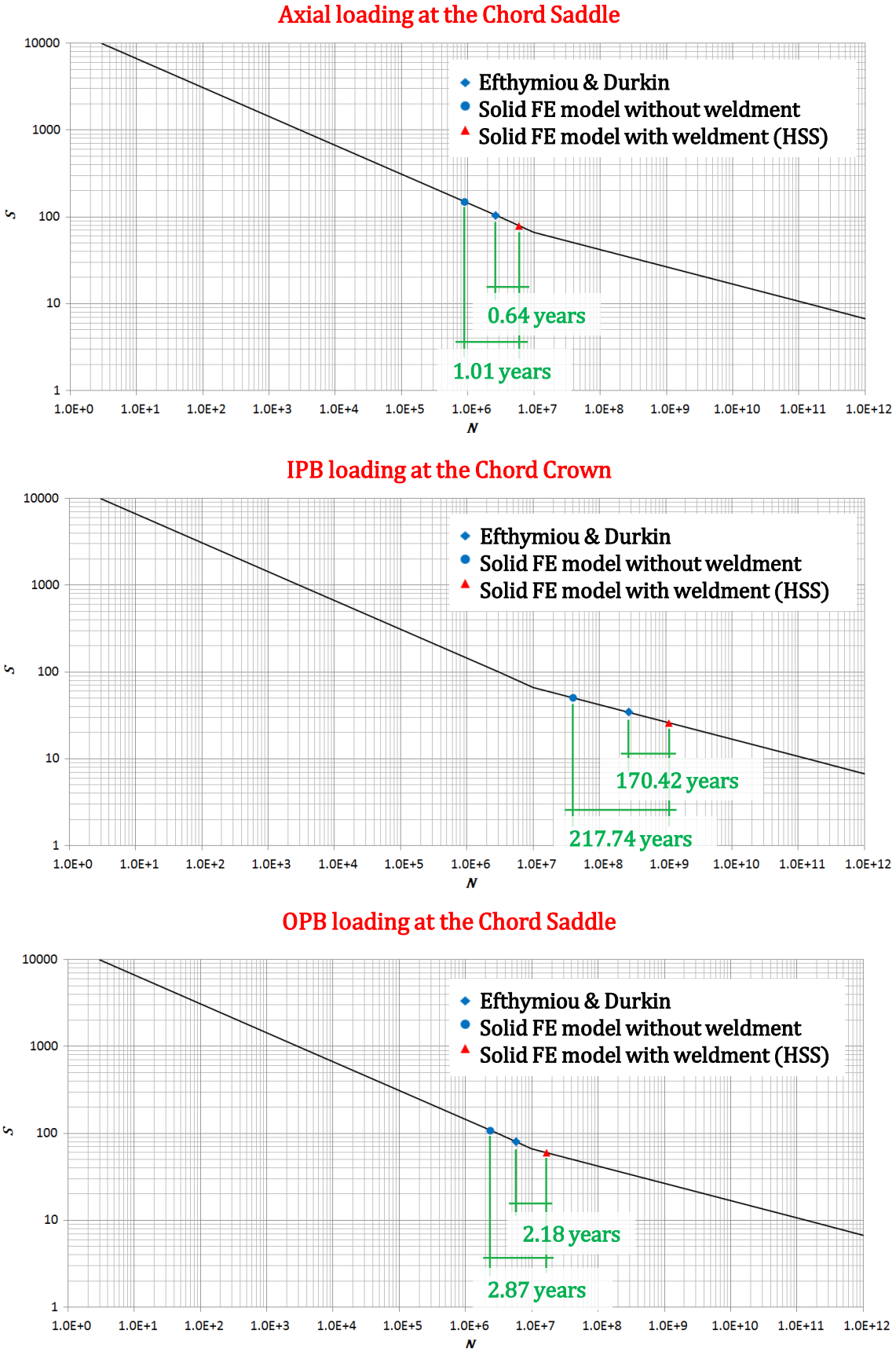

Figure 4-9 Service life comparison.

It should be noted that all authors of the studies reviewed in Section 4.1 agree that the SCF parametric equations must be different, depending on the type of joint and applied load. The mode of loading affects the fatigue strength; however, the T' curve does not make any distinction between joint types or applied loads. This effect of the mode of loading on the fatigue strengths means that the S-N curve approach may not be suitable for predicting the fatigue life of all joint geometries and modes of loading.

Aiming to observe how these under-predictions of the service life affect investment costs, the chord thickness was reduced until the SCFs of the complete profile solid FE model reached approximately the same values as Efthymiou & Durkin's SCFs for the previous thickness. The total reduction of the T-joint was 12.24%, and the SCFs are shown in Table 4-8.

Table 4-8 SCFs of the complete profile solid FE model with the thickness reduction.

	Efthymiou & Durkin's SCF T_{ref}	**Complete profile solid FE model $0.86\,T_{ref}$**
Axial loading	6.602	6.466
IPB loading	2.175	1.596
OPB loading	5.060	4.744

All the SCF parametric equations for all three load cases proposed by Kuang et al. [18], Gibstein [251], Efthymiou & Durkin [254], Hellier et al. [256], and Chang & Dover [257] [258] for tubular T-, Y-, X-, K-, TK- and DT-joints have the same type of constraints. Therefore, it is assumed that this reduction is representative of all the different joint intersections; although the magnitude of the total reduction will vary across different structural configurations.

In 2012, the average investment cost of offshore wind farms was €3.43m per MW [263], the foundations represent around 22% of this cost [264] (€0.75m per MW). Assuming that the material costs of the legs and bracings of the jacket are about one third of the total foundation [265], which could be reduced by 12.24%, around €30,787 per MW could be saved. Approximately 1 GW of Offshore Wind was connected to the grid in Europe during 2012 [263]; hence, notionally (assuming a steel jacket construction, which was not the case) we could deduce that

approximately €30.8m could have been reduced from this investment cost without any real effect in structural performance but by simply modelling the weld profile effect on the hot spot stress. Whereas these installations have been largely monopile structures to date, in future there is likely to be an increased number of steel jacket structures as larger turbines and deeper water conditions are encountered. It is therefore important to remember that small over-predictions of the SCFs could inadvertently result in a very large increase in investment costs.

4.4 Maximum SCF position and weld size influence

The existing SCF parametric studies spanned diverse joint parameters, thus their validity ranges are slightly different. For example, the lower limit of γ for the Chang & Dover equations is 7.6 while for the LR equations it is 10. The Case nº102 (α=12.94, β=0.77, γ=8.08, and τ=1), which is within the validity ranges of the Chang and Dover equations but not within LR equation limits, shows that the highest stress concentrations are located at -41.6º and 41.6º, opposite to what the predictions indicate (see Figure 4-10). It was analysed whether the position change was due to welding, by modelling the joint without weldment. It was observed that the weld strongly influences the value of the maximum stress concentration and slightly affects the position thereof, but even without weld the lower limit of γ for Chang & Dover equations seems to be incorrect.

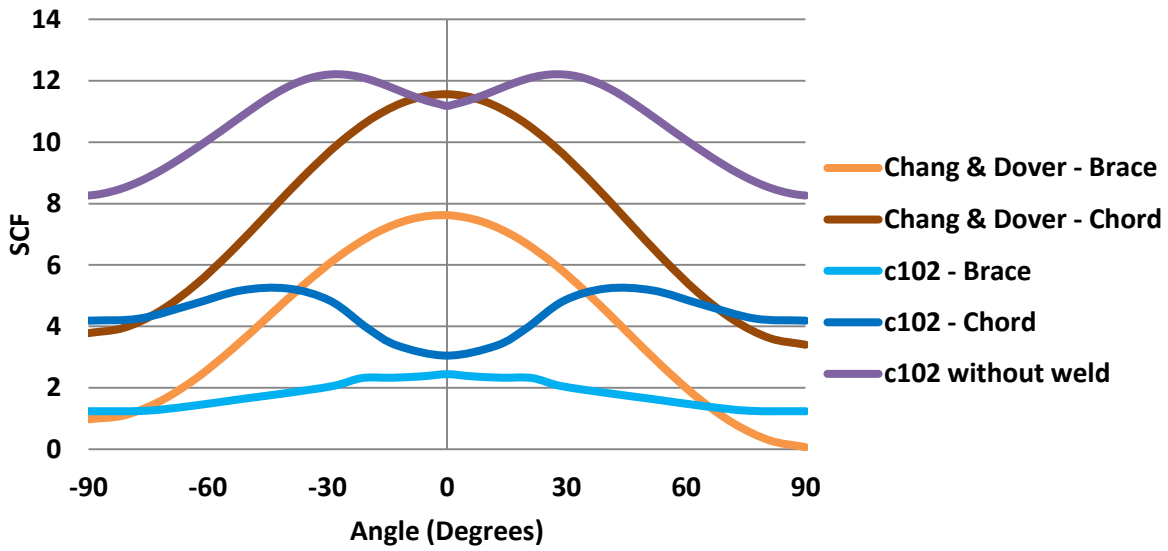

Figure 4-10 SCF distributions from crown to crown.

Because of this, a new simulation was run by changing γ from 8.08 to 10.46 (leaving the remaining values equal) to be within both validity ranges. The highest stress concentration was located at the saddle (see Figure 4-11), therefore, it does not seem appropriate to apply Chang & Dover equations if the value of γ is not over 10.

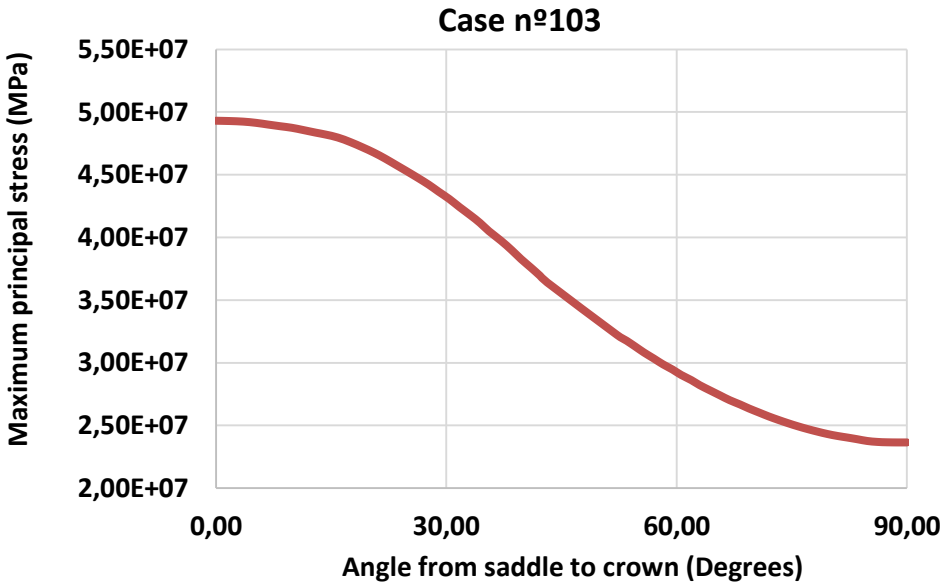

Figure 4-11 Stress distribution at the weld toe for Case nº103.

All the existing parametric equations agree that for a T-joint subjected to axial loading with all the geometric ratios within the limits shown in Table 4-9, the maximum stress concentration is located at the saddle (θ = 0º); however, it has been observed that some of the models do not satisfy this (as shown Table 4-10).

Table 4-9 Common validity limits.

Geometric parameter ranges
$6.21 \leq \alpha \leq 40.0$
$0.3 \leq \beta \leq 0.8$
$10 \leq \gamma \leq 32.0$
$0.2 \leq \tau \leq 1.0$

Table 4-10 Highest stress concentration location.

	α	β	γ	τ	**Angle (Degrees)**
Case 53	15.22	0.71	10.95	0.48	19.66
Case 54	20.44	0.71	10.95	0.48	20.53
Case 56	17.83	0.71	13.53	0.59	21.49
Case 27	17.39	0.71	14.38	0.79	10.22
Case 29	21.74	0.71	14.38	0.79	16.46

The weld profile is equal for all of the cases shown in Table 4-10. The case nº53 was modelled without weld in order to check if the location shift was a result of the weld influence. The maximum stress concentration was located at the saddle, proving that the weld profile may greatly impact both on the position and value of the highest stress concentration. Consequently, this model was rebuilt considering five different profiles to analyse the influence of the weld size.

Table 4-11 and Figure 4-12 show the weld profile parameters applied and summarise the results obtained.

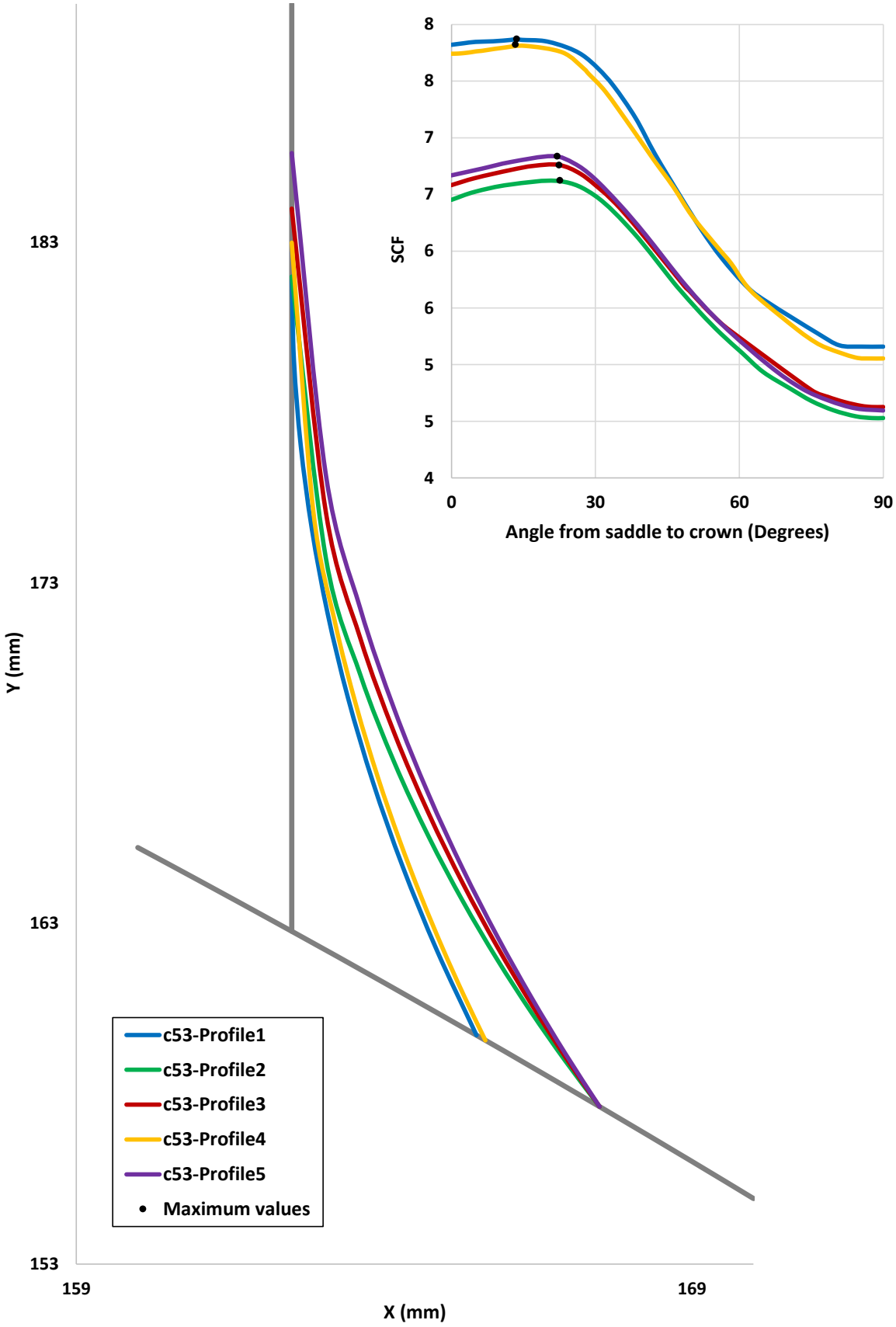

Figure 4-12 Weld size influence.

Table 4-11 Weld size influence.

	$\mathbb{R}$	ω	F	Weld Leg Lengths at the saddle (mm)		ζ (Degrees) at the saddle	SCF_{notch}	Position (Degrees)
				AB	AD			
Profile 1	2	52	3	19.22	4.28	7.67	7.87	13.58
Profile 2	2	52	5	19.22	7.18	11.60	6.62	22.58
Profile 3	4	52	5	21.22	7.18	10.74	6.76	22.38
Profile 4	3	52	4	20.22	4.49	7.65	7.82	13.28
Profile 5	5.63	52	5	22.85	7.18	10.12	6.84	22.00

The highest stress concentration was obtained with the Profile 1 configuration, which is formed by the smallest leg lengths. The weld size of Profile 4 was increased by expanding proportionally both weld leg lengths of Profile 1, to try to maintain the same weld angle, causing a decrease in the stress concentration. This indicates that an increase in weld size favours the reduction of stress concentration. Profile 2 was modelled by increasing the weld angle (i.e. increasing the fillet weld size, $F_2 > F_1$) without modifying the vertical weld leg length (i.e. equal root opening and end preparation angle) of Profile 1. This increment brings a stress concentration decline and moves its location away from the saddle. Profiles 3 and 5 were modelled by increasing the vertical weld leg length (i.e. increasing the root opening, $\mathbb{R}_5 > \mathbb{R}_3 > \mathbb{R}_2$) without modifying the fillet weld size, which entails a reduction of the weld angle. The Profile 5 weld angle is smaller than that of Profile 3, which is smaller than the Profile 2 weld angle (i.e. $\zeta_5 < \zeta_3 < \zeta_2$). These decreases result in a rise of the stress concentration and a position shift towards the saddle; the greater the decrease in weld angle, the greater the stress concentration and the proximity to the saddle. An increase of the vertical weld leg length does not imply a reduction of stress concentration. Therefore, the most critical parameter for the highest stress magnitude and location is the weld angle.

The SCF for the joint without the weldment is 9.93, which is reduced by around 20.7% by modelling Profile 1 while for Profile 2 it is 33.4%. It is not possible to quantify these differences in terms of fatigue life predictions by applying the S-N

curves because the extrapolation points of the HSS are not defined for locations other than the saddle or the crown. However, these differences clearly show that there will be a great impact on the number of cycles predicted, since an over-prediction of the SCF for axial loading (20 MPa) of 23.98% could represent a fatigue life under-prediction of 56.11%, as shown in Section 4.3.

4.5 Concluding Remarks

From the study carried out, it can be concluded that the existing parametric equations for predicting hot spot SCFs are very conservative and not useful for optimisation. Moreover, these equations are not able to predict where the greatest stress concentration will be located.

The weld profile may be used to shift the highest stress concentration location to a less critical place besides reducing the stress magnitude. The increment of the weld size favours the reduction of the stress concentration. The most critical parameter is the weld angle; increasing it brings a stress concentration decline and moves its location away from the saddle.

SCFs should be carried out by modelling solid joints which include the weldment, and should be based on notch stresses measured on the external surface at the weld toe, since slight overestimations of the SCFs represent a great reduction in predicted service lives (even differences over 100 years). Use of SCFs obtained from the complete weld profile FE models allow the design of structures with the same service life but reduced WT, reducing the capital cost of an offshore wind farm, or extending their effective service life.

5 STRESS INTENSITY FACTORS IN TUBULAR T-JOINT CRACKS

5.1 State-of-the-Art of fatigue crack growth analysis in tubular joints

Numerous studies have been carried out for assessing and modelling the uncertainty in fatigue crack growth in tubular joints, since cracks may compromise the integrity of the structure, and because crack growth estimations are needed for maintenance and safety requirements.

Cracks produced at the weld toe of tubular joints caused by cyclic fatigue loading are represented by a semi-elliptical surface crack, which is defined by the crack depth (a) and crack length ($2c$) (see Figure 5-1). Generally, multiple small fatigue cracks initiate which finally merge to form a long unified crack [266]. The shape of the crack changes during growth, extending around the circumference and increasing in crack depth, depending on: the initial crack shape, the crack initiation site, the geometry of the structure, the loading modes, the material's anisotropy, and the environmental conditions. The crack shape development can be determined by plotting the crack aspect ratio (a/c) versus the normalised crack depth (a/T).

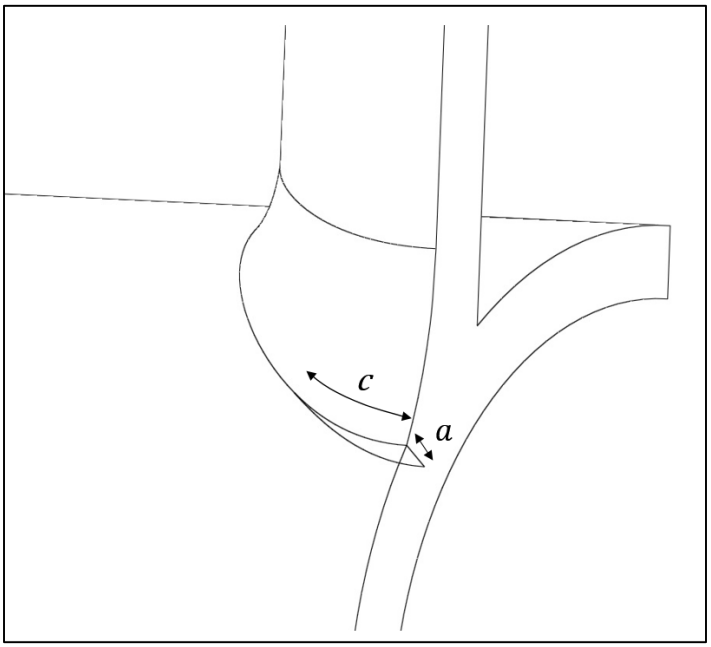

Figure 5-1 Typical fatigue crack at weld toe of a tubular joint.

Although the crack depth is the controlling parameter for fatigue analysis, both depth and surface length are required for the assessment of the remaining life of cracked components [267]. Moreover, during underwater inspection, crack length is relatively easy to measure accurately than crack depth and some common inspection techniques may not provide information on crack depth [268]. Therefore, several researches have been carried out to produce better predictions of the growth of the crack aspect ratio in welded tubular joints (such as Ref. [268] and [267]) and the relationship between crack length growth and remaining fatigue life (such as Ref. [269] and [270]). Despite the ongoing efforts of researchers there is a lack of accurate solutions for predicting crack aspect ratio evolution, which has been identified as representing the biggest hindrance to good estimations of the remaining ultimate capacity [271].

Several SIF solutions for weld toe cracks in offshore tubular joints have been developed, both empirically and numerically, over the years with different levels of accuracy. Some proposed solutions have been derived by a combination of these approaches. The basis for and background to each of the most relevant models is presented below.

5.1.1 Empirical Y factor solutions

Empirical models derive Y factors from experimentally measured crack growth data, on the basis of the Paris-Erdogan Law for the joint with known material fatigue properties. Then the SIF may be expressed as follows:

$$K = Y\ \sigma_{HS} \sqrt{\pi a} \qquad \textbf{Eq. 5-1}$$

Where a is the crack depth, and σ_{HS} is the HSS.

The most successful models are: the Average Stress Model, the Two-Phase model, and the Modified Average Stress Model.

5.1.1.1 The Average Stress (AVS) Model [272]

Random load large-scale fatigue tests on T- and Y-joints of 16 mm chord WT have shown that the HSS is, by itself, insufficient to describe the behaviour of different modes of loading. It was considered that the average stress around the

interception may influence the crack growth behaviour, and it was found that the results could be described by the following expression:

$$Y = (0.73 - 0.18\,S)\left[\frac{T}{a}\right]^{0.24+0.06\,S} \quad \textbf{Eq. 5-2}$$

Where a is the crack depth, T is the chord WT, and S is the ratio of HSS concentration factor (SCF_{HS}) to average SCF (SCF_{av}) at any location of the joint intersection. The SCF_{av} is defined as follows:

$$SCF_{av} = \frac{1}{\pi}\int_0^{\pi} SCF_{HS}(\theta)\,d\theta \quad \text{(for axial loading and OPB)} \quad \textbf{Eq. 5-3}$$

$$SCF_{av} = \frac{1}{\pi}\int_{-\pi/2}^{\pi/2} SCF_{HS}(\theta)\,d\theta \quad \text{(for IPB)} \quad \textbf{Eq. 5-4}$$

The fatigue strength is dependent on WT, which was not reflected in that database since it consisted only of 16 mm joints. To incorporate this dependence into the earlier analysis, the thickness correction developed using the UKOSRP Phase I data [273] was considered, and Eq. 5-2 was formulated as:

$$Y_{AVS} = (1.18 - 0.32\,S)\,T^{0.13-0.02\,S}\left[\frac{T}{a}\right]^{0.24+0.06\,S} \quad \textbf{Eq. 5-5}$$

Where a is the crack depth, T is the chord WT, and S is the ratio of SCF_{HS} to SCF_{av}.

5.1.1.2 The Two Phase Model (TPM) [274]

A series of static axial loading fatigue tests on large-scale tubular X-joints of 25, 35 and 45 mm chord WT and the dataset used for the AVS model have shown that the major difference between the crack growth curves is in the early crack growth (when a<0.25T approximately). The growth tends to be much slower as the WT decreases during the initial stage. Consequently, the Y data for each joint were divided into the two phases, and the Y factor was defined as follows:

$$Y_{TPM} = M\,(0.669 - 0.1625\,S)\left(\frac{T}{0.016}\right)^{0.11}\left[\frac{T}{a}\right]^{(0.353+0.057\,S)\left(\frac{T}{0.016}\right)^{-0.099}} \quad \textbf{Eq. 5-6}$$

$$M = 1 \qquad \text{for } a > 0.25\,T \quad \text{(Propagation phase)} \qquad \textbf{Eq. 5-7}$$

$$M = \left(\frac{0.25\,T}{a}\right)^{-p} \qquad \text{for } a < 0.25\,T \quad \text{(Early crack growth phase)} \qquad \textbf{Eq. 5-8}$$

$$p = 0.231\left(\frac{T}{0.016}\right)^{-1.71} \beta^{0.31} {SCF_{HS}}^{0.18} \qquad \textbf{Eq. 5-9}$$

Where T is the chord wall thickness, SCF_{HS} is the HSS concentration factor, β is the diameter ratio, and S is the ratio of SCF_{HS} to SCF_{av}.

5.1.1.3 The Modified AVS Model [22]

A series of variable amplitude corrosion fatigue tests on large-scale tubular T-joints of 16-19 mm chord WT showed that the TP model predicts much greater fatigue strengths for initial flaw sizes of less than 0.25 mm deep than those indicated by the experimental results. Moreover, the analysis shown that the AVS model predicts the shape of the Y factor curve very well. However, for small crack depths, the experimental Y factors are approximately 15% lower than the predicted ones. Therefore, the Y factor takes the form:

$$Y_{M\,AVS} = 0.85\,(1.18 - 0.32\,S)\,T^{0.13-0.02\,S}\left[\frac{T}{a}\right]^{0.24+0.06\,S} \qquad \textbf{Eq. 5-10}$$

Where a is the crack depth, T is the chord wall thickness, and S is the ratio of SCF_{HS} to SCF_{av}.

Ref. (10) points that the Modified AVS model performs particularly well, providing an excellent fit to its experimentally derived Y factors for the T-joint tests at all crack depths. Both of the AVS models predict the shape of the curve very well; however, the TPM models the early crack growth region poorly (despite being the most sophisticated) and under-predicts the Y factors significantly. Although, as Ref. [275] points out, the efficiency of all these solutions is limited because of the scarce number of experimental results used to derive these models.

5.1.2 Numerical K factor solutions

BS 7910 [276] affirms that numerical methods provide the most realistic predictions of SIFs. Among all numerical fracture mechanics approaches (see Section 1.3.2) developed for the modelling of fatigue crack growth in welded tubular joints, it is worth highlighting the FE method and the weight function method because of their versatility.

The FE method (see Section 1.4) is widely used, since it is the most versatile of all numerical approaches. Generating good quality models is a difficult process because of the complex geometry at the welds and cracks. Different techniques for modelling have been implemented over the years to address this difficulty. Some studies, such as Ref. [277] or [278], used the line-spring concept introduced by Ref. [279]. The surface crack is modelled as a series of line-spring elements, which have both stretching and bending resistance, inserted between shell elements. The spring constants vary according to the depth of the crack. Ref. [280] shows that the lack of weld modelling caused an over-prediction of the brace stresses, and an attempt was made to simulate the effect of the weld by using shell elements but it was unsuccessful. Ref. [281] proved that the accuracy of this technique in producing SIFs for cracks of moderate depths is good; however, both for the very shallow and very deep cracks it is poor. Consequently, despite being computationally more economical than other techniques, it may not be suitable for extensive parametric studies.

The FE studies which seemed to produce the most accurate models used 3D 20-node quadratic isoparametric elements for all tubes and welds [282]. Many commercial FEA packages (such as ABAQUS [77], ASTER [283] and ANSYS [284]) include these types of element and may be used to model tubular joints; but generating an adequate quality mesh with solid elements is very complicated and the most time-consuming work because sharp angles, which may result in highly distorted elements, must be avoided. ANSYS Workbench [285] has incorporated a powerful tool called Pre-Meshed Crack, where the crack is independently modelled by a focused tubular mesh along the crack front which will connect to a pre-existing mesh; however, this tool cannot be used to model

the cracked tubular joint because the crack surface is not contained in a plane. There are a number of 3D crack pre-processor software applications (for example, FEACrack [286] and PRETUBE [287]) which capture crack features quite accurately. The most well-known parametric SIF equations were derived by Ref. [288] using this FE technique (see Section 5.1.2.1 for more details), which are still used as reference by the BS 7910 guide. The main drawbacks of modelling using these pre-processors are the limitation in the weldment design and the lack of a dense weld mesh to produce convergence.

To overcome these issues, Ref. [289] created 3D cracked T-butt models and mapped them into tubular joint intersections. The downside is that only one quarter of the joint may be modelled and the crack has to be placed at the crown or saddle. One step further towards being able to change the location and the length of the crack easily was achieved by Ref. [290], who developed a mesh generating routine for transforming crack elements around a plane curve into crack elements for a doubly curved semi-elliptical surface crack around an intersection. First the mesh for the chord is generated in a rectangular flat plate, with a width equal to the circumference of the chord's outside surface, using concentric circles. Then the circles are transformed into oval curves, to represent the intersection curves and the curves inside. The crack elements are generated separately in a plane, using collapsed quadratic elements for the first ring around the front curve and quadratic elements for other rings. Next the coordinate transformation procedure is applied for obtaining the doubly curved, semi-elliptical surface crack. After this the whole group can be inserted into the plane mesh, where twin nodes need to be created along the crack faces and the crack elements should replace some elements and be connected properly to their adjacent elements. Finally, the chord should be mapped from the plane and connected to the brace, which includes the weld. 20-node quadratic solid elements are used throughout the joint. The drawback of this routine is that the connection between the crack elements and their adjacent elements for a surface crack is very complicated. Furthermore, Ref. [291] points out that the aspect ratio of the crack elements in the model is still very large, and therefore developed a systemic FE modelling procedure for generic cracked welded Y-joints. The most

notable differences are that the joint is divided into nine zones which are generated individually and merged together later, and the rings around the crack front consist of prism elements. Based on this procedure Ref. [292] derived a set of parametric equations for SIFs of cracked tubular T- and Y-Joints. More details of this parametric analysis will be given in Section 5.1.2.2.

Both Ref. [290] and [291] are good guides for the modelling of cracked tubular T-joints, since they provide some of the required equations, but the derivation of the code is not straightforward. Consequently, some FEA packages – such as ABAQUS [77], ASTER [283], and Morfeo [293] – have incorporated the eXtended Finite Element Method (XFEM) [294]. The XFEM was implemented in order to alleviate the computational burden associated with the insertion of arbitrary cracks into an FE model [295]. Its key advantages are that it allows the modelling of a crack independently of the mesh and the propagation path does not require remeshing [296]. However, some studies have concluded that the XFEM tool of the FEA packages requires further implementation [297] [298].

The weight function was first introduced by Ref. [65] and later generalized by Ref. [66]. They proved that the unknown SIF ($K^{(1)}$) for a symmetrical load system can be obtained by integrating the product of the weight function for a crack in a particular geometric configuration ($w(a,x)$) and the stress distribution on the crack face before the crack occurred ($\sigma(x)$), as follows:

$$K^{(1)} = \int_0^a w(a,x)\sigma(x)\ dx \qquad \textbf{Eq. 5-11}$$

Where a is the crack depth, and x is the distance from the crack mouth.

Ref. [66] demonstrated that a cracked geometry configuration has a unique weight function independently of the loading from which it was derived. The weight function for a symmetrical problem can be calculated based on the principle of the strain energy release rate, and is expressed as follows:

$$w(a,x) = \frac{E'}{2K^{(2)}}\frac{\partial u^{(2)}}{\partial a} \qquad \textbf{Eq. 5-12}$$

Where $K^{(2)}$ is the reference SIF, $u^{(2)}$ is the reference crack opening displacement, and E' is an appropriate elastic modulus (for an isotropic material: E for plane stress and $\frac{E}{1-\nu^2}$ for plane strain; and for anisotropic materials see Ref. [299]).

The definition of the crack opening displacement (COD) field has been identified as the main hindrance in the determination of weight functions. The most common approaches have been summarised and evaluated by Ref. [300], concluding that applying a multiple reference state (MRS) weight function approach is highly advantageous because it is mathematically the least involved and extremely reliable.

Tubular joints are complex geometries, thus often to know one reference SIF solution is an arduous process, leading to estimate SIF solutions by using simple flat plate or T-butt solutions in conjunction with appropriate loading-shedding models or boundary correction functions (also known as magnification factors). Two of the most popular plate/T-butt weight function solutions used in tubular joint analyses are the Oore and Burns' formulation [301] and the Niu-Glinka unit solution [302]. Nevertheless, their accuracy is limited since these approaches ignore the effect of the tube curvature. For instance, the Oore and Burns' equations validity range in welded tubular joints has been limited to $\frac{a}{T} < 0.2$ [274].

Through a similar procedure, but also assuming that the relative influence of the weld toe for the deepest point SIF of a semi-elliptical surface crack in a thin pipe is the same as that for an edge crack of the same depth in a flat plate under the same stress distribution, Ref. [260] derived a set of SIF parametric equations for a semi-elliptical surface saddle crack in a tubular welded joint. More details will be given in Section 5.1.2.3.

To summarise, three sets of SIF parametric equations for weld toe cracks of tubular joints derived by numerical methods are available in the literature, which are outlined in the following sections. Opposite to the SCF parametric equations,

these SIF formulations were derived by modelling or taking into account the weld. Nevertheless, how different weld profiles affect SIFs was not considered.

5.1.2.1 Rhee et al.'s formula [288]

This FE based SIF solution was developed by the analysis of 40 three-dimensional cracked tubular T-joint models subjected to axial, IPB and OPB loading. Cracks were placed at the saddle, whose surfaces were characterised by being flat and normal to the chord wall surface in the crack depth, while in the longitudinal direction were along the weld toe. The region along the brace-chord intersection was modelled using 20-node isoparametric elements, 8-node thick shell elements for the brace and chord regions, and 15-node elements for the transition. The crack tip singularity was represented by a number of 3D collapsed quarter point elements along the crack front.

The SIF for the deepest point along the crack front for a tubular T-joint under axial loading is expressed by the following equation:

$$K = F_g \, F_i \, F_s \, \sigma_{nom} \sqrt{\pi a} \qquad \textbf{Eq. 5-13}$$

Where σ_{nom} is the nominal stress, a is the crack depth, F_g is the joint geometry factor, F_i is the crack size factor, and F_s is the joint and crack coupling factor. These factors are given by:

$$F_g = 0.2749 \, \beta^{-0.6225-1.2685 \ln \beta} \, \gamma^{1.3191-0.1661 \ln \tau} \, \tau^{1.6621+0.3704 \ln \beta} \qquad \textbf{Eq. 5-14}$$

$$F_i = \beta^{0.35621 P_1 - 0.0956 P_2} \, \gamma^{0.0983 P_1 + 0.2298 P_2 - 0.0817 {P_2}^2} \, \tau^{-0.0762 P_1} \qquad \textbf{Eq. 5-15}$$

$$F_s = \left(\frac{a}{T}\right)^{p_1} \left(\frac{3c}{d}\right)^{p_2} \qquad \textbf{Eq. 5-16}$$

$$p_1 = -0.8669 - 0.2198 \, P_1 - 0.0162 \, {P_1}^2 - 0.475 \, {P_2}^2 - 0.1667 \, {P_2}^3 - 0.0193 \, {P_2}^4 \qquad \textbf{Eq. 5-17}$$

$$p_2 = 0.0777 + 1.0531 \, P_1 - 0.582 \, {P_1}^2 + 0.081 \, {P_1}^3 - 0.7001 \, P_2 - 0.064 \, {P_2}^2 + 0.006 \, {P_2}^3 \qquad \textbf{Eq. 5-18}$$

$$P_1 = \ln\left(\frac{a}{T}\right) \quad \textbf{Eq. 5-19}$$

$$P_2 = \ln\left(\frac{3c}{d}\right) \quad \textbf{Eq. 5-20}$$

Where β is the brace to chord diameter ratio, γ is the chord wall slenderness ratio, τ is the brace to chord thickness ratio, T is the chord thickness, c is the half crack length, and d is the brace diameter.

The model is valid in the geometric parameter ranges shown in Table 5-1, and the value of α was set at 12 which was considered great enough to neglect the boundary effect of the chord.

Table 5-1 Validity limits.

Geometric parameter ranges
$0.4 \leq \beta \leq 0.8$
$10 \leq \gamma \leq 20$
$0.3 \leq \tau \leq 1.0$
$0.05 \leq a/T \leq 0.8$
$0.05 \leq 3c/d \leq 1.2$

5.1.2.2 Chiew et al.'s parametric equations [292]

This FE based set of parametric equations was derived from the analysis of 95 basic joint geometrical cases of cracked tubular T- and Y-joints subjected to axial, IPB and OPB loading. Both chord ends of all models were fixed. The weld thickness was defined in accordance with the AWS code [303]. The semi-elliptical shape was assumed for the surface cracks, which were located at various positions around the joint intersection. Also, it was assumed that cracks propagate in the direction normal to the chord surface.

These models were generated using an automatic mesh generator, where the whole welded T-joint is divided into different zones. The mesh of each zone is generated individually with a different element density and merged together to form the complete mesh. Only one layer of 3D elements is generated in the far field, while more than one layer of elements is employed near the intersection.

Transition regions are used to increase the number of layers. Two rings of focused elements are used around the crack tip: the first ring consists of 27 quarter-point quadratic prism elements along the thickness, and the mesh density is reduced to nine prism elements for the second ring. After the models were generated, contact surfaces were defined to prevent penetration. A more detailed description of this mesh procedure is given in Ref. [291] and [304].

The SIF for the deepest crack front point at the saddle (θ = 0º) for tubular T- and Y-joints under axial loading is expressed by the following equations:

$$K = Y_g\, Y_i\, Y_s\, Y_\varphi\, \sigma_{nom}\, \sqrt{\pi a} \qquad \textbf{Eq. 5-21}$$

$$Y_g = 0.2402\, \beta^{G1} \gamma^{G2} \tau^{G3} \qquad \textbf{Eq. 5-22}$$

$$G1 = -0.5692 - 0.6852 \ln \beta \qquad \textbf{Eq. 5-23}$$

$$G2 = 1.6643 + 0.3462 \ln \tau \qquad \textbf{Eq. 5-24}$$

$$G3 = -0.1518 \ln \tau - 0.687\ (\ln \beta)^2 \qquad \textbf{Eq. 5-25}$$

$$Y_s = \beta^{Q1} \gamma^{Q2} \tau^{Q3} \qquad \textbf{Eq. 5-26}$$

$$Q1 = 1.5177\, A + 0.211\, A^2 + 0.1407\, C^2 - 0.2502\, AC + 0.4639\, A \ln \beta \qquad \textbf{Eq. 5-27}$$

$$Q2 = -0.6725\, A + 0.144 \ln \gamma \qquad \textbf{Eq. 5-28}$$

$$Q3 = 0.0548\, A + 0.3309\, C + 0.1233\, C^2 \qquad \textbf{Eq. 5-29}$$

$$Y_\varphi = (\sin \varphi)^P \qquad \textbf{Eq. 5-30}$$

$$P = 1.3 + 0.3 \ln \beta + 0.13 \ln \gamma - 0.06\, A - 0.15\, C - 0.4 \ln(\sin \varphi) \qquad \textbf{Eq. 5-31}$$

$$Y_i = \left(\frac{a}{T}\right)^{S1} \left(\frac{c}{d}\right)^{S2} \qquad \textbf{Eq. 5-32}$$

$$S1 = 2.4674 + 0.96\, A + 0.136\, A^2 + 1.0636\, C - 0.1186\, C^2 \qquad \textbf{Eq. 5-33}$$

$$S2 = 1.2438 + 0.3282\, C + 0.075\, C^2 + 0.8013\, A^2 + 0.1235\, A^3 \qquad \textbf{Eq. 5-34}$$

$$A = \ln(a/T) \qquad \textbf{Eq. 5-35}$$

$$C = \ln(c/d) \qquad \textbf{Eq. 5-36}$$

Where β is the brace to chord diameter ratio, γ is the chord wall slenderness ratio, τ is the brace to chord thickness ratio, φ is the brace to chord inclination angle, T is the chord thickness, c is half crack length, and d is the brace diameter.

The equations are valid within the geometric parameter ranges shown in Table 5-2, and the value of α was set at 15.7 which was considered large enough to neglect the chord boundary effect.

Table 5-2 Validity limits.

Geometric parameter ranges
$0.2 \leq \beta \leq 0.9$
$5.08 \leq \gamma \leq 31.75$
$0.2 \leq \tau \leq 1.0$
$0.05 \leq a/T \leq 0.8$
$0.05 \leq c/d \leq 0.75$
$a/c \leq 1$
$31^{o} \leq \varphi \leq 149^{o}$
$0^{o} \leq \theta \leq 90^{o}$

5.1.2.3 Chang-Dover's parametric equations [275]

In this study a new weight function, for the deepest point of a semi-elliptical surface crack at the saddle position in a tubular welded T-joint, was derived using the Petroski-Achenbach crack opening displacement expression [305] and assuming the following relationship:

$$\frac{{K_s}^{tj}}{{K_s}^{tp}} = \frac{{K_e}^{\alpha}}{{K_e}^{p}} \qquad \textbf{Eq. 5-37}$$

Where ${K_s}^{tj}$ is the SIF for the deepest point of a semi-elliptical surface crack at the saddle position in a tubular welded T-joint under the local stress distribution $\sigma(x)$, ${K_s}^{tp}$ is the SIF for the deepest point of an external longitudinal surface crack in a thin pipe subjected to the same stress distribution, ${K_e}^{\alpha}$ is the SIF for an edge crack in a T-butt welded joint under the same stress distribution, and ${K_e}^{p}$ is the SIF for an edge crack in a flat plate subjected to the same stress distribution. The weight function for the deepest point of longitudinal semi-elliptical surface cracks

in thin pipes was available from Ref. [306], and the weight functions for an edge crack in a plate and an edge crack emanating from the weld toe in a T-butt joint were available from Ref. [307].

A SIF database was established by integrating this new weight function with the University College London's uncracked T-butt through-wall stress distribution results [308]. After performing numerous regression analyses, a new set of SIF parametric equations was derived for membrane and bending loading respectively:

$$K_s{}^{tj} = Y^{tj}\,\sigma_{HS}\sqrt{\pi a} \qquad \textbf{Eq. 5-38}$$

$$Y^{tj} = Y_M{}^{tj}(1 - DoB) + Y_B{}^{tj}(DoB)\,R_B \qquad \textbf{Eq. 5-39}$$

$$Y_M{}^{tj} = \exp\left[C_0 + C_1\,\frac{a}{T} + C_2\left(\frac{a}{T}\right)^2\right]\left(\frac{a}{T}\right)^{C_3} \qquad \textbf{Eq. 5-40}$$

$$Y_B{}^{tj} = C_0 + C_1\,\frac{a}{T} + C_2\left(\frac{a}{T}\right)^2 + C_3\ln\frac{a}{T} \qquad \textbf{Eq. 5-41}$$

$$R_B = 0.5\cos\left(\frac{\pi a}{T}\right) + 0.5 \qquad \textbf{Eq. 5-42}$$

Where σ_{HS} is the HSS, a is the crack depth, DoB degree of bending, and Y^{tj} is the normalised correction factor ($Y_M{}^{tj}$ under pure membrane loading and $Y_B{}^{tj}$ under pure bending loading, whose coefficients are defined in Appendix A).

All equations are valid in the geometric parameter ranges shown in Table 5-3:

Table 5-3 Validity limits.

Geometric parameter ranges
$\pi/6 \le \zeta_t \le \pi/3$
$0.01 \le \rho/T \le 0.066$
$0.1577 \le L/T \le 4$
$0.01 \le a/c \le 1$
$0.01 \le a/T \le 0.8$

Where ζ_t is the weld toe angle, and ρ is the weld toe radius.

5.1.3 Y factor solutions derived by combined approaches

5.1.3.1 Monahan's Model [309]

The results from constant amplitude large-scale fatigue tests on X-joints and multi-brace nodes under IPB and OPB loading have shown that accurate modelling of the SIF in welded tubular joints was possible using a modified Newman-Raju flat plate solution, if the half crack aspect ratio remained low ($a/2c$ ≤ 0.05) and the influence of weld geometry and restraint were properly accounted for.

The Newman-Raju flat plate solution [310] was derived using the results of a 3-D FE analysis of semi-elliptical cracks in an elastic flat plate. This solution accounts for both tensile and bending loads, and at the deepest point of the defect takes the form of:

$$K = \frac{F_M\,\sigma_M + F_B\,\sigma_B}{\Phi}\sqrt{\pi a} \qquad \textbf{Eq. 5-43}$$

$$Y_{NR} = \frac{F_M\,(1 - DoB) + F_B\,DoB}{\Phi} \qquad \textbf{Eq. 5-44}$$

$$\Phi = \sqrt{1 + 1.464\left(\frac{a}{c}\right)^{1.65}} \qquad \textbf{Eq. 5-45}$$

$$F_M = \left[M_1 + M_2\left(\frac{a}{T}\right)^2 + M_3\left(\frac{a}{T}\right)^4\right] f_w \qquad \textbf{Eq. 5-46}$$

$$f_w = \sqrt{\sec\left(\frac{\pi c}{w}\sqrt{\frac{a}{T}}\right)} \qquad \textbf{Eq. 5-47}$$

$$M_1 = 1.13 - 0.09\frac{a}{c} \qquad \textbf{Eq. 5-48}$$

$$M_2 = -0.54 - 0.09\frac{0.89}{0.2 + a/c} \qquad \textbf{Eq. 5-49}$$

$$M_3 = 0.5 - \frac{1}{0.65 + a/c} + 14\left(1 - \frac{a}{c}\right)^{24} \quad \textbf{Eq. 5-50}$$

$$F_B = \left[1 + G_1\frac{a}{T} + G_2\left(\frac{a}{T}\right)^2\right] F_M \quad \textbf{Eq. 5-51}$$

$$G_1 = -1.22 - 0.12\frac{a}{c} \quad \textbf{Eq. 5-52}$$

$$G_2 = 0.55 - 1.05\left(\frac{a}{c}\right)^{0.75} + 0.47\left(\frac{a}{c}\right)^{1.5} \quad \textbf{Eq. 5-53}$$

Where σ_M and σ_B are the membrane and bending stresses, F_M and F_B are the correction functions for the membrane and bending stresses, Φ is a complete elliptical integral of the second kind, DoB is the degree of bending, f_w is the plate width correction function for a plate with a finite width (w), a is the crack depth, c is half crack length and T is the plate thickness.

The moment through the cracked ligament is constant in cracked flat plates, whereas it is dependent on the crack depth in tubular joints. Ref. [311] proposed a linear moment release (LMR) function which provides an acceptable means of correcting for the stress redistribution accompanying crack propagation (i.e. load shedding). The membrane component of the through thickness stress is left independent of crack depth, while the bending component is decreased according to:

$$\sigma_B = \sigma_{Bo}\left(1 - \frac{a}{T}\right) \quad \textbf{Eq. 5-54}$$

Where σ_B is the bending stress at the crack tip, σ_{Bo} is the bending stress at the surface, a is the crack depth and T is the chord thickness.

For small cracks, it is necessary to include the effect of the non-uniform stress gradient caused by the weld toe. The procedure outlined by Ref. [312] (summarised in Figure 5-2) was used to account for the weld toe discontinuity, allowing the computation of a non-uniform stress correction (NSC) factor (Y_g) from a known through thickness stress distribution in the presence of a weld. This factor is given by:

$$Y_g = \frac{2}{\pi}\sum_{i=1}^{n}\frac{\sigma_{x_i}}{\sigma}\left(sin^{-1}\left(\frac{x_{i+1}}{a}\right) - sin^{-1}\left(\frac{x_i}{a}\right)\right)$$ **Eq. 5-55**

Where σ is the nominal stress without the stress concentration for the element under consideration, σ_{x_i} is the discrete stress range of the i-th element, x is the distance from the crack centre line, and $2a$ is the crack length.

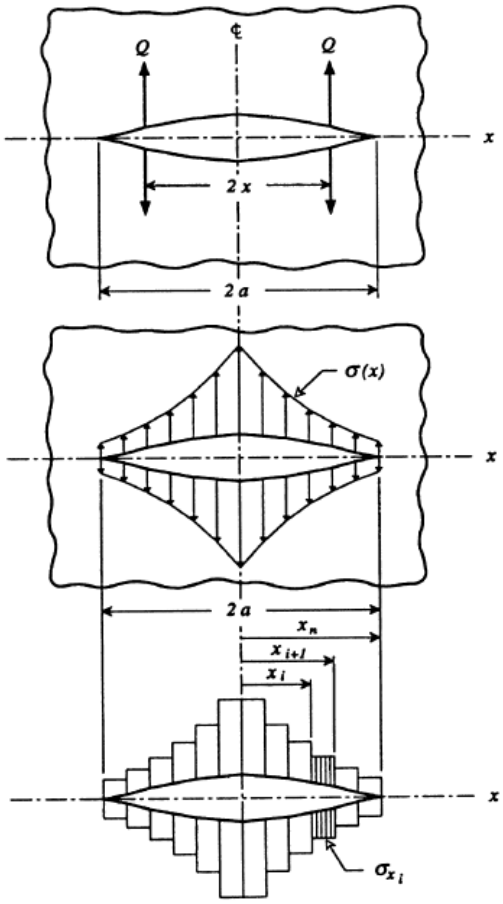

Figure 5-2 Albrecht's Method for calculating Y_g [313].

To account for the influence of the crack aspect ratio, Ref. [309] defined a crack shape correction (CSC) factor by comparing the experimental Y factors with those obtained by a modified flat plate solution which included an NSC factor and the LMR model. This factor is expressed as follows:

$$\Psi_c = \frac{Y_{EXP}}{Y_{NR+NSC+LMR}}$$ **Eq. 5-56**

Plotting the values of Ψ_c against $a/2c$, for all the cases studied which were within the weld angle validity range, there appears to be the following correlation:

$$\Psi_c = 1 \qquad for\ a/2c \leq 0.05 \qquad \textbf{Eq. 5-57}$$

$$\Psi_c = \frac{1}{1 + 0.7\left(\frac{a}{2c} - 0.05\right)^{0.4}} \qquad for\ 0.05 < a/2c < 0.26 \qquad \textbf{Eq. 5-58}$$

This CSC factor may not be directly applicable to geometries other than X-shaped joints since all the experimental Y factors were derived from tests conducted on a combination of X and multi-braced tubular joints.
Finally, the proposed equation is given by:

$$Y_{MONAHAN} = Y_{NR+NSC+LMR+CSC} = \frac{(F_M\,(1 - DoB) + F_B\,DoB)\,Y_g\,\Psi_c}{\Phi} \qquad \textbf{Eq. 5-59}$$

Monahan's model is not recommended for cases where the DoB ratios are less than 0.83 or more than 0.92. Moreover, this model produces conservative results in cases where the half crack aspect ratio is above 0.05.

5.1.3.2 Myers's crack shape correction factor for T-joints [313]

This CSC function was developed under the same assumptions as Monahan's CSC function. The difference is that the experimental Y factors were obtained through several constant amplitude axial loading fatigue tests on full-scale T-shaped joints of 16 mm chord WT. This function is given by:

$$\Psi_c = 0.9 \qquad for\ a/2c \leq 0.05 \qquad \textbf{Eq. 5-60}$$

$$\Psi_c = \frac{1}{1 + 0.7\left(\frac{a}{2c} - 0.04\right)^{0.4}} - 0.1 \qquad for\ a/2c > 0.05 \qquad \textbf{Eq. 5-61}$$

5.1.3.3 Etube et al.'s Model [314]

Several variable amplitude loading fatigue tests on full-scale Y-joints were realised in order to incorporate the effect of the crack aspect ratio into the SIF models used for fatigue crack growth prediction, since none of the above empirical models (Section 5.1.1) take into account the crack shape evolution

effect. The best fit average curve obtained for the different crack shape evolution curves takes the form:

$$2c = 58.533\ a^{0.7194} \quad \textbf{Eq. 5-62}$$

This curve was used to model the Y factor solution proposed by Monahan [309] to obtain an equation with the form of the AVS model. Then by combining the modified solution with the deviation from the experimental data, which was modelled by the Gumbel distribution, the Y factor was formulated as:

$$Y_{ETUBE} = A\,[\frac{T}{a}]^{0.22+0.06\,S} - Exp[-Exp(\left(A - \frac{a}{c}\right)\left(\frac{a}{T}\right))] \quad \textbf{Eq. 5-63}$$

$$A = 0.56 - 0.18\,S \quad \textbf{Eq. 5-64}$$

Where a is the crack depth, c is the half crack surface length, T is the chord wall thickness, and S is the ratio of SCF_{HS} to SCF_{av}.

5.2 Finite Element Analyses

Following this exhaustive state-of-the-art review, the SOLIDWORKS 3D CAD software and the ABAQUS/CAE FEA product suite were used for modelling uncracked and cracked tubular T-joints in order to calculate the SIFs. The numerical calculations have been carried out on a 16-core machine with 192 GB of shared memory RAM.

5.2.1 Modelling and meshing

The restrictions of the brace and chord lengths, and the recommendations provided by the AWS Welding code [261] used for the complete weld profile solid FE tubular T-joint models, as explained in Section 4.2.3, were also applied to the cracked tubular T-joint models. The density, Young's modulus and Poisson's ratio were taken to be 7850 kg/m^3, 210 GPa and 0.3 respectively; which match the mechanical properties employed by Ref. [315].

All the models were axially loaded, and subjected to a nominal stress of 6 MPa. This value was chosen randomly, since it does not influence the shape factor (Y).

The nominal stress was defined as the total applied load divided by the hollow cross-sectional area of the brace. Both chord ends were rigidly fixed.

The surface cracks are characterised by a semi-elliptical shape. Tubular T-joint axially loaded specimen tests show that cracks grow along the chord surface at the weld toe and in depth through the thickness following a curving path under the weld [316]. Nevertheless, it was considered that the crack would propagate from the weld toe into the thickness of the chord in the direction normal to the chord surface because that is the shortest path to reduce the stiffness of the joint quickly. Cracks will appear in the region subjected to the highest stress concentration. Tubular joints will withstand combined loads; therefore, it is difficult to predict the crack location. In this research, the cracks are placed at the joint saddle regardless of the highest stress concentration location, aiming to analyse how axial loading affects an existing crack which grew as a result of other combined loads or a defect.

Once the cracked geometry is built, the T-joint part is divided into several regions (see Figure 5-3) using different partition tools to create mesh boundaries in order to help the refinement. These regions produce a smooth transition between the fine mesh around the crack and weld and the coarse mesh of the zones away from the crack. The mesh generation is the most time-consuming work because of the complex geometry at the crack and the weld. Moreover, meshing is a critical part since it influences the accuracy, convergence and speed of the results.

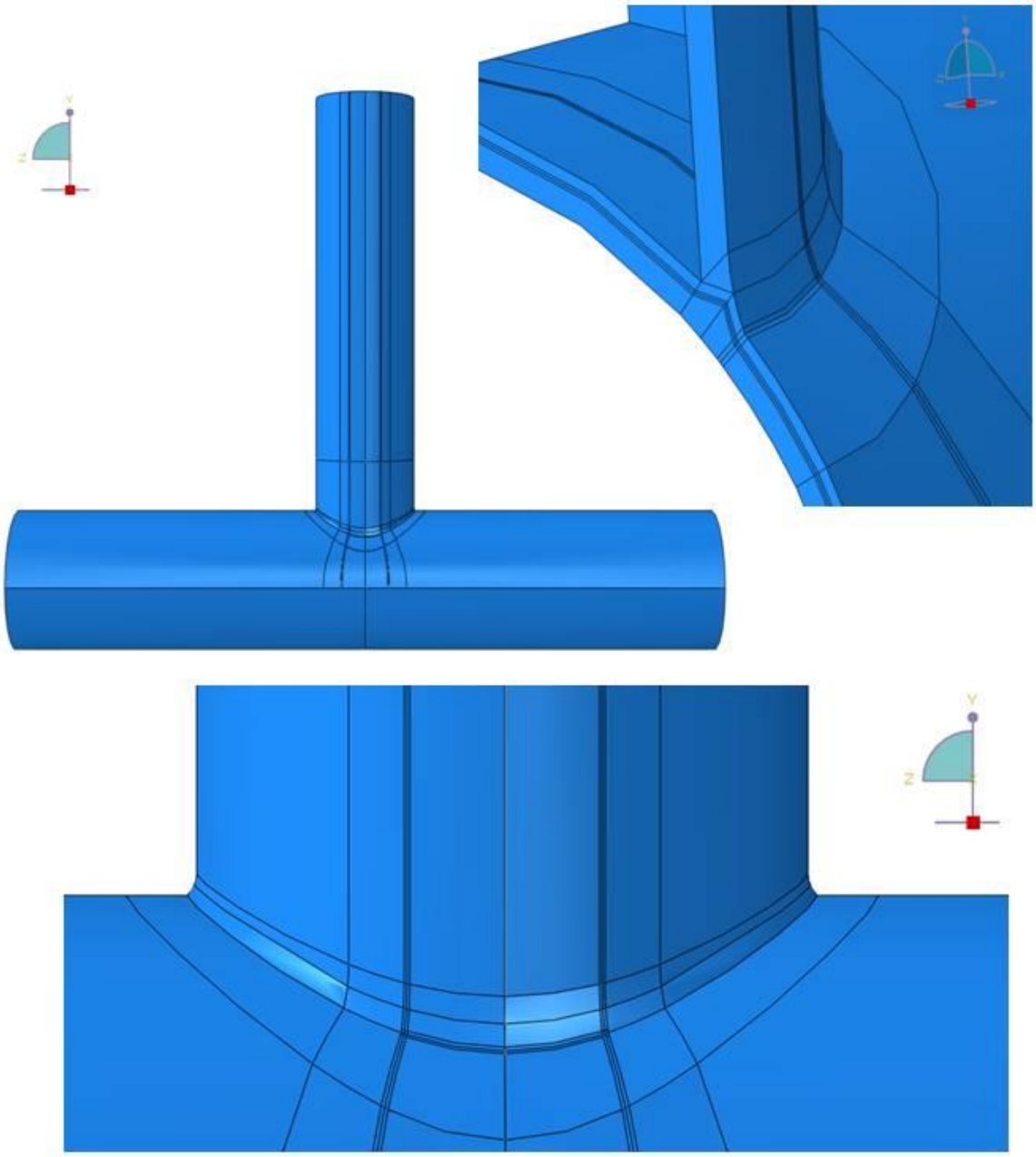

Figure 5-3 Partitioning into regions.

In the first place, as the deepest point of the crack is in the symmetry plane, it was checked that it is possible to apply symmetry boundary conditions (see Figure 5-4).

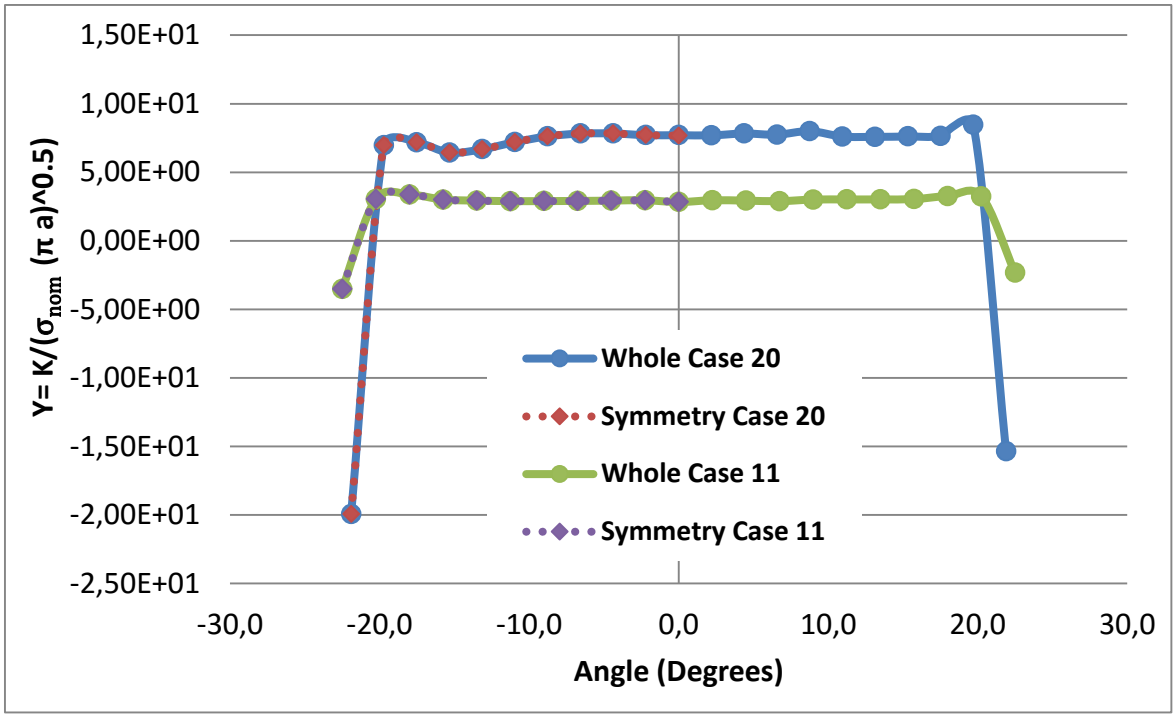

Figure 5-4 Analysing symmetry boundary conditions.

Linear elements with reduced integration were applied in Section 4.2.2 to be consistent with the previous SCF studies, but in this part of the research the aim is to derive the optimum SIF value. Clearly, the greater the number of elements and the more Gaussian integration points per element there are, the more accurate the output will be; but the cost of computation time has to be taken into account. A comparison has been made between four element types: linear elements with reduced integration (C3D8), linear elements with full integration (C3D8R), quadratic elements with reduced integration (C3D20R), and quadratic elements with full integration (C3D20). It was concluded that C3D20 elements are the most favourable option since 8-node elements does not provide accurate results (see **Figure 5-5**) and the difference in running time is not significant enough as for not selecting the most precise elements (see Table 5-4).

Table 5-4 Cost of computation comparison

	K_I (Pa $m^{1/2}$)	Nº Elements	Nº Nodes	Wall time (Sec)
C3D8R	6.212E+06	42156	49937	20
C3D8	5.285E+06	42156	49937	28
C3D20R	6.954E+06	42156	191851	109
C3D20	6.940E+06	42156	191851	126

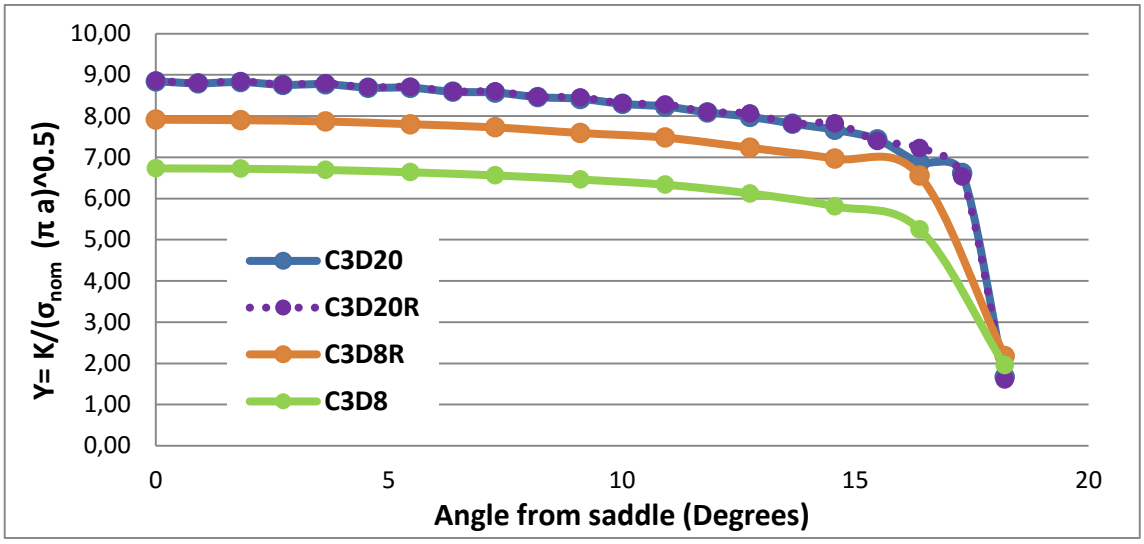

Figure 5-5 Element type comparison.

Before mesh refinement, it was tested whether it was possible to combine hexahedrons (C3D20) with tetrahedrons (C3D10) in order not to excessively increase the number of nodes and to avoid unnecessary computational cost. A tie constraint was used to link the surface of the partition with hexahedrons to the surface of the partition with tetrahedrons, preventing any relative motion between them, because nodes will not match. The first model is formed by 10356 hexahedral elements and 68846 tetrahedral elements, and the second one by 6195 and 77923 respectively. Both models have considerably overestimated the SIF values along the crack front (see Figure 5-6). Moreover, the stress distribution does not follow the same trend, as shown in Figure 5-7.

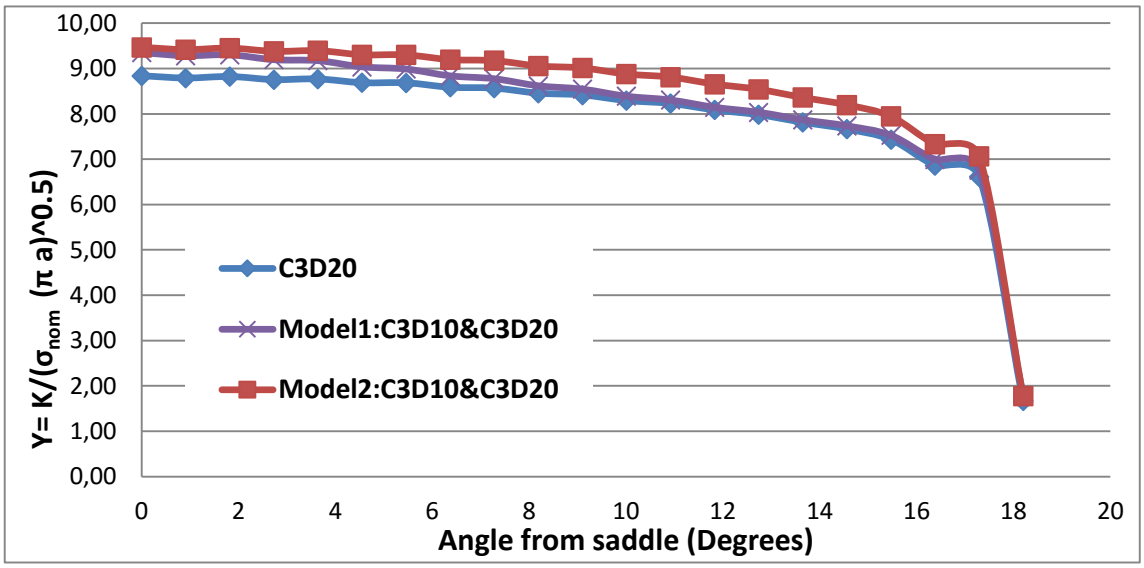

Figure 5-6 Analysis of the combined elements mod

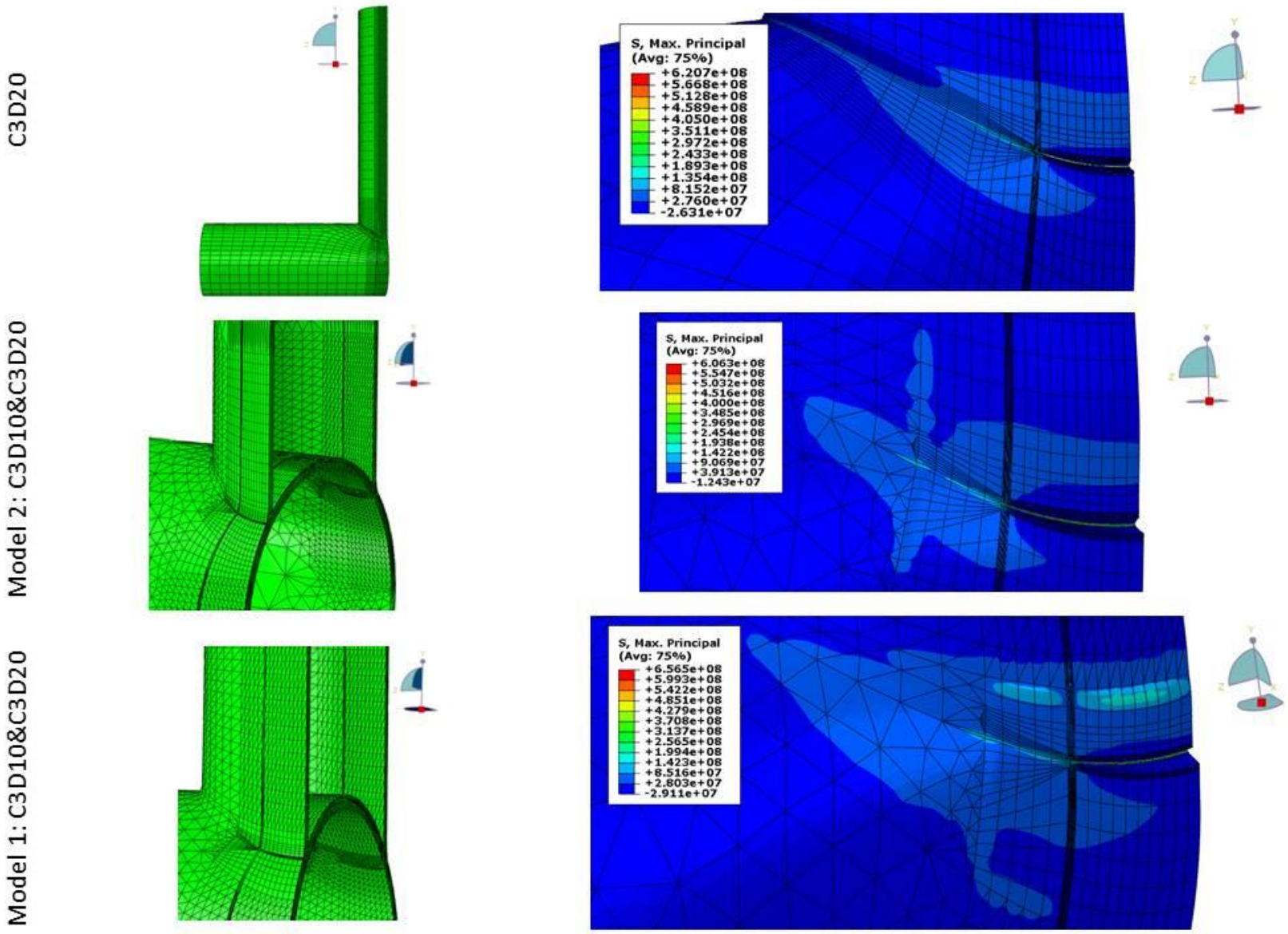

Figure 5-7 Maximum principal stresses of the combined elements models.

Consequently, as these models combining different type of elements may not be used, submodelling was applied in order to study in detail the area around the crack with a refined mesh based on interpolation of the solution from a relatively coarse global model. First, the global model had to be created and analysed, and then the submodel had to be created and the driving region specified. Three submodels (see Figure 5-8) were analysed to prove that the driving region selected is appropriate. It was concluded that these three models may be used since the solutions for all of them are quite accurate and the stress distributions are correct (see Table 5-5). Therefore, Submodel 3 was selected to proceed with the research as it is formed by the lower number of nodes. The driving region of this model is located at a distance of $7a$.

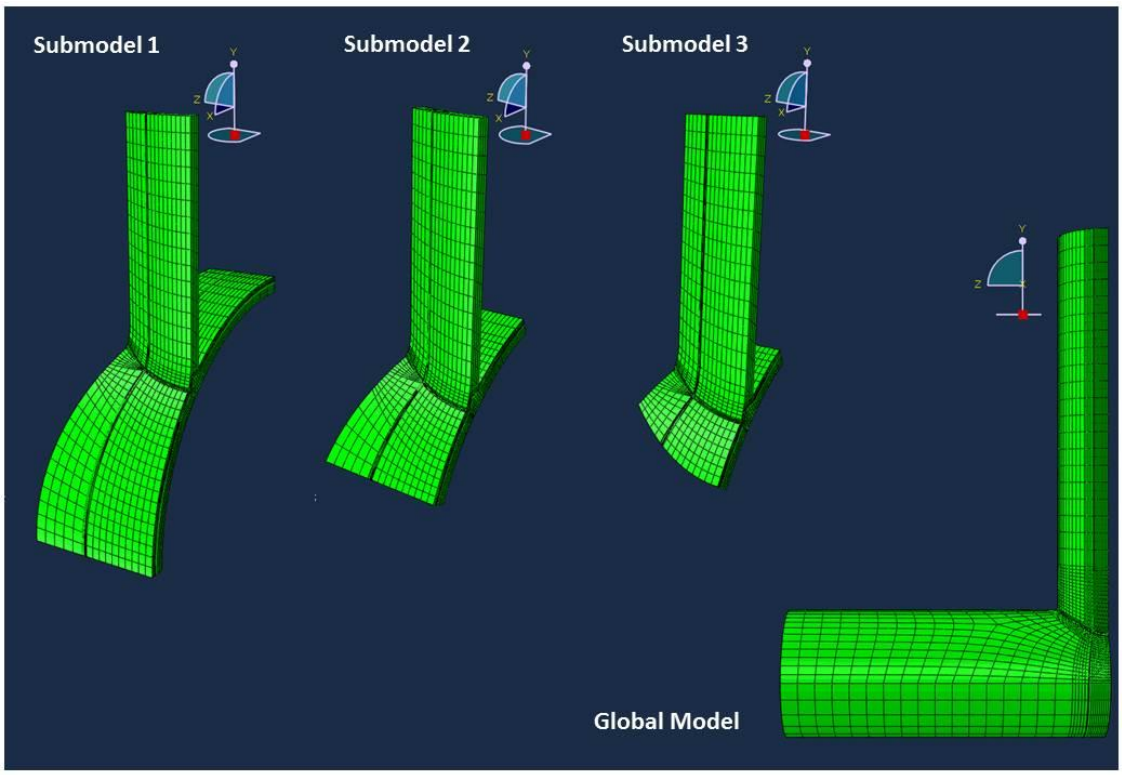

Figure 5-8 Submodels geometry.

Table 5-5 Comparative analysis of submodeling accuracy.

	K_I (Pa $m^{1/2}$)	Elements	Nodes
C3D20 Reference model	6.940E+06	42156	191851
C3D20 Global model	7.826E+06	22610	107193
C3D20 Submodel1	6.947E+06	12897	59175
C3D20 Submodel2	6.946E+06	11049	50951
C3D20 Submodel3	6.945E+06	9663	44783

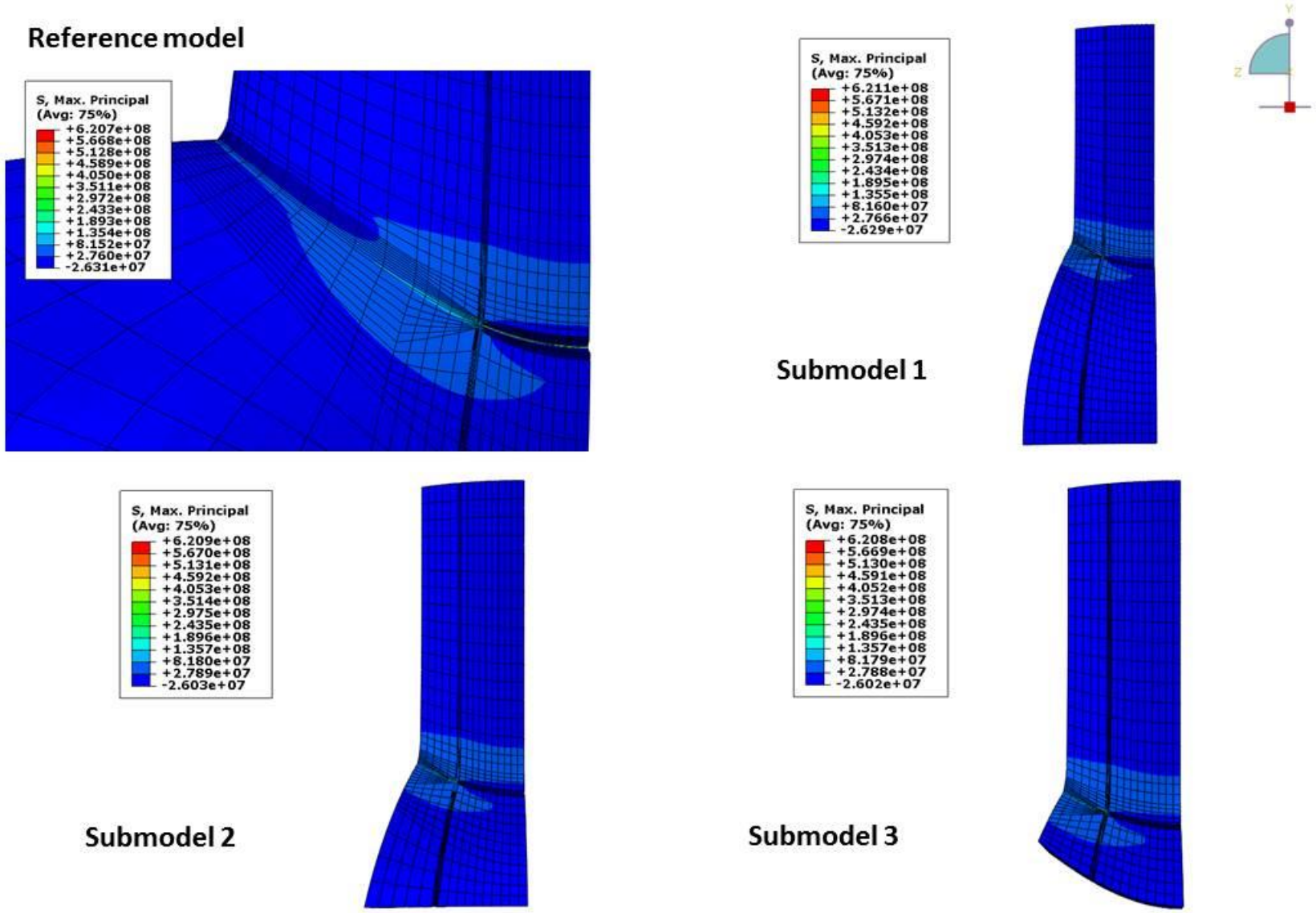

Figure 5-9 Maximum principal stresses of the submodels.

A convergence test was carried out, aiming to verify that the meshes used for this research were sufficiently fine to accurately predict the SIFs. The sizes of the elements which form part of the contours to be evaluated were 0.24 mm, 0.17 mm, 0.13 mm, 0.11 mm and 0.1 m. A bias ratio of 3.5 was selected for meshing the rest of the model. The comparison of SIF values (see Table 5-6) shows a good convergence. The finest mesh was selected for the rest of the analysis as there is an acceptable compromise between computational time and accuracy.

Table 5-6 Comparison between the SIFs at the saddle from coarse to fine meshes.

	K_I (Pa $m^{1/2}$)	Elements	Nodes
C3D20 Submodel3	6.945E+06	9663	44783
Refinement1	6.943E+06	72505	310936
Refinement2	6.940E+06	158326	669622
Refinement3	6.938E+06	284869	1193455
Refinement4	6.937E+06	306795	1283741

5.2.2 Defining the crack extension direction

In ABAQUS/CAE, the contour integral has been selected to compute the fracture characterizing parameter (SIF) and to study the onset of cracking for this research since it does not require further implementation. However, a contour integral estimate does not predict how a crack will propagate, thus it is necessary to specify the crack extension direction ($\vec{q}$) along the crack front. ABAQUS/CAE also allows the option of defining the normal ($\vec{n}$) to the crack plane but it can be specified just once, thus it will be the same for all the nodes. In this research, the crack surfaces are not contained within a plane and the crack fronts are doubly curved, thus the direction of the normal to the crack plane varies along the crack front. Using the $\overrightarrow{q}$ option, it is possible to specify a crack extension direction per node.

A Matlab routine, which requires two input datasets, has been developed to define the different directions. The first set is formed by all the crack tip nodes ($N1$), and the second one is composed of the nodes located at the top of the elements forming the upper part of the crack front ($N2$), as shown in Figure 5-10.

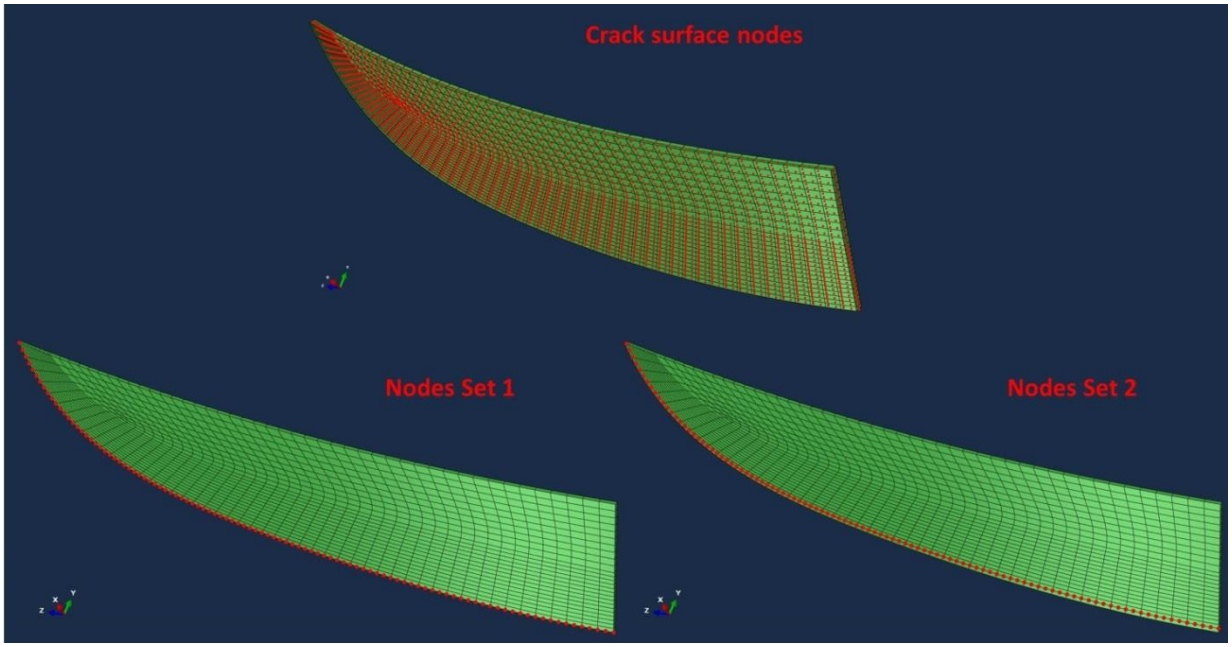

Figure 5-10 Input datasets.

Each node of the crack tip is contained in two osculating planes, as shown in Figure 5-11; $Plane\ 1$ is formed by $P1(i)$, $P1(i+1)$ and $P2(i)$, and $Plane\ 2$ by $P1(i)$, $P1(i-1)$ and $P2(i)$. $\vec{q}_i$ is the resultant of $\vec{q}_1(i)$ and $\vec{q}_2(i)$, which are contained in $Plane\ 1$ and $Plane\ 2$ respectively. $\vec{q}_1(i)$ and $\vec{q}_2(i)$ are perpendicular to $\overrightarrow{P1(i)P1(i+1)}$ and $\overrightarrow{P1(i)P1(i-1)}$ respectively.

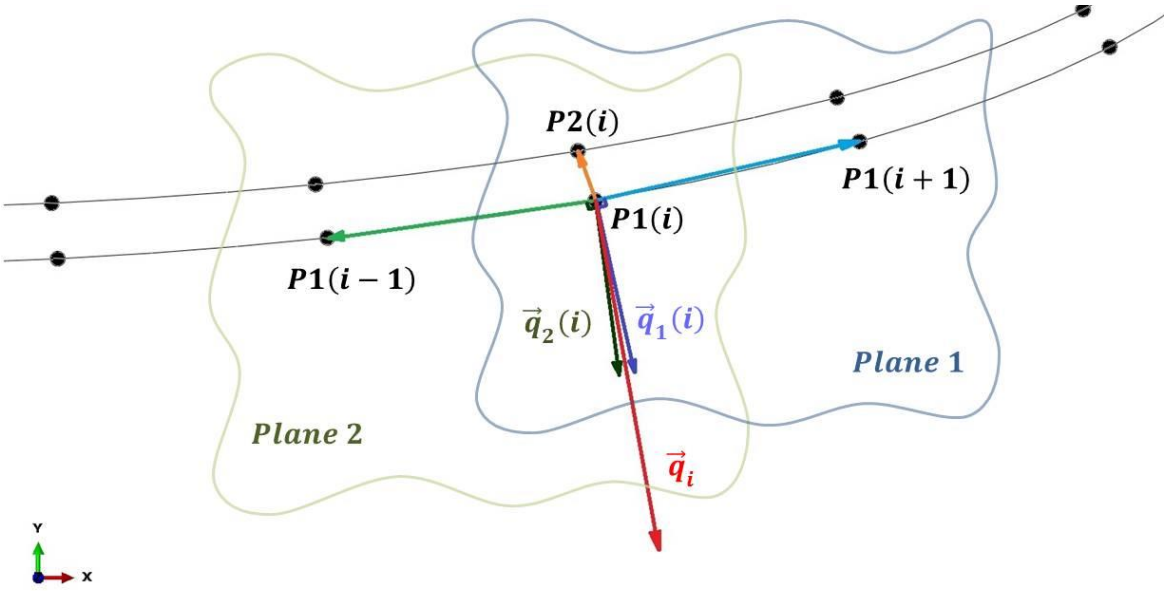

Figure 5-11 Parameters used for defining $\vec{q}_i$.

It is possible to define $\vec{q}_1(i)$ and $\vec{q}_2(i)$ by selecting any point in their direction and then normalising the calculated vector, since they are unit vectors. The y-component of these random points must be lower than the y-component of $P1(i)$, thus a value of 0.1m has been assumed randomly. Therefore, $\vec{q}_i$ is calculated by solving the two equation systems shown below, and an example of the final result is shown in Figure 5-12.

$Equation\ System\ 1$:

$$\det\left(\vec{q}_1(i), \overrightarrow{P1(\imath)P1(\imath+1)}, \overrightarrow{P1(\imath)P2(\imath)}\right) = 0 \quad \textbf{Eq. 5-65}$$

$$\vec{q}_1(i).\overrightarrow{P1(\imath)P1(\imath+1)} = 0 \quad \textbf{Eq. 5-66}$$

$$y = 0.1 \quad \textbf{Eq. 5-67}$$

$Equation\ System\ 2$:

$$\det\left(\vec{q}_2(i), \overrightarrow{P1(\imath)P1(\imath-1)}, \overrightarrow{P1(\imath)P2(\imath)}\right) = 0 \quad \textbf{Eq. 5-68}$$

$$\vec{q}_2(i).\overrightarrow{P1(\imath)P1(\imath-1)} = 0 \quad \textbf{Eq. 5-69}$$

$$y = 0.1 \quad \textbf{Eq. 5-70}$$

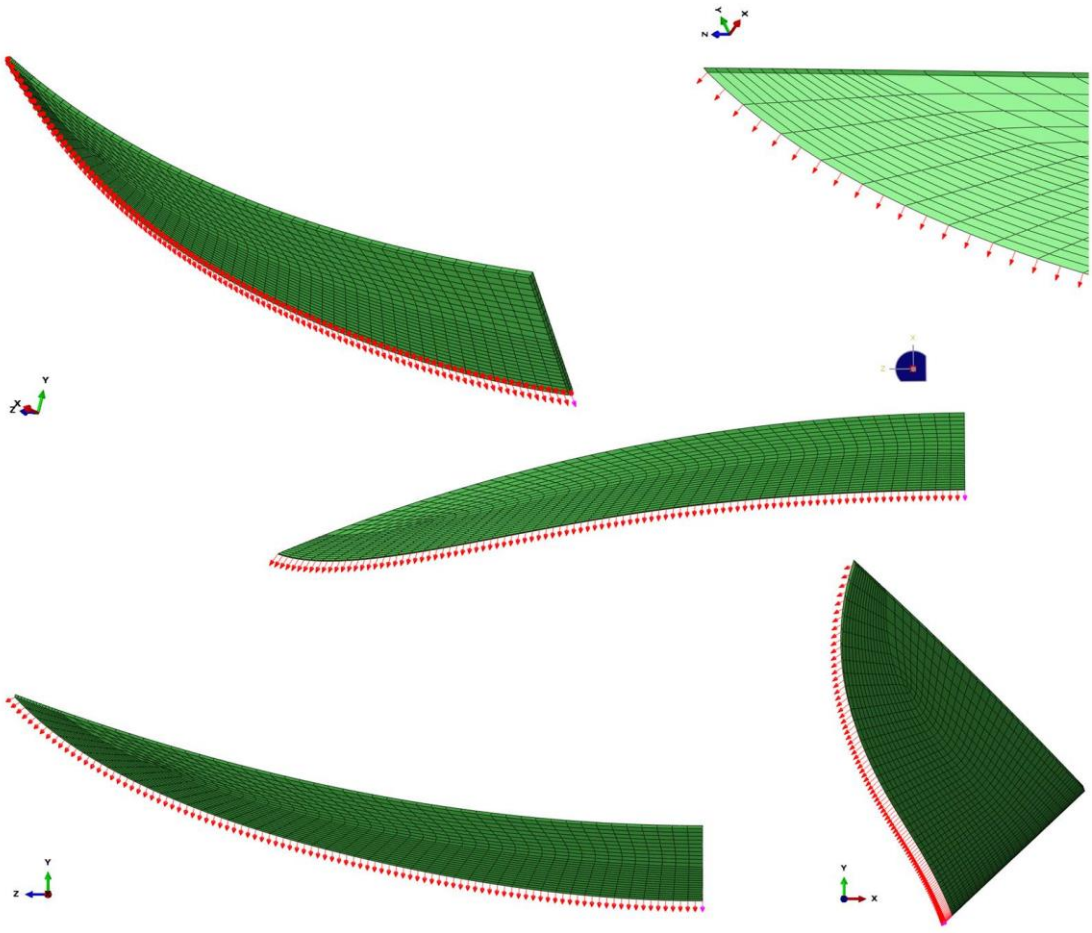

Figure 5-12 Crack extension vectors shown from different points of view.

It has been verified that the Matlab routine works properly by building a model with a penny shaped crack, as shown in Figure 5-13.

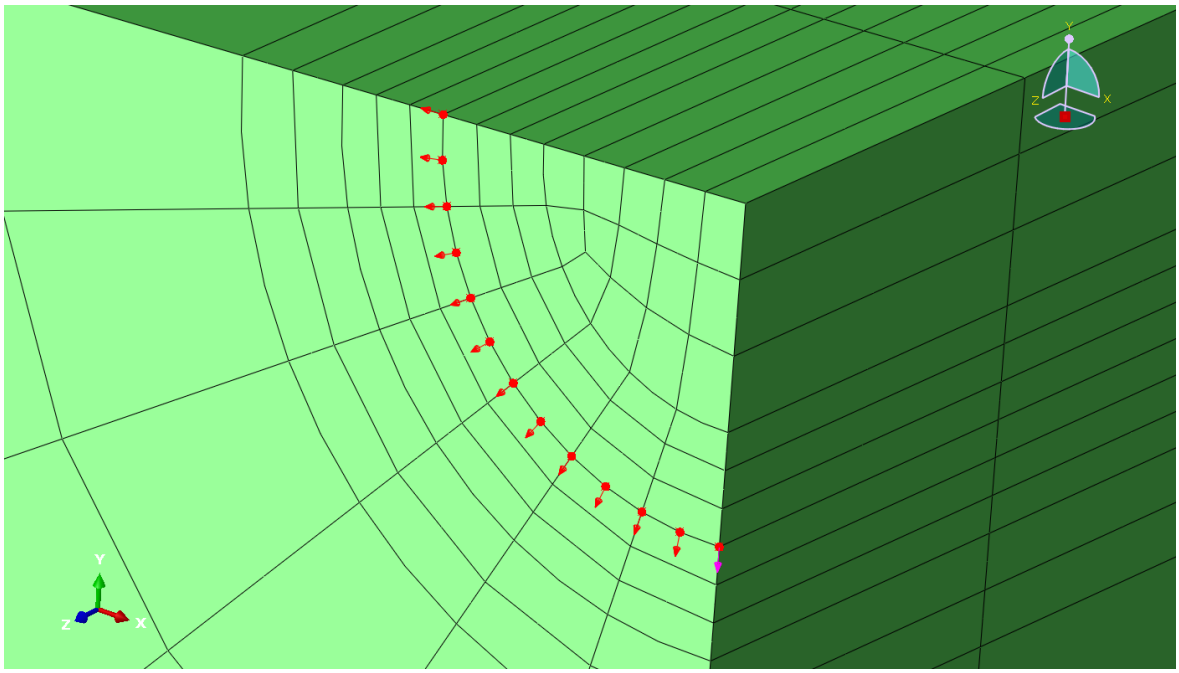

Figure 5-13 Crack extension vectors of a penny shaped crack.

5.2.3 Models validation

Ref. [317] and [318] presented a variation of the Y factor with normalised crack depth for a particular size (see Table 5-7) tubular welded T-joint subjected to axial loading. Neither of these publications provided information of the weld profile; however, Ref. [319] conducted a series of tests on this particular size of tubular welded T-joint using out-of-plane bending and reported the weld profile used (see Figure 5-14). Therefore, it was assumed that the weld profile of Ref. [317] and [318] is also the same. These measurements were used to assess the effectiveness of the FE models.

Table 5-7 Joint Dimensions.

Chord diameter (mm)	460 [317] - 457 [318]
Chord thickness (mm)	16
Brace diameter (mm)	324
Brace thickness (mm)	12.7
Brace to chord diameter ratio	0.7
Chord wall slenderness ratio	14.3 [317] - 14.4 [318]
Brace to chord thickness ratio	0.8
Joint angle	90º

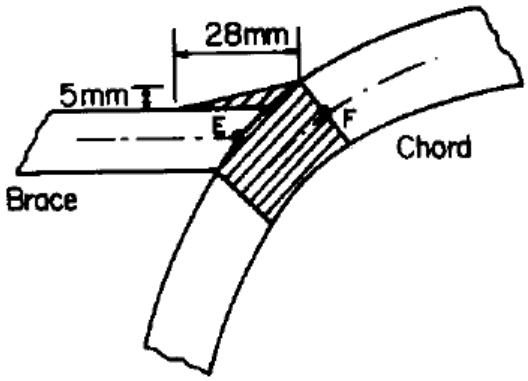

Figure 5-14 Weld profile [319].

Cases 20 to 24 were modelled in concordance with the experimental T-joint geometry, whose results are summarised in Figure 5-15. This shows the comparisons of the SIFs obtained from the FE models with those from the fatigue tests, from which it can be seen that there is a good agreement. Therefore, the proposed methodology can be used to calculate the SIFs of the cracked tubular joints under axial loading.

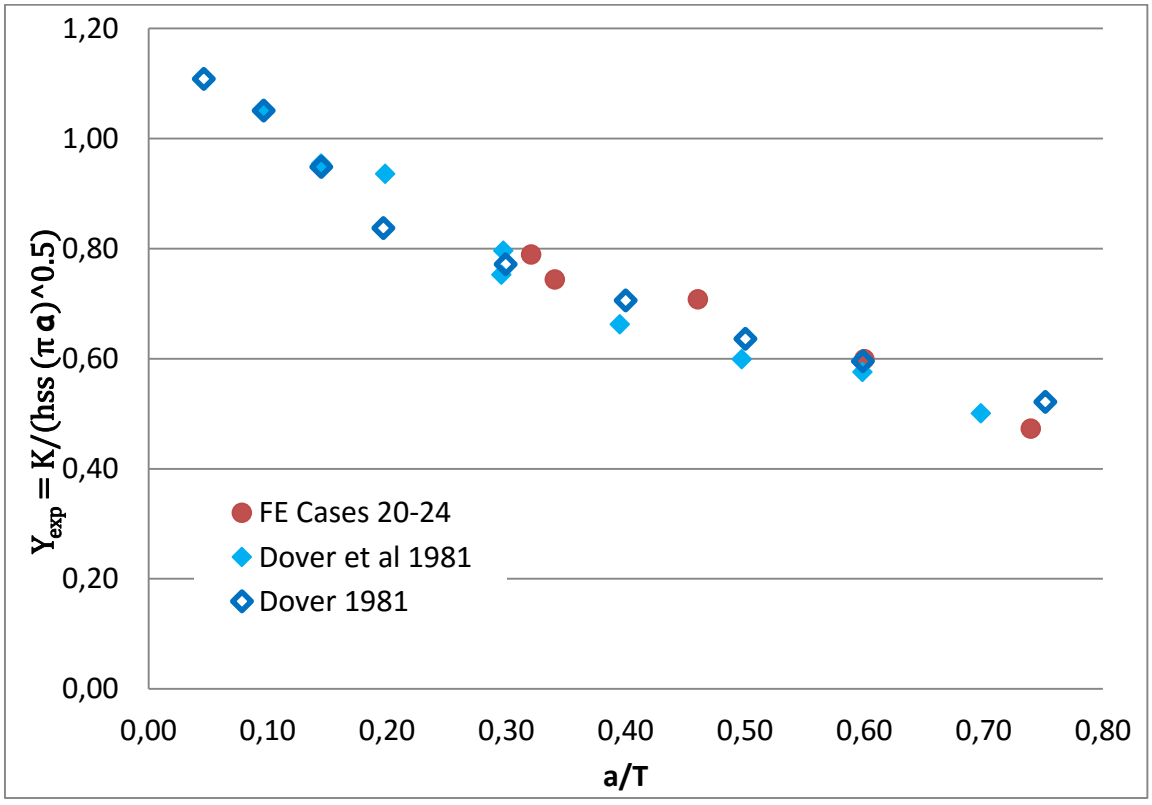

Figure 5-15 Y factors comparison.

5.3 Parametric Study

One hundred and thirteen FE models were built covering a wide range of geometrical parameter and crack profiles for data generation purposes, aiming to capture their relationship to the SIFs (see Appendix B). The chord length varies from 2200 to 7883mm. The chord diameter varies from 355.6 to 914mm, and the brace diameter varies from 114.5 to 457mm. The chord thickness varies from 11.3 to 32mm, and the brace thickness varies from 6.6 to 25.4mm. A variety of crack shapes may occur in fatigue tests on tubular welded joints; therefore, the semi-elliptical crack depth varies from 3.42 to 18.79mm, and the crack length varies from 32.7 to 216.9mm.

The parameter ranges of the models analysed are summarised in Table 5-8.

Table 5-8 Validity limits.

Geometric parameter ranges
$10 \leq \alpha \leq 25.9$
$0.25 \leq \beta \leq 0.77$
$7 \leq \gamma \leq 30.31$
$0.36 \leq \tau \leq 1.0$
$0.17 \leq a/T \leq 0.88$
$0.08 \leq a/c \leq 0.43$

This database of results has been used to derive new parametric equations for the calculation of the stress intensity modification factor for the deepest point along the crack front for a tubular T-joint under axial loading. Then the SIF may be expressed as follows:

$$K = Y\ \sigma_{nom}\ \sqrt{\pi a} \qquad \textbf{Eq. 5-71}$$

Where a is the crack depth, and σ_{nom} is the nominal stress.

The statistical package IBM SPSS [240] was used for performing both linear and non-linear multiple regression analysis. The methodology used in deriving the equations is explained in the following sections.

5.3.1 The Linear Regression Model

A first attempt was made using a linear adjustment, and the departure from normality was analysed. It was observed that the distribution for Y (the dependent variable) was skewed to the right and leptokurtic, i.e. the results with low Y values were predominant. Moreover, Case 95 seemed to be an outlier (Figure 5-16).

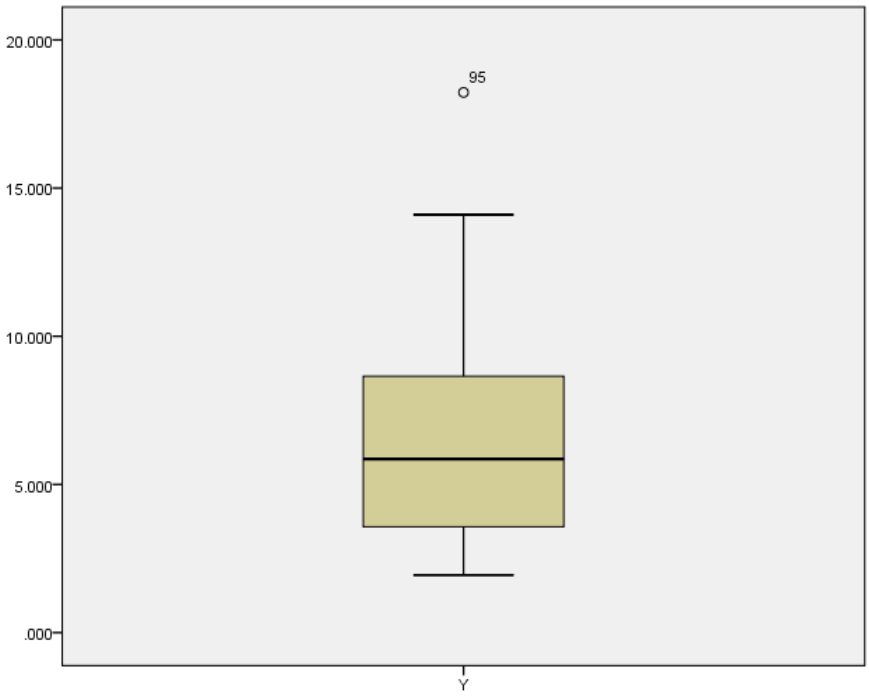

Figure 5-16 Box plot of Sample 1 (113 FE models).

Therefore, this case was not considered and the sample was randomly reduced until the explained variable followed a fairly normal distribution (p-value of the Shapiro-Wilk's test=0.052 > 0.05). The reduced sample was composed of 91 FE model results.

The chord stub slenderness ratio (α), the brace to chord diameter ratio (β), the chord wall slenderness ratio (γ), the brace to chord thickness ratio (τ), the maximum SCF using the notch stress (SCF), angle in radians where the highest SCF is located (θ), the degree of bending at the saddle (DoB), the normalised crack depth $\left(\frac{a}{T}\right)$ and half crack aspect ratio $\left(\frac{a}{2c}\right)$ were considered as independent variables, and several transformations and combinations were tested; but to meet

all the assumptions of the Linear Regression Model (see Section 3.2.2) the best alternative was of the form:

$$Y_{LINEAL} = 16.332 + 0.165\,SCF - 4.457\,\theta - 11.115\,DoB - 26.121\left(\frac{a}{2c}\right) - 3.547\left(\frac{a}{T}\right) \quad \textbf{Eq. 5-72}$$

The LSM was used for estimating the regression coefficients, as in Section 3.2.2.

The t-test (p-values < 0.05) indicates that both independent variables make a statistically significant unique contribution to the prediction, and that the intercept has to be included in the analysis. The ANOVA verifies that the explanatory variables jointly provide significant information about the response variable (F=75.52, p-value < 0.05). The multiple coefficient of determination (R^2) indicates that 90.3% of the variance in the Y factor can be predicted by a combination of the independent variables selected.

Residuals in the scatter plot are randomly dispersed (see Figure 5-17). The Shapiro-Wilk test (p-value=0.076) shows that the residuals' distribution is fairly normally distributed with skewness (-0.468, SE=0.253) and kurtosis (0.249, SE=0.5) within the span. The Durbin-Watson statistic (1.23) indicates that there is no autocorrelation. Although there is no pattern of heteroscedasticity (see Figure 5-18), the Breusch-Pagan test [320] was also used to probe it, examining that the squared residuals are not linearly related to the independent variables. The variance inflation factors are smaller than $\frac{1}{1-R^2}$ [321] showing that there is no multicollinearity problem.

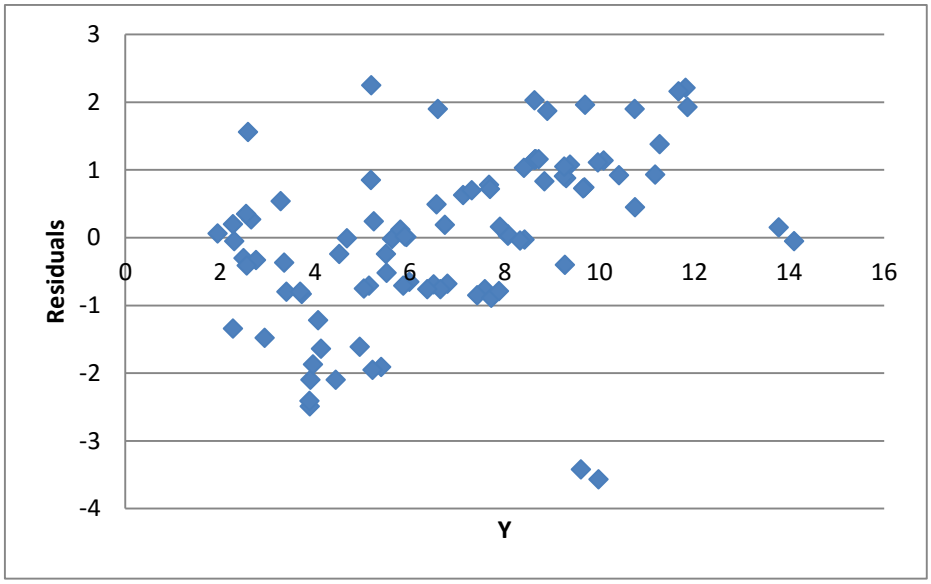

Figure 5-17 Residual Plot of the Linear Model.

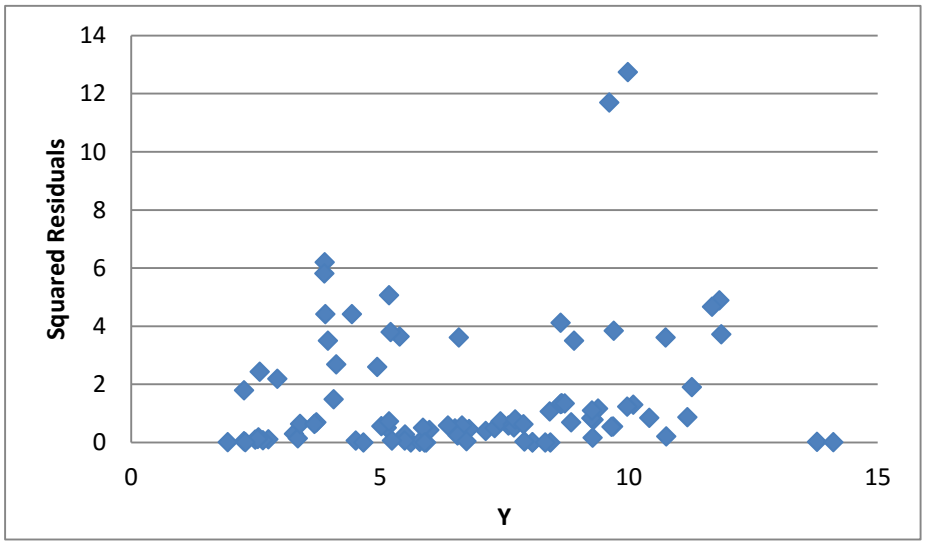

Figure 5-18 Squared Residual Plot of the Linear Model.

5.3.2 The Non-Linear Regression Models

The large-scale fatigue tests on T-joints, such as Ref. [317] and [318], show that the Y factors may be related to $\frac{a}{T}$ using a Power Regression Model, which is expressed as follows:

$$Y = C_1 \left(\frac{a}{T}\right)^{C_2} \quad \text{Eq. 5-73}$$

Therefore, the FE results were divided in different groups, depending on their geometric parameters, and their regression coefficients were derived. The results are summarised in Table 5-9.

Table 5-9 Power Regresssion Coefficients.

	C_1	C_2	Number of FE models
Group 1	4.0732	-0.482	7
Group 2	4.263	-0.653	8
Group 3	1.6354	-0.561	3
Group 4	2.2934	-0.152	4
Group 5	4.0338	-0.51	7
Group 6	5.398	-0.687	3
Group 7	2.6781	-0.308	3
Group 8	4.3511	-0.524	3
Group 9	5.1118	-0.624	3
Group 10	6.5957	-1.22	3
Group 11	1.9124	-0.425	5
Group 12	1.6652	-0.529	7
Total			56

It was checked that both C_1 and C_2 follow normal distributions. Next, it was analysed if by using linear regression analyses, both C_1 and C_2 could be related to α, β, γ, τ, SCF, θ, and DoB. Satisfying all the assumptions of the Linear Regression Model (see Section 3.2.2), the best solutions are of the form:

$$C_1 = 12.485 + 0.056\,SCF - 2.935\,\theta - 12.09\,DoB \quad \textbf{Eq. 5-74}$$

$$C_2 = -0.248 - 0.012\,SCF \quad \textbf{Eq. 5-75}$$

The coefficients of determination indicate that 95.1% and 87.8% of the variance in C_1 and C_2 can be predicted by a combination of the independent variables selected respectively. The linear regression coefficients of Eq. 5-74 and Eq. 5-75 were used as starting values for deriving the non-linear regression coefficients, considering the Y factor results of the sample formed by the 56 FE models, and the Y factor curve is formulated as:

$$Y_{NL\_1} = (15.577 + 0.071\,SCF - 3.664\,\theta - 16.23\,DoB)\left(\frac{a}{T}\right)^{-0.361-0.008\,SCF} \quad \textbf{Eq. 5-76}$$

Where 90.6% of the variance in the Y factor can be predicted by a combination of the independent variables.

The crack aspect ratio influences the Y factor values; as it was not possible to consider this parameter in the previous non-linear regression analysis, it was analysed if the residuals could be related to this. The proposed Y factor solutions considering the deviations are:

$$Y_{NL\_2} = 6.264 + (4.218 + 0.093\,SCF - 2.004\,\theta - 6.015\,DoB)\left(\frac{a}{T}\right)^{-0.717-0.005\,SCF} - 28.73\,\frac{a}{2c} \quad \textbf{Eq. 5-77}$$

$$Y_{NL\_3} = \mathrm{C}_0\left(\frac{T}{a}\right)^{-0.412-0.006\,SCF} + 6.134\left[Exp\left(\frac{a}{2c} - \mathrm{C}_0\right)\right]^{2.358} \quad \textbf{Eq. 5-78}$$

$$\mathrm{C}_0 = 18.005 + 0.078\,SCF - 4.313\,\theta - 19.51\,DoB$$

Where 94.5% of the variance in Y_{NL_2} can be predicted by a combination of the independent variables, while it is 91.2% in Y_{NL_3}.

Finally, the coefficients of Eq. 5-77 and Eq. 5-78 were used as starting values for deriving the curves of the sample formed by all the FE models (113 cases), and the proposed Y factor solutions are:

$$Y_{NL\_4} = 8.22 + (1.739 + 0.102\,SCF - 1.794\,\theta - 3.564\,DoB)\left(\frac{a}{T}\right)^{-0.751-0.003\,SCF} - 39.479\,\frac{a}{2c} \quad \textbf{Eq. 5-79}$$

$$Y_{NL\_5} = \mathrm{C}_0\left(\frac{T}{a}\right)^{0.009-0.012SCF} + 2.712\left[Exp\left(\frac{a}{2c} - \mathrm{C}_0\right)\right]^{0.761} \quad \textbf{Eq. 5-80}$$

$$\mathrm{C}_0 = 9.59 + 0.045\,SCF - 4.209\,\theta - 6.233\,DoB$$

Where 90.1% of the variance in Y_{NL_4} can be predicted by a combination of the independent variables, while it is 76.4% in Y_{NL_5}. The R-squared values have decreased, especially for the case of Y_{NL_5}, but still the reliability is higher since the number of specimens considered more than doubled (from 56 to 113).

5.4 Validity of proposed equations

Firstly, the validity of the proposed equations was assessed against the test results of Ref. [313]. The six specimens tested during this investigation were all T-shaped, large scale, tubular welded joints and were performed under axial load control, but only T1 and T2 were tested in air. The differences in the results were not very significant, thus only specimen T1 was considered, whose characteristics are summarised in Table 5-10.

Table 5-10 Specimen T1.

$\boldsymbol{\alpha}$	7.26
$\boldsymbol{\beta}$	0.71
$\boldsymbol{\gamma}$	14.28
$\boldsymbol{\tau}$	1
$\boldsymbol{Average\ brace\ weld\ leg\ length}$	24.8 mm
$\boldsymbol{Average\ chord\ weld\ leg\ length}$	12.2 mm
$\boldsymbol{SCF_{hss}}$	11.48

These parameters were used to build a new FE model in order to calculate the maximum notch SCF, its angle of location, and the DoB. The hot spot SCF was used to modify the Y factors in order to be able to calculate SIFs as a function of the nominal stress. Some discrepancies will be produced by considering average values for the weld leg lengths, since the comparison is not made between exactly the same specimens, but it helps to judge with greater understanding.

Figure 5-19 is a graphic summary of the results and facilitates the comparison between all the models. Y_{LINEAR} curve is the worst shape prediction curve, thus the non-linear regression model seems to be preferable for relating the Y factor with the independent variables. The Y_{NL_2} curve is the best shape prediction curve; the overestimation is constant along the values of the normalised crack

depth. Moreover, it is characterised by the coefficient of determination. The $Y_{\mathrm{Eq.5-73}}$, Y_{NL_1}, and Y_{NL_3} models predict the shape of the $Y_{Exp.}$ factor curve quite well, but the magnitude of the exponent is a bit higher and deviations are superior for the lowest values of a/T. This curve should have represented better the lowest side since there are no results for values of a/T exceeding 0.8. Therefore, the linear regression model is still the best alternative to relate the residuals to the crack aspect ratio. Among these three curves, Y_{NL_3} is the most deviated, although it considers the effect of the crack aspect ratio and is the one with a higher coefficient of determination. Therefore, obtaining lower deviations could be expected but improving the general agreement with the FE results does not imply improving the results of a particular specimen. The Y_{NL_4} model predicts the Y factors for normalised crack depths of less than 0.1 really well but it considerably overestimates the rest. Although its reliability is quite high, as it was derived from the largest sample and the R-squared is 0.901, further work has to be done to change the regression coefficients in order to improve the shape of the curve. The downside of the Y_{NL_5} model is that the magnitude of the exponent is low, underestimating the Y factors for normalised crack depths of less than 0.2 (while it overestimates the Y factors for normalised crack depths of more than 0.2). If a safety factor were to be applied to avoid underestimations, the overestimations would be even higher.

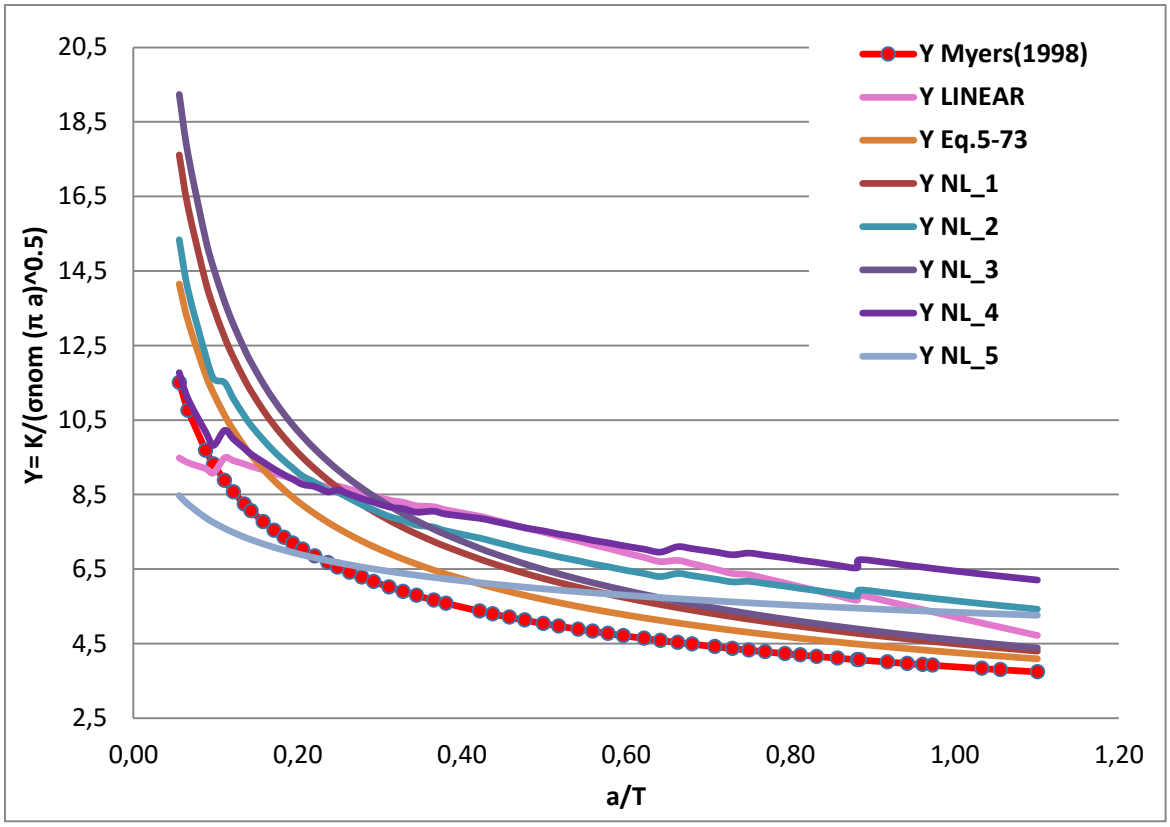

Figure 5-19 Proposed models comparison.

Lastly, the validity of the proposed equation was also evaluated by comparing the results obtained from the models defined in Section 5.1. The properties of the T-joint used for the model comparisons are summarised in below. The crack aspect ratio values were taken from Ref. [313].

Table 5-11 Tubular welded joint details.

T	16 mm
d	324 mm
β	0.71
γ	14.28
τ	1
$Brace\ weld\ leg\ length$	24.8 mm
$Chord\ weld\ leg\ length$	12.2 mm
$Average\ SCF_{HSS}$	11.24
SCF_{HSS}	11.48
SCF_{notch}	11.48
DoB	0.728
θ	0.071

As shown in Figure 5-20, it can be seen that the stress intensity modification factors calculated from the models of Section 5.1 do not agree with each other, which implies that there will be considerable discrepancies in fatigue life estimations by using the Paris equation.

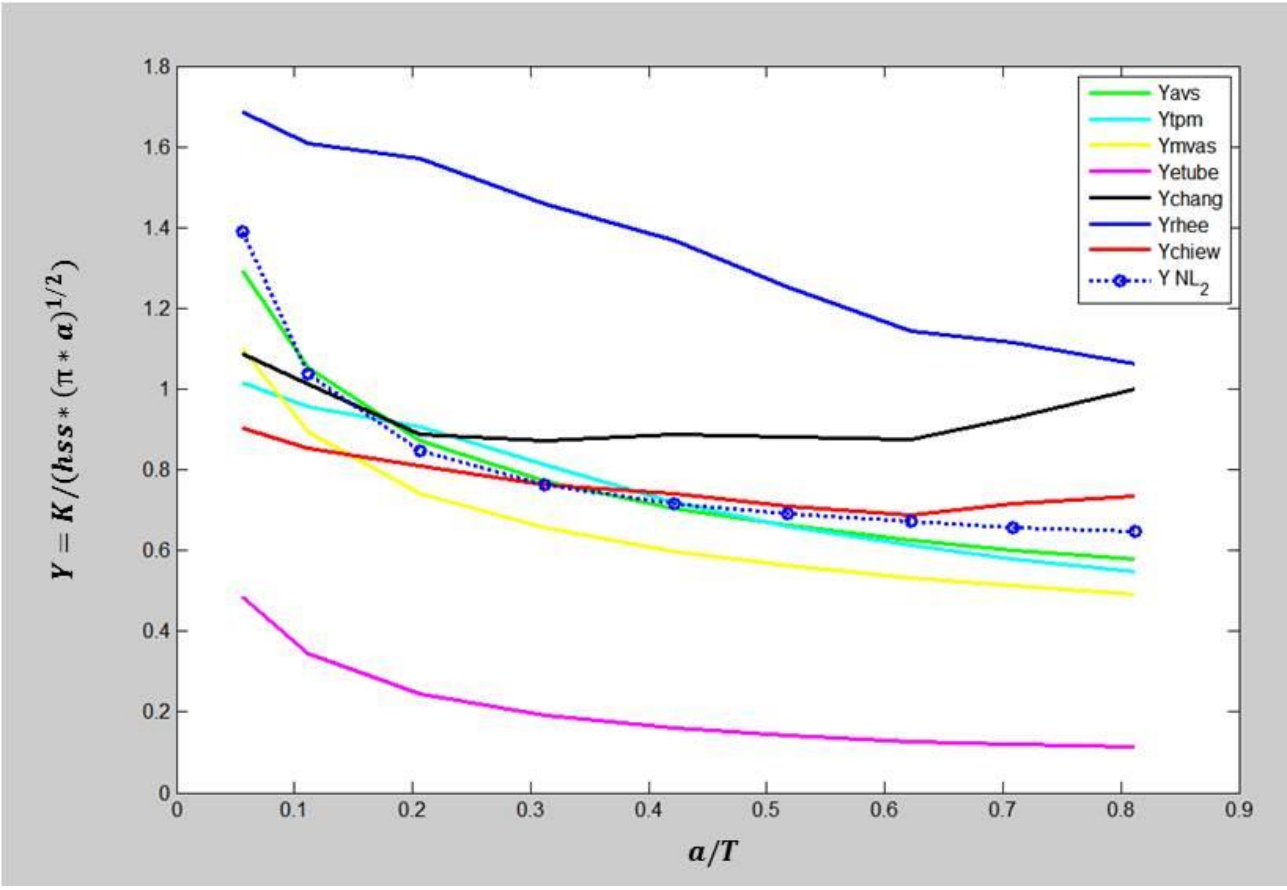

Figure 5-20 Comparison of Y factors from different models.

Rhee et al.'s model [288] is the most conservative model since it predicts the highest Y factor values (much larger than others), which agrees with previous observations made by Ref. [292]. Etube et al.'s Model [314] is the most unconservative model; the predictions are much smaller than others which suggests that employing this formulation may be unsafe. Ref. [314] noticed through fatigue tests on Y-joints that the Average Stress model, the Two-Phase model and the Modified AVS model were overestimating the Y factors; thus, some modifications were incorporated to previous models in order to derive a new equation able to predict less conservative values. However, the brace to chord

inclination angle was not incorporated into this new equation, which may have led to this underestimation.

The AVS and Modified AVS models were based on fatigue tests on T-joints with fairly similar geometry details as the geometry used for the comparison; therefore, they are considered to be the most reliable models for validation. Chiew et al.'s parametric equations [292] and Chang-Dover's parametric equations [275] do not seem to predict well the shape of the Y factor curve. Applying the Ref. [292] model could produce some underestimations for values of a/T lower than 0.15 if compared with the Modified AVS model or 0.3 with the AVS model. Using Ref. [275] could produce significant overestimations for values of a/T greater than 0.2 and especially for values around 0.8. However, the non-linear regression model proposed (Y_{NL_2}, Eq. 5-77) in this research seems to predict the shape of the Y factor curve quite satisfactorily. The Y factor results obtained from this equation are a bit more conservative than those estimated by the Modified AVS model, the small overestimation for all values of a/T being constant. Compared with the AVS model, the discrepancies of the predictions for values of a/T lower than 0.4 are almost negligible.

5.5 Concluding Remarks

Several SIF solutions for weld toe cracks in offshore tubular joints have been developed both empirically and numerically over the years since fatigue life predictions are needed both for maintenance and safety requirements. However, it was noticed that predictions derived from the different methods may not necessarily agree with each other, thus there will be significant discrepancies in fatigue life estimations using the Paris equation. Some studies do not consider the weld profile or the crack aspect ratio effects, which are key parameters. Thus, more research must be carried out in order to have a better understanding of these effects.

In order to enhance the SIF predictions and reduce the uncertainties, an exhaustive evaluation of the calculation of SIFs through complete weld profile Solid FE tubular T-joint models was performed. By mean of the convergence test,

it was shown that 20-node elements are the most favourable option to provide accurate results. The efficiency of the FE models was validated against experimental results, and then the accuracy of the proposed model assessed against experimental results and results from other models. A relationship between the maximum SCF_{notch}, θ, DoB, and SIF is confirmed. Therefore, the methodology followed is a reliable numerical approach for deriving the SIF at the deepest point of a semi-elliptical surface saddle crack in a tubular welded T-joint.

6 SYNOPSIS

6.1 Overall Summary and Conclusions

Fossil energy resources contain significant amounts of carbon that are released during combustion. In contrast to fossil fuels and nuclear power, wind power is considered to be a ‘carbon neutral’ technology since it does not emit CO_2 during wind turbine operation. However, its popularity has always fluctuated with the price of fossil fuels, since nowadays wind electricity production cannot compete with nuclear or coal electricity production. The electricity production cost is derived as the sum of all the capital expenditure cost and the operational expenditure cost over the service life of the project, divided by the total energy output of the project. Therefore, maximising electricity production, minimising costs, and extending the effective service life are the key challenges in order to make the wind industry more economically efficient.

The higher wind speed of the marine environment, unrestricted space, and lower social impact are increasing the interest in offshore wind energy. The trend is to move further away from the coast into deeper waters and install higher capacity machines; thus affecting installation, foundations and O&M costs. Therefore, lowering the costs is likely to be the greatest challenge, since this involves optimising every stage of development, manufacture, installation, and operation in order to reduce both the capital and operational expenditure. Support structures account for a great percentage of a project's total cost and are thought to be one of the main drivers for reducing costs. Foundations and towers should be fit for purpose, extending their effective service life but avoiding costs of oversizing. There must be a balance between design reliability and cost reduction.

The fatigue strength assessment is crucial for estimating the service life of offshore tubular welded joints, both in the design stage, through the S-N Approach, and the in-service stage by the LEFM Approach. The experience in offshore oil and gas installations has been utilised when applying these

approaches to offshore wind energy, but through the research work in these areas it has been observed that it leads to over-conservationism.

During the exhaustive review undertaken in the Third Chapter, of the HSS design S-N curves recommended by the different standards, it was noticed that:

Both Girth Weld and Tubular Joint S-N curves have been developed using best judgement by leading specialists, but for Offshore Wind Support Structures, the curves are based on unrepresentative tests on a range of samples with varying degrees of quality control and reporting. For instance, Girth Weld S-N curves are based on small diameter tubulars likely to be more affected by misalignment than the larger diameter girth welds encountered in offshore wind applications. Specimens need to be as representative as possible of the true situation. It is not always possible to test full-scale geometries and the evidence is that the choice of fatigue test specimen is critical to the resulting S-N curve. The most influential aspects are: parent material, welding specification, loading and boundary conditions, plate thickness, misalignment, residual stresses, and environmental conditions. On the other hand, the most fatigue test data were obtained in the late 1990s; and the steel grades, welding processes, and flaw detection processes have greatly advanced since then. Therefore, they are not fit for cost effective design optimisation.

All the design curves were taken to be that corresponding to a 2.3% probability of failure (two standard deviations of $logN$ below the mean) in order to account for the uncertainties in life associated with material, loading, and environmental conditions, which seems to provide too conservative predictions considering that the risks and the safety requirements of offshore wind farms are not the same as for offshore oil and gas platforms. A slight increase in the probability of failure by changing the fatigue design curve margins could lead to a major decrease in investment costs.

There are large differences in predicting the fatigue life of Girth Welds, depending on the standard or guide selected as reference. These differences could even be superior to 50% in the functioning of the weldment characteristics, the thickness and stress range. DNV Flush Ground and As-welded Curves are the most

conservative of all currently used design curves for Girth Welds. Both BS and DNV curves seem to be on the safe side in the low-cycle regime for the available data from fatigue tests on full-scale girth welds; however, even they might be considered too conservative and it might be possible to consider an S-N curve for 84.1% probability of survival (one standard deviation of $logN$ below the mean). However, it is not possible to judge BS and DNV curves with respect to the high-cycle regime because of the lack of data. Both flush ground and as-welded fatigue test data have generally been obtained for the low-cycle regime, so fatigue tests with lower stress ranges would be required for assessing the fatigue limits. Furthermore, it is inappropriate to apply the Thickness Correction factor for the Flush Ground Girth Welds, and its formulation for the rest of the weldment configurations is debatable.

The T' Curve used for predicting the fatigue life of Tubular Joints is not the most accurate fit that may be obtained through the regression analysis of the available data. It was proved that the lifespan predictions are impaired by failing to distinguish between the different types of joint configuration and applied loads. As happens with the Girth Weld curves, fatigue tests for the high-cycle regime would be required for assessing the fatigue limits. Even without considering the circumstances; the RC 4, which was derived in Section 3.2.2.2 using the largest sample size and considering both stress range and thickness as explanatory variables, provides more accurate predictions than the T' curve. Therefore, it is more convenient to incorporate the chord thickness effect as an explanatory variable from the beginning of the regression analysis, rather than to apply a Thickness Correction Factor later. The residual analysis indicates that it may be appropriate to divide the data in groups depending on the stress range in order to incorporate more than two changes of slope and decrease the deviations. Moreover, it is not evident that the logarithmic transformation is the best transformation for the regression analysis in all the stress ranges.

Over the years much research has been carried out towards the estimation of the HSS range by means of the SCF. The Fourth Chapter reviews the existing SCF parametric equations for tubular T-joints. Some empirical equations were based

on the strain gauge measurements of numerous tests on tubular joints under the three principal modes of loading – axial, IPB and OPB. All those tests however, did not consider the geometry of the weld profile. The HSSs were derived following DEn recommendations, using maximum principal stresses from outside the notch zone. The high costs of testing scaled steel models led most of the studies to use shell FE models for deriving the SCF parametric equations for all three load cases. These studies measured the stresses at the mid-section of the brace-chord intersection without considering the effect of a weld fillet; except for the Efthymiou & Durkin's models, where welds were modelled using three-dimensional 16 node shell elements in the brace and the chord, and eight node shell elements in the weld regions. The stresses in that publication were obtained by extrapolating maximum principal stresses to the weld toes in accordance with DEn recommendations.

A comparison between the fatigue life predictions obtained by the Efthymiou & Durkin's SCFs and the HS SCFs of 3D solid FE models considering the weldment was performed. The validation of the 3D solid FE models with the weldment was carried out by analysing the results obtained by 3D solid and 3D shell FE models without the weldment, as they were used in obtaining the existing parametric equations. The SCF_{HS} values of the complete weld profile FE models are lower than the Efthymiou & Durkin's SCFs. In order to know to what extent the slight variations on the SCF values affect the fatigue life predictions, an assessment using the HSS T' curve was carried out. The results clearly showed that even slight overestimations of the SCFs will represent a great reduction on service lives (even differences over 100 years), since the scale is logarithmic. This reduction in the service life affects the design, i.e. structures would be oversized. Aiming to observe how these under-predictions of the service life affect investment costs, the chord thickness was reduced until the SCFs of the complete profile solid FE model reached approximately the same values as Efthymiou & Durkin's SCFs for the previous thickness. The total reduction of the T-joint was 12.24%, and assuming that this reduction is representative for all the different joint intersections, it was observed that approximately 0.9% of the investment costs per MW could be saved.

All the existing parametric equations agree that for a T-joint subjected to axial loading with all the geometric ratios within the limits shown in Table 4-9, the maximum stress concentration is located at the saddle (θ = 0º); however, it has been observed that some of the models do not satisfy this. By modelling different weld profiles, it was proved that the weld profile may greatly impact on both the position and the value of the highest stress concentration. An increase in weld size favours the reduction of stress concentration. The most critical parameter is the weld angle; increasing it brings a stress concentration decline and moves its location away from the saddle.

For the complete weld profile of solid FE models, both hot spot and notch stresses may be used to calculate the SCFs. Generally notch SCFs are higher than hot spot SCFs, although the increase is not proportional. Selecting the HSS as a reference could lead to designing a structure very conservatively, since applying safety factors when the notch SCF is smaller than the hot spot SCF will produce a very high overestimation.

Therefore, the existing parametric equations for predicting hot spot SCFs are not accurate, very conservative and not useful for optimisation. SCFs should be carried out by modelling solid joints which include the weldment, and should be based on notch stresses measured on the external surface at the weld toe, since slight overestimations of the SCFs represent a great reduction in predicated service lives.

Once it was proved that the design stage could be improved, the in-service stage was assessed. Cracks may compromise the integrity of the structure and crack growth estimations are needed for maintenance and safety requirements. Numerous studies have been carried out for assessing and modelling the uncertainty in fatigue crack growth in tubular joints. The Fifth Chapter gives a review of the main SIF solutions for weld toe cracks in offshore tubular joints, which were developed empirically or numerically (or by a combination of these approaches). It was observed that estimations calculated by the different models may not necessarily agree with each other, which indicates that there will be significant discrepancies in fatigue life estimations using the Paris equation. In

order to improve the SIF predictions and reduce the uncertainties a comprehensive evaluation of the calculation of SIFs through complete weld profile Solid FE tubular T-joint models was performed. The efficiency of the FE models was validated against the experimental results. By mean of the convergence test, it was proved that 20-node elements are the most favourable option, since 8-node elements do not provide accurate results, reinforcing the conclusion that the parametric equations derived by 8-node shell elements cannot be precise. A regression analysis of the computed results was performed to produce a new SIF parametric equation for the deepest point of a semi-elliptical surface crack at the saddle of tubular welded joints, as a function of the maximum SCF (derived considering the notch stress), the angle in radians where the highest SCF is located, the DoB at the saddle, the normalised crack depth, the crack aspect ratio, and the nominal stress. Then the predictions from this new equation were validated against experimental results and results from other models. The number of FE models used for the derivation were not overly large, therefore the reliability is limited. However, it has been proved that the methodology followed is a reliable numerical approach for deriving SIFs.

As a summary, the conclusions have been classified within the following two groups:

<u>Major conclusions</u>

- It is possible to achieve a good compromise between design reliability and capital and operational expenditure reduction in order to enhance the competitiveness of the Offshore Wind industry, by optimising the approaches used both in the design and in-service stages.
- The weld profile may greatly impact on both the position and the value of the highest stress concentration. An increase in weld size favours the reduction of stress concentration.
- The existing parametric equations for predicting hot spot SCFs are not accurate, very conservative and not useful for optimisation.

- SCFs should be carried out by modelling solid joints which include the weldment, and should be based on notch stresses measured on the external surface at the weld toe.
- The existing models for estimating SIFs do not necessarily agree with each other, which implies significant discrepancies in fatigue life estimations using the Paris equation.
- The SIF parametric equation for the deepest point of a semi-elliptical surface crack at the saddle of tubular welded joints under axial loading based on the maximum SCF_{notch}, θ, DoB, $\frac{a}{T}$ and $\frac{a}{2c}$, and derived from 3D solid FE models, produces accurate results. Therefore, the methodology followed is a reliable numerical approach for predicting SIFs.

Minor conclusions

- Both Girth Weld and Tubular Joint S-N curves are generally based on unrepresentative tests for Offshore Wind Support Structures.
- The fatigue limits are not clearly defined, since both Girth Weld and Tubular Joint fatigue test data were mostly obtained for the low-cycle regime.
- The fatigue design curve margins seem to be a source of conservatism.
- There are large differences in predicting the fatigue life of Girth Welds depending on the standard or guide selected as reference. All of them seem to be on the safe side; therefore, selecting the most conservative standard will lead to oversizing.
- It is inappropriate to apply the Thickness Correction factor to the Flush Ground Girth Welds and its formulation for the rest of the weldment configurations is debatable.
- The lifespan predictions of the T' curve are impaired by failing to distinguish between the different types of joint configuration and applied loads.
- It is convenient to incorporate the chord thickness effect as an explanatory variable from the beginning of the regression analysis, and it may be

appropriate to divide the data into groups, depending on the stress range, in order to incorporate more than two changes of slope.

- Even slight overestimations of the SCFs will represent a great reduction in service lives (even differences over 100 years), and will increase the investment costs.
- 8-node elements do not provide accurate results for estimating SCFs or SIFs.

6.2 Recommendations for Future Research

Following the conclusions of this research, it is appropriate to outline the purposes derived from it:

- To update the current Girth Weld and Tubular Joint S-N curves in air and seawater environment testing specimens more representative of the Offshore Wind Support Structures. Considering both low and high-cycle regimes to have a better understanding of the fatigue limits.
- To derive new S-N curves for the different joint configurations, and modes of loading.
- To incorporate the WT as an independent variable in the S-N curve, rather than apply the Thickness Correction Factor, in order to improve accuracy.
- Future analysis of the S-N curves should take into account the change of the slope in more than two sections, aiming to avoid great deviations.
- To assess the appropriate design margins for the development of design curves from mean data curves.
- To derive new notch SCF parametric equations considering the weld profile effect for each type of joint configuration and mode of loading.
- To derive new equations able to predict the maximum stress concentration location.
- To relate the HSS with the notch stress, to make compatible the use of the S-N curves and the SCF parametric equations.
- To extend the validity range of the SIF parametric equation, even considering shorter cracks.

- To increase the reliability of the SIF parametric equation by including more FE models.
- To derive new SIF parametric equations for each type of joint configuration and mode of loading.
- To derive standard solutions for modes II and III equivalent to that for mode I.
- To consider the characteristics of multiple axes of loading.

REFERENCES

1. Schwartz, P. Energy Strategy for the Future. Energy Star. Available from: http://www.energystar.gov/buildings/about-us/research-and-reports/energy-strategy-future [Accessed: 24 July 2015]

2. Conti, J. and Holtberg, P. (2011) International Energy Outlook 2011. Available from: http://www.eia.gov/forecasts/ieo/pdf/0484(2011).pdf [Accessed: 19 December 2011]

3. International Energy Agency (2011) WORLD ENERGY OUTLOOK 2011 FACTSHEET. How will global energy markets evolve to 2035? Available from: http://www.aplng.com.au/pdf/World_Energy_Outlook_2011_factsheet.pdf [Accessed: 21 July 2015]

4. IPCC (2007) Fourth Assessment Report: Climate Change 2007. 4.3.1 Fossil fuels. Available from: https://www.ipcc.ch/publications_and_data/ar4/wg3/en/ch4s4-3-1.html [Accessed: 14 July 2015]

5. Think Global Green (2008) Methane. Available from: http://www.thinkglobalgreen.org/METHANE.html [Accessed: 5 July 2015]

6. Tans, P. and Keeling, R. Trends in Atmospheric Carbon Dioxide. Earth System Research Laboratory. Available from: http://www.esrl.noaa.gov/gmd/ccgg/trends/ [Accessed: 8 July 2015]

7. The White House. Climate Change Over the Next 100 Years. Available from: http://clinton5.nara.gov/Initiatives/Climate/next100.html [Accessed: 25 July 2015]

8. Climate Change — Adapting to The Impacts, by Communities in Northern Peripheral Regions. Available from: http://www.clim-atic.org/about%20climate%20change%20adaptation.html [Accessed: 18 July 2015]

9. Australian Academy of Science (2004) Getting into hot water – global warming and rising sea levels. Available from: https://www.science.org.au/node/35454#.VbM4ZPmqpBc [Accessed: 9 July 2015]

10. Smith, K.R.; Corvalán, C.F. and Kjellström, T. (1999) How much global ill health is attributable to environmental factors? Epidemiology 10(5): 573-584.

11. Starfelt, N. and Wikdahl, C-E. Economic Analysis of Various Options of Electricity Generation. Available from: http://manhaz.cyf.gov.pl/manhaz/strona_konferencja_EAE-2001/15%20-%20Polenp~1.pdf [Accessed: 18 January 2012]
12. BBC (2014) Kyoto Protocol. Available from: http://www.bbc.co.uk/climate/policies/kyoto.shtml [Accessed: 20 July 2015]
13. European Commission (2010) Citizens' summary. EU climate and energy package. Available from: http://ec.europa.eu/clima/policies/package/docs/climate_package_en.pdf [Accessed: 2 June 2015]
14. European Science Foundation (2010) Marine Renewable Energy. Research Challenges and Opportunities for a new Energy Era in Europe. Available from: http://www.esf.org/fileadmin/Public_documents/Publications/MB_vision_document2.pdf [Accessed: 25 June 2015]
15. Gilmartin, M. (2010) The economics of marine energy in Scotland & the UK. Forum on Economics of Marine Renewable Energy, HMRC, UCC, Cork.
16. Straub, D. (2004) Generic approaches to risk based inspection planning for steel structures. Institute of Structural Engineering, Swiss Federal Institute of Technology, ETH Zürich. Available from: http://e-collection.library.ethz.ch/eserv/eth:1550/eth-1550-01.pdf [Accessed: 25 May 2015]
17. Department of Energy (1984) Offshore Installations: Guidance on Design and Construction. Her Majesty's Stationery Office, London.
18. Kuang, J.G.; Potvin, A.B. and Leick, R.D. (1975) Stress concentration in tubular joints. Offshore Technology Conference, OTC 2205, pp. 593-612, Houston, Texas.
19. Pilkey, W.D. and Pilkey, D.F. (2008) Peterson's stress concentration factors. 3rd Ed. John Wiley and Sons, Hoboken, New Jersey.
20. Chryssanthopoulos, M.K. and Righiniotis, T.D. (2006) Fatigue reliability of welded steel structures. Journal of Constructional Steel Research 62 (11): 1199-1209.

21. Chang, E. (1997) Parametric Study for Non-Destructive Fatigue Strength Evaluation of Offshore Tubular Welded Joints. PhD Thesis, Department of Mechanical Engineering, UCL, London.
22. Austin, J.A. (1995) The role of corrosion fatigue crack growth mechanisms in predicting the fatigue life of offshore tubular joints. PhD Thesis, Department of Mechanical Engineering, UCL, London.
23. Dover, W.D. and Petrie, J.R. (1976) In-Plane Bending Fatigue of a Tubular Welded T Joints. Proc. Int. Conf. on Fatigue Testing and Design, SEE, Vol. 1, Paper 19, London.
24. Brennan, F. (1992) Fatigue and Fracture Mechanics Analysis of Threaded Connections. PhD Thesis, Department of Mechanical Engineering, UCL, London.
25. Potter, J. and Watanabe, R. (1989) STP1006 Development of Fatigue Loading Spectra, ASTM special technical publication.
26. Pook, L. (1975) Analysis and Applications of Fatigue Crack Growth Data. The Journal of Strain Analysis for Engineering Design 10: 242-250.
27. Miner, M.A. (1945) Cumulative Damage in Fatigue. Journal of Applied Mechanics 67: A159-A164.
28. Pook, L.P. (1983) The role of crack growth in metal fatigue. National Engineering Laboratory, East Kilbride, Metals Society, Glasgow.
29. Griffith, A.A. (1921) The phenomena of rupture and flow in solids. Philosophical Transactions of the Royal Society of London, Series A, Vol.221, pp. 163–198, London.
30. Griffith, A.A. (1925) The theory of rupture. Proc. 1st Int. Cong. on Applied Mechanics. pp. 55-63, Ed Bienzo and Burgers, Waltman.
31. Inglis, C.E. (1913) Stresses in a plate due to the presence of cracks and sharp corners. Transactions of the Institute of Naval Architects, Vol. 55, pp.219-241.
32. Irwin, G.R. (1948) Fracture dynamics. Fracturing of Metals, pp. 147-166, American Society for Metals, Cleveland.
33. Orowan, E. (1948) Fracture and strength of solids. Report on Progress in Physics, XII, pp.185-232.

34. Irwin, G.R. (1956) Onset of fast crack propagation in high strength steel and aluminium alloys. Proc. 2nd Sagamore Ordnance Materials Conference, Vol.2, pp.289-305.
35. Irwin, G.R. (1957) Analysis of stresses and strains near the end of a crack traversing a plate. Journal of Applied Mechanics 24: 361–64.
36. Monahan, C.C. (1995) Early Fatigue Crack Growth at Welds. Computational Mechanics Publications, Southampton, UK.
37. Macdonald, K.A. (2011) Fracture and fatigue of welded joints and structures. Woodhead Publishing, Cambridge.
38. Stephens, R.I.; Stephens, R.R. and Fuchs, H.O. (2001) Metal Fatigue in Engineering. 2nd Ed. John Wiley & Sons, Canada.
39. Paris, P. and Erdogan, F. (1963) A critical analysis of crack propagation laws. Journal of Basic Engineering, Series D, 85(4): 528-534.
40. International Institute of Welding (1995) Stress Determination for Fatigue Analysis of Welded Components. Abington Publishing, Cambridge.
41. Rooke, D.P.; Baratta, F.I. and Cartwright, D.J. (1981) Simple methods of determining stress intensity factors. Engineering Fracture Mechanics 14(2): 397-426.
42. Kam, J.CP. (1989) Structural Integrity of Offshore Tubular Joints. PhD Thesis, Department of Mechanical Engineering, UCL, London.
43. Murakam, Y. (1987) Stress Intensity Factors Handbook. Pergamon Press, Oxford.
44. Rooke, D.P. and Cartwright, D.J. (1976) Compendium of stress intensity factors. HMSO, London.
45. Westergaard, H.M. (1934) Stresses at a crack, size of the crack and the bending of reinforced concrete. Proc. of the American Concrete Institute, Vol. 30, pp.93-102.
46. Westergaard, H.M. (1937) Bearing pressures and cracks. Journal of Applied Mechanics 6: A.49-A.53.
47. Smith, F.W.; Emery, A.F. and Kobayashi, A.S. (1967) Stress intensity factors for semi-circular cracks, Part 2 Semi-infinite solid. Journal of Applied Mechanics 34: 953-959.

48. Theocaris, P. S. (1970) Local yielding around a crack tip in Plexiglas. Journal of Applied Mechanics 37: 409–415.
49. Gross, B.; Srawley, J.E. and Brown, W.F. (1964) Stress intensity factors for a single edge-notch tension specimen by boundary collocation of a stress function. NASA TN-D2395.
50. Duddear, T.D. and Gorman, H.J. (1973) The determination of mode I stress-intensity factors by holographic interferometry. Experimental Mechanics 13: 145-149.
51. Muskhelishvili, N.I. (1953) Some basic problems of the mathematical theory of elasticity. Noordhooff International, Leyden.
52. Nisitani, H. (1968) Two-dimensional stress problem solved using electric digital computer. Bulletin of Japan Society of Mechanical Engineers, Vol. 11, pp. 14-23.
53. Liu, H. W. and Ke, J. S. (1973) Chapter 4 Moire Method. Experimental Techniques in Fracture Mechanics. SESA. Ames, Iowa State University Press, pp.111-165. In: Tseng, C-G. (1985) A crack closure study on 2024 T351 aluminum alloy in the Moire method. PhD Thesis, Iowa State University.
54. Rooke, D.P. (1986) An improved compounding method for calculating stress-intensity factors. Engineering Fracture Mechanics 23: 783-792.
55. Gdoutos, E. E. and Theocaris, P. S. (1978) A photoelastic determination of mixed-mode stress intensity factors. Experimental Mechanics 18: 87-96.
56. Eshelby, J.D. and Bilby, B.A. (1968) Dislocations and the theory of fracture. In: Maugin, G.A. (2013) Continuum Mechanics Through the Twentieth Century - A Concise Historical Perspective. Springer.
57. Bonesteel, R. M.; Pipers, D. E. and Davinroy, A. T. (1978) Compliance and calibration of double cantilever beam (DCB) specimens. Engineering Fracture Mechanics 10: 425-428.
58. Quinlan, P.M. (1964) The torsion of an irregular polygon. Proc.Roy.Soc. Vol.282A. In: Aliabadi, M.H. and Rooke, D.P. (1991) Numerical fracture mechanics. Computational Mechanics Publications, Southampton, U.K.

59. Dally, J.W. and Berger, J. R. (1993) The role of the electrical resistance strain gauge in fracture research. Experimental techniques in fracture mechanics III, Society for Experimental Mechanics, pp.1-39.
60. Chan, S.K.; Tuba, I.S. and Wilson, W.K. (1970) On the Finite Element Method in Linear Fracture Mechanics. Engineering Fracture Mechanics 2: 1-17.
61. Mavrothanasis, F.I. and Pavlou, D.G. (2007) Mode-I stress intensity factor derivation by a suitable Green's function. Engineering Analysis with Boundary Elements 31: 184-190.
62. Sneddon, I.N. (1972) The Use of Integral transforms. McGraw-Hill, New York.
63. Liskovets, O.A. (1965) The method of lines. Differential equations 1: 1308-1323.
64. Bergan, P.G. and Aamodt, B. (1976) On the principle of superposition for stress intensity factors. Engineering Fracture Mechanics 8: 437-440.
65. Bueckner, H. (1970) A novel principle for the computation of stress intensity factors. ZAMM - Journal of Applied Mathematics and Mechanics 50:529-546.
66. Rice, J.R. (1972) Some remarks on elastic crack-tip stress field. International Journal of Solids and Structures 8: 751-758.
67. Shih, C.F.; deLorenzi, H.G. and German, M.D. (1976) Crack extension modeling with singular quadratic isoparametric elements. International Journal of Fracture 12: 647–651.
68. Hinto, E. and Campbell, J. (1974) Local and global smoothing of discontinuous finite element function using a least squares method. International Journal for Numerical Methods in Engineering 8: 461-480.
69. Morais, A.B. (2007) Calculation of stress intensity factors by the force method. Engineering Fracture Mechanics 75: 739-750.
70. Pu, S.; Hussain, M. and Lorensen, W. (1978) The collapsed cubic isoparametric element as a singular element for crack problems. International Journal for Numerical Methods in Engineering 12: 1727-1742.
71. Wen, P.H.; Aliabadi, M.H. and Rooke, D.P. (1995) A contour integral for the evaluation of stress intensity factors. Applied Mathematical Modelling 19: 450-455.

72. Nikishkov, G.P. and Atluri, S.N. (1987) Calculation of fracture mechanics parameters for an arbitrary three-dimensional crack, by the equivalent domain integral method. International Journal for Numerical Methods in Engineering 24: 1801-1821.

73. Rice, J.R. (1968) A path independent integral and the approximate analysis of strain concentration by notches and cracks. Journal of Applied Mechanics 35: 379-386.

74. Parks, D.M. (1974) A stiffness derivative finite element technique for determination of crack tip stress intensity factors. International Journal of Fracture 10: 487-502.

75. Shivakumar, K.N.; Tan, P.W. and Newman, Jr. J.C. (1988) Virtual crack-closure technique for calculating stress intensity factors for cracked three dimensional bodies. International Journal of Fracture 36: 43-50.

76. Chow, W.T. and Atluri, S.N. (1995) Finite element calculation of stress intensity factors for interfacial crack using virtual crack closure integral. Computational Mechanics 16: 417-425.

77. ABAQUS (2013) Abaqus/CAE User's Manual, v. 6.13. Dassault Systémes Simulia Corp., Providence, RI, USA.

78. Irwin, G.R. (1958) Fracture. Handbuch der Physik/Encyclopedia of Physics, Vol. 3/6, pp. 551-590.

79. Rybicki, E.F. and Kanninen, M.F. (1977) A finite element calculation of stress intensity factors by a modified crack closure integral. Engineering Fracture Mechanics 9: 931-938.

80. Fawaz, S.A. (1998) Application of the virtual crack closure technique to calculate stress intensity factors for through cracks with an elliptical crack front. Engineering Fracture Mechanics 59: 327–342.

81. Wang, X.; Penel, G.; Swearingen, S.; Aune, R.; Kan,W.; and Fu, L. (2015) Reliability-Based Fracture Mechanics Approach to Fatigue Design of Julia Flowline. The Twenty-fifth International Offshore and Polar Engineering Conference; Kona, Hawaii, USA. International Society of Offshore and Polar Engineers.

82. Singh, R.P. and Gupta, A. (1988) S-N curve vs fracture mechanics approach to fatigue analysis of steel jacket platforms, International Journal of Fatigue 10(1): 49-53.
83. Sørensen, J.D. and Toft, H.S. (2010) Probabilistic Design of Wind Turbines, Energies 3: 241-257.
84. DNV (2014) DNV-OS-J101 OFFSHORE STANDARD. Design of Offshore Wind Turbine Structures. Det Norske Veritas, Norway.
85. Sørensen, J. (2004) Notes in Structural Reliability Theory And Risk Analysis, Aalborg University.
86. Zienkiewicz, O.C.; Taylor, R.L. and Zhu, J.Z. (2013) The Finite Element Method: its Basis and Fundamentals. 7th Ed. Elsevier Ltd, Oxford.
87. Cook, R.D. (1995) Finite Element Modeling for Stress Analysis. John Wiley & Sons, New York.
88. Heinrich, J.C. and Pepper, D.W. (1999) The Intermediate Finite Element Method: Fluid Flow And Heat Transfer Applications. Taylor & Francis, New York.
89. ABAQUS (2012) Abaqus 6.12 Analysis User's Manual. Volume IV: Elements. Dassault Systémes Simulia Corp., Providence, RI, USA.
90. Dvorak, P. (2011) Global offshore wind market could be 80 GW by 2020. Wind Power Engineering and Development. Available from: http://www.windpowerengineering.com/construction/offshore-renewable-energy-to-2020-a-report/ [Accessed: 12 July 2015]
91. Lozano-Minguez, E.; Kolios, A.J. and Brennan, F.P. (2011) Multi-criteria assessment of offshore wind turbine support structures. Renewable Energy 36: 2831-2837.
92. Department for Business Enterprise & Regulatory Reform (2008) Review of reef effects of offshore wind farm structures and potential for enhancement and mitigation. Available from: http://webarchive.nationalarchives.gov.uk/+/http://www.berr.gov.uk/files/file43528.pdf [Accessed: 02 July 2015].
93. GlobalData (2014) Global Cumulative Wind Power Capacity to More than Double by 2020, Led by China, says GlobalData. Available from: http://energy.globaldata.com/media-center/press-releases/power-and-

resources/global-cumulative-wind-power-capacity-to-more-than-double-by-2020-led-by-china-says-globaldata [Accessed: 12 July 2015]
94. University of Strathclyde (2012) Papers of James Blyth. Available from: http://www.strath.ac.uk/archives/iotm/march2012/ [Accessed: 29 June 2015]
95. TelosNet Web Development (2002) Part 2 - 20th Century Developments. Available from: http://telosnet.com/wind/20th.html [Accessed: 29 May 2015]
96. Jeffrey La Favre (1998) The Brush Mansion and Family Life. Available from: http://www.lafavre.us/brush/mansion.htm [Accessed: 29 May 2015]
97. Oxford Dictionary of National Biography (2009) Blyth, James (1839-1906). Available from: http://www.oxforddnb.com/view/article/100957 [Accessed: 10 April 2015]
98. Warnes, K. Poul La Cour pioneered windmill power in Denmark. History? Because it's here! Available from: http://windowstoworldhistory.weebly.com/poul-la-cour-pioneered-wind-power-in-denmark.html [Accessed: 29 June 2015]
99. The Guardian (2008) Timeline: The history of wind power. Available from: http://www.theguardian.com/environment/2008/oct/17/wind-power-renewable-energy [Accessed: 29 June 2015]
100. Wind Charger. The Jacobs Wind Electric Company. Available from: http://www.windcharger.org/Wind_Charger/Jacobs_Wind_Electric_Co..html [Accessed: 30 June 2015]
101. Hoose, S. (2011) Wind power propels family's trade. Available from: http://www.jacobswind.net/wp-content/uploads/2011/02/Minneapolis-Star-1982.pdf [Accessed: 30 June 2015]
102. Schelbergen, M. (2013) Structural Optimization of Multi-Megawatt, Offshore Vertical Axis Wind Turbine Rotors. Available from: http://www.lr.tudelft.nl/fileadmin/Faculteit/LR/Organisatie/Afdelingen_en_Leerstoelen/Afdeling_AEWE/Wind_Energy/Education/Masters_Projects/Finished_Master_projects/doc/Mark_Schelbergen_r.pdf [Accessed: 15 July 2015]
103. U.S. Department of Energy. History of Wind Energy. Available from: http://energy.gov/eere/wind/history-wind-energy [Accessed: 30 June 2015]

104. Cory, K.; Couture, T. and Kreycik, C. (2009) Feed-in Tariff Policy: Design, Implementation, and RPS Policy Interactions. Available from: http://www.nrel.gov/docs/fy09osti/45549.pdf [Accessed: 01 July 2015]
105. Cory, K.; Couture,T.; Kreycik,C. and Williams,E. (2010) A Policymaker's Guide to Feed-in Tariff Policy Design. Technical Report, National Renewable Energy Laboratory, Colorado, USA. Available from: http://www.nrel.gov/docs/fy10osti/44849.pdf [Accessed: 01 July 2015]
106. U.S. Department of Energy (2011) Historic Wind Development in New England: The Age of PURPA Spawns the "Wind Farm". Available from: https://archive.today/oAc5 [Accessed: 30 June 2015]
107. Wind Energy Center (2014) Alumni and the Early Wind Industry. Available from: http://www.umass.edu/windenergy/about.history.alumni.php [Accessed: 30 June 2015]
108. Kaldellis, J.K. and Zafirakis, D. (2011) The wind energy (r)evolution: A short review of a long history. Renewable Energy 36: 1887-1901.
109. European Wind Energy Association (2009) Pure Power, Wind energy targets for 2020 and 2030. Available from: http://www.ewea.org/fileadmin/ewea_documents/documents/publications/reports/Pure_Power_Full_Report.pdf Accessed: 01 July 2014]
110. Energy Systems Research Unit. Offshore Wind Turbines. Available from: http://www.esru.strath.ac.uk/EandE/Web_sites/98-9/offshore/wind/wintr.htm [Accessed: 01 July 2014]
111. Dalén, G. (2011) Offshore Wind Power. Encyclopedia of Sustainability Science and Technology, pp. 7425-7445.
112. 4C Offshore. Project Details for Vindeby. Available from: http://www.4coffshore.com/windfarms/vindeby-denmark-dk06.html [Accessed: 30 June 2015]
113. Ackermann, T. and Söder, L. (2002) An overview of wind energy-status 2002. Renewable and Sustainable Energy Reviews 6: 67-128.
114. European Wind Energy Association (2013) Deep water - The next Step for offshore wind energy. Available from:

http://www.ewea.org/fileadmin/files/library/publications/reports/Deep_Water.pdf [Accessed: 02 July 2014]
115. 4C Offshore. Hywind - Metcentre. Available from: http://www.4coffshore.com/windfarms/Hywind-Norway-NO04.html [Accessed: 16 July 2014]
116. Energy Efficiency news (2008) UK becomes world leader in offshore wind. Available from: http://www.energyefficiencynews.com/articles/i/1456/ [Accessed: 02 July 2014]
117. European Wind Energy Association (2014) The European offshore wind industry - key trends and statistics 2013. Available from: http://www.ewea.org/fileadmin/files/library/publications/statistics/European_offshore_statistics_2013.pdf [Accessed: 02 July 2014]
118. European Wind Energy Association (2014) Wind in power 2013 European statistics. Available from: http://www.ewea.org/fileadmin/files/library/publications/statistics/EWEA_Annual_Statistics_2013.pdf [Accessed: 02 July 2014]
119. 4C Offshore. Donghai Bridge 100 MW offshore wind power demonstration project. Available from: http://www.4coffshore.com/windfarms/donghai-bridge-100mw-offshore-wind-power-demonstration-project-china-cn01.html [Accessed: 06 July 2014]
120. 4C Offshore. Welcome to the Global Offshore Wind Farms Database. Available from: http://www.4coffshore.com/windfarms/ [Accessed: 07 July 2014]
121. Global Wind Energy Council (2013) Our latest article on big ambitions ahead for Asian offshore wind. Available from: http://www.gwec.net/read-latest-article-big-ambitions-ahead-asian-offshore-wind/ [Accessed: 07 July 2015]
122. Clean Technica (2014) America's 1st Offshore Wind Farm May Be Commissioned By 2016. Available from: http://cleantechnica.com/2014/03/03/americas-first-offshore-wind-farm-may-commissioned-2016/ [Accessed: 07 July 2015]
123. Valentine, K. (2014) The First American Offshore Wind Farm Could Be Up And Running By 2016. Available from:

http://thinkprogress.org/climate/2014/02/27/3337871/cape-wind-secures-financing/ [Accessed: 07 July 2015]
124. Cape Wind (2014) Cape Wind Project Overview & Benefits. Available from: http://www.capewind.org/what [Accessed: 10 July 2015]
125. European Wind Energy Association (2011) UpWind - Design limits and solutions for very large wind turbines. Available from: http://www.ewea.org/fileadmin/ewea_documents/documents/upwind/21895_UpWind_Report_low_web.pdf [Accessed: 21 July 2015]
126. London Array. The project. Available from: http://www.londonarray.com/the-project/ [Accessed: 20 July 2015]
127. 4C Offshore. London Array Phase 1. Available from: http://www.4coffshore.com/windfarms/london-array-phase-1-united-kingdom-uk14.html [Accessed: 20 July 2014.]
128. 4C Offshore. Greater Gabbard. Available from: http://www.4coffshore.com/windfarms/greater-gabbard-united-kingdom-uk05.html [Accessed: 20 July 2014]
129. 4C Offshore. Anholt. Available from: http://www.4coffshore.com/windfarms/anholt-denmark-dk13.html. [Accessed: 20 July 2014]
130. 4C Offshore. BARD Offshore 1. Available from: http://www.4coffshore.com/windfarms/bard-offshore-1-germany-de23.html [Accessed: 20 July 2014]
131. 4C Offshore. Walney Phase 1. Available from: http://www.4coffshore.com/windfarms/walney-phase-1-united-kingdom-uk31.html [Accessed: 20 July 2014]
132. 4C Offshore. Walney Phase 2. Available from: http://www.4coffshore.com/windfarms/walney-phase-2-united-kingdom-uk32.html [Accessed: 20 July 2015]
133. 4C Offshore. Thornton Bank phase I. Available from: http://www.4coffshore.com/windfarms/thornton-bank-phase-i-belgium-be01.html [Accessed: 20 July 2014]

134. 4C Offshore. Thornton Bank phase II. Available from: http://www.4coffshore.com/windfarms/thornton-bank-phase-ii-belgium-be09.html [Accessed: 20 July 2014]
135. 4C Offshore. Thornton Bank phase III. Available from: http://www.4coffshore.com/windfarms/thornton-bank-phase-iii-belgium-be10.html [Accessed: 20 July 2014]
136. 4C Offshore. Sheringham Shoal. Available from: http://www.4coffshore.com/windfarms/sheringham-shoal-united-kingdom-uk27.html [Accessed: 20 July 2014]
137. Vattenfall (2014) Thanet Offshore Wind Farm. Available from: http://www.vattenfall.co.uk/en/thanet-offshore-wind-farm.htm [Accessed: 20 July 2014]
138. 4C Offshore. Thanet. Available from: http://www.4coffshore.com/windfarms/thanet-united-kingdom-uk29.html [Accessed: 20 July 2014]
139. 4C Offshore. Lincs. Available from: http://www.4coffshore.com/windfarms/lincs-united-kingdom-uk13.html [Accessed: 20 July 2014]
140. 4C Offshore. Horns Rev 2. Available from: http://www.4coffshore.com/windfarms/horns-rev-2-denmark-dk10.html [Accessed: 20 July 2014]
141. 4C Offshore. Rødsand 2. Available from: http://www.4coffshore.com/windfarms/r%c3%b8dsand-2-denmark-dk11.html [Accessed: 20 July 2014]
142. Wagner, H-J. and Mathur, J. (2013) Introduction to Wind Energy Systems: Basics, Technology and Operation. 2nd Ed. Green Energy and Technology, Springer, London.
143. Salameh, Z. (2014) Renewable Energy System Design. 1st Ed. Elsevier Inc., Oxford, UK.
144. Ahmed, S. (2011) Wind energy: theory and practice. 2nd Ed. PHI Learning Private Ltd, New Delhi.

145. Paraschivoiu, I. (2001) Wind Turbine Design: With Emphasis on Darrieus Concept. École Polytechnique de Montréal, Canada.
146. Cahay, M.; Luquiau, E.; Smadja, C. and Silvert, F. (2011) Use of a Vertical Wind Turbine in an Offshore Floating Wind Farm. Offshore Technology Conference, Houston, Texas.
147. GCK Technology Inc. The Gorlov Helical Turbine. Available from: http://www.gcktechnology.com/GCK/pg2.html [Accessed: 16 July 2015]
148. Balineni, S.C.; Krishna, S.R.; Kumar, B.S. and Kumar, G.V. (2011) Design and fabrication of Savonius vertical axis wind turbine. Available from: http://grietinfo.in/projects/MAIN/Mech/MECH-PROJECT%20REPORT%20OF%20VWAT-DOC.pdf [Accessed: 16 July 2015]
149. Hemami, A. (2012) Wind Turbine Technology. Cengage Learning, New York, USA.
150. Bir, G. and Jonkman, J. (2008) Modal Dynamics of Large Wind Turbines with Different Support Structures. 27th Int. Conf. on Offshore Mechanics and Arctic Engineering, Estoril, Portugal.
151. Kolios, A.; Collu, M.; Chahardehi, A.; Brennan, F.P. and Patel, M.H. (2010) A Multi-Criteria Decision Making Method to Compare Support Structures for Offshore Wind Turbines. European Wind Energy Conference and Exhibition, Warsaw.
152. Musial, W., Butterfield, S. and Ram, B. (2006) Energy from Offshore Wind. Available from: http://www.nrel.gov/wind/pdfs/39450.pdf [Accessed: 17 July 2014]
153. Van der Tempel, J.; de Vries, W. and Cerda Salzmann, D. (2007) Improving fatigue resistance for monopiles using Ultrasonic Impact Treatment (UIT). Offshore Engineering, Delft University of Technology.
154. ARUP (2010) Gravity Base Foundations. Available from: http://www.arup.com/Services/~/media/Files/PDF/Publications/Brochure/Arup_Gravity_Base_Foundations_Brochure.ashx [Accessed: 18 July 2015]
155. 4C Offshore. Gravity Based Support Structures. Available from: http://www.4coffshore.com/windfarms/gravity-based-support-structures-aid274.html [Accessed: 18 July 2014]

156. Gravitas Offshore (2011) Available from: http://www.arup.com/~/media/Files/PDF/Publications/Brochure/Gravitas_brochure_FINAL_PRESS_QUALITY2.ashx [Accessed: 18 July 2015]
157. Vici Ventus Technology AS (2011) Offshore Wind Turbines: Concrete Foundations. Available from: http://www.viciventus.no/getfile.php/Dokumenter/GBF_product_sheet_231111.pdf [Accessed: 18 July 2015]
158. Nielsen, H.L. (2013) Universal Foundation Suction Bucket. A solution in support for offshore wind. Available from: http://www.windpower.org/download/1922/14_Universal_Foundation_Suction_Bucket_Henrik_Lundorf.pdf [Accessed: 18 July 2015]
159. Ibsen, L.B., Liingaard, M. and Nielsen, S.A. (2005) Bucket Foundation, a status. Available from: http://vbn.aau.dk/files/57365677/Proceedings._Bucket_Foundation__a_status [Accessed: 18 July 2015]
160. 4C Offshore. Tripod Support Structures. Available from: http://www.4coffshore.com/windfarms/tripod-support-structures-aid273.html [Accessed: 18 July 2014]
161. 4C Offshore. Jacket or Lattice Structures. Available from: http://www.4coffshore.com/windfarms/jacket-or-lattice-structures-aid271.html [Accessed: 18 July 2014]
162. Offshore Wind.biz. (2014) Dong Energy Signs Another Suction Bucket Deal with SPT Offshore. Available from: http://www.offshorewind.biz/2014/05/22/dong-energy-signs-another-suction-bucket-deal-with-spt-offshore/ [Accessed: 18 July 2014]
163. Sanz-Martínez, M., Natarajan, A. and Henriksen, L.C. (2013) Feasibility study of a semi floating spar buoy wind turbine anchored with a spherical joint to the sea floor. Available from: http://www.innwind.eu/~/media/Sites/innwind/Publications/SemiFloatingSpar_final.ashx [Accessed: 18 July 2014]
164. Butterfield, S.; Musial, W. and Jonkman, J. (2005) Engineering Challenges for Floating Offshore Wind Turbines. Available from:

http://wind.nrel.gov/public/SeaCon/Proceedings/Copenhagen.Offshore.Wind.2005/documents/papers/Future_innovative_solutions/S.Butterfield_Engineering_Challenges_for_Floating.pdf [Accessed: 18 July 2015]
165. BSI (2009) BS EN 61400-3:2009 Wind turbines - Part 3: Design requirements for offshore. British Standards Institution, London.
166. Wilson, J.F. (2003) Dynamics of Offshore Structures. John Wiley & Sons, Inc., New Jersey.
167. Hsu, T.H. (1984) Applied Offshore Structural Engineering. Gulf Publishing, Houston.
168. American Petroleum Institute (1993) Recommended Practice for Planning, Designing and Constructing Fixed Offshore Platforms - Load and Resistance Factor Design.
169. Patel, M.H. (1989) Dynamics of offshore structures. Butterworths, London.
170. Gaythwaite, J. (1981) The Marine Environment and Structural Design. Van Nostrand Reinhold, New York.
171. Faltinsen, O. (1990) Sea Loads on Ships and Offshore Structures. Cambridge University Press, Cambridge, U.K.
172. Rademakers, L.W.M.M. and Braam, H. (2002) O&M Aspects of the 500 MW Offshore wind farm at NL7. DOWEC 10080 rev 2. Available from: https://www.ecn.nl/fileadmin/ecn/units/wind/docs/dowec/10080_002.pdf [Accessed: 12 July 2014]
173. Rademakers, L.W.M.M.; Braam, H.; Zaaijer, M.B. and van Bussel, G.J.W. (2004) Assessment and Optimisation of operation and maintenance of offshore wind turbines. Available from: https://www.ecn.nl/fileadmin/ecn/units/wind/docs/dowec/2003-EWEC-O_M.pdf [Accessed: 13 July 2015]
174. Fingersh, L.; Hand, M. and Laxson, A. (2006) Wind Turbine Design Cost and Scaling Model . Technical Report NREL/TP-500-40566. Available from: http://www.nrel.gov/docs/fy07osti/40566.pdf [Accessed: 13 July 2014]
175. Pinar-Pérez, J.M.; García-Márquez, F.P.; Tobias, A. and Papaelias, M. (2013) Wind turbine reliability analysis. Renewable and Sustainable Energy Reviews 23: 463–472.

176. Lozano-Minguez, E. (2010) Multi-criteria analysis of the optimal offshore wind turbine support structures. MSc Thesis, Cranfield University, UK.
177. Navigant Consulting, Inc. (2013) Offshore Wind Market and Economic Analysis. Annual Market Assessment. Available from: http://www1.eere.energy.gov/wind/pdfs/offshore_wind_market_and_economic_analysis_10_2013.pdf [Accessed: 21 July 2015]
178. Ernst & Young (2009) Cost of and financial support for offshore wind. Department of Energy and Climate Change. Available from: http://webarchive.nationalarchives.gov.uk/+/http://www.berr.gov.uk/files/file51142.pdf [Accessed: 21 July 2015]
179. Renewables Advisory Board (2010) Value breakdown for the offshore wind sector. Available from: https://www.gov.uk/government/uploads/system/uploads/attachment_data/file/48171/2806-value-breakdown-offshore-wind-sector.pdf [Accessed: 21 July 2015]
180. Clean Energy Pipeline (2014) Offshore Wind Project Cost Outlook 2014 Edition. Available from: http://www.cleanenergypipeline.com/Resources/CE/ResearchReports/Offshore%20Wind%20Project%20Cost%20Outlook.pdf [Accessed: 16 July 2015]
181. International Renewable Agency (2012) Renewable Energy Technologies: Cost Analysis Series. Volume 1: Power Sector, Issue 5/5. Available from: http://www.irena.org/DocumentDownloads/Publications/RE_Technologies_Cost_Analysis-WIND_POWER.pdf [Accessed: 21 July 2015]
182. Blanco, I. and Kjaer, C. (2009) Wind at Work. Wind energy and job creation in the EU. Available from: http://www.ewea.org/fileadmin/ewea_documents/documents/publications/Wind_at_work_FINAL.pdf [Accessed: 21 July 2015]
183. American Wind Energy Association (2012) Offshore wind: America's new energy opportunity. Available from: http://www.aweablog.org/blog/post/offshore-wind-americas-new-energy-opportunity_2 [Accessed: 21 July 2015]
184. Parliamentary Office of Science and Technology (2006) Footprint of Electricity Generation. Available from:

http://www.parliament.uk/documents/post/postpn268.pdf [Accessed: 14 July 2015]
185. Langhamer, O. (2012) Artificial Reef Effect in relation to Offshore Renewable Energy Conversion: State of the Art. Available from: http://www.hindawi.com/journals/tswj/2012/386713/ [Accessed: 14 July 2015]
186. European Wind Energy Association (2012) Positive environmental impacts of offshore wind farms. Available from: http://www.ewea.org/fileadmin/files/members-area/information-services/offshore/research-notes/120801_Positive_environmental_impacts.pdf [Accessed: 14 July 2015]
187. Hammar, L.; Wikström, A. and Molander, S. (2014) Assessing ecological risks of offshore wind power on Kattegat cod. Renewable Energy 66(C): 414-424.
188. U.S. Department of the Interior (2011) Effects of EMFs from undersea power cables on elasmobranchs and other marine species. Available from: http://mhk.pnl.gov/sites/default/files/publications/EMF_from_Undersea_Power_Cables_on_Elasmobranches.pdf [Accessed: 13 July 2015]
189. Drewitt, A.L. and Langston, R.H.W. (2006) Assessing the impacts of wind farms on birds. IBIS 148(s1): 29–42.
190. Desholm, M. and Kahlert, J. (2005) Avian collision risk at an offshore wind farm. Available from: http://rsbl.royalsocietypublishing.org/content/1/3/296.full [Accessed: 14 July 2015]
191. Snyder, B. and Kaiser, M.J. (2009) Ecological and economic cost-benefit analysis of offshore wind energy. Renewable Energy 34(6): 1567–1578.
192. Wahlberg, M. and Westerberg, H. (2005) Hearing in fish and their reactions to sounds from offshore wind farms. Available from: http://mhk.pnnl.gov/sites/default/files/publications/Hearing_in_Fish_and_Reaction_to_Offshore_Wind.pdf [Accessed: 14 July 2015]
193. Madsen, P. T.; Wahlberg, M.; Tougaard, J.; Lucke, K. and Tyack, P. (2006) Wind turbine underwater noise and marine mammals: implications of current knowledge and data needs. Available from: http://www.int-res.com/articles/meps2006/309/m309p279.pdf [Accessed: 14 July 2015]

194. Brandt,M.J.; Diederichs, A. and Nehls, G. (2009) Harbour porpoise responses to pile driving at the Horns Rev II offshore wind farm in the Danish North Sea. Available from: http://www.ens.dk/sites/ens.dk/files/undergrund-forsyning/vedvarende-energi/vindkraft-vindmoeller/havvindmoeller/miljoepaavirkninger-3/BioConsult%20Harbour%20porpoises.pdf [Accessed: 14 July 2015]

195. Nedwell, J.; Langworthy, J. and Howell, D. (2003) Assessment of sub-sea acoustic noise and vibration from offshore wind turbines and its impact on marine wildlife; initial measurements of underwater noise during construction of offshore windfarms, and comparison with background noise. Available from: http://users.ece.utexas.edu/~ling/2A_EU1.pdf [Accessed: 14 July 2015]

196. Parvin, S.J. and Nedwell, J.R. (2006) Underwater noise survey during impact piling to construct the Burbo Bank Offshore Wind Farm. COWRIE – ACO-04-2002. Available from: http://www.subacoustech.com/wp-content/uploads/726R0103.pdf [Accessed: 14 July 2015]

197. DONG Energy, Vattenfall, The Danish Energy Authority and The Danish Forest and Nature Agency (2006) Danish Offshore Wind – Key Environmental Issues. Available from: http://188.64.159.37/graphics/Publikationer/Havvindmoeller/danish_offshore_wind.pdf [Accessed: 14 July 2015]

198. Carstensen, J.; Henriksen, O. D. and Teilmann, J. (2006) Impacts of offshore wind farm construction on harbour porpoises: acoustic monitoring of echo-location activity using porpoise detectors (T-PODs). Marine Ecology Progress Series 321: 295-308

199. Vanhellemont, Q. and Ruddick, K. (2014) Turbid wakes associated with offshore wind turbines observed with Landsat 8. Remote Sensing of Environment 145: 105-115.

200. University of Maryland, Center for Environmental Science (2013) Offshore Wind Energy. Available from: http://www.umces.edu/cbl/wind [Accessed: 14 July 2015]

201. Edwards, I. (2011) Overcoming Challenges for the Offshore Wind Industry and Learning from the Oil and Gas Industry. Available from: http://www.power-

cluster.net/Portals/6/Offshore%20wind%20report%20Overcoming%20Challenges%20for%20the%20Offshore%20Wind%20Industry.pdf [Accessed: 19 July 2015]
202. Offshore Design Engineering Ltd. (2007) Study of the costs of offshore wind generation. Available from:
http://www.ode-ltd.co.uk/renewables/dti%20Costs%20of%20Offshore%20Wind%20Generation%20by%20ode.pdf [Accessed: 19 January 2011]
203. Gurney, T.R. (1976) Fatigue design rules for welded steel joints. The Welding Institute Research Bulletin, Vol. 17.
204. BSI (1972) BS 153-3A: Specification for steel girder bridges loads. British Standards Institution, London.
205. BSI (1980) BS 5400-10: Steel, concrete and composite bridges, Part 10-Code of practice for fatigue. British Standards Institution, London.
206. BSI (1993) BS 7608, Code of practice for Fatigue design and assessment of steel structures. British Standards Institution, London.
207. Hobbacher, A. (1982) Design recommendations for cyclic loaded welded steel structures. International Institute of Welding doc. XIII-998-81/XV-494-81, Welding in the World, Vol. 20.
208. European Convention for Constructional Steelwork (1985) Recommendations for the fatigue design of steel structures - Technical Committee 6, Lausanne.
209. Maddox, S.J. (1993) International efforts on fatigue of welded constructions. A review of Commission XIII activities, Welding in the World, Pergamon Press Ltd, Vol. 31., pp. 86-92.
210. BSI (1992) Eurocode 3: Design of steel structures - Part 1.1: General rules and rules for buildings (Draft for development), DD ENV 1993-1-1:1992. British Standards Institution, London.
211. Hobbacher, A. (1996) Fatigue Design of Welded Joints and Components. Recommendations of IIW Joint Working Group XII-1539-96/XV-845-96. International Institute of Welding, Abington Publishing, Cambridge.

212. BSI (2005) Eurocode 3: Design of steel structures - Part 1-9: Fatigue, BS EN 1993-1-9:2005. British Standards Institution, London.
213. Lotsberg, I. and Larsen, P.K. (2001) Developments in Fatigue Design Standards for Offshore Structures. Proc. 11th Int. Offshore and Polar Engineering Conference, Stavenger, Norway.
214. Haagensen, P.J. (2011) Design codes. Available from: http://www.betongrehabilitering.net/ikbViewer/Content/832096/Haagensen%20P7%20Design%20codes.pdf [Accessed: 26 July 2015]
215. DNV (2011) Recommended Practice DNV-RP-C203 Fatigue Design of offshore steel structures. Det Norske Veritas, Norway.
216. DNV (2005) Recommended Practice DNV-RP-C203. Fatigue Design of Offshore Steel Structures. Det Norske Veritas, Norway.
217. HSE (1999) Background to new fatigue guidance for steel joints and connections in offshore structures, Offshore Technology Report - OTH920390. Health and Safety Executive, Liverpool.
218. Mohaupt, U.H.; Burns, D.J.; Kalbfleisch, J.G.; Bell, R. and Vosikovsky, O. (1987) Fatigue crack development, thickness and corrosion effects in welded plate to plate joints. Proc. 3rd Int. Conf. on Steel in Marine Structures, Delft.
219. BSI (2014) BS 7608, Guide to fatigue design and assessment of steel products. British Standards Institution, London.
220. Berge, S. (1985) On the effect of plate thickness in fatigue of welds. Engineering Fracture Mechanics, 21(2): 423-435. In: Connolly, M.P.M. (1986) A fracture mechanics approach to the fatigue assessment of tubular welded Y and K-joints. PhD Thesis, Department of Mechanical Engineering, UCL, London.
221. Macdonald, K.A. and Maddox, S.J. (2002) New guidance for fatigue design of pipeline girth welds. Engineering Failure Analysis, 10(2): 177-197.
222. Zhang, Y-H.; Maddox, S.J. and Stacey, A. (2008) Re-evaluation of fatigue curves for flush ground girth welds. Proc. 12th Int. Symposium on Tubular Structures (ISTS), Shanghai, China.
223. Maddox, S.J. and Zhang, Y.H. (2008) Comparison of fatigue of girth-welds in full-scale pipes and small-scale strip specimens. Proc. 27th Int. Conf. on Offshore Mechanics and Arctic Engineering, Estoril, Portugal.

224. Ørjasæter, O.L.; Knagenhjelm, H.O. and Haagensen, P.J. (2008) Scale effects - Correlation of fatigue capacity for full-scale pipes and small-scale specimens. Proc. 27th Int. Conf. on Offshore Mechanics and Arctic Engineering, Estoril, Portugal.
225. Pereira, M. (2004) Growth of through-wall fatigue cracks in brace members. TWI Ltd Research Report 224 for the Health and Safety Executive.
226. Salama, M.M. (1999) Fatigue design of girth welded pipes and the validity of using strips. Proc. 18th Inter. Conf. on Offshore Mechanics and Arctic Engineering, Newfoundland, Canada.
227. Wastberg, S. and Salama, M.M. (2007) Fatigue testing and analysis of full scale girth welded tubulars. Proc. 26th Int. Conf. on Offshore Mechanics and Arctic Engineering, San Diego, USA.
228. Wirsching, P.; Karsan, D.I. and Hanna, S.Y. (1995) Fatigue/fracture reliability and maintainability analysis of the Heidrum TLP tether system. Proc. 14th Int. Conf. on Offshore Mechanics and Arctic Engineering, Copenhagen, Denmark.
229. UEG (1985) Design of tubular joints for offshore structures, Volume 2. UEG Offshore Resarch, Norwich.
230. American Petroleum Institute (1972) Recommended Practice for Planning, Designing and Constructing Fixed Offshore Platforms, API RP 2A. 13th Ed. Washington DC.
231. American Welding Society (1972) Structural Welding Code-Steel, AWS D1.1-72. 1st Ed. Miami.
232. Her Majesty's Stationery Office (1984) Background to new fatigue design guidance for steel welded joints in offshore structures. Report of the Department of Energy Guidance Notes Revision Drafting Panel, London.
233. Department of Energy (1977) Offshore Installations: Guidance on design, construction and certification. Her Majesty's Stationery Office Publications, London.
234. Marshall, P.W. (1974) General Considerations for Tubular Joint Design. Int. Conf. on Welding in Offshore Constructions, The Welding Institute, Paper 2.

235. Marshall, P.W. (1974) Basic considerations for Tubular Joint Design in Offshore Construction. WRC Bulletin 193.
236. Smedley, G.P. (1973) Welded Steel Structures-The Avoidance of Fatigue and Fracture. Structures in the Ocean Conference, University of California.
237. Gurney, T.R. and Maddox, S.J. (1973) A Re-Analysis of Fatigue Data for Welded Joints in Steel. Welding Research International 3(4): 1-54.
238. Failure Control Ltd. and MaTSU (1999) Background to new fatigue guidance for steel joints and connections in offshore structures. Health and Safety Executive, Offshore Technology Report - OTH 920390.
239. Failure Control Engineering & Materials Consultants (2000) Fatigue Design Curves for Welded Joints in Air & Seawater Under Variable Amplitude Loading. Health & Safety Executive, Offshore Technology report OTH 1999 058.
240. IBM (2013) GPL Reference Guide for IBM SPSS Statistics. Available from: www-01.ibm.com/suppor/docview.wss?uid=swg27038407#en [Accessed: 21 July 2015]
241. Gujarati, D.N. and Porter, D.C. (2010) Essentials of Econometrics. McGraw Hill, New York.
242. Pearson, K. (1895) Notes on regression and inheritance in the case of two parents. Proceedings of the Royal Society of London 58: 240-242.
243. Durbin, J. and Watson, G. S. (1950) Testing for Serial Correlation in Least Squares Regression - I. Biometrika 37 (3–4): 409–428.
244. Bartlett, M.S. (1937) Properties of sufficiency and statistical tests. Proceedings of the Royal Statistical Society, Series A 160, pp. 268-282.
245. Shapiro, S.S. and Wilk, M.B. (1965) An Analysis of Variance Test for Normality (Complete Samples). Biometrika 52(3/4): 591-611.
246. Fisher, R.A. (1912) On an Absolute Criterion for Fitting Frequency Curves. Messenger of Mathematics 41: 155-160.
247. Box, G.E.P. and Cox, D.R. (1964) An analysis of transformations (with discussion). Journal of the Royal Statistical Society - Statistical Methodology 26: 211-252.
248. BSI (2003) BS ISO 12107:2003 Metallic materials - Fatigue testing - Statistical planning and analysis of data. British Standards Institution, London.

249. James, G.; Witten, D.; Hastie, T. and Tibshirani, R. (2013) An Introduction to Statistical Learning with Applications in R. Springer Science & Business Media, New York.
250. Lloyd's Register of Shipping (1997) Stress concentration factors for simple tubular joints. Assessment of Existing and development of new parametric formulae. Health and Safety Executive - Offshore Technology Report, London.
251. Gibstein, M. B. (1978) Parametric stress analysis of T-joints. European Offshore Steels Research Seminar, Paper 26, Cambridge, UK.
252. Wordsworth, A.C. and Smedley, G. P. (1978) Stress concentrations at unstiffened tubular joints. European Offshore Steels Research Seminar, Paper 31, Cambridge, UK.
253. Wordsworth, A.C. (1981) Stress concentration factors at K and KT tubular joints. Fatigue in Offshore Structural Steels Conference, Institution of Civil Engineers, London.
254. Efthymiou, M. and Durkin, S. (1985) Stress concentrations in T/Y and gap/overlap K-joints. Proc. Conf. on Behaviour of Offshore Structures, pp. 429-440, Elsevier Science Publishers, Amsterdam.
255. Smedley, P.A. and Fisher, P.J. (1991) Stress concentration factors for simple tubular joints. Proc. 1st Int. Offshore and Polar Engineering Conference, Edinburgh.
256. Hellier, A.K.; Connolly, M.P. and Dover, W.D. (1990) Stress concentration factors for tubular Y- and T-joints. International Journal of Fatigue 12(1): 13-23.
257. Chang, E. and Dover, W.D. (1998) Prediction of stress distributions along the intersection of tubular Y and T-joints. International Journal of Fatigue 21(4): 361-381.
258. Chang, E. and Dover, W.D. (1999) Parametric equations to predict stress distributions along the intersection of tubular X and DT-joints. International Journal of Fatigue 21(6): 619-635.
259. SOLIDWORKS (2011) Student's Guide to Learning SolidWorks Software. Dassault Systémes - SolidWorks Corporation, Massachusetts, USA.

260. Shao, Y.B.; Du, Z.F. and Lie, S.T. (2009) Prediction of hot spot stress distribution for tubular K-joints under basic loading. Journal of constructional Steel Research 65(10-11):2011-2026.
261. American Welding Society (2006) Structural Welding Code - Steel. ANSI AWS D1.1/D1.1M:2006, Miami.
262. Irvine, N.M. (1981) Review of Stress Analysis Techniques used in UKOSRP. Fatigue in Offshore Structural Steels. Proceedings of Conference at the Institute of Civil Engineers, London.
263. European Wind Energy Association (2013) The European offshore wind industry - key trends and statistics 2012. Available from: http://www.ewea.org/fileadmin/files/library/publications/statistics/European_offshore_statistics_2012.pdf [Accessed: 21 July 2015]
264. Ernst & Young (2009) Cost of and financial support for offshore wind. Department of Energy and Climate Change. Available from: http://webarchive.nationalarchives.gov.uk/+/http://www.berr.gov.uk/files/file51142.pdf [Accessed: 21 July 2015]
265. Seidel, M. (2007) Jacket substructures for the REpower 5M wind turbine. Conference Proceedings European Offshore Wind 2007, Berlin.
266. Kawahara, M. and Iwasaki, T. (1978) Analysis of fatigue crack growth behavior in welded tubular T-joints. Proc. of the Annual Offshore Technology Conference, Vol. 3, pp. 1719-1728.
267. Kam, J.C.P., Dover, W.D. and Ma, C.N. (1994) The Prediction of Crack Shape Development for In-service Cracks in Offshore Welded Tubular Joints. Marine Structures 8(1): 37-65.
268. Ma, C.N. and Kam, J.C.P. (1991) Crack shape evolution in tubular welded joints. NDT and E International 24(6):291-302.
269. Niu, X.N., Wickham, A.H.S. and Frieze, P.A. (1990) Fracture Mechanics and Simplified Analyses in Probabilistic Remaining Life Calculations for Jacket Structures. Proc. 4th Int. Conf. Integrity of Offshore Structures, Glasgow.
270. Tweed, J.H. (1987) Remaining Life of Defective Tubular Joints: Depth of Crack Growth in UKOSRP II and Implications. Department of Energy. Offshore Technology Report OTH 87 287. Her Majesty's Stationery Office, London.

271. Etube, L.S., Brennan, F.P. and Dover, W.D. (1999) Review of empirical and semi-empirical Y factor solutions for cracked welded tubular joints. Marine Structures 12(9-10): 565-583.
272. Dover, W.D. and Dharmavasan, S. (1982) Fatigue fracture mechanics analysis of T and Y joints. Offshore Technology Conference, Paper 4404, Houston.
273. Peckover, R.S.; Fraser, R.A.W.; Crisp, H.G.; Long, D.; Chadwick, E.A. and Thorpe, T.W. (1988) United Kingdom Offshore Steels Research Project - Phase 1, Final Report - OTH 88 282. Her Majesty's Stationery Office, London.
274. Kam, J.C-P. (1989) Structural integrity of offshore tubular joints subject to fatigue. PhD Thesis, Department of Mechanical Engineering, UCL, London.
275. Chang, E. and Dover, W.D. (2005) Weight function and stress intensity factor for a semi-elliptical surface saddle crack in a tubular welded joint. Journal of Strain Analysis for Engineering Design 40(4): 301-326.
276. BSI (2013) BS 7910: Guide to methods for assessing the acceptability of flaws in metallic structures. British Standards Institution, London.
277. Huang, X. and Hancock, J.W. (1988) The stress intensity factors of semi-elliptical cracks in a tubular welded T-joint under axial loading. Engineering Fracture Mechanics 30(1): 25-35.
278. Haswell, J.V. (1992) A general fracture mechanics model for a cracked tubular joint derived from the results of a finite element parametric study. : Proc. of the 11th Offshore Mechanics and Arctic Engineering Conference III(b) pp. 267-74, Calgary, Canada.
279. Rice, J.R. and Levy, N. (1972) The Part-Through Surface Crack in an Elastic Plate. Journal of Applied Mechanics 39: 185-194.
280. Bowness, D. and Lee, M.M.K. (1993) Stress fields and stress intensity factors in tubular joints. Proc. 12th Int. Conf. on Offshore Mechanics and Arctic Engineering, pp.839-846. Glasgow
281. Bowness, D. and Lee, M.M.K. (1995) A finite element study of stress fields and stress intensity factors in tubular joints. The Journal of Strain Analysis for Engineering Design 30 (2): 135-142.

282. Lee, M.M.K. (1999) Strength, stress and fracture analyses of offshore tubular joints using finite elements. Journal of Constructional Steel Research 51(3): 265-286.
283. Abrams, M. and Hook, S. (2002) ASTER User Handbook Version 2. NASA.
284. ANSYS (2012) ANSYS Mechanical User Guide. Swanson Analysis Systems Inc., Canonsburg.
285. ANSYS (2009) ANSYS Workbench User's Guide. Swanson Analysis Systems Inc., Canonsburg, PA.
286. FEACrack (2013) User's Manual. Quest Integrity Group, Boulder, USA.
287. PRETUBE (1991) User's Manual. Veritas Sesam System, Det Norske Veritas Industry Ltd, Norway.
288. Rhee, C.; Han, H. and Gibson, G. (1991)Reliability of Solution Method and Empirical Formulas of Stress Intensity Factors for Weld Toe Cracks of Tubular Joints. Proc. 10th Offshore Mechanics and Artic Engineering Conference 3: 441-452.
289. Bowness, D. and Lee, M.M.K. (1995) The development of an accurate model for the fatigue assessment of double curved cracks in tubular joints. International Journal of Fracture 73(2):129-147.
290. Cao, J.J.; Yang, G.J.; Packer, J.A. and Burdekin, F.M. (1998) Crack modeling in FE analysis of circular tubular joints. Engineering Fracture Mechanics 61(5-6): 537-553.
291. Chiew, S.P.; Lie, S.T.; Lee, C.K. and Huang, Z.W. (2001) Stress intensity factors for a surface crack in a tubular T-joint. International Journal of Pressure Vessels and Piping 78(10): 677-685.
292. Chiew, S.P.; Lie, S.T.; Lee, C.K. and Huang, Z.W. (2003) Parametric Equations for Stress Intensity Factors of Cracked Tubular T&Y-Joints. Proc. 13th Int. Offshore and Polar Engineering Conference, Honolulu, Hawaii, USA.
293. MORFEO (2011) V1.5.2 User’s Manual. Cenaero, Brussels.
294. Moës N, Dolbow J, Belytschko, T. (1999) A finite element method for crack growth without remeshing. International Journal for Numerical Methods in Engineering 46(1):131-150.

295. Shi, J.; Chopp, D.; Lua, J.; Sukumar, N. and Belytschko, T. (2010) Abaqus implementation of extended finite element method using a level set representation for three-dimensional fatigue crack growth and life predictions. Engineering Fracture Mechanics 77(14): 2840-2863.
296. Gigliotti, L. (2012) Assessment of the applicability of XFEM in Abaqus for modeling crack growth in rubber. MSc Thesis, KTH School of Engineering Sciences, Stockholm, Sweden.
297. Giner, E.; Sukumar, N.; Tarancon, J.E. and Fuenmayor, F.J. (2009) An Abaqus implementation of the extended finite element method. Engineering Fracture Mechanics 76(3): 347-368.
298. Zamiri-Akhlaghi, F. (2014) Welding Simulation and Fatigue Assessment of Tubular K-Joints in High-Strength Steel. PhD Thesis, École Polytchnique Fédérale de Lausanne, Switzerland.
299. Sih, G.C.; Paris, P.C. and Irwin, G.R. (1965) On cracks in rectilinearly anisotropic bodies. International Journal of Fracture Mechanics 1(3): 189-203.
300. Brennan, F.P. (1994) Evaluation of stress intensity factors by multiple reference state weight function approach. Theoretical and Applied Fracture Mechanics 20(3): 249-256.
301. Oore, M. and Burns, D.J. (1980) Estimation of stress intensity factors for embedded irregular cracks subjected to arbitrary normal stress fields. Proc. 4th Int. Conf. on Pressure Vessel Technology, London.
302. Niu, X. and Glinka, G. (1989) Stress-intensity factors for semi-elliptical surface cracks in welded joints. International Journal of Fracture 40(4): 255-270.
303. American Welding Society (1996) ANSI/AWS D1.1-96 Structural Welding Code-Steel. Miami, USA.
304. Lie, S.T.; Lee, C.K. and Wong, S.M. (2003) Model and mesh generation of cracked tubular Y-joints. Engineering Fracture Mechanics 70(2): 161-184.
305. Petroski, H.J. and Achenbach, J.D. (1978) Computation of the weight function from a stress intensity factor. Engineering Fracture Mechanics 10(2): 257-266.

306. Wang, X. and Lambert, S.B. (1993) Stress intensity factors and weight functions for longitudinal semi-elliptical surface cracks in thin pipes. International Journal of Pressure Vessel & Piping 65(1): 75-87.
307. Niu, X. and Glinka, G. (1987) The weld profile effect on stress intensity factors in weldments. International Journal of Fracture 35(1): 3-20.
308. Brennan, F. P.; Peleties, P. and Hellier, A. K. (2000) Predicting weld toe stress concentration factors for T and skewed T-joints. International Journal of Fatigue 22(7): 573-584.
309. Monahan, C.C. (1994) Early fatigue crack growth in offshore structure. PhD Thesis, Department of Mechanical Engineering, UCL, London.
310. Newman, J.R. and Raju, I.S. (1981) An empirical stress-intensity factor equation for the surface crack. Engineering Fracture Mechanics 15(1-2): 185-192.
311. Aaghaakouchak, A.; Glinka, G. and Dharmavasan, S. (1989) A Load Shedding Model for Fracture Mechanics Analysis of Fatigue Cracks in Tubular Joints. Proc. 8th Int. Conf. Offshore Mechanics and Arctic Engineering, Vol. II, pp.159-165, The Hague.
312. Albrecht, P. and Yamada, K. (1977) Rapid Calculation of Stress Intensity Factors. Journal of the Structural Division 103(2): 377-389.
313. Myers, P.T. (1998) Corrosion fatigue and fracture mechanics of high strength jack up steels. PhD Thesis, Department of Mechanical Engineering, UCL, London.
314. Etube, L.S.; Brennan, F.P. and Dover, W.D. (2000) A new method for predicting stress intensity factors in cracked welded tubular joints. International Journal of Fatigue 22(6): 447-456.
315. Huang, X. (1986) A fracture mechanics analysis of the fatigue reliability of tubular welded joints. PhD Thesis, University of Glasgow, U.K.
316. Noordhoek, C. and Verheul, A. (1984) Comparison of the ACPD Method of In-depth Fatigue Crack Growth Monitoring with the Crack Front Marking Technique. Delft University of Technology. Department of Civil Engineering. Report 6-84-13. In: Ritchie, D. and Voermans, C.W.M. (1987) Stress intensity

factors in an offshore tubular joint test specimen. 4th Int. Conf. on Numerical Methods in Fracture Mechanics, San Antonio, TX.
317. Dover, W.D. (1981) Fatigue fracture mechanics analysis of offshore structures. International Journal of Fatigue 3(2): 52-60.
318. Dover, W.D.; Chaudhury, G.K. and Dharmavasan, S. (1981) Experimental and finite element comparison of local stress and compliance in tubular weld T-joints. Int. Conf. - Steel in Marine Structures, Paris.
319. Dover, W.D. and Holdbrook, S.J. (1980) Fatigue crack growth in tubular welded connections. International Journal of Fatigue 2(1): 37-43.
320. Breusch, T.S. and Pagan, A.R. (1979) A Simple Test for Heteroscedasticity and Random Coefficient Variation. Econometrica 47(5): 1287-1294.
321. Freud, R.J.; Wilson, W.J. and Sa, P. (2006) Regression Analysis. Statistical Modeling of a Response Variable. Academic Press, Elsevier, California, USA.
322. Google (2014) Currency calculator. Available from: https://www.google.es/webhp?sourceid=chrome-instant&ion=1&espv=2&ie=UTF-8#q=us+dollar+to+euro [Accessed 21 July 2014]

APPENDICES

Appendix A Chang-Dover's parametric equation coefficients

a) Subjected to membrane loading

$$C_o = -\left(\frac{a}{c}\right)^{0.271+0.0108/\zeta_t}\left(\frac{L}{T}\right)^{-0.02714/\zeta_t} exp\left[0.6805 - \frac{0.07525}{\frac{L}{T}} - \frac{0.1702}{\sin\zeta_t} - \frac{0.0016}{\left(\frac{a}{c}\right)^2}\right.$$
$$\left. + 1.7858\left(\frac{a}{c}\right)^4 - 1.274\,\frac{\rho}{T} - 1.871\left(\frac{a}{c}\right)^3 + \frac{0.02618}{\frac{a}{c}}\right]$$

$$C_1 = 2.833 - 0.144\sqrt{\frac{a}{c}} + 9.63\left(\frac{a}{c}\right)^4 - 10.49\left(\frac{a}{c}\right)^3 - 2.051\,\frac{\rho/T}{\zeta_t} + \frac{0.00459}{\frac{a}{c}}$$
$$- \frac{0.0781}{\frac{L}{T}} - 0.0428\frac{L/T}{\zeta_t}$$

$$C_2 = -6.798 - 3.289\ln\left(\frac{a}{c}\right) + 9.034\,\frac{a}{c} + \frac{0.00106}{\left(\frac{a}{c}\right)^2} - 2.772\left(\frac{a}{c}\right)^4 - \frac{0.1858}{\frac{a}{c}}$$
$$+ 0.0185\frac{L/T}{\zeta_t} + 1.248\,\frac{\rho}{T}$$

$$C_3 = -0.09611 + \frac{0.02331}{\frac{L}{T}} - 0.2307\sin\zeta_t - 0.1577\sqrt{\frac{a}{c}} + 0.671\,\zeta_t\frac{\rho}{T} - 0.663\left(\frac{a}{c}\right)^4$$
$$+ 0.757\left(\frac{a}{c}\right)^3 + 0.0315\ln\left(\frac{a}{c}\right) + 0.00956\frac{L/T}{\zeta_t} - 0.0237\,\ln\left(\frac{L}{T}\right)$$

b) Subjected to bending loading

$$C_o = -1.525 - 0.481\zeta_t\frac{L}{T} + 0.2098\left(\frac{L}{T}\right)^2 - \frac{0.00018}{\left(\frac{a}{c}\right)^2} + 2.035\frac{a}{c} - 0.055\frac{\ln\left(\frac{a}{c}\right)}{\zeta_t}$$
$$+ \frac{0.1316}{\frac{L}{T}} - 3.07\left(\frac{a}{c}\right)^3 + \frac{0.658}{\sin\zeta_t} + \frac{0.0246}{\frac{a}{c}} + 1.96\left(\frac{a}{c}\right)^4 + 0.264\frac{\ln\left(\frac{L}{T}\right)}{\zeta_t}$$
$$- 0.344\frac{\frac{L}{T}}{\zeta_t} - 0.00419\left(\frac{L}{T}\right)^4 + 6.59\zeta_t\frac{\rho}{T} - 11.49\frac{\left(\frac{\rho}{T}\right)^2}{L/T} - 2.59\frac{\rho}{T}\frac{a}{c}$$

$$C_1 = 4.042 - 13.72\left(\frac{a}{c}\right)^{1.5} - \frac{0.0938}{\frac{a}{c}} + \frac{0.279}{\sin\zeta_t} - \frac{0.1831}{\frac{L}{T}} - 23.32\left(\frac{a}{c}\right)^{3} - 13.4\,\zeta_t\,\frac{\rho}{T}$$
$$+ \frac{0.00066}{\left(\frac{a}{c}\right)^{2}} - 13.1\left(\frac{a}{c}\right)^{4} - 0.3483\frac{\ln\left(\frac{L}{T}\right)}{\zeta_t} + 0.434\ln\left(\frac{L}{T}\right) + 25.4\frac{\left(\frac{\rho}{T}\right)^{2}}{L/T}$$
$$+ 0.1231\frac{\ln\left(\frac{a}{c}\right)}{\zeta_t} + 1.33\ln\zeta_t + 6.12\frac{\rho}{T}\zeta_t\frac{a}{c}$$

$$C_2 = -4.006 + \frac{0.21729}{\frac{a}{c}} - 2.926\left(\frac{a}{c}\right)^{2} - \frac{0.00154}{\left(\frac{a}{c}\right)^{2}} + 5.56\frac{a}{c} + \frac{0.38}{\sin\zeta_t} + 3.47\,\zeta_t\frac{\rho}{T}$$
$$+ \frac{0.0325}{L/T}$$

$$C_3 = -\left(\frac{a}{c}\right)^{0.1457/\zeta_t}\left(\frac{L}{T}\right)^{0.146} exp\left[0.521 - 0.566\frac{a/c}{\zeta_t} - \frac{0.1272}{\frac{L}{T}} - 1.1\sqrt{\frac{a}{c}}\right.$$
$$\left. - 0.0751\frac{L/T}{\zeta_t} + 0.0798\left(\frac{a}{c}\right)^{2}\frac{L}{T} - \frac{0.00049}{\frac{a}{c}\,\frac{L}{T}} - 3.303\frac{\rho}{T}\right]$$

Appendix B 3D solid FE models

	α	β	γ	τ	$\mathbb{R}$ (mm)	ω (°)	F (mm)	a (mm)	c (mm)	a/T	K_I (Pa m$^{1/2}$)	$Y_I\ nom$	$SCF\ max$	θ (rad)	DoB
Case 1	19.12	0.77	7.00	1.00	4.000	50	12.7	7.94	55.14	0.3126	2359300.0	2.490	14.131	0.014	0.535
Case 2	16.87	0.77	7.00	1.00	4.000	50	12.7	12.20	59.74	0.4803	2766550.0	2.355	12.735	0.014	-
Case 3	14.62	0.77	7.00	1.00	4.000	50	12.7	7.94	55.14	0.3126	2520483.3	2.660	11.343	0.014	0.589
Case 4	12.37	0.77	7.00	1.00	4.000	50	12.7	10.07	57.43	0.3965	2849900.0	2.670	16.338	0.579	0.743
Case 5	16.87	0.77	7.00	1.00	4.000	50	12.7	7.94	55.14	0.3126	2430883.3	2.565	-	-	-
Case 6	14.62	0.77	7.00	1.00	4.000	50	12.7	10.07	57.43	0.3965	2753850.0	2.580	11.343	0.014	0.589
Case 7	12.37	0.77	7.00	1.00	4.000	50	12.7	12.20	59.74	0.4803	2966133.3	2.525	16.338	0.579	0.743
Case 8	12.94	0.77	7.00	1.00	4.000	50	12.7	7.94	55.14	0.3126	2607766.7	2.752	10.418	0.373	0.597
Case 9	12.94	0.77	7.00	1.00	4.000	50	12.7	10.07	57.43	0.3965	2825666.7	2.648	10.418	0.373	0.597
Case 10	12.94	0.77	7.00	1.00	4.000	50	12.7	12.20	59.74	0.4803	2941100.0	2.504	10.418	0.373	0.597
Case 11	23.23	0.77	7.00	1.00	4.000	50	6.35	12.70	58.05	0.5000	3064000.0	2.557	23.885	0.502	0.712
Case 12	23.23	0.77	7.00	1.00	4.000	50	6.35	7.20	80.17	0.2833	3226283.3	3.576	23.885	0.502	0.712
Case 13	23.23	0.77	7.00	1.00	4.000	50	6.35	15.74	61.85	0.6198	3025850.0	2.268	23.885	0.502	0.712
Case 14	23.23	0.77	7.00	1.00	4.000	50	6.35	9.90	54.26	0.3896	3023533.3	2.858	23.885	0.502	0.712
Case 15	30.00	0.77	7.00	1.00	4.000	50	6.35	12.70	58.05	0.5000	2766500.0	2.308	-	-	-
Case 16	25.87	0.77	7.00	1.00	4.000	50	6.35	15.74	61.85	0.6198	3025383.3	2.267	25.868	0.483	0.596
Case 17	20.25	0.77	7.00	1.00	4.000	50	6.35	7.20	80.17	0.2833	3222800.0	3.572	21.693	0.512	0.762
Case 18	13.50	0.77	7.00	1.00	4.000	50	6.35	9.90	54.26	0.3896	3460583.3	3.271	17.273	0.560	0.736
Case 19	20.25	0.77	7.00	1.00	4.000	50	6.35	7.20	80.17	0.2833	3354150.0	3.718	21.693	0.512	0.762
Case 20	10.00	0.71	14.38	0.79	2.844	57	5	9.60	65.42	0.6000	7417566.7	7.119	19.033	1.551	0.796
Case 21	10.00	0.71	14.38	0.79	2.844	57	5	5.13	60.70	0.3206	7142583.3	9.377	19.033	1.551	0.796
Case 22	10.00	0.71	14.38	0.79	2.844	57	5	5.45	54.06	0.3406	6937200.0	8.836	19.033	1.551	0.796

Case 23	10.00	0.71	14.38	0.79	2.844	57	5	7.37	63.07	0.4606	7673566.7	8.405	19.033	1.551	0.796
Case 24	10.00	0.71	14.38	0.79	2.844	57	5	11.83	67.91	0.7396	6500166.7	5.619	19.033	1.551	0.796
Case 25	14.35	0.71	14.38	0.79	2.844	57	5	9.60	65.42	0.6000	7610466.7	7.304	19.733	1.551	0.796
Case 26	12.17	0.71	14.38	0.79	2.844	57	5	11.83	67.91	0.7396	6706200.0	5.797	19.633	1.551	0.801
Case 27	17.39	0.71	14.38	0.79	2.844	57	5	5.13	60.70	0.3206	7383183.3	9.693	19.700	1.392	0.793
Case 28	19.57	0.71	14.38	0.79	2.844	57	5	7.37	63.07	0.4606	7874833.3	8.625	19.681	1.336	0.790
Case 29	21.74	0.71	14.38	0.79	2.844	57	5	5.45	54.06	0.3406	6985150.0	8.897	19.700	1.284	0.787
Case 30	16.96	0.71	15.30	0.84	2.844	57	5	9.60	65.42	0.6386	8399983.3	8.062	22.039	1.571	0.698
Case 31	17.83	0.71	15.30	0.84	2.844	57	5	5.13	60.70	0.3412	8509483.3	11.172	22.014	1.571	0.667
Case 32	10.00	0.71	16.79	0.93	2.844	57	5	5.45	54.06	0.3978	9306983.3	11.855	25.230	1.555	0.699
Case 33	16.09	0.71	15.30	0.84	2.844	57	5	7.37	63.07	0.4902	8836316.7	9.679	22.067	1.571	0.699
Case 34	15.65	0.71	13.53	0.75	2.844	57	5	11.83	67.91	0.6959	6364800.0	5.503	18.118	1.499	0.741
Case 35	13.48	0.71	15.30	0.84	2.844	57	5	9.60	65.42	0.6386	8396383.3	8.058	22.048	1.571	0.700
Case 36	12.17	0.71	13.53	0.75	2.844	57	5	11.83	67.91	0.6959	6354583.3	5.494	17.891	1.530	0.776
Case 37	13.91	0.71	15.30	0.84	2.844	57	5	5.13	60.70	0.3412	8578666.7	11.263	22.075	1.571	0.700
Case 38	13.04	0.71	15.30	0.84	2.844	57	5	7.37	63.07	0.4902	8810333.3	9.650	22.013	1.571	0.700
Case 39	10.00	0.71	15.65	0.86	2.844	57	5	5.45	54.06	0.3707	8170333.3	10.407	22.035	1.555	0.700
Case 40	14.35	0.71	12.78	0.71	2.844	57	5	9.60	65.42	0.5333	6239600.0	5.988	16.667	1.571	0.777
Case 41	14.35	0.71	12.78	0.71	2.844	57	5	7.37	63.07	0.4094	6196666.7	6.787	16.667	1.571	0.777
Case 42	14.35	0.71	12.78	0.71	2.844	57	5	5.13	60.70	0.2850	5770566.7	7.576	16.667	1.571	0.777
Case 43	14.35	0.71	12.78	0.71	2.844	57	5	11.83	67.91	0.6572	5936800.0	5.133	16.667	1.571	0.777
Case 44	14.35	0.71	12.78	0.71	2.844	57	5	8.11	63.85	0.4506	6225683.3	6.501	16.667	1.571	0.777
Case 45	10.00	0.71	12.78	0.71	2.844	57	5	9.60	65.42	0.5333	6105933.3	5.860	16.322	1.571	0.778
Case 46	10.00	0.71	12.78	0.71	2.844	57	5	7.37	63.07	0.4094	6064450.0	6.642	16.322	1.571	0.778
Case 47	10.00	0.71	12.78	0.71	2.844	57	5	5.13	60.70	0.2850	5650516.7	7.418	16.322	1.571	0.778
Case 48	10.00	0.71	12.78	0.71	2.844	57	5	11.83	67.91	0.6572	5811616.7	5.024	16.322	1.571	0.778
Case 49	10.00	0.71	12.78	0.71	2.844	57	5	8.11	63.85	0.4506	6093166.7	6.362	16.322	1.571	0.778
Case 50	20.43	0.71	10.95	0.48	5.633	52	5	9.60	65.42	0.4571	3488300.0	3.348	10.648	1.212	0.831

Case 51	15.22	0.71	10.95	0.48	5.633	52	5	9.60	65.42	0.4571	3534266.7	3.392	10.457	1.228	0.792
Case 52	20.43	0.71	10.95	0.48	5.633	52	5	5.13	60.70	0.2443	3095783.3	4.064	10.648	1.212	0.831
Case 53	15.22	0.71	10.95	0.48	5.633	52	5	5.13	60.70	0.2443	3137983.3	4.120	10.457	1.228	0.792
Case 54	20.43	0.71	10.95	0.48	5.633	52	5	7.37	63.07	0.3510	3360733.3	3.681	10.648	1.212	0.831
Case 55	15.22	0.71	10.95	0.48	5.633	52	5	7.37	63.07	0.3510	3404833.3	3.729	10.457	1.228	0.792
Case 56	17.83	0.71	13.53	0.59	5.633	52	5	5.13	60.70	0.3018	4993416.7	6.556	14.729	1.196	0.796
Case 57	17.83	0.71	13.53	0.59	5.633	52	5	9.60	65.42	0.5647	5394866.7	5.177	14.729	1.196	0.796
Case 58	15.22	0.71	13.53	0.59	5.633	52	5	9.60	65.42	0.5647	5398600.0	5.181	14.601	1.196	0.919
Case 59	15.22	0.71	13.53	0.59	5.633	52	5	5.13	60.70	0.3018	5014250.0	6.583	14.601	1.196	0.919
Case 60	14.35	0.71	14.38	0.79	2.844	57	5	7.37	63.07	0.4606	7900233.3	8.653	19.733	1.551	0.796
Case 61	12.61	0.71	14.38	0.79	2.844	57	5	7.37	63.07	0.4606	7873100.0	8.624	19.677	1.551	0.797
Case 62	16.52	0.71	14.84	0.82	2.844	57	5	11.83	67.91	0.7632	6852383.3	5.924	20.930	1.552	0.792
Case 63	12.17	0.71	14.84	0.82	2.844	57	5	11.83	67.91	0.7632	6815083.3	5.892	20.816	1.552	0.794
Case 64	12.94	0.77	7.00	1.00	4.000	50	12.7	14.33	99.49	0.5642	3238566.7	2.544	10.418	0.373	0.597
Case 65	15.75	0.77	7.00	1.00	4.000	50	6.35	18.79	108.43	0.7398	2826716.7	1.939	18.582	0.541	0.723
Case 66	14.35	0.71	14.38	0.79	2.844	57	5	5.13	60.70	0.3206	7076983.3	9.291	19.733	1.551	0.796
Case 67	23.23	0.77	7.00	1.00	4.000	50	6.35	4.20	54.15	0.1654	2689200.0	3.902	23.885	0.502	0.712
Case 68	12.17	0.71	14.38	0.79	2.844	57	5	5.13	60.70	0.3206	7041650.0	9.245	19.633	1.551	0.801
Case 69	12.37	0.77	7.00	1.00	4.000	50	6.35	4.20	54.15	0.1654	3107416.7	4.509	16.338	0.579	0.743
Case 70	12.04	0.50	14.28	0.50	6.000	52	6	10.50	49.23	0.3281	5876233.3	5.392	22.058	1.571	0.785
Case 71	12.04	0.50	14.28	0.50	6.000	52	6	12.67	61.60	0.3959	6238100.0	5.211	22.058	1.571	0.785
Case 72	12.04	0.50	14.28	0.50	6.000	52	6	6.87	16.37	0.2147	4617783.3	5.239	22.058	1.571	0.785
Case 73	12.04	0.50	14.28	0.50	6.000	52	6	8.79	20.50	0.2747	4652150.0	4.666	22.058	1.571	0.785
Case 74	17.52	0.40	22.83	0.73	2.200	45	4	4.82	17.23	0.3213	8720916.7	11.812	44.882	1.571	0.841
Case 75	17.52	0.40	22.83	0.73	2.200	45	4	6.33	20.93	0.4220	8530983.3	10.083	44.882	1.571	0.841
Case 76	17.52	0.40	22.83	0.73	2.200	45	4	7.86	25.17	0.5240	7937600.0	8.419	44.882	1.571	0.841
Case 77	14.60	0.40	22.83	0.73	2.200	45	4	4.82	17.23	0.3213	8613550.0	11.666	44.297	1.571	0.841
Case 78	14.60	0.40	22.83	0.73	2.200	45	4	6.33	20.93	0.4220	8428033.3	9.961	44.297	1.571	0.841

Case 79	14.60	0.40	22.83	0.73	2.200	45	4	7.86	25.17	0.5240	7843966.7	8.320	44.297	1.571	0.841
Case 80	14.00	0.25	12.51	0.36	5.000	54	3	3.42	25.30	0.1869	2417300.0	3.887	11.332	1.571	0.845
Case 81	14.60	0.40	30.31	0.97	2.200	45	4	6.33	20.93	0.5602	11657166.7	13.777	72.758	1.571	0.789
Case 82	14.60	0.40	30.31	0.97	2.200	45	4	7.86	25.17	0.6956	9052050.0	9.601	72.758	1.571	0.789
Case 83	14.00	0.25	12.51	0.36	5.000	54	3	6.75	28.50	0.3689	2561833.3	2.932	11.332	1.571	0.845
Case 84	12.23	0.25	12.51	0.36	5.000	54	3	3.42	25.30	0.1869	2412283.3	3.879	11.299	1.571	0.853
Case 85	14.00	0.25	14.31	0.41	5.000	54	3	3.42	25.30	0.2138	3070816.7	4.938	12.979	1.571	0.846
Case 86	14.00	0.25	13.47	0.39	5.000	54	3	3.42	25.30	0.2012	2757733.3	4.434	12.885	1.571	0.850
Case 87	12.01	0.25	13.47	0.39	5.000	54	3	4.53	26.40	0.2665	2827850.0	3.951	12.826	1.571	0.850
Case 88	14.60	0.40	18.72	0.60	2.200	45	4	6.33	20.93	0.3459	6486650.0	7.666	30.698	1.487	0.806
Case 89	14.60	0.40	18.72	0.60	2.200	45	4	4.82	17.23	0.2634	6380116.7	8.641	30.698	1.487	0.806
Case 90	23.02	0.40	18.72	0.60	2.200	45	4	7.86	25.17	0.4295	6346916.7	6.732	30.953	1.487	0.803
Case 91	23.02	0.40	18.72	0.60	2.200	45	4	6.33	20.93	0.3459	6501566.7	7.684	30.953	1.487	0.803
Case 92	23.02	0.40	18.72	0.60	2.200	45	4	4.82	17.23	0.2634	6431800.0	8.711	30.953	1.487	0.803
Case 93	23.02	0.40	30.31	0.97	2.200	45	4	7.86	25.17	0.6956	9405583.3	9.976	75.917	1.571	0.789
Case 94	23.02	0.40	30.31	0.97	2.200	45	4	6.33	20.93	0.5602	11931666.7	14.102	75.917	1.571	0.789
Case 95	23.02	0.40	30.31	0.97	2.200	45	4	4.82	17.23	0.4265	13459166.7	18.229	75.917	1.571	0.789
Case 96	23.02	0.40	21.41	0.69	2.200	45	4	4.82	17.23	0.3013	7926300.0	10.735	39.177	1.571	0.831
Case 97	23.02	0.40	21.41	0.69	2.200	45	4	6.33	20.93	0.3956	7830533.3	9.255	39.177	1.571	0.831
Case 98	23.02	0.40	21.41	0.69	2.200	45	4	7.86	25.17	0.4913	7447300.0	7.899	39.177	1.571	0.831
Case 99	20.44	0.40	21.41	0.69	2.200	45	4	4.82	17.23	0.3013	7934966.7	10.747	48.477	1.571	0.838
Case 100	20.44	0.40	21.41	0.69	2.200	45	4	6.33	20.93	0.3956	7840200.0	9.266	48.477	1.571	0.838
Case 104	12.94	0.77	7.00	1.00	4.000	50	12.7	5.81	52.74	0.2286	2126300.0	2.624	10.418	0.373	0.597
Case 105	10.00	0.71	14.38	0.79	2.844	57	5	4.37	52.32	0.2731	6555633.3	9.325	19.033	1.551	0.796
Case 106	10.00	0.71	14.38	0.79	2.844	57	5	3.59	48.17	0.2245	6264700.0	9.829	19.033	1.551	0.796
Case 107	10.00	0.71	14.38	0.79	2.844	57	5	14.07	69.99	0.8793	4331100.0	3.434	19.033	1.551	0.796
Case 108	14.35	0.71	12.78	0.71	2.844	57	5	4.11	55.30	0.2283	5370900.0	7.878	16.667	1.571	0.777
Case 109	14.35	0.71	12.78	0.71	2.844	57	5	14.07	70.26	0.7816	5005366.7	3.968	16.667	1.571	0.777

Case 110	10.00	0.71	12.78	0.71	2.844	57	5	4.11	55.30	0.2283	5257750.0	7.712	16.322	1.571	0.778
Case 111	10.00	0.71	12.78	0.71	2.844	57	5	14.07	70.26	0.7816	5187866.7	4.113	16.322	1.571	0.778
Case 112	14.00	0.25	12.51	0.36	5.000	54	3	4.53	26.36	0.2474	2489983.3	3.480	11.332	1.571	0.845
Case 113	14.00	0.25	12.51	0.36	5.000	54	3	7.31	29.63	0.3995	2573533.3	2.830	11.332	1.571	0.845
Case 114	14.00	0.25	12.51	0.36	5.000	54	3	9.44	32.40	0.5158	2370533.3	2.294	11.332	1.571	0.845
Case 115	14.00	0.25	12.51	0.36	5.000	54	3	5.64	33.46	0.3080	2529783.3	3.168	11.332	1.571	0.845
Case 116	14.00	0.25	12.51	0.36	5.000	54	3	11.79	37.91	0.6441	2350416.7	2.036	11.332	1.571	0.845